

Granitoids from the European Variscides: an approach to their emplacement and tectonometamorphic history

Dissertation
zur Erlangung des Doktorgrades
der Naturwissenschaften

vorgelegt beim Fachbereich Geowissenschaften / Geographie
der Johann Wolfgang Goethe - Universität
in Frankfurt am Main

von
Elena Galadí-Enríquez
aus Córdoba

Frankfurt am Main 2007

D30

vom Fachbereich Geowissenschaften / Geographie der Johann Wolfgang Goethe –
Universität als Dissertation angenommen

Dekan: Prof. Dr. Gerhard Brey

Gutachter: Prof. Dr. Gernold Zulauf, Prof. Dr. Jesús Galindo-Zaldívar

Datum der Disputation: 19.12.2007

Acknowledgments

I would like to dedicate a couple of words to the people who made it possible for this work to get done...

... first of all, thanks to the directors of this PhD thesis, Prof. Dr. Gernold Zulauf and Prof. Dr. Jesús Galindo-Zaldívar, for the confidence they put on me at the beginning and during the course of the work

... the members of the Bavarian Environment Agency, especially Dr. Johann Rohrmüller, who showed a particular interest in my work and facilitated the financial support for the geological mapping in the Bavarian Forest and related investigations

... the Ministerio de Educación, Cultura y Deporte of Spain, for the financial support during the first phase of this work

... the staff of the Department of Geodynamics at the University of Granada, especially Prof. Dr. Fernando Simancas, Prof. Dr. González-Lodeiro and Dr. Antonio Azor, for inviting me to take part in the activities of their investigation group

... the people of different German and Spanish universities who made their valuable contribution to this work, Dr. Florian Heidelberg, Dr. Wolfgang Dörr, Dr. Fernando Álvarez-Lobato, Dr. Wolfgang Siebel, Dr. Heidi Höfer, Dr. Volker von Seckendorff, Prof. Dr. Giselher Propach and Gudrun Klein

... the Institute of Geology and Mineralogy of the University Erlangen-Nürnberg, at which some part of my investigations was carried out

... the colleagues who mapped the Bavarian Forest with me, especially Ulrich Blaha, who showed me impressive outcrops

... my scientific brothers and sisters, now scattered all around the world, Patricia Ruano, Fernando Bohoyo, Carlos Marín-Lechado, Sandra Romano, Gautier Njiekak, Thomas Klein, Mathurin Enama Mengong and Janet Zulauf

... the people I met working in the Bavarian Forest, especially the Tauer family

... the one who introduced me to the world of Geology at the secondary school, José Valdivia, thanks for the marvellous lessons and the story about Alfred Wegener

... my parents, my brothers and sister and their families, Rüdiger, for being there...

To all of them... Thanks... Danke... Gracias!

Abstract

This work analyses several granitic bodies of the Variscan Orogen of Central and Western Europe in order to improve our knowledge about different aspects of their evolution, regarding their ascent and emplacement mechanisms, as well as their deformation history. The study areas concerned in this work are located in two sections of the Variscan Orogen: the Iberian and the Bohemian Massifs.

In the Iberian Massif two granitoid bodies showing mainly magmatic structures and no appreciable solid-state deformation, namely the La Bazana pluton and the Nisa-Albuquerque batholith, were studied in order to decipher their ascent and emplacement history. Their study was undertaken by means of classical techniques of structural geology and petrology, as well as geophysical (gravimetric and magnetic) methods.

The La Bazana pluton is a small, sub-circular body in map view that intruded into Cambrian slates, metagreywackes and volcanics of the Ossa-Morena Zone in the core of a late upright antiform. The intrusion took place at the end of or after the main Variscan ductile deformations. The granite shows a dome-shaped fabric pattern. Magmatic foliations usually dip shallowly towards the host rock. The NW—SE regional attitude of the main foliation in the country rock accommodates to the dome shape of the pluton, showing gentle deflections around it. Flattening of the host rock on top of the granite is indicated by boudinaged and folded veins. These structures are thought to be caused by the upward pushing of the magma during its ascent and arrival at the site of emplacement. The level of final emplacement was deduced from the mineral associations in the thermal aureole to be of 7–10 km in depth. Aeromagnetic data reveal no significant anomalies related to the granite, meaning that it is homogeneous in composition. Models of the residual gravity anomaly related to the granite body show that the granite has a teardrop–pipe shape widened at its top. The modelled granite thickness varies, depending on the assumed density contrasts, between 4 and 10 km, whereas its teardrop–pipe shape remains nearly unchanged. The results suggest that the magma ascended diapirically through the middle crust until reaching a level of higher viscosity, where final emplacement accompanied by late-magmatic lateral expansion and vertical shortening took place.

The Nisa-Albuquerque batholith is a 1000 km² granitic body that intruded during the Late Carboniferous into rocks of the Central Iberian Zone, the Central Unit, and the Ossa-Morena Zone after the Variscan ductile deformation phases. Its cartographic shape is elongate and parallel to the NW—SE to WNW—ESE Variscan structures. The structure of the dominant facies, i.e. the Coarse-Grained Granite, is characterized by chaotic fabrics in the eastern part, NW—SE striking fabrics in the central sector and N—S striking fabrics in the western part. In general, the fabric parallels the longest dimension of the batholith, the external contacts and the regional foliation in the host rocks, except in the westernmost termination where it is strongly oblique to the regional foliation.

Several datings on the Coarse-Grained Granite yielded ages between 285 and 310 Ma. Its intrusion depth was estimated to be 7-10 km. The batholith is gravimetrically modelled as an east-southeast inclined cylinder-shaped body that becomes flat-floored and superficial to the west. The models revealed the existence of a prominent root at the eastern termination of the batholith. The eastern root, which coincides with the more leucocratic, younger facies, is interpreted as a feeding channel. The internal fabric in the central part of the batholith can be explained as a result of the combination of nearly uniform to non-coaxial flow, producing NW—SE striking magmatic fabrics. The N—S striking fabrics at the western end of the batholith are interpreted as an effect of the deceleration flow and the pushing of incoming magma batches. The intrusion is viewed as a continuous lateral magma flow from the eastern root guided towards the west through the southern limb of a kilometre-scale antiform. As mass-transfer mechanisms, a combination of rigid translation of the country rocks, stoping, and possibly ballooning is proposed.

In the Bohemian Massif several small granitoid bodies showing a strong solid-state deformation were studied in order to integrate their tectonometamorphic history in the geotectonic framework of the south-western Bohemian Massif, focusing principally on the deformation phase referred to as D_3 . The methods used in this region were: geological mapping, optical microscopy, electron backscatter diffraction (EBSD), strain analysis, X-ray fluorescence analysis, electron microprobe analysis and piezometry.

The study area is situated in the southern Bavarian Forest, in the area located between the Bayerischer Pfahl and the Danube shear zones in the neighbourhood of the Fürstenstein Pluton. The rocks which crop out here belong to the Moldanubian Zone. These are mainly high-grade gneisses and migmatites derived from sedimentary protoliths with intercalations of magmatic rocks. The most important metamorphic event, the Variscan one, is characterized by high temperature and low pressure and linked to anatexis. It occurred between 330 and 316 Ma in the study area.

The research related to the geological mapping of the topographic sheet 1:25000 No. 7246 Tittling delivered valuable basis information for this PhD thesis. The results allowed a better understanding of some of the rock types present in the southern Bavarian Forest, as well as the discovery of several granitic bodies affected by D_3 .

A succession of magmatic bodies of dioritic to granitic composition intruded at different stages of the Variscan Orogeny. The more mafic bodies, of dioritic to granodioritic composition, intruded at around 335 Ma. Small granitoid stocks and dykes intruded pervasively in the migmatites between 322 ± 5 and 331 ± 9 Ma. One of these bodies, the Saunstein granite dyke, intruded at 324.4 ± 0.8 Ma. Mainly after the intrusion of the former small granitic bodies, the igneous activity concentrated in the areas of the Fürstenstein and the Hauzenberg plutons: The Saldenburg granite and the Hauzenberg granite II intruded at 315 ± 3 Ma and 320 ± 3 Ma, respectively. The last magmatic episode ascribed to the Variscan Orogeny in the study area is represented by sub-

volcanic dykes of rhyolitic to basaltic andesitic composition. Two datings on these rocks yielded 302 ± 7 and 299.0 ± 2.3 Ma. The shape and structure of all of these intrusives reflects to some extent the thermal evolution of the crust in which they ascended and froze. Elliptical, irregular or elongate intrusive bodies, usually older than ~ 310 Ma, intruded into a relatively hot crust. The way they ascended is not well known, but the exploitation of pre-existing anisotropies seems to be the most efficient mechanism in this context. Some contribution of diapirism is conceivable in some of the largest and more equidimensional bodies, such as the Hauzenberg granite II and the Saldenburg granite. The emplacement of granitic end-members was accompanied by pervasive stoping of the dioritic to granodioritic and migmatitic country rocks. The intrusive bodies younger than ~ 310 Ma are dykes of sharp and planar contacts, suggesting ascent by means of dyking in a relatively cold crust.

The major tectonic features of the study area can be described in the context of the so-called Bayerischer Pfahl shear-zone system, extending over more than 200 km at the south-western border of the Bohemian Massif. It consists of subvertical NW—SE trending dextral shears, subsidiary NNW—SSE trending dextral shears and conjugate NE—SW trending sinistral shears. The latter have been active over a wide time and temperature span ranging from amphibolite facies to near-surface conditions. The Bayerischer Pfahl shear-zone system was probably active, at least during its ductile history, under compression in N—S to NNW—SSE direction.

Four ductile deformation phases are proposed for the study area. D_1 produced high-temperature fabrics under upper amphibolite to granulite facies conditions, probably coinciding with the thermal peak of the regional high-temperature/low-pressure metamorphism. Its kinematics is unknown. D_1 is usually obscured by later deformation phases, but still identifiable as a relict. D_2 occurred under amphibolite to upper greenschist facies conditions, as evidenced by lattice-preferred orientation patterns and microfabrics. It is responsible for a subvertical NW—SE striking foliation in migmatites developed under dextral simple shear and for the deformation at the Bayerischer Pfahl shear-zone system at its earlier stages. Most of the dioritic to granodioritic bodies and some of the granitic ones intruded prior to or during this deformation phase, in which the main compression was probably oriented in N—S to NNW—SSE direction.

Many granitoid dykes and stocks were found to be affected by sinistral shear along subvertical planes trending ENE to ESE. Since this deformation, which is called D_3 in the present work, is not compatible with a N—S to NNW—SSE compression, it is proposed that these sinistral shear zones in granites do not belong to the Bayerischer Pfahl shear-zone system and constitute themselves a separated one, which is called “ D_3 shear-zone system”. D_3 took place under upper greenschist to lower amphibolite facies conditions (~ 480 – 550°C), as supported by the observed fabrics and quartz lattice-preferred orientation patterns. Both the intrusion and the deformation of the granites affected by D_3 occurred at deep to intermediate levels of the crust (27–14 km), whereas the

deformation took place under NE—SW compression. Datings on two of the deformed granites yielded 324.4 ± 0.8 Ma (Saunstein granite) and 315.0 ± 1.0 Ma (Untermittendorf rhyolite): Thus, the age of D_3 is most probably ~ 315 Ma, although an episodic D_3 involving some additional, older pulses, is also conceivable. Nevertheless, quartz lattice-preferred orientation patterns and microfabrics show similar characteristics in all the studied samples, suggesting that D_3 was localised in time and that the deformation temperature was in most cases not influenced by any advective heat carried by the sheared intrusives themselves. In other words, the intrusion of most of the sheared granitoids was pre-kinematic with respect to D_3 .

After D_3 the N—S to NNW—SSE compression which governed D_2 was restored, giving way to the next deformation phase D_4 , which was linked to further deformation at and next to the principal shears of the Bayerischer Pfahl shear-zone system under greenschist facies conditions.

The causes for the change of the stress field leading to a NE—SW compression during D_3 might be related to (1) global changes in the dynamics of the tectonic plates in late Variscan times, (2) orogenic collapse leading to the sinking of the Teplá-Barrandian and lateral extrusion of the surrounding Moldanubian rocks, (3) distortion of the regional stress field by local intrusion of large stocks, such as the Saldenburg granite of the Fürstenstein Massif, or (4) distortion of the regional stress field due to the existence of ephemeral releasing bends in the Bayerischer Pfahl shear zone during its early evolution.

In addition to the conclusions about the emplacement and tectonometamorphic evolution of the studied intrusives in their regional geological context, the present work also constitutes a contribution to general questions usually found in structural geology works and in studies concerning the ascent and emplacement of granitic magmas.

Regarding the ascent and emplacement of granitic magmas, the La Bazana granite constitutes a field example of how felsic melts may reach the upper crust by diapirism. The observed lens shape at its upper part suggests that diapiric granites could evolve from teardrop shapes towards flat geometries during their final emplacement, by means of lateral expansion at the top.

The La Bazana and Nisa-Albuquerque intrusions illustrate that the migration direction, final location and shape of intrusive bodies is conditioned by the structure (anisotropy and heterogeneity) of the country rock. Thus, the aforementioned bodies intruded into antiformal structures at middle to upper levels of the crust. Reaching progressively more viscous levels, the magma stopped its upward movement and switched from vertical to horizontal migration. In the case of a small granitic body like the La Bazana pluton, this lateral movement may be limited and more or less radial. In the case of bigger intrusions, like the Nisa-Albuquerque batholith, this sideward migration may reach

several tens of kilometres and polarize toward preferred orientations conditioned by regional structures.

Stoping is usually regarded as a process operating mostly in the upper crust, as observed for example in the Nisa-Albuquerque batholith, but the present work shows that it can play an important role also in deeper levels. Thus, the intrusion of several stocks, whose age might be similar to the one of the Saunstein dyke (~324 Ma), provoked pervasive stoping of the dioritic to granodioritic and migmatic country rocks. Also the emplacement of the Saldenburg granite was accompanied by stoping. In both cases, intrusion depths exceeded 15 km.

Our results indicate that diapirism is a valid ascent mechanism even at intermediate to upper levels of the crust, as exemplified by the La Bazana pluton. But evidence supporting indirectly the viability of diapirism can be found in other intrusives. In both the Iberian and the Bohemian Massif, it is common to find repeated intrusion of several magma batches at the same location. This holds for the Nisa-Albuquerque batholith and other composite intrusive bodies of the Iberian Massif; the Fürstenstein and the Hauzenberg plutons constitute also good examples of this, as well as several granodioritic to dioritic stocks all over the Bavarian Forest, which are systematically intruded by younger granites, i.e. younger magma batches use to benefit from older ones for their ascent. This constitutes a strong argument suggesting that some thermal and mechanical models that reject diapirism as a valid ascent mechanism oversimplify the real conditions governing the rheological behaviour of the Earth's crust. These models usually regard magmas as isolated bubbles ascending through a homogeneous or nearly homogeneous crust. Further models of magma ascent should consider the crust as a thermally, compositionally and rheologically heterogeneous body, and the magmas not as isolated, but much more as nested batches following each other along thermally and mechanically prepared pathways.

Regarding the deformation of granitoid rocks, it has been shown that quartz oblique foliations have a short-lived strain memory. The quartz shape preferred orientation reflects only the very last strain increment and can therefore be misleading when used without corroboration of further criteria to infer the sense of shear of a given deformation phase.

Another conclusion of this research concerns the interpretation of quartz lattice-preferred orientation patterns. On the one hand, rocks which have suffered a weak deformation can develop relatively well-defined quartz lattice preferred orientation patterns: The application of the electron backscatter diffraction technique constitutes an excellent tool for the investigation of rocks which may appear nearly undeformed at first glance. On the other hand, for the interpretation of quartz lattice-preferred orientation patterns it is necessary to bear in mind that their development is conditioned not only by the deformation temperature, but also by other factors amongst which the grain size of the rock seems to be a critical one: Fine-grained rocks tend to deform by means of

grain-boundary sliding instead of dislocation creep, which results in the development of poorly-defined lattice-preferred orientation patterns or in the destruction of pre-existing ones. This applies for primary small grain sizes, but also for small grain sizes achieved during progressive deformation, i.e. lattice-preferred orientation patterns might weaken or even disappear by increasing strain.

The influence of the grain size in the activation of certain deformation mechanisms leaves its imprint not only in the lattice-preferred orientation patterns observed, but also in the microfabrics developed. As long as some fine-grained domains of the rock accommodate most of the strain by grain boundary sliding, some others like for example porphyroclasts or coarse-grained domains might remain nearly undeformed or show varying deformation intensities, even though the temperature would be high enough to allow their recrystallization. This effect becomes especially patent in rocks with bimodal grain-size distribution, as exemplified by the Untermittlerdorf rhyolite.

Strain localisation is a widespread phenomenon observed in many deformed rocks, also in the Bavarian Forest. The deformation referred to as D_3 is preferentially localised in granites. This is due to the fact that granites are usually richer in quartz than the surrounding country rocks, and therefore weaker. Thus, granites constituted soft corridors at which deformation concentrated. Strain localisation is a self-feeding process: As shown in the Saunstein dyke, once the deformation starts at a given location of the rock, the reduction in grain size promotes grain boundary sliding; in the same way, fluid access gives way to reaction softening or hydrolytic weakening, and formation of white mica in cleavage domains also promotes grain boundary sliding. The result is the permanent concentration of the deformation there where it initiates.

Finally, the phenomenon of strain localisation has important implications for the reliability of dated igneous rocks when used as time markers for deformations. Ductile deformations might not occur *en masse*, but rather in a spatially localized fashion. This is due to several factors, mainly: 1) As already mentioned, different rock types show different rheological behaviour, either due to thermal or mineralogical contrasts, i.e. hot rocks and rocks rich in quartz are softer and tend to accommodate more strain than surrounding rocks, and it obviously does not mean that the surrounding rocks are younger at all; 2) even though a given rock body might be softer than the surroundings, whether it accommodates some strain or not depends also on its position and geometry, i.e. only soft rock bodies with favourable geometry, orientation and position will be able to accommodate strain and rigid translation of adjacent blocks. As we saw in the Bavarian Forest, the deformations D_2 to D_4 did not always affect all the rocks present in the region, and this is not necessarily due to a post-kinematic genesis with respect to the considered deformation phase. Thus, special care is needed when inferring the deformation history of a region based on the deformation of dated igneous rocks as time markers.

Zusammenfassung

Die vorliegende Arbeit analysiert verschiedene Aspekte der Entwicklung mehrerer Granitoide des Variszischen Orogens Zentral- und Westeuropas, unter Berücksichtigung sowohl ihrer Aufstiegs- und Platznahmemechanismen als auch ihrer Deformationsgeschichte. Die Arbeitsgebiete liegen in zwei Bereichen des Variszischen Orogens: in der Iberischen Masse und der Böhmisches Masse.

In der Iberischen Masse sind zwei granitoide Körper mit dem Ziel untersucht worden, ihre Aufstiegs- und Platznahmegeschichte zu entschlüsseln. Diese sind der La Bazana Pluton und der Nisa-Alburquerque Batholith, deren Struktur auf magmatische Prozesse und nicht auf Deformation in festem Zustand zurückzuführen ist. Für die Untersuchungen wurden klassische Techniken der Strukturgeologie und Petrologie ebenso wie geophysikalische (gravimetrische und magnetische) Methoden angewendet.

Der La Bazana Pluton ist ein kleiner, rundlicher Körper, der in den Kern einer späten Antiform in kambrische Tonschiefer, Metagrauwacke und vulkanische Gesteine der Ossa-Morena Zone intrudierte. Die Intrusion erfolgte am Ende der oder nach den variszischen duktilen Hauptdeformationen. Der Granit zeigt eine Domstruktur. Magmatische Foliationen fallen in der Regel flach nach außen ein. Das NW—SE-gerichtete Streichen der regionalen Hauptfoliation des Nebengesteins passt sich an die Form des Plutons an. Gefaltete und boudinierte Adern im darüberliegenden Nebengestein weisen auf eine Plättungsdeformation hin. Diese Strukturen entstanden möglicherweise durch den Druck des aufsteigenden Magmas. Die Intrusionstiefe wurde anhand der Mineralparagenesen des Kontakthofes auf etwa 7—10 km geschätzt. Die aeromagnetischen Daten offenbaren keine ausgeprägten Anomalien in Verbindung mit dem Granit. Dies bedeutet, dass der Granit in seiner Zusammensetzung homogen ist. Die gravimetrischen Modelle zeigen, dass der Granit tropfen- bis rohrförmig ist, wobei er sich im oberen Teil erweitert. Die modellierte Mächtigkeit des Granits variiert je nach angenommenem Dichtekontrast zwischen 4 und 10 km. Die Form des Granits bleibt dagegen bei verschiedenen Annahmen für den Dichtekontrast nahezu unverändert. Es wird interpretiert, dass das Magma durch die mittlere Kruste diapirisch aufstieg, bis es auf eine Zone höherer Viskosität traf, in der die Platznahme erfolgte und laterale Ausbreitung und vertikale Plättung des Nebengesteins stattfanden.

Der Nisa-Alburquerque Batholith ist ein 1000 km² großer granitischer Körper, der in Gesteine der Zentral-Iberischen Zone, der Badajoz-Córdoba Scherzone und der Ossa-Morena Zone intrudierte. Die Intrusion fand nach den variszischen duktilen Hauptdeformationen im Oberkarbon statt. Er ist parallel zu den NW—SE-gerichteten variszischen Strukturen gestreckt. Die interne Struktur der dominierenden Fazies (der Grobkörnige Granit) ist durch folgende Merkmale charakterisiert: (1) chaotische Struktur im östlichen Bereich, (2) NW—SE-gerichtete Struktur im Zentralbereich, (3) N—S-gerichtete Struktur im westlichen Bereich. Im Allgemeinen ist die innere Struktur des

Granits parallel zu der Längsachse des Plutons, zu den Kontakten und zu der Foliation des Nebengesteins ausgerichtet, abgesehen vom westlichen Ende, in dem die Struktur schräg zu den genannten Richtungen orientiert ist. Mehrere Datierungen des Grobkörnigen Granits ergaben Alter zwischen 285 und 310 Ma. Die Intrusionstiefe wurde auf 7-10 km geschätzt. Die gravimetrischen Modelle zeigen, dass der Batholith die Form eines nach Ost-Südosten eintauchenden Zylinders besitzt, der nach Westen hin flacher wird und näher an der Oberfläche liegt. Die Modelle offenbaren die Existenz einer mächtigen Wurzelzone am östlichen Ende des Batholiths. Diese fällt räumlich mit den leukokraten, jüngeren Fazies zusammen. Daher wird die Wurzelzone als Zufuhrkanal interpretiert. Die innere Struktur im Zentralbereich des Batholiths kann das Ergebnis von nahezu gleichmäßigem bis nicht-koaxialem Fluß sein, wodurch die NW—SE-gerichtete Struktur entsteht. Die N—S-gerichtete Struktur des westlichen Bereichs wird als das Ergebnis der Verlangsamung des Fließens und der Ankunft aufeinander folgender Magmaschübe interpretiert. Die Intrusion wird als andauernder, seitlicher Magmafluß von der östlichen Wurzelzone nach Westen hin angesehen, wobei das Magma an der südlichen Flanke einer kilometergroßen Antiform kanalisiert wurde. Die Platznahme des Magmas wurde von der prä-existierenden Struktur des Nebengesteins gefördert und durch eine Kombination aus rigider Translation des Nebengesteins, *stoping* und *ballooning* ermöglicht.

In der Böhmisches Masse wurden mehrere kleine granitoide Körper analysiert, die im Subsolidus-Bereich deformiert wurden. Das Ziel der Untersuchungen war, ihre tektonometamorphe Geschichte in den geotektonischen Rahmen des Bayerischen Waldes zu integrieren, insbesondere in Hinsicht auf die Deformationsphase, die D₃ genannt wurde. Die in der vorliegenden Arbeit verwendeten Methoden sind: geologische Kartierung, optische Mikroskopie, Diffraktion rückgestreuter Elektronen (EBSD), Strainanalyse, Röntgenfluoreszenzanalyse, Elektronenstrahlmikrosondenanalyse und Piezometrie.

Das Arbeitsgebiet befindet sich im Vorderen Bayerischen Wald im Bereich zwischen der Bayerischer-Pfahl-Scherzone und der Donaustörung in der Umgebung des Fürstensteiner Plutons. Die hier vorkommenden Gesteine gehören zur Moldanubischen Zone. Diese sind hauptsächlich hochgradige Gneise und Migmatite, die aus sedimentären Edukten mit Einschaltungen aus magmatischen Gesteinen entstanden sind. Die Variszische Metamorphose ist hier durch hohe Temperatur und niedrigen Druck charakterisiert. Sie steht mit der Migmatisierung der Gesteine in Verbindung und erfolgte im Arbeitsgebiet zwischen 330 und 316 Ma.

Die Untersuchungen im Rahmen der geologischen Kartierung des Blattes TK25 Nr. 7246 Tittling lieferten wertvolle Grundlagen für diese Dissertation. Die Ergebnisse ermöglichten eine bessere Kenntnis der im Vorderen Bayerischen Wald vorkommenden Gesteine, ebenso wie die Entdeckung mehrerer, von D₃ überprägter, granitischer Körper.

Während verschiedener Stadien der Variszischen Orogenese intrudierten magmatische Gesteine dioritischer bis granitischer Zusammensetzung. Die mafischeren Körper, deren Zusammensetzung dioritisch bis granodioritisch ist, intrudierten gegen 335 Ma. Kleine granitoide Stöcke und Gänge intrudierten in die Migmatite zwischen 322 ± 5 und 331 ± 9 Ma. Einer dieser Körper, der Saunsteiner Granitgang, intrudierte bei 324.4 ± 0.8 Ma. Nach der Intrusion der vorher genannten kleinen Granitoidkörper konzentrierte sich die magmatische Aktivität auf den Bereich des Fürstensteiner und des Hauzenberger Plutons. Der Saldenburger Granit und der Hauzenberger Granit II intrudierten bei 315 ± 3 Ma bzw. 320 ± 3 Ma. Als jüngste magmatische Gesteine der Variszischen Orogenese drangen subvulkanische Gänge rhyolithischer bis basaltisch-andesitischer Zusammensetzung ein. Datierungen dieser Gesteine ergaben Alter von 302 ± 7 und 299.0 ± 2.3 Ma. Die Form und Struktur all dieser Körper spiegelt in gewissem Maße die thermische Entwicklung der Kruste wider, in die sie intrudierten. Elliptische, ungleichmäßige oder ausgedehnte Körper, mit einem Alter unter ~ 310 Ma, intrudierten in eine relativ warme Kruste. Ihr Aufstigsmechanismus ist nicht gut bekannt, aber das Ausnutzen von prä-existierenden Anisotropien erscheint in diesem Kontext am effizientesten. Eine gewisse Mitwirkung von Diapirismus bei den größeren, gleichförmigen Körpern, wie dem Hauzenberger Granit II und dem Saldenburger Granit, ist ebenso plausibel. Die Platznahme der granitischen Endglieder wurde von *Stoping* der umgebenden Migmatite und der älteren magmatischen Fazies begleitet. Die Körper, die jünger als ~ 310 Ma sind, bilden geradlinige Gänge mit scharfen Kontakten, was für einen Aufstieg durch *Dyking* in einer relativ kalten Kruste spricht.

Die primären tektonischen Elemente der Untersuchungsregion stehen in Zusammenhang mit dem Bayerischer-Pfahl-Scherzonen-System, das sich über mehr als 200 km am südwestlichen Rand der Böhmisches Masse verfolgen lässt. Dieses besteht aus NW—SE-gerichteten, dextralen subvertikalen Scherzonen, subsidiären NNW—SSE-gerichteten dextralen Scherzonen und dazu konjugierten NE—SW-gerichteten, sinistralen Scherzonen. Diese sind in einem ausgedehnten Zeit- und Temperaturfenster von hochduktilen amphibolitfaziellen bis spröden Bedingungen aktiv gewesen. Das Bayerischer-Pfahl-Scherzonen-System war, zumindest während seiner duktilen Geschichte, unter N—S- bis NNW—SSE-gerichteter Kompression aktiv.

Vier duktile Deformationsphasen wurden im Untersuchungsgebiet vorgeschlagen. D_1 ergab Hochtemperatur-Strukturen unter Bedingungen der Amphibolit- bis Granulitfazies, wahrscheinlich während des thermischen Höhepunkts der Hochtemperatur-Niedrigdruck-Metamorphose. Ihre Kinematik ist unbekannt. D_1 ist in der Regel durch spätere Deformationen überprägt, ist aber noch an reliktschen Gefügemerkmalen zu erkennen. D_2 fand unter Bedingungen der unteren Amphibolit- bis oberen Grünschieferfazies statt, wie die Quarz-Texturen und Mikrostrukturen belegen. Sie ist für die subvertikale Foliation der Migmatite in Richtung NW—SE verantwortlich, die unter dextraler Scherung entstand, ebenso wie für die Deformation am Bayerischer-Pfahl-

Scherzonen-System in seinen früheren Stadien. Die meisten dioritischen bis granodioritischen und manche der granitischen Körper intrudierten vor oder während dieser Phase, in der die Hauptkompression N—S- bis NNW—SSE-gerichtet war.

Viele granitoide Stöcke und Gänge sind von sinistraler Scherung entlang ENE- bis ESE-streichender Flächen betroffen. Diese Deformation ist inkompatibel mit einer Kompression in Richtung N—S bis NNW—SSE. Daher wird vorgeschlagen, dass sie eine neue Deformationsphase darstellt, die D_3 genannt wurde. Die sinistralen, ENE- bis ESE-streichenden Scherzonen bilden das sogenannte „ D_3 Scherzonen-System“, das als unabhängig vom Bayerischer-Pfahl-Scherzonen-System angesehen wird. D_3 erfolgte unter Bedingungen der oberen Grünschiefer- bis unteren Amphibolitfazies (~ 480 - 550°C), wie die Quarz-Texturen und Mikrostrukturen belegen. Sowohl die Intrusion als auch die Deformation von Graniten, die von D_3 betroffen sind, geschahen in tiefen bis intermediären Krustenniveaus. D_3 erfolgte unter NE—SW-gerichteter Kompression. Datierungen an zwei deformierten Granitoiden ergaben Alter von 324.4 ± 0.8 Ma (Saunsteiner Granit) und 315.0 ± 1.0 Ma (Untermittendorfer Rhyolith). Dies bedeutet, dass das Alter von D_3 sehr wahrscheinlich bei 315 Ma liegt, wobei ein episodisches Auftreten von D_3 , in dem noch andere, ältere Deformationsereignisse vor 315 Ma stattfanden, auch denkbar ist. Trotzdem sind die Texturen und Mikrostrukturen aller untersuchten Proben ähnlich. Dies ist ein Hinweis darauf, dass D_3 auf einen engen Zeitraum begrenzt war und dass die Deformationstemperatur in den meisten Fällen von keinerlei advektiver Wärmezufuhr beeinflusst war. Das heißt, das Eindringen der meisten zerscherten Granitoide war prä-kinematisch in Bezug auf D_3 .

Nach D_3 verlief die Richtung der Hauptkompression wieder in Richtung N—S bis NNW—SSE. Dies setzte die nächste Deformationsphase D_4 in Gang. D_4 war mit weiterer Deformation an und in der Nähe von den Hauptstörungen des Bayerischer-Pfahl-Scherzonen-Systems unter grünschieferfaziellen Bedingungen verbunden.

Die Ursachen der Änderung des Stressfeldes, die zu einer Kompression in Richtung NE—SW führten, können mit folgenden Prozessen in Verbindung stehen: (1) mit globalen Änderungen der Dynamik der tektonischen Platten in spätvariszischer Zeit, (2) mit orogenem Kollaps assoziiert mit der Absenkung des Teplá-Barradiums und der lateralen Extrusion moldanubischer Unterkruste, (3) mit Störungen des regionalen Spannungsfeldes durch lokale Magmaintrusion, wie die des Saldenburger Granits im Fürstensteiner Massiv, oder (4) mit Störungen des regionalen Spannungsfeldes durch die Existenz kurzlebiger *Releasing Bends* während der Frühgeschichte der Bayerischer-Pfahl-Scherzone.

Zusätzlich zu den Schlussfolgerungen über die Platznahme und die tektonometamorphe Entwicklung der untersuchten Magmatite in ihrem regionalen geologischen Kontext liefert die vorliegende Arbeit einen Beitrag zu generellen Fragen, die üblicherweise in strukturgeologischen Studien und in Arbeiten über Aufstieg und Platznahme von granitischen Magmen auftreten.

In Bezug auf die Aufstiegs- und Platznahmemechanismen granitischer Magmen stellt der La Bazana Granit ein Beispiel dafür dar, dass felsische Schmelzen die obere Kruste durch Diapirismus erreichen können. Die beobachtete Linsenform seines oberen Bereichs weist darauf hin, dass sich diapirische Granite während ihrer Platznahme durch seitliche Ausbreitung von tropfenförmigen zu flachen Geometrien entwickeln können.

Die Intrusionen von La Bazana and Nisa-Alburquerque illustrieren, dass die Migrationsrichtung, die Endposition und die Form intrusiver Körper durch die Struktur (Anisotropie und Heterogenität) des Nebengesteins beeinflusst werden. Die genannten Körper intrudierten in Antiform-Strukturen in der mittleren bis oberen Kruste. Beim Erreichen von Stockwerken mit progressiv höherer Viskosität stoppte das Magma seine vertikale Migration und fing an, sich horizontal zu bewegen. Im Falle eines kleinen Körpers, wie des La Bazana Plutons, dürfte die seitliche Ausbreitung begrenzt und mehr oder weniger radial sein. Im Falle eines größeren Körpers, wie des Nisa-Alburquerque Batholiths, dürfte die seitliche Ausbreitung mehrere zehner Kilometer erreichen und sich in Vorzugsrichtungen orientieren, die von der regionalen Struktur bedingt werden.

Stoping wird als ein Prozess angesehen, der sich meistens in der oberen Kruste abspielt, wie beispielsweise am Nisa-Alburquerque Batholith beobachtet. Die vorliegende Arbeit zeigt, dass *Stoping* auch in tieferen Stockwerken der Kruste eine wichtige Rolle spielen kann. Auf diese Weise wurde die Intrusion mehrerer Granitoide, deren Alter ähnlich zu dem des Saunsteiner Granits sein dürfte (~ 324 Ma), von intensivem *Stoping* der umgebenden Migmatite und Diorite bis Granodiorite begleitet. Auch die Intrusion des Saldenburger Granits verursachte *Stoping* des Nebengesteins. In beiden Fällen erfolgte die Intrusion tiefer als 15 km.

Die Ergebnisse dieser Arbeit weisen darauf hin, dass Diapirismus sogar in intermediären bis oberen Niveaus der Kruste stattfinden kann, wie am Beispiel des La Bazana Plutons vorgeschlagen wurde. Aber weitere, indirekte Hinweise auf Diapirismus können auch in anderen Intrusivkörpern gefunden werden. Sowohl in der Iberischen als auch in der Böhmischen Masse sind wiederholte Intrusionen mehrerer Magmaschübe an derselben Stelle häufig. Beispiele liefern der Nisa-Alburquerque Batholith und andere zusammengesetzte Intrusivkörper der Iberischen Masse, sowie der Fürstensteiner Pluton, der Hauzenberger Pluton und einige granodioritische bis dioritische Stöcke im Bayerischen Wald, in die systematisch granitische Schmelzen eingedrungen sind: Jüngere Magmaschübe nutzen für ihren Aufstieg dieselben Pfade, entlang denen die älteren emporstiegen. Dies spricht dafür, dass thermische und mechanische Modelle, die Diapirismus als Aufstiegsmechanismus ablehnen, die rheologischen Bedingungen der Erdkruste zu sehr vereinfachen. Diese Modelle sehen häufig Magmen als isolierte Schübe an, die durch eine homogene oder nahezu homogene Kruste emporsteigen. Zukünftige Modelle sollten die heterogene Natur der Erdkruste bezüglich der Temperatur, der Zusammensetzung und der Rheologie berücksichtigen. Ebenfalls sollten

sie die Magmen nicht als isolierte, sondern als aufeinander folgende Schübe betrachten, die entlang vorerwärmter und vordeformierter Bahnen aufeinander folgen.

Bezüglich der Deformation granitoider Gesteine wurde gezeigt, dass schräge Gefüge in quarzreichen duktilen Scherzonen leicht überprägt werden. Quarz-Schrägfoliationen spiegeln nur das allerjüngste Straininkrement wider und können daher irreführend sein, wenn sie ohne Bestätigung durch andere Scherkriterien für die Ableitung des Schersinns einer bestimmten Deformationsphase verwendet werden.

Eine andere wichtige Schlussfolgerung dieser Arbeit betrifft die Interpretation von Quarz-Texturen. Einerseits können auch schwach deformierte Gesteine relativ gut ausgeprägte Quarz-Texturen entwickeln. Daher ermöglicht die Verwendung von Rückstreuелеktronenbildern (EBSD) die Untersuchung der Gesteine, die beim ersten Blick nahezu undeformiert erscheinen. Andererseits muss man bei der Interpretation von Quarz-Texturen beachten, dass ihre Entwicklung nicht nur von der Temperatur beeinflusst wird, sondern auch von anderen Faktoren, unter denen die Korngröße sehr wichtig zu sein scheint: Feinkörnige Gesteine tendieren dazu, durch Korngrenzgleiten anstatt Versetzungskriechen zu deformieren. Dies führt dazu, dass bei feinkörnigen Gesteinen keine Texturen entstehen oder prä-existierende Texturen verschwinden. Dieses Phänomen gilt für primär feinkörnige Gesteine, aber auch für kleine Korngrößen, die während progressiver Deformation zustande kommen, d.h. Texturen können bei der Intensivierung der Deformation abgeschwächt werden oder gar verschwinden.

Die Rolle der Korngröße bei der Aktivierung bestimmter Deformationsmechanismen prägt nicht nur die Texturen, sondern auch die Mikrostrukturen. Solange feinkörnige Gesteinsdomänen existieren, die einen großen Teil des *Strains* durch Korngrenzgleiten aufnehmen können, werden Porphyroklasten und grobkörnige Domänen sogar bei hoher Temperatur einen niedrigen oder variierenden *Strain* erleiden. Dieser Effekt wird in Gesteinen mit bimodaler Korngrößenverteilung wie dem Untermittlerdorfer Rhyolith offensichtlich.

Strainlokalisierung ist ein übliches Phänomen, das in vielen Gebieten und auch im Bayerischen Wald beobachtet wird. D₃ ist meistens nur in Graniten zu finden. Dies ist darauf zurückzuführen, dass Granite quarzreicher und daher schwächer als ihre Umgebung sind. Daher stellen Granite schwache Bahnen dar, in denen Strainlokalisierung bevorzugt stattfindet. Strainlokalisierung ist ein sich selbst verstärkender Prozess: Wenn die Deformation an einer gewissen Stelle anfängt, findet Korngrößenverkleinerung statt, die die Deformation durch Korngrenzgleiten begünstigt; der Zugang von Fluiden führt zur weiteren Schwächung des Gesteins und zur Entstehung von Hellglimmer, die wieder das Korngrenzgleiten fördert. Die Folge ist eine permanente Konzentration der Deformation an der Stelle, an der sie beginnt.

Zum Schluss wird auf die Bedeutung der Strainlokalisierung hingewiesen, wenn datierte Magmatite als Zeitmarken für die relative zeitliche Einstufung von Deformationen

verwendet werden. Die vorliegende Arbeit zeigt, dass duktile Deformation stark lokalisiert auftreten kann. Dies ist im Wesentlichen auf folgende Faktoren zurückzuführen: 1) Verschiedene Gesteinstypen weisen unterschiedliches rheologisches Verhalten auf, entweder wegen thermischer oder wegen mineralogischer Kontraste, das heißt warme Gesteine und Gesteine mit hohem Quarzgehalt sind mechanisch schwächer und tendieren dazu, mehr *Strain* als umgebende Gesteine aufzunehmen; 2) sogar unter der Annahme, dass ein Gestein schwächer als seine Umgebung wäre, hängt es von seiner Position und Geometrie ab, ob es von einer Verformung betroffen wird oder nicht. Das heißt, nur mechanisch weiche Gesteine mit günstiger Geometrie, Orientierung und Lage sind dazu geeignet, die Verformung in sich zu konzentrieren und die rigide Bewegung angrenzender Blöcke zu ermöglichen. Wie im Bayerischen Wald beobachtet wurde, wurden von den Deformationen D_2 bis D_4 nicht immer alle existierenden Gesteine betroffen und dies ist nicht notwendigerweise auf eine post-kinematische Genese der undeformierten Gesteine zurückzuführen. Daher ist bei der Verwendung der datierten Magmatite als Zeitmarken für Deformationen Vorsicht geboten.

Resumen

Este trabajo analiza diferentes cuerpos graníticos del Orógeno Varisco de Europa Central y Occidental con el fin de mejorar nuestro conocimiento sobre algunos aspectos de su evolución, contemplando tanto sus mecanismos de ascenso y emplazamiento como su historia de deformación. Las áreas de estudio involucradas se localizan en dos sectores del Orógeno Varisco: los Macizos Ibérico y de Bohemia.

En el Macizo Ibérico se han estudiado dos cuerpos graníticos, cuya estructura es predominantemente magmática y no muestra signos de deformación en estado sólido, con el fin de descifrar su historia de ascenso y emplazamiento: el plutón de La Bazana y el batolito de Nisa-Alburquerque. Este estudio se ha realizado utilizando técnicas clásicas de geología estructural y petrología, así como métodos geofísicos (gravimetría y magnetometría).

El plutón de La Bazana es un cuerpo pequeño de forma cartográfica subcircular encajado en pizarras, metagrauvas y rocas volcánicas cámbricas de la Zona de Ossa-Morena y situado en el núcleo de un antiforame recto tardío. El granito muestra un patrón de fábrica en forma de domo. Las foliaciones magmáticas suelen buz suavemente hacia el encajante. La foliación regional principal de dirección NO—SE se acomoda a la forma en domo del plutón, describiendo deflexiones alrededor de él. El aplastamiento sufrido por el encajante a techo del granito queda reflejado en la existencia de venas plegadas y boudinadas. Estas estructuras se formaron probablemente como consecuencia del empuje del magma durante su ascenso y emplazamiento. El nivel de emplazamiento se estima en unos 7-10 km a partir de las asociaciones minerales observadas en la aureola de contacto. Los datos aeromagnéticos no revelan ninguna anomalía asociada al granito, lo que indica que éste es homogéneo. Los modelos de las anomalías gravimétricas residuales sugieren que el granito tiene forma de pitón a gota invertida, con cierta expansión en su parte superior. El espesor modelizado del granito varía entre 4 y 10 km, según los contrastes de densidad considerados, mientras que su forma apenas cambia. Se interpreta que el magma ascendió diapíricamente a través de la corteza media hasta alcanzar un nivel de alta viscosidad, donde el magma se emplazó expandiéndose lateralmente y dando lugar al aplastamiento de las rocas suprayacentes.

El batolito de Nisa-Alburquerque es un cuerpo granítico de 1000 km² que intruyó en rocas de la Zona Centroibérica, la Unidad Central y la Zona de Ossa-Morena en el Carbonífero Superior, después de las principales fases variscas de deformación dúctil. Su forma cartográfica es alargada, extendiéndose en dirección NO—SE paralelamente a las estructuras variscas. La estructura interna de su facies principal, el Granito de Grano Grueso, se caracteriza por fábricas caóticas en la parte oriental, fábricas de orientación NO—SE en el sector central y fábricas N—S en la parte oeste. En general, la fábrica es paralela al eje mayor del cuerpo, a los contactos externos y a la foliación regional del

encajante. Varias dataciones del Granito de Grano Grueso indican edades comprendidas entre 285 y 310 Ma. Su profundidad de intrusión se estima en unos 7-10 km. Los modelos gravimétricos sugieren que el batolito tiene forma de cilindro horizontal inclinado hacia el ESE, de fondo más plano y somero hacia el oeste. Los modelos ponen de manifiesto la existencia de una raíz prominente en el extremo oriental, coincidiendo con las facies más leucocráticas y jóvenes, que probablemente representa la zona principal de alimentación. La fábrica interna del batolito en su parte central se interpreta como el resultado de una combinación de flujo cuasi uniforme a no coaxial, que produce las fábricas de dirección NW—SE. La fábrica N—S de la parte occidental se interpreta como el resultado de la deceleración del flujo magmático y el empuje de sucesivos pulsos de magma. La intrusión es concebida como un flujo lateral continuado de magma partiendo de la raíz oriental y guiado hacia el oeste a lo largo del flanco sur de un antiforame kilométrico. Como mecanismos principales de transferencia de masas se propone una combinación de traslación rígida del encajante, *stoping* e inflamamiento.

En el Macizo de Bohemia se estudiaron varios cuerpos graníticos pequeños que sufrieron una fuerte deformación en estado sólido con el fin de integrar su historia tectonometamórfica en el marco geotectónico del Bosque de Baviera. El estudio se centra principalmente en la fase de deformación denominada D₃. Los métodos utilizados en este trabajo son: cartografía geológica, microscopía óptica, difracción de electrones retrodispersados (EBSD), análisis del strain, análisis de fluorescencia de rayos X, análisis de microsonda electrónica y piezometría.

El área de estudio se localiza en el Bosque de Baviera meridional, en la parte comprendida entre las zonas de cizalla del Bayerischer Pfahl y del Danubio, en el área que circunda el plutón de Fürstenstein. Las rocas que aquí se encuentran pertenecen a la Zona Moldanúbica. Éstas son predominantemente gneisses de alto grado y migmatitas derivadas de protolitos sedimentarios con intercalaciones de rocas magmáticas. El evento metamórfico más importante, de edad varisca, está caracterizado por altas temperaturas y bajas presiones y viene acompañado de anatexia. Éste ocurrió en el área de estudio entre 330 y 316 Ma.

Las investigaciones relacionadas con la cartografía de la hoja topográfica 1:25000 n° 7246 Tittling aportaron una buena información de base para esta tesis. Los resultados permitieron un mejor conocimiento de las rocas aflorantes en el Bosque de Baviera meridional, así como la localización de numerosos cuerpos graníticos afectados por D₃.

En diferentes estadios de la Orogenia Varisca intruyeron magmas de composición diorítica a granítica. La edad de los cuerpos más máficos, de composición diorítica a granodiorítica, es de unos 335 Ma. Entre 322 ± 5 y 331 ± 9 Ma intruyeron de manera ubicua pequeños stocks y diques de granitoides. Uno de ellos, el dique granítico de Saunstein, tiene una edad de 324.4 ± 0.8 Ma. Esencialmente tras estos últimos granitoides, la actividad magmática se concentró en las áreas de los plutones de Fürstenstein y Hauzenberg: el granito de Saldenburg y el granito de Hauzenberg II

intruyeron hace 315 ± 3 Ma y 320 ± 3 Ma respectivamente. El último episodio magmático atribuido a la Orogenia Varisca está representado por diques subvolcánicos de composición riolítica a basalto-andesítica. Dos dataciones de estas rocas suministraron edades de 302 ± 7 y 299.0 ± 2.3 Ma. La forma y estructura de todos estos cuerpos intrusivos refleja en cierta medida la evolución térmica de la corteza en que ascendieron y se emplazaron. Los cuerpos elípticos, irregulares o elongados, en general más antiguos de ~ 310 Ma, intruyeron en un encajante relativamente caliente. Su modo de ascenso es poco conocido, pero el aprovechamiento de anisotropías preexistentes parece el mecanismo más efectivo en este contexto. Cabe esperar cierta contribución de ascenso diapírico en los cuerpos más equidimensionales y de mayor tamaño, como el granito de Hauzenberg II y el de Saldenburg. El emplazamiento de las facies graníticas vino acompañado de un *stoping* intenso de las migmatitas y dioritas a granodioritas encajantes. Los cuerpos intrusivos más jóvenes de ~ 310 Ma son diques planares de contactos muy netos, que sugieren un ascenso por *dyking* en una corteza relativamente fría.

Los elementos tectónicos más destacables del área se pueden describir en el contexto del sistema de zonas de cizalla del Bayerischer Pfahl, que se observa a lo largo de más de 200 km en el margen suroccidental del Macizo de Bohemia. Este sistema está formado por zonas de cizalla subverticales de dirección NO—SE dexas, zonas de cizalla subsidiarias de dirección NNO—SSE dexas y zonas de cizalla conjugadas de orientación NE—SO sinistras. Éstas fueron activas en un amplio rango de tiempo y temperaturas desde facies de anfibolitas hasta condiciones subsuperficiales. El sistema de zonas de cizalla del Bayerischer Pfahl fue activo probablemente, al menos durante su historia dúctil, bajo compresión N—S a NNO—SSE.

Se proponen cuatro fases de deformación dúctil en el área de trabajo. D_1 produjo fábricas de alta temperatura en condiciones de facies de anfibolitas a granulitas, probablemente coincidiendo con el pico térmico del metamorfismo de alta temperatura y baja presión. La cinemática de esta fase es desconocida. D_1 fue prácticamente oscurecida por deformaciones posteriores, pero queda aún reflejada en fábricas relícticas. D_2 ocurrió en condiciones de facies de anfibolitas a esquistos verdes, tal y como indican las texturas de orientación cristalográfica preferente de cuarzo y las microfábricas. Esta fase es responsable de la foliación subvertical de dirección NO—SE en migmatitas, desarrollada bajo cizalla simple dextral, y de la deformación en el sistema de zonas de cizalla del Bayerischer Pfahl en sus estadios tempranos. La mayoría de los cuerpos dioríticos a granodioríticos y algunos graníticos intruyeron antes de o durante esta fase, en la que la compresión principal se dirigía en dirección N—S a NNO—SSE.

Se han encontrado numerosos diques y *stocks* graníticos afectados por una cizalla sinistral a lo largo de planos subverticales de dirección ENE a ESE. Ya que esta deformación, denominada D_3 , no es compatible con una compresión N—S a NNO—SSE,

se propone que estas zonas de cizalla sinistral en granitos no pertenecen al sistema de zonas de cizalla del Bayerischer Pfahl y constituyen uno propio, denominado "sistema de zonas de cizalla D₃". La fase D₃ tuvo lugar en condiciones de facies de esquistos verdes a anfibolitas (~480-550°C), como evidencian las texturas de orientación cristalográfica preferente de cuarzo y las microfábricas. Tanto la intrusión como la deformación de los cuerpos afectados por D₃ ocurrió en zonas intermedias a profundas de la corteza (27-14 km), mientras que la deformación tuvo lugar bajo compresión en dirección NE—SO. Las dataciones de cuerpos afectados por D₃ proporcionan edades de 324.4 ± 0.8 Ma (granito de Saunstein) y 315.0 ± 1.0 Ma (riolita de Untermitteldorf). Así pues, la edad de D₃ se aproxima probablemente a 315 Ma, aunque es asimismo concebible que D₃ haya sido episódica, es decir, con uno varios eventos adicionales anteriores a 315 Ma. De cualquier modo, las texturas de orientación cristalográfica preferente de cuarzo y las microfábricas muestran características similares en todas las muestras estudiadas, lo que sugiere que D₃ fue localizada en el tiempo y la temperatura de deformación, en la mayoría de los casos, no estuvo influenciada por el calor advectivo aportado por los granitoides que fueron deformados. En otras palabras, la intrusión de la mayoría de los granitoides cizallados fue precinemática con respecto a D₃.

Después de D₃ se restauró la compresión de dirección N—S a NNO—SSE que rigió D₂, dando paso a la siguiente fase de deformación D₄, que se asocia a una deformación localizada en las cercanías de las cizallas principales del sistema del Bayerischer Pfahl en condiciones de facies de esquistos verdes.

Las causas del cambio del campo de esfuerzos que desembocó en la compresión NE—SO puede relacionarse con (1) cambios globales en la dinámica de las placas tectónicas en tiempos tardivariscos, (2) colapso orogénico relacionado con el hundimiento del bloque Teplá-Barrándico y la extrusión lateral de rocas moldanúbicas, (3) distorsión del campo de esfuerzos regional a causa de la intrusión local de grandes *stocks* como el granito de Saldenburg, localizado en el macizo intrusivo de Fürstenstein o (4) distorsión del campo de esfuerzos regional a causa de la existencia de *releasing bends* efímeros en la zona de cizalla del Bayerischer Pfahl durante su evolución temprana.

Además de las conclusiones acerca del emplazamiento y la evolución tectonometamórfica de las rocas intrusivas estudiadas en su marco geológico regional, este trabajo constituye una contribución más a aspectos generales frecuentemente discutidos en trabajos de geología estructural y en estudios sobre el ascenso y emplazamiento de magmas graníticos.

En cuanto al ascenso y emplazamiento de magmas graníticos, el granito de La Bazana constituye un ejemplo real de cómo los fundidos félsicos pueden alcanzar diapíricamente la corteza superior. La forma lenticular observada en su parte alta sugiere que los diapiros graníticos pueden evolucionar desde formas de gota hacia geometrías planas durante su emplazamiento final por medio de expansión lateral en su techo.

Las intrusiones de La Bazana y Nisa-Alburquerque sirven para ilustrar que la dirección de migración, la localización final y la forma de los cuerpos están condicionadas por la estructura (anisotropía y heterogeneidad) del encajante. Así, los cuerpos mencionados intruyeron en estructuras antiformales en zonas intermedias a altas de la corteza. Al ir alcanzando niveles progresivamente más viscosos durante su ascenso, el magma bloqueó su movimiento en vertical y comenzó a migrar horizontalmente. En el caso de cuerpos pequeños como el plutón de La Bazana, el movimiento lateral puede ser limitado y más o menos radial. En el caso de cuerpos mayores como el batolito de Nisa-Alburquerque, la migración lateral puede llegar a varias decenas de kilómetros y se orienta en direcciones preferentes marcadas por la estructura regional.

El *stoping* suele considerarse como un proceso que opera predominantemente en la corteza superior, como se ha visto en el batolito de Nisa-Alburquerque, pero en esta tesis se muestra que también puede ser importante en niveles más profundos. En este sentido, la intrusión de numerosos *stocks*, cuya edad debe de aproximarse a la del dique de Saunstein (~324 Ma), provocó un *stoping* intenso en las dioritas a granodioritas y migmatitas de caja. También el emplazamiento del granito de Saldenburg vino acompañado de *stoping*. En ambos casos la profundidad de emplazamiento se sitúa más allá de 15 km.

Nuestros resultados indican que el diapirismo es un mecanismo de ascenso válido en niveles intermedios a altos de la corteza, caso que viene a ilustrar el granito de La Bazana. Pero también hay evidencias indirectas de diapirismo en otras intrusiones. Tanto en el Macizo Ibérico como en el de Bohemia es común encontrar intrusión repetida de varios pulsos de magma en el mismo lugar. Este es el caso del batolito de Nisa-Alburquerque y de otros cuerpos compuestos del Macizo Ibérico; los plutones de Fürstenstein y de Hauzenberg también constituyen buenos ejemplos de ello, así como un gran número de *stocks* dioríticos a granodioríticos repartidos por todo el Bosque de Baviera, que fueron sistemáticamente intruidos por granitos más jóvenes, esto es, los pulsos de magma jóvenes suelen beneficiarse de los más antiguos en su ascenso. Esto constituye un argumento de peso que sugiere que algunos modelos térmicos y mecánicos que rechazan el diapirismo como mecanismo de ascenso válido simplifican en exceso las condiciones reales que gobiernan el comportamiento reológico de la corteza terrestre. Estos modelos suelen considerar los magmas como bolsas aisladas que ascienden a través de una corteza homogénea o casi homogénea. Futuros modelos deben considerar la corteza como un cuerpo térmica, composicional y reológicamente heterogéneo, y los magmas no como bolsas aisladas, sino más bien asociadas, ascendiendo en cadena a lo largo de canales precalentados y predeformados.

En cuanto a la deformación de granitoides, se ha mostrado que las foliaciones oblicuas de cuarzo poseen una memoria de deformación muy corta. La orientación preferente de forma de los granos de cuarzo refleja tan solo el último incremento de deformación interna. Esta orientación preferente puede por ello llevar a conclusiones erróneas si se

usa sin la corroboración de otros criterios cinemáticos a la hora de establecer el sentido de cizalla de una deformación dada.

Otra de las conclusiones de esta investigación se refiere a la interpretación de texturas de orientación cristalográfica preferente de cuarzo. Por una parte, rocas que han sufrido una deformación suave pueden desarrollar texturas de orientación cristalográfica preferente relativamente bien marcadas. Así, la aplicación de la difracción de electrones retrodispersados constituye una herramienta excelente para el estudio de deformaciones en rocas que parecen indeformadas a primera vista. Por otra parte, para la interpretación de texturas de orientación cristalográfica preferente es necesario tener en mente que su desarrollo está condicionado no sólo por la temperatura de deformación, sino también por otros factores, entre los cuales el tamaño de grano parece ser de especial importancia: rocas de grano fino tienden a deformarse por deslizamiento en los bordes grano en vez de por migración de dislocaciones, lo cual da como resultado el desarrollo de texturas de orientación cristalográfica preferente poco acentuadas o la destrucción de texturas preexistentes. Esto es así para tamaños de grano finos primarios, pero también para tamaños de grano fino adquiridos durante la deformación progresiva, esto es, las texturas de orientación cristalográfica preferente pueden debilitarse o incluso desaparecer con el incremento del *strain*.

La influencia del tamaño de grano en la activación de determinados mecanismos de deformación deja su huella no sólo en los patrones de orientación cristalográfica preferente, sino también en las microfábricas desarrolladas. Siempre y cuando existan dominios de grano fino que acomoden gran parte de la deformación por deslizamiento en los bordes grano, otras partes de la roca, como porfiroclastos o dominios de grano grueso, pueden permanecer casi indeformados o mostrar intensidades de deformación variables, a pesar de que la temperatura sea relativamente alta. Este efecto se vuelve especialmente patente en rocas con distribución de tamaños de grano bimodal, como la riolita de Untermittlerdorf.

La localización del *strain* es un fenómeno común en muchas rocas deformadas, también en el Bosque de Baviera. La deformación denominada D_3 se localiza preferentemente en granitos. Esto se debe al hecho de que los granitos suelen contener mayor cantidad de cuarzo y por tanto ser más débiles que el encajante. Así pues, en el Bosque de Baviera los granitos constituyeron corredores débiles en los que la deformación se concentró. La localización del *strain* es un fenómeno retroalimentado: como se ha visto en el dique de Saunstein, una vez que la deformación comienza en un lugar concreto de la roca, la reducción de tamaño de grano promueve el deslizamiento en los bordes grano; el acceso de fluidos provoca ablandamiento y la formación de mica blanca en dominios de clivaje acentúa el deslizamiento en los bordes grano. El resultado es la permanente concentración de la deformación allí donde se inicia.

Finalmente, el fenómeno de localización del *strain* tiene importantes implicaciones en la fiabilidad de rocas ígneas datadas cuando éstas se utilizan como marcadores para

determinar la edad relativa de las fases de deformación. Este estudio muestra que las deformaciones dúctiles pueden tener un carácter localizado en el espacio. Esto se debe a varios factores, principalmente: 1) tipos de rocas diferentes tienen un comportamiento reológico diferente, ya sea por contrastes de temperatura o mineralógicos; así, rocas más calientes o más ricas en cuarzo son más débiles y tienden a absorber más deformación que las rocas circundantes; 2) incluso en el supuesto de que un cuerpo de roca dado sea más débil que las rocas circundantes, el que sufra algo de deformación o no viene también condicionado por su posición y geometría: sólo cuerpos de roca débiles y con geometría, orientación y posición favorables son capaces de deformarse y de permitir la traslación rígida de bloques adyacentes. Tal y como se ha visto en el Bosque de Baviera, las deformaciones D_2 a D_4 han afectado sólo a algunas de las rocas presentes en la región, y esto no es necesariamente debido a que las rocas indeformadas presenten una génesis postcinemática respecto a las deformaciones. Por ello, el uso de rocas ígneas datadas como marcadores temporales de las deformaciones debe hacerse con precaución.

Contents

1. Introduction	27
1.1. The Variscan Orogeny	27
1.2. The Iberian and Bohemian Massifs	29
1.3. Migration and deformation of granitoids	34
2. Aims	40
3. Methods	42
3.1. Gravimetry	42
3.2. Magnetometry	44
3.3. Structural inventory of pluton-host rock systems	48
3.4. Geological mapping	50
3.5. Microfabrics and optical microscopy	51
3.6. Quartz textures by means of electron backscatter diffraction	52
3.7. Strain analysis	55
3.8. X-ray fluorescence analysis	55
3.8.1. Isocon diagram	56
3.8.2. Zr-thermometry	56
3.9. Electron microprobe analysis	57
3.9.1. Phengite barometry	57
3.9.2. Feldspar composition	57
3.10. Piezometry	57
4. Investigations on granitoids of the Ossa-Morena and Central Iberian Zones, Iberian Massif ..	59
4.1. Geographic overview	59
4.2. The La Bazana pluton	60
4.2.1. Introduction	60
4.2.2. Petrography and structure of the La Bazana pluton and its country rocks	61
4.2.3. Three-dimensional granite geometry	66
4.2.4. Ascent and emplacement model: discussion	71
4.3. The Nisa-Alburquerque batholith	74
4.3.1. Introduction	74
4.3.2. Petrography and structure of the Nisa-Alburquerque batholith and its country rocks	76
4.3.3. Geometry of the Nisa-Alburquerque batholith	79
4.3.4. Ascent and emplacement model: discussion	83
5. Investigations on granitoids of the Moldanubian Zone, Bohemian Massif	86
5.1. Geographic overview	86
5.2. Geological setting and previous works	87
5.2.1. The Moldanubian Zone in the study area	87
5.2.2. The Bayerischer Pfahl shear zone and the Bayerischer Pfahl shear-zone system	91
5.2.3. The intrusive bodies	93
5.2.4. The sheared granites	96
5.2.5. Deformation phases in the Moldanubian Zone: open questions	96
5.3. Results	99
5.3.1. Geological mapping in the Passau Forest	99
5.3.1.1. Migmatic rocks	100
5.3.1.2. Metamorphosed magmatic rocks	107

5.3.1.3. Metamorphosed sedimentary rocks	112
5.3.1.4. Magmatic rocks out of the Fürstenstein pluton	114
5.3.1.5. Magmatic rocks of the Fürstenstein pluton.....	117
5.3.1.6. Dykes.....	126
5.3.1.7. Mineralisations	129
5.3.1.8. Fault rocks.....	130
5.3.2. Deformation phases in migmatites of the study area: D ₁ and D ₂	131
5.3.2.1. D ₁	131
5.3.2.2. D ₂	131
5.3.3. D ₃ and sinistrally sheared granites: the D ₃ shear-zone system	133
5.3.3.1. Geographic distribution of sinistrally sheared granites.....	135
5.3.3.2. The case study of the Saunstein granite dyke	136
5.3.3.3. The case study of the Untermitteldorf dyke	153
5.3.3.4. Other sinistrally sheared granites	164
5.3.4. Deformation at the Bayerischer Pfahl shear-zone system: some new results	173
5.3.4.1. The Bayerischer Pfahl shear zone at the Große Ohe	174
5.3.4.2. The Bayerischer Pfahl shear zone and the Patersdorf granite.....	182
5.3.4.3. The Buchberger Leite.....	188
5.4. Discussion: global consideration of sheared granitoids	191
5.4.1. Fabrics, textures and strain	191
5.4.1.1. Oblique foliations as shear-sense indicators	191
5.4.1.2. Development of lattice-preferred orientation in quartz	192
5.4.1.3. Deformation mechanisms vs. temperature and grain-size.....	192
5.4.1.4. Strain localization	193
5.4.2. Migration of intrusives in the southern Bavarian Forest	194
5.4.3. Shear-zone systems and conditions governing their evolution.....	195
5.4.4. Significance of D ₃ in the Bavarian Forest and the Bohemian Massif	198
5.4.5. Geodynamic models.....	201
5.4.5.1. Models based on regional processes.....	201
5.4.5.2. Models based on local processes.....	207
6. Conclusions.....	211
6.1. Migration of granitoids in the Iberian Massif.....	211
6.2. Tectonometamorphic evolution of the Bavarian Forest.....	212
6.3. Ascent and emplacement of granitoids	215
6.4. Deformation of granitoids.....	216
7. Perspectives.....	219
References	221
Appendixes:	
Appendix 1: geological map of sheet No. 7246 Tittling, Bavaria (Germany)	
Appendix 2: sampling sites	
Appendix 3: microprobe analyses of phengites	
Appendix 4: microprobe analyses of feldspars	
Appendix 5: abbreviations	

1. Introduction

1.1. The Variscan Orogeny

The Variscan belt is a large Palaeozoic chain extending over 8000 km from the Ouachitas and Southern Appalachians to the Caucasus. Its evolution has been studied and partly reconstructed on the basis of plate tectonics. It was built between 500 and 250 Ma from the convergence and collision of two main continents: Laurentia-Baltica to the northwest and Gondwana to the southeast (see Franke (2000) and Matte (2001) for recent reviews). The small microplates known as Avalonia and Armorica were situated between these two continents. Avalonia was detached from Gondwana in the early Ordovician, drifting northward and opening the Rheic Ocean, while the Iapetus closed by southward and then northward subduction beneath the Taconic arc of Newfoundland. Avalonia was then docked to Laurentia and Baltica, reaching an equatorial position in the Silurian. Armorica detached from Gondwana opening the Galicia-Southern Brittany Ocean and drifted northward from the Ordovician to the Devonian independently from Avalonia, although the extent of the ocean separating it from Gondwana is still being discussed. Armorica docked to Laurentia and Baltica before the Carboniferous collision between Gondwana and Laurentia-Baltica (see plate tectonics evolution model by Matte (2001) shown in Fig. 1.1-1). The convergence resulted in the closure of at least three oceanic basins (Iapetus, Rheic and Galicia-Southern Brittany oceans) whose oceanic rocks are now preserved in some places as sutures.

The European Variscides extending from Poland to Iberia (Fig. 1.1-2) show a complex sinuous pattern with two main virgations: the Ibero-Armorican and the Bohemian. The main sections through the Variscides show that it is a fan-like orogen with opposite vergences of nappes and recumbent folds migrating toward external Carboniferous basins. Sutures are found on both sides of the belt and they are the roots of large nappes containing ophiolitic rocks and/or high-pressure rocks.

Most of the pre-Mesozoic basement of Western Europe is formed by Proterozoic to Carboniferous terranes deformed, in part metamorphosed, and intruded by various types of granitoids before the Permian. The basement outcrops in various stable massifs which suffered little deformation after the Permian. In addition, drilling has also revealed the basement beneath the various Meso-Cenozoic basins. The pre-Mesozoic basement of the Alpine, Pyrenean and Betic chains is also part of the Variscan belt. Most metamorphic terranes and most of the granites crop out in a broad central zone which was unroofed in some regions to a depth of 25 km before the deposition of Upper Carboniferous and Permian strata.

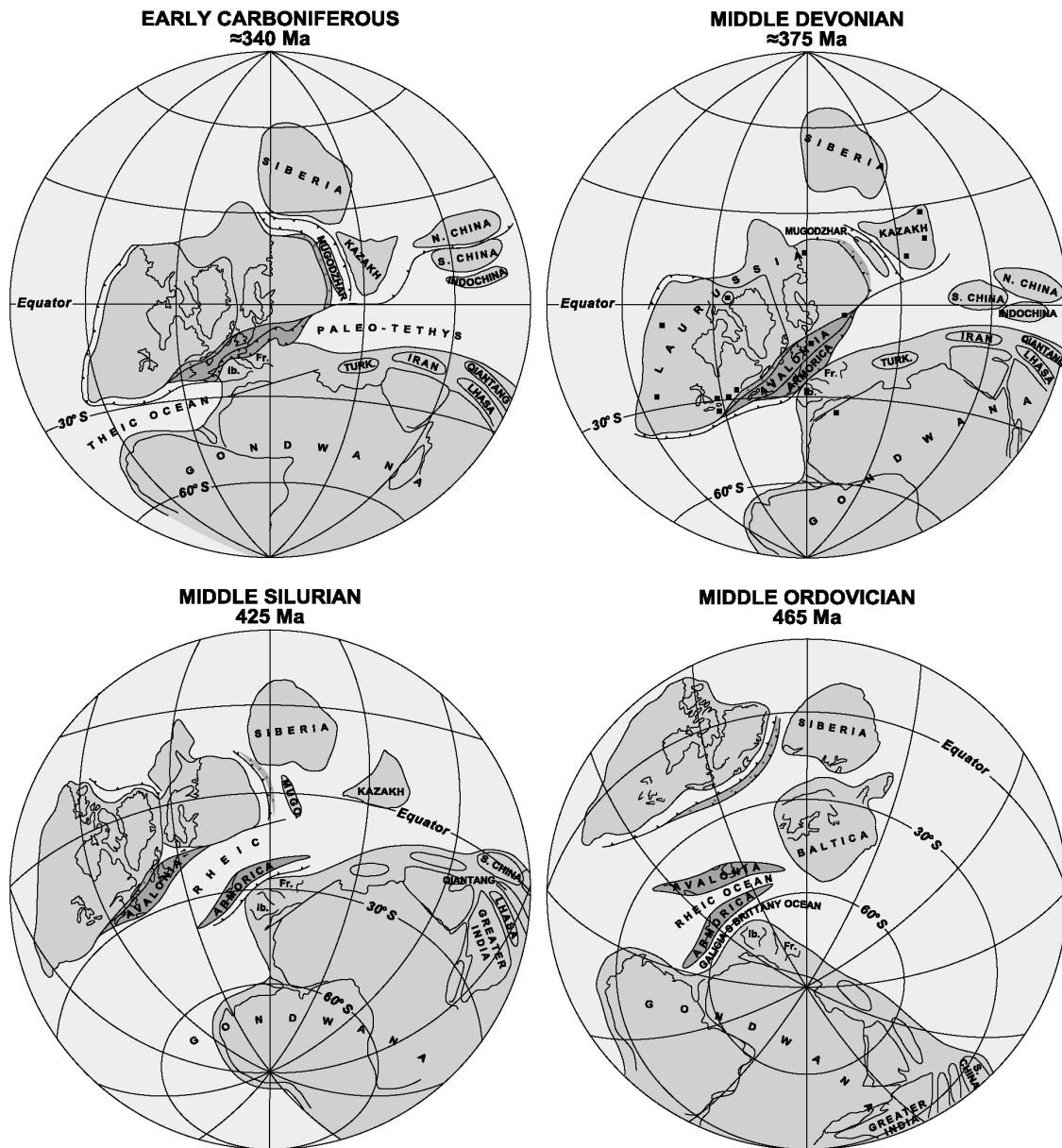


Figure 1.1-1. Tentative Palaeozoic reconstructions from middle Ordovician (465 Ma) to Lower Carboniferous (340 Ma), after Matte (2001).

The belt was severely eroded before the Permian time and was dismembered during Mesozoic plate motion and the opening of the Atlantic Ocean. It is now separated into two branches on the two sides of the Atlantic: on the western side the Appalachians extending from the Ouachitas to Newfoundland, and on the eastern side the Mauritanides on the western coast of Africa and the Variscan belt extending from north Africa and south Iberia to the Bohemian Massif and the Caucasus.

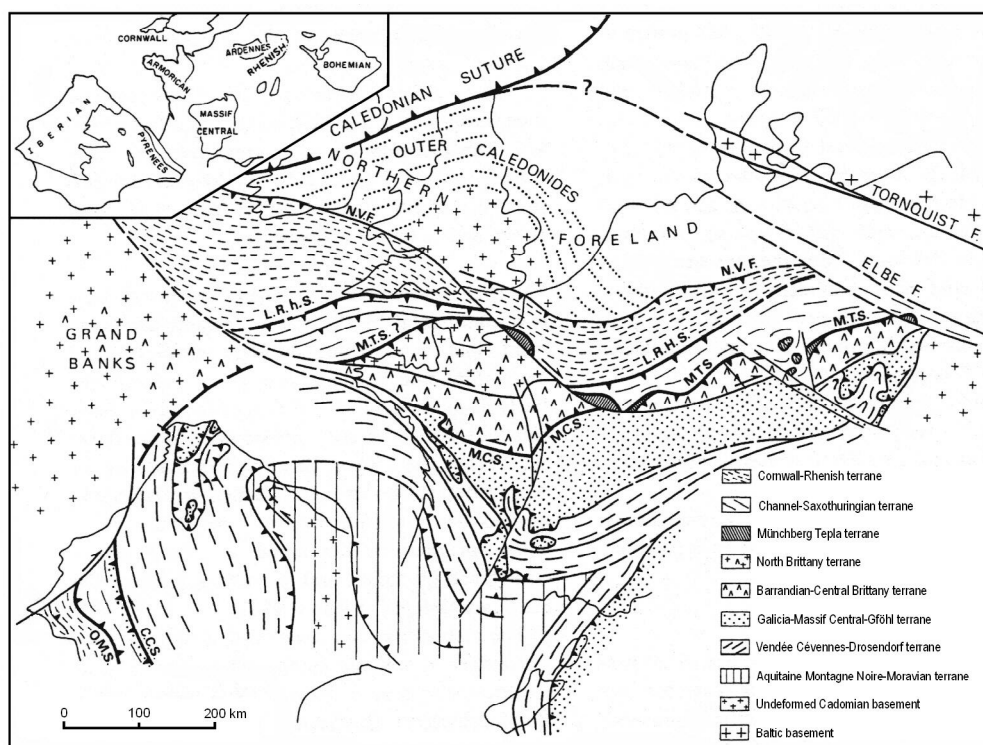


Figure 1.1-2. Structural sketch map of the European Variscides, redrawn after Matte (1991). The main Variscan massifs of central and western Europe are shown on the upper left corner of the picture. N.V.F. = northern Variscan front; L.R.H.S. = Lizard-Rhenish suture; M.T.S. = Münchberg-Tepla suture; M.C.S. = Massif Central suture; C.C.S. = Coimbra-Córdoba suture; O.M.S. = Ossa Morena suture. The Iberia and Corsica-Sardinia blocks are represented in their possible Permian position relative to Europe.

1.2. The Iberian and Bohemian Massifs

The Iberian Massif (Fig. 1.2-1) provides the best cross section through the Variscan belt of Western Europe with its classical fan-like arrangement. The first classification of the Iberian Massif in zones was proposed by Lotze (1945). Later, this classification was modified by several authors (e.g. Julivert et al., 1972, 1974). The modern classification regards 6 zones, which are (Fig. 1.2-1):

- Cantabrian Zone
- West Asturian-Leonese Zone
- Central Iberian Zone
- Galicia-Trás-os-Montes Zone
- Ossa-Morena Zone
- South Portuguese Zone

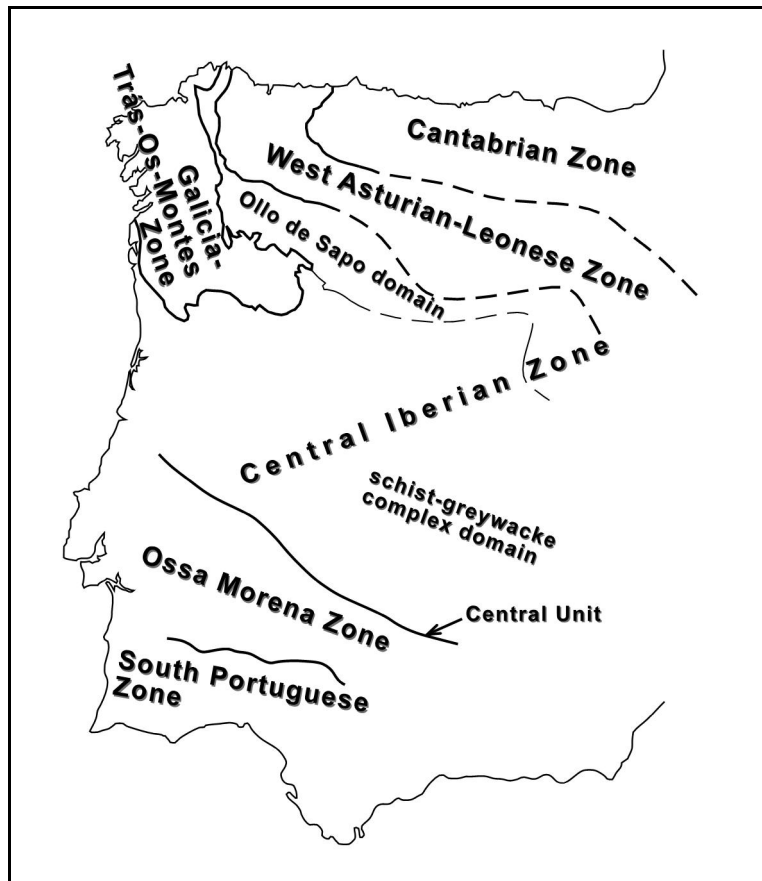


Figure 1.2-1. Sketch of the Iberian Massif indicating its tectonic subdivision in zones, simplified after Pérez-Estaún and Bea (2004).

According to the vergence of the structures, the Iberian Massif was subdivided into two branches (Julivert and Martínez, 1983) separated by the Badajoz-Córdoba shear zone (also called Coimbra-Córdoba shear zone or Central Unit), the latter being considered to be an orogenic suture: the northern branch comprises the Cantabrian, West Asturian-Leonese, Central Iberian and Galicia-Trás-os-Montes Zone; the southern branch is composed by the Ossa-Morena and South Portuguese Zone. The Cantabrian and the South Portuguese Zone show the typical features of external zones, whereas the rest are considered to build up the internal zone of the orogen.

The Cantabrian Zone is characterized by thin-skinned tectonics with thrusts and associated folds. Metamorphism and tectonic foliation are usually absent. The stratigraphic sequence includes Cambrian to Carboniferous rocks. Neoproterozoic rocks crop out in the western sector, at the so-called Narcea Antiform. Igneous activity is scarce, but extending all over the Palaeozoic as volcanic episodes, more frequent in the Lower Palaeozoic, and late-Variscan intrusions.

The West Asturian-Leonese Zone shows a thick Cambro-Ordovician sequence. Post-Devonian rocks are almost absent, except for a few discordant carboniferous deposits. Its structure is characterized by E-vergent folds crosscut by E-vergent thrusts and a late fold generation with upright axial planes. In this zone tectonic foliations are well developed and the rocks underwent low- to medium-grade metamorphism. Magmatic

rocks are found in form of volcanic episodes of Neoproterozoic and Palaeozoic age and pre-Variscan to Variscan granitoid intrusions.

In the Central Iberian Zone two domains are distinguished: the Olla de Sapo domain to the north and the schist-greywacke complex domain to the south. In the Olla de Sapo domain gneisses, syn-tectonic granites, and high-grade metamorphic rocks are exposed. The folds in this area are overturned and vergent to the E and NE. The schist-greywacke complex domain is characterized by pre-Ordovician, low-grade shales and greywackes and late-orogenic granites. Upright folds are typical for this domain, except for the southernmost area (allochthonous unit), in which recumbent NE-vergent folds are found.

The Galicia-Trás-os-Montes Zone is an allochthonous slab overthrust onto the Central Iberian Zone. It is composed by fragments of a passive continental margin, rocks affected by rifting processes, ophiolitic units and fragments of a volcanic arc. This allochthonous slab is thought to be rooted at the Badajoz-Córdoba suture.

The Ossa-Morena Zone is built up of Upper Proterozoic to Carboniferous rocks with variable metamorphic grade. The folds here are asymmetric or recumbent and vergent to the SW. Thrusts show a top-to-SW sense of movement. A younger upright folding is also observed. The magmatism here was pervasive and took place during three periods: at the end of the Precambrian, Cambrian-Ordovician and Carboniferous (Sánchez Carretero et al., 1990; Pérez-Estaún and Bea, 2004).

The South Portuguese Zone is separated from the Ossa-Morena Zone by rocks with oceanic affinity (Ossa-Morena suture sensu Matte (2001)). It is built up of very low-grade, Middle/Upper Devonian to Autunian rocks. Its structure is characterized by folds and thrusts verging to the SW. Important sulphide deposits are associated to a Lower Carboniferous vulcanosedimentary complex.

The modern tectonic subdivision of the mid-European Variscides in zones is based on the proposals of Suess (1903) and Kossmat (1927). Although modern tectonic subdivisions show some differences in detail (e.g. Franke 1989; Matte et al., 1990; Matte, 1991; Dallmeyer et al., 1995; Franke, 2000), they usually regard the following zones from north to south (Fig. 1.2-2):

- Rhenohercynian Zone.
- Saxothuringian Zone, including the Mid-German Crystalline High.
- Moldanubian Region, composed of the Moldanubian Zone sensu stricto and the Teplá-Barrandian Zone.
- Moravo-Silesian Zone.

All of the zones are exposed in the Bohemian Massif, except for the Rhenohercynian Zone, which crops out in other massifs further to the north and northwest.

The Rhenohercynian is a typical foreland fold-thrust belt. It can be traced at least from SW England through E Germany and correlated with the Moravo-Silesian of Austria and even with the South Portuguese Zone of Iberia. The Rhenohercynian Zone is made up of an autochthonous part and several allochthonous units underlain by a crystalline Cadomian basement. The autochthon is characterized by neritic and hemipelagic sequences, mostly of Devonian age. The allochthonous units comprise ocean floor and active margin sequences. Its structure is characterized by folds and thrusts verging to the NW. The metamorphic grade is normally very low, reaching greenschist facies conditions at the Northern Phyllite Zone. The presence of extensive submarine basaltic rocks is characteristic for this zone.

The Mid-German Crystalline Rise forms part of the Saxothuringian Zone. It is composed of metamorphic and magmatic complexes. The metamorphic complexes comprise metasedimentary, migmatic and metamagmatic rocks. The magmatic complexes are represented by plutonic bodies of variable composition, age of intrusion and degree of deformation. Most of the complexes of the Mid-German Crystalline Rise were subjected to regional metamorphism under lower to upper amphibolite facies conditions.

The southern part of the Saxothuringian Zone, i.e. excluding the Mid-German Crystalline Rise, is usually referred to as Saxothuringian Basin. It is dominated by relatively low-grade sedimentary and volcanic rocks. Two facies realms are distinguished: the Thuringian and the Bavarian facies. The Bavarian facies rocks represent nappes emplaced on paraautochthonous sequences developed in Thuringian facies. Most of the Saxothuringian shows a very-low metamorphic grade. Greenschist facies conditions or higher are locally observed. The structure of the Saxothuringian Belt is characterized by large NE-trending syn- and antiforms. These fold structures are transected by NW-trending fault zones. Repeatedly changing tectonic regimes resulted in the formation of numerous distinct plutonic-volcanic suites.

Some allochthonous nappes, containing eclogites and peridotites amongst other rock types, were overthrust from SE onto the Saxothuringian series. These constitute the tectonic klippen of Münchberg, Wildenfels, and Frankenberg, which are erosional remnants of one or more nappe piles presumably rooted at the boundary between the Saxothuringian Zone and the Moldanubian Region. This boundary is considered to be a major suture. The allochthonous nappes show a tectonic sequence characterized by inversion of the stratigraphy and the metamorphic grades.

The Moldanubian Region of the Bohemian Massif can be subdivided into two tectonostratigraphic units: the Teplá-Barrandian, which crops out mainly in the Czech Republic, and, west and south of it, the Moldanubian *sensu stricto*. The Moldanubian *sensu stricto* will be referred to as "Moldanubian Zone" in this work.

The Teplá-Barrandian constitutes a median massif between the N- and the S-facing parts of the orogen. It is the best-preserved fragment of the Cadomian Orogen in central Europe. The basement consists of late Proterozoic sediments and arc-related volcanic rocks, which have undergone very low-grade to amphibolite facies metamorphism and deformation at the boundary Precambrian/Cambrian (Zulauf et al., 1999). The Cadomian basement is overlain by Cambrian to middle Devonian sedimentary and volcanic rocks. Some parts of the margins of the Teplá-Barrandian are lined by eclogite facies and mantle rocks. These margins probably represent sutures, but were later overprinted by crustal-scale normal faulting (Zulauf, 1994). Early Variscan (Devonian) low-grade metamorphism and deformation affected the continental basement and its Palaeozoic cover.

The Moldanubian Zone contains mainly high-grade gneisses and migmatites of supracrustal origin, orthogneisses, granulites and numerous Variscan post-tectonic granitoid intrusions. Matte et al. (1990) and Franke (2000) distinguished two main tectonostratigraphic units: the Drosendorf and the Gföhl units, separated by the Main Moldanubian Thrust which places the high-pressure rocks of the Gföhl unit onto the paraautochthonous Drosendorf unit. The boundary between both units is characterized by the presence of granulites, eclogites and peridotites. In large areas of the Moldanubian Zone the flat attitude of the foliation has been folded into large, open antiforms, and the mineral and stretching lineation trends NW—SE, corresponding to the transport direction (Matte et al., 1990). As will be seen in the next chapters, the structure of the Moldanubian Zone is much more complicated in detail.

The Moravo-Silesian Zone is separated from the Moldanubian Zone by a major NE—SW trending, NW-dipping dextral shear zone which probably reworked an older SE-facing thrust. It consists of a Cadomian basement unconformably overlain by Devonian to Carboniferous sediments and volcanics. Deformation and metamorphism increase toward the boundary with the Moldanubian and along strike toward the northeast. The large-scale deformation corresponds to a north-eastward displacement of the Moldanubian onto the Moravo-Silesian. In addition, the Carboniferous foredeep shows upright NE—SW trending folds with a steeply dipping fan-like slaty cleavage and horizontal stretching lineation due to the same transpressional dextral tectonics.

1.3. Migration and deformation of granitoids

Intrusive rocks provide valuable information about orogenic processes. Their chemistry, age and structure can deliver a big amount of data regarding not only their evolution, but also that of the melt source and the crust in which they ascended and froze.

In the Variscan Belt of Europe, studies on igneous rocks are abundant, especially regarding geochemical and petrological aspects (e.g. Finger et al., 1997; González

Menéndez, 1998; Siebel, 1998; Villaseca et al., 1998a, 1998b; Bea et al., 1999; Salman, 2004). Nevertheless, studies integrating structural information (e.g. Büttner, 1999; Yenes et al., 1999; Simancas et al., 2000; Galadí-Enríquez et al., 2003) are scarcer, maybe because structural geologists considered for a long time that igneous rocks constitute rather isotropic bodies.

Beyond petrological, geochemical and geochronological matters, the work on structural aspects of intrusive rocks has experienced an important development in recent years (e.g. Paterson et al., 1989, 1998). Structures developed during the magmatic phase, also called hypersolidus phase, as well as those formed after freezing, i.e. the subsolidus phase, have been the object of numerous studies.

One of the important aspects of intrusive rocks is the way they rise through the Earth's crust and emplace at their final location and how this evolution can be deciphered in the field. In the last decades, the mechanisms of magma migration, i.e. of ascent and emplacement, have been profusely studied. Structural geologists have paid increasing attention to the fabrics of magmatic rocks. Recent works show that magmatic rocks are rarely isotropic and, in particular intrusive ones, always exhibit their own internal structure which, together with their shape and their relationships with the country rock, provides key information for the reconstruction of their emplacement, their subsolidus and, in favourable cases, even their ascent history (e.g. Paterson et al., 1989; Vigneresse, 1995a; Dehls et al., 1998; Paterson et al., 1998; Brown and Triggvason, 2001; Gouly et al., 2001; Haederle and Atherton, 2002).

The ascent of granitic magmas has been envisaged by most authors as a process occurring in the Earth's crust by means of two end-member mechanisms: diapirism and dyking. Weinberg (1999) proposed a third mechanism, namely "pervasive migration", which is invoked as a process linking the melt formation and its extraction from the source and the ulterior ascent either by dyking or diapirism. A distinction is usually made between acid and basic magmas, since their viscosity and density relative to the host rock strongly control their ability to ascend as diapirs or through dykes. In the present work we will mainly concentrate on the intrusion mechanisms of acid magmas, given that the studied rocks are mostly granitic in composition. Paterson and Miller (1998) consider the ascent as a complex process in which four main mechanisms play a role. These are diapirism, dyking, ascent along pre-existing faults, and heterogeneous flow in migmatic rocks.

The diapirism is basically the ascent of melts in form of drop-shaped or elliptical batches which soften and push aside the surrounding wall rock as they pass through. The driving force of ascent is supposed to be the buoyancy of less dense acid magmas flowing upwards inside a denser host rock, with more or less influence of the regional stress field. The field evidence for diapirism must be sought in the shape and internal structure of the pluton, as well as in the structures recorded by the country rocks, such as concentric foliation patterns, subvertical magmatic lineations, steep contact surfaces,

rim synclines or strongly sheared aureoles with pluton-side-up sense of movement, depending on the section exposed on the present erosion level. Nevertheless, this evidence might be easily obscured by later emplacement and deformation processes (England, 1990). Some examples of plutons, which are supposed to have ascended as diapirs, are found in the literature, such as the Northern Arran granite (England, 1992; Gouly et al., 2001), the Saraya granite (Pons et al., 1991) or the Tenpeak, Oval Peak, Entiat and Hall Canyon plutons (Miller and Paterson, 1999). Several theoretical and experimental models (Berner et al., 1972; Dixon, 1975 and references therein; Marsh, 1982 and references therein) support the viability of the ascent of diapirs and provide information about the structures expected in and around them, which are partially found in natural examples. Diapirism is not accepted by many authors, due in part to the lack of diagnostic field evidence and to thermomechanical considerations suggesting that the diapirs must spend much of their energy in softening the surrounding rocks, which would quickly cause their crystallisation and "thermal death". However, it is accepted by many others that diapirism works and that it does best in the hot lower crust. Furthermore, whereas one single diapir can probably ascend only a short distance, a succession of two or more nested diapirs exploiting one single "thermally prepared" pathway might be able to penetrate the entire crust (Marsh, 1982).

In the last years, diapirism has been discredited as a transport mechanism. Some authors consider it to be inefficient, either irrespective of the crustal level considered or at least above the brittle-ductile transition (Bateman, 1984; Clemens and Mawer, 1992; Petford et al., 1993; Vigneresse, 1995b; Petford, 1996; Clemens, 1998; Petford et al., 2000). The dyking theory has attained support in the geological community since some mechanical and mathematic models showed that relatively narrow dykes (>2 m) are able to feed enough amounts of acid melt into magma chambers without freezing in only some hundred years (Petford et al., 1993, 1994; Petford, 1996; Petford et al., 2000). The development of self-propagating fractures (dykes) in the crust is possible at the tip of magma-filled gashes due to the concentration of stresses (Lister and Kerr, 1991; Clemens and Mawer, 1992). Many plutons have been interpreted as the result of the ascent of magma through dykes and shear zones, such as the granitoid plutons of the Tulle anticline (Roig et al., 1998), the Cordillera Blanca batholith (Petford et al., 1993), the Cardenchoa pluton (Simancas et al., 2000), the La Alberca-Béjar granitic area (Yenes et al., 1999), the Millevaches massif (Gébelin et al., 2006); the Dzhabyk batholith (Brown and Tryggvason, 2001), the Coastal batholith of Peru (Haederle and Atherton, 2002) or the Cabeza de Araya pluton (Vigneresse and Bouchez, 1997). Nevertheless, Rubin (1995) proposed that dyking is definitely efficient for basic melts, but might become inefficient in carrying rhyolitic magmas out of the source region.

Some authors conciliate the ascent of magmas both as diapirs and along pre-existing or self-propagating discontinuities, depending on the rheological conditions and, therefore, on the crustal level considered. Thus, it is possible that magmas start their rise as

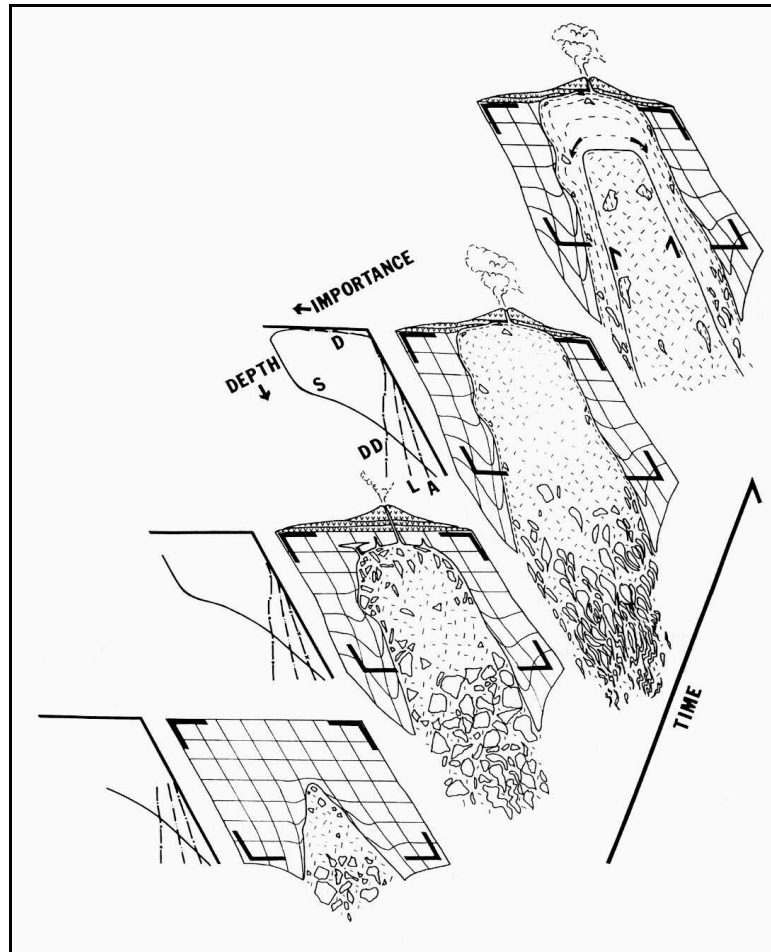
diapirs in the hot lower crust and continue their ascent along dykes once the diapir cools down. Basic magmas would never be able to build diapirs due to their low viscosity and high density, whereas felsic magmas are more likely to rise as diapirs. Intermediate magmas might swap from diapirs to dykes during their evolution (Bateman, 1984; Weinberg, 1996).

Although partly linked to the ascent mechanisms, the emplacement mechanisms are usually regarded as independent from the way the magma arrived to its final location. In the literature it is common to find a classification of emplacement mechanisms into forceful and passive types, depending on whether the rate of buoyant uprise exceeds the rate of tectonic cavity opening or vice versa. However, Paterson and Fowler (1993) consider this classification misleading, since several mechanisms may operate in the same pluton at different stages and the stress field governing the emplacement is always a combination of both regional and magma-induced stresses. The emplacement mechanisms must account for the strain patterns observed in and around plutons, but also for the "room problem", i.e. the way the space for the intrusion is created. As a consequence, Paterson and Fowler (1993) and Paterson and Vernon (1995) prefer to use the terms "near-" and "far-field material transfer processes" when referring to the emplacement mechanisms (Fig. 1.3-1).

The stoping mechanism consists on piercing and fracturing the wall rock by brittle processes. The resulting blocks, provided they are dense enough, sink towards the bottom of the magma chamber. Although some stoping may operate during ascent, for example in the case of piercing diapirs, it is thought to dominate rather at high crustal levels, and therefore to be most important as emplacement mechanism.

The emplacement may be aided by the vertical and horizontal displacement of the wall rock, either by ductile or brittle processes. In cauldron subsidence, space for pluton emplacement is created by down-dropping a roughly cylindrical block along a steeply-dipping ring fault. Downward country rock return flow has been invoked for the emplacement of diapirs and lopoliths. Roof uplift or "doming" and shortening create some space for the emplacement of laccoliths. Also non-piercing diapirs may cause some doming and shortening in the overburden as they arrive to their emplacement site. Horizontal shortening of the country rocks is often observed around concordant plutons. The deformation around intrusions, caused by magma-driven forces and more or less conditioned by tectonic stresses and pre-existing structures, has been studied by means of analogue and theoretical models by several authors (Román Berdiel et al., 1995; Schwerdtner, 1995; Román Berdiel et al., 1997; Benn et al., 1998; Kerr and Pollard, 1998; Benn et al., 2000; Acocella and Mulugeta, 2002; Corti et al., 2005) and observed in natural examples (e.g. Cruden, 1998; Morgan et al., 1998; Wang et al., 2000; Acocella and Mulugeta, 2001).

Figure 1.3-1. Sketch showing one scenario of temporally changing near- and far-field material-transfer processes during emplacement of concentrically expanded plutons, after Paterson and Vernon (1995). Each time-slice section is areally balanced in the region outlined by the thick black corners. Material displaced during emplacement of the pluton is shown outside these corners. Diagrams to left show relative importance of different material-transfer processes. D = doming of roof rocks, S = stoping, DD = ductile shortening, L = rigid translation of wall rock, A = assimilation. The relative importance of material transfer processes changes with depth, time and distance from pluton, magnitudes will vary from pluton to pluton. Final time slice shows possible magma flow patterns during emplacement of younger magma pulse.



Ballooning is defined by Paterson and Vernon (1995) as the relatively symmetrical, radial expansion of a magma chamber where its centre does not move significantly relative to a far-field reference frame. Typical ballooning plutons show a concentric facies zonation and a flattening-type deformation increasing its intensity from the centre to the margins.

The opening of potential voids in sites of local or regional extension, such as fold hinges or pull-aparts, has been invoked by many authors as a space-making mechanism for plutons (e.g. McCaffrey, 1992; Aranguren et al., 1996, 1997).

Zone melting is the partial melting and assimilation of the overlying country rock. It may aid the ascent and emplacement of magma mostly in the ductile crust, but its importance is probably limited in shallow levels.

Sheeting is the accretion process of successive magma batches into an elongated plutonic body, usually tectonically controlled (Paterson and Miller, 1998) and often associated to high-strain zones (Vegas et al., 2001).

Due in part to their allochthonous character, intrusive rocks are particularly useful for the reconstruction of geological processes. After emplacement, intrusive rocks get involved in deformation together with their country rocks. Thus, it is possible to perform a relative dating of intrusion and deformation events based on the deformations recorded by the intrusives and their country rocks, i.e. these bodies constitute important time markers for the determination of the age and duration of a given deformation phase. Works on structural aspects of intrusives benefit from geochronological studies: The latter can help to translate relative datings into absolute values.

Granitic systems have been studied by several authors (e.g. Zen, 1988; Johannes and Holtz, 1996): Studies concerning their phase relationships and solidus temperature are abundant. An important advantage of granitic rocks is their mineralogy. They are rich in minerals like quartz, feldspar and mica. Quartz occurs in most of the crustal rocks in a wide range of pressure and temperature conditions. Its rheological behaviour has been profusely studied. As a consequence, quartz textures and microstructures are well known and can provide much information about the deformation mechanisms that operated during their development and, therefore, about the PT conditions governing the deformation (e.g. Passchier and Trouw, 1996, and references therein). Feldspar is the most abundant mineral in the Earth's crust. Its rheological behaviour under different temperature conditions is relatively well known as well (e.g. Tullis, 1983). Thus, its microfabrics can also deliver information about the tectonothermal evolution of the rocks containing it. Finally, the composition of white mica has been studied and used as geobarometric indicator (Massonne and Schreyer, 1987; Massonne and Szpurka, 1997). Therefore, the composition of magmatic and synkinematic white mica can also place constraints on the PT path followed by granitic rocks from their emplacement to their deformation. All of these considerations make granitic rocks especially interesting for the study of the tectonometamorphic evolution of orogens.

2. Aims

The goal of this work is to investigate both evolution stages in the history of Variscan granitoids: the hypersolidus and the subsolidus stages. With this aim, some intrusive bodies, which can be suitable for the study of their evolution either in the subsolidus or in the hypersolidus phase, were selected. The methods used for this research are adapted to the particular aim pursued in every case, to the specific plutonic body, to the geological conditions and to the equipment available at the host institution.

The study areas are located in two different parts of the Variscan Orogen: the Iberian and the Bohemian Massifs (Fig. 2-1).

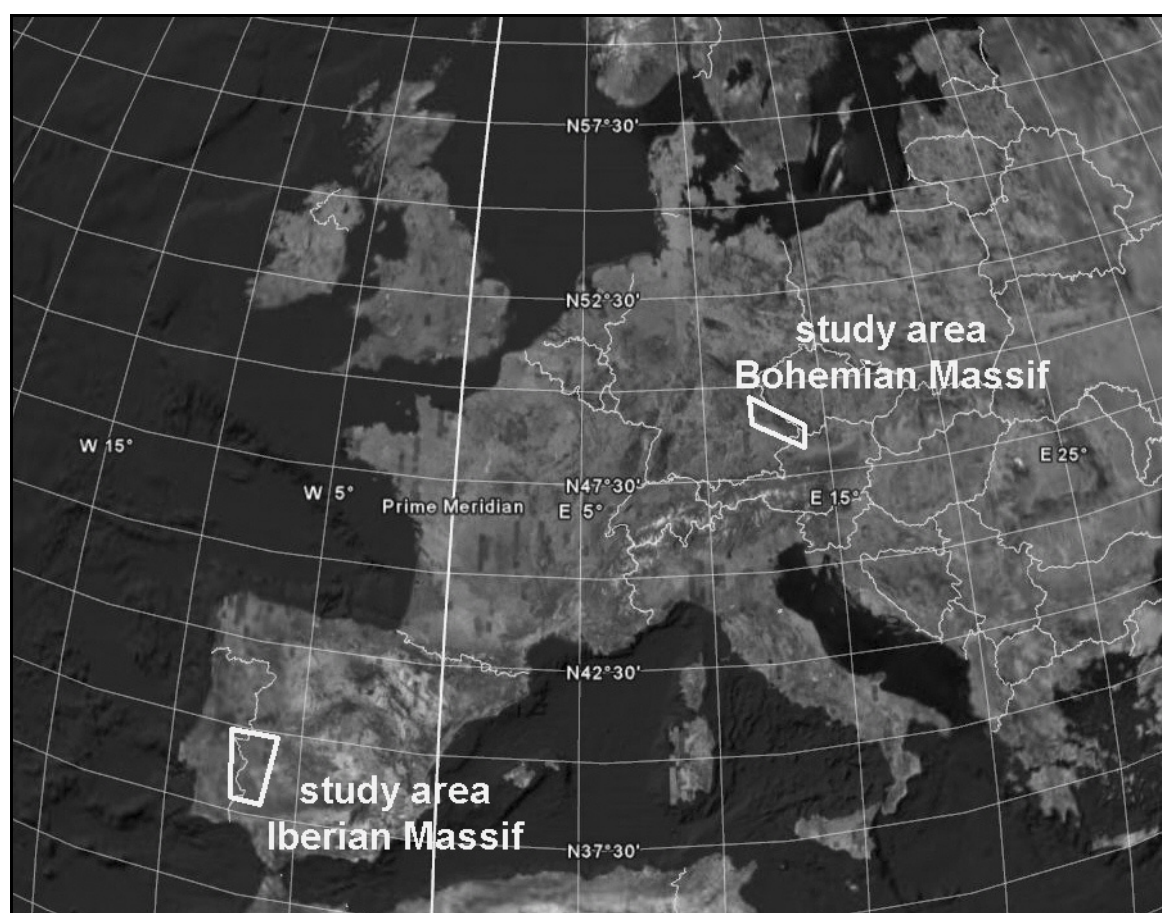


Figure 2-1. Geographic location of the study areas. Source: Google Earth.

Two intrusive bodies of the Iberian Massif were selected to investigate mostly their hypersolidus history: the La Bazana Pluton and the Nisa-Alburquerque batholith. Both of them intruded after the ductile Variscan deformation phases and are therefore thought to preserve a shape and structure conditioned or at least influenced by the mechanisms operating during their ascent and emplacement. The first aim of this research is to

extract from these well-exposed granitic bodies of the Iberian Massif as much information as possible about their hypersolidus evolution. This goal can be achieved by (1) studying their three-dimensional shape by means of gravity data modelling and (2) describing the internal structure and petrography of both the intrusive bodies and their contact aureoles. Magnetometric measurements constitute a good complement to detect facies zonations in the granitic bodies and heterogeneities in the country rocks. The research on granitoids of the Iberian Massif was supported by the equipment and staff of the University of Granada (Spain).

Some different granitic bodies from the Bohemian Massif were selected for the study of their subsolidus history. Most of the studied bodies are sinistrally sheared granites with foliation planes trending WNW—ESE to WSW—ENE, which can deliver valuable information about the tectonic evolution of the Bavarian Forest before and after their emplacement. Key questions to be solved are:

- Under which conditions did the emplacement and deformation of these igneous bodies take place? Did they intrude syn-kinematically?
- What kind of geometrical and temporal relationships do exist between different intrusion and deformation phases?
- How can we integrate these sheared granites in the tectonic evolution of the Bavarian Forest?

An array of different techniques was applied in order to solve these questions. These techniques are: geological mapping, optical microscopy, electron backscatter diffraction (EBSD), strain analysis, X-ray fluorescence analysis, electron microprobe analysis and piezometry. The research on granitoids of the Bohemian Massif was supported by the equipment and staff of the University of Frankfurt a.M. (Germany).

3. Methods

3.1. Gravimetry

The information about the shape of granitic plutons is often restricted to the section cut by the present erosion surface. Some authors have attempted to infer their deep shape based on surface observations concerning their internal structure. Nevertheless, there are several examples in which this method has been proven to fail (Paterson et al., 1998). Thus, the use of geophysical methods is essential in order to constrain their three-dimensional geometry.

Since the density of acid igneous rocks (2.50-2.81 g/cm³) is usually lower than the one of surrounding country rocks, generally of metapelitic composition (2.40-3.30 g/cm³), gravity data are appropriate for determining the shape of granitic plutons at depth (Vigneresse, 1990). This has already been recognised by many authors, who have successfully applied this method in granites and were thus able to propose an emplacement model in the light of the obtained geometries (e.g. Améglio et al., 1997; Vigneresse and Bouchez, 1997; Yenes et al., 1999; Sant'Ovaia et al., 2000; Simancas et al., 2000; Gouly et al., 2001; Kurian et al., 2001; Haederle and Atherton, 2002; Talbot et al., 2005).

In the next lines, the procedure followed to measure, process and model gravity data in small regions on land is briefly described.

The magnitude of gravity depends on five factors: latitude, elevation, topography, earth tides, and density variations in the subsurface. Gravity exploring is concerned with anomalies due to the last factor, and therefore, the effect of the other ones must be removed, i.e. we must make corrections to reduce gravity readings to the values they would have on an equipotential surface of reference such as the geoid. In addition, the measured gravity is affected by instrumental drift. Gravity anomalies are usually expressed in miligal (mGal).

Due to the rotation of the Earth and its equatorial bulge, the magnitude of gravity increases towards the poles. The theoretical value of gravity is given by the equation

$$g_t = 978031.846 (1 + 0.005278895 \sin^2 \varnothing + 0.000023462 \sin^4 \varnothing) \text{ (mGal)},$$

where \varnothing is the latitude.

Earth-tide correction. The movement of the Sun and the Moon produces gravity changes of up to 0.3 mGal. Since these changes are smooth and slow, they can be eliminated together with the instrument drift correction.

Free-air correction. In order to remove the effect due to the differences in elevation between stations, the free-air correction must be applied by using the following expression:

$$\Delta g_{FA} / \Delta R = 2\gamma M_e / R_e^3 = 2g / R_e = 0.3086 \text{ (mGal/m)},$$

where ΔR is the vertical distance between the station and the reference surface, γ the universal gravitational constant ($6.672 \cdot 10^{-11} \text{ N m}^2 / \text{kg}^2$), M_e the mass of the Earth, and R_e the Earth's radius ($\sim 6368 \text{ km}$).

Bouguer correction. The Bouguer correction accounts for the attraction of material between the station and the datum plane, supposing that this material forms a continuous, infinite slab of constant thickness and density. The correction is calculated as follows:

$$\Delta g_B / \Delta R = 2\pi\gamma\rho = 0.04192\rho \text{ (mGal/m)},$$

where ρ is the slab density in g/cm^3 .

Terrain correction. This correction eliminates the effect of neighbouring hills and valleys, both producing a decrease in the magnitude of gravity. The correction is usually calculated by dividing the area into compartments and comparing the elevation within each compartment with the station elevation. The gravity effect is then calculated for every sector and the contribution of all sectors is summed.

When all the above-mentioned corrections have been applied, the Bouguer anomaly is obtained:

$$A_{BOU} = g_{OBS} - g_t + \Delta g_{FA} - \Delta g_B + \Delta g_{TE}$$

i.e. Bouguer anomaly = observed gravity value – theoretical gravity value + free-air correction – Bouguer correction + terrain correction.

Relative gravity measurements were recorded with a Master model Worden gravimeter, with temperature compensation and precision of 0.01 mGal. Measurement points were positioned by GPS and a barometric altimeter that has a precision of 0.5 m in altitude. Measurements were carried out in cycles of less than 3 hours in order to allow the linear correction of gravimeter and altimeter drifts. Altimetric data were obtained at base stations from topographic maps. After drift correction of barometric altimetry data, the altitude was determined for each measurement station. Relative gravity data were calibrated with the absolute gravity value of one of the base stations of the *Instituto Geográfico Nacional* (National Geographic Institute) situated at several locations of the Spanish territory. Absolute gravity data in each field station made it possible to calculate the Bouguer anomaly. A standard density that corresponds to the average density of crustal rocks (2.67 g/cm^3) was applied for Bouguer correction. The terrain effect was ignored, however, since the topography of the study areas is smooth, and the contribution of the topographic effect is expected to be small compared to the obtained anomalies. Bouguer anomaly maps were constructed by interpolating gravity values between measurement points using the kriging method.

Bouguer anomaly maps show a superposition of anomalies resulting from density changes at various depths. Some anomalous masses lie at depths in the zone of

interest, some result from deeper masses, and some from shallower ones. As the source of an anomaly deepens, the anomaly becomes more spread out and its amplitude decreases. The effect of shallow masses (near-surface noise) is usually of short wavelength. It can be removed largely by smoothing short-wavelength anomalies. The effects of deep-seated masses are called the regional anomaly. The gravity field after near-surface noise and the regional have been removed is called the residual anomaly; it presumably represents effects of the intermediate zone of interest.

The separation of regional and residual anomalies can be made using different graphical and analytical methods. Vigneresse (1990) suggested that a convenient residual is obtained when the zero contour level of the residual anomaly map outlines the studied granitic body.

When the residual anomaly has been obtained, the shape of the anomalous body can be modelled. Whatever the modelling procedure used, the ambiguity of the models can be considerably reduced by the available geological information, such as the density contrast or the position and dip of the contacts. Furthermore, not all the imaginable shapes that fit the data are geologically plausible. In this respect, the geological background of the interpreter plays an important role. In the direct method, the source body is approximated by slices of finite thickness. The effect of each slice is computed, assuming a polygonal shape. After comparison with the measured data, the geometry of the source is modified until a good fit between the observed and computed anomalies is reached. This is the procedure followed in the present work. The inverse method involves determining the geometry and physical properties of the source from measurements of the anomaly.

3.2. Magnetometry

In order to detect facies zonations in the studied igneous bodies and heterogeneities in their country rocks, measurements of the intensity of the magnetic field were carried out during the gravimetric and geological surveys. These measurements are cheap and easy and provide additional information about the geology of the study area. The basics of this geophysical method are described below.

As exposed by Telford et al. (1995), the modern and the classical magnetic theories differ in basic concepts. Classical magnetic theory is similar to electrical and gravity theory; its basic concept is that point magnetic poles are analogous to point electrical charges and point masses, with a similar inverse-square law for the forces between the poles, charges or masses. Magnetic units in the cgs-emu system are based on this concept. SI units are based on the fact that a magnetic field is electrical in origin. Its basic unit is the dipole, which is created by a circular electrical current.

The cgs-emu system begins with the concept of magnetic force given by Coulomb's law:

$$F = (\rho_1 \rho_2 / \mu r^2) r_1,$$

where F is the force on ρ_2 in dynes, the poles of strength ρ_1 and ρ_2 are r centimetres apart, μ is the magnetic permeability of the medium, and r_1 is a unit vector directed from ρ_1 toward ρ_2 .

The magnetizing field or magnetic field strength H' is defined as the force on a unit pole:

$$H' = F / \rho_2 = (\rho_1 / \mu r^2) r_1,$$

where the prime indicates that H is in cgs-em units. H' is measured in oersteds (equivalent to dynes per unit pole).

According to the modern theory, a magnetic field is a consequence of the flow of an electrical current. As expressed by Ampère's law, a current I in a conductor of length Δl creates, at a point P, a magnetizing field H given by

$$\Delta H = (I \Delta l) r_1 / 4\pi r^2$$

where H has the SI dimension amperes per meter ($= 4\pi \cdot 10^{-3}$ oersted), r and Δl are in meters, I is in amperes, and ΔH , r_1 , and $I \Delta l$ have the directions indicated in Fig. 3.2-1.

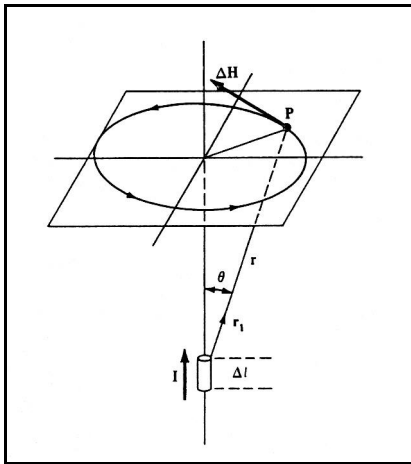


Figure 3.2-1. Ampère's law. A current I through a length of conductor Δl creates a magnetizing field ΔH at a point P, taken from Telford et al. (1995).

The orbital motions of electrons around an atomic nucleus constitute circular currents and cause atoms to have magnetic moments. Molecules also have spin, which gives them magnetic moments. A magnetisable body placed in an external magnetic field becomes magnetized by induction. The magnetization is measured by the magnetic polarization or magnetization intensity M . The lineup of internal dipoles produces a field M which, within the body, is added to the magnetizing field H . M and H have the same dimensions (ampere / meter). For low magnetic fields, M is proportional to H and is in the direction of H . The degree to which a body is magnetized is determined by its magnetic susceptibility k , which is defined by

$$M = kH$$

Magnetic susceptibility in electromagnetic units (emu) differs from that in SI units by the factor 4π , i.e.

$$k_{SI} = 4\pi k'_{emu}$$

The magnetic susceptibility is the fundamental rock parameter in magnetic prospecting. The magnetic response of rocks and minerals is determined by the amounts and susceptibilities of magnetic materials in them.

The magnetic induction B is the total field, including the effect of magnetization. It can be written

$$B = \mu_0 (H + M) = \mu_0 (1 + k) H = \mu \mu_0 H, \text{ or}$$

$$B' = H' + 4\pi M' = (1 + 4\pi k') H' = \mu H'$$

when H and M are in the same direction, as is usually the case. The SI unit for B is the tesla (T) = N/A·m. The electromagnetic unit for B' is the gauss (= 10^{-4} tesla). The permeability of free space μ_0 has the value $4\pi \cdot 10^{-7}$ Wb/A·m or N/A². In vacuum $\mu = 1$ and in air $\mu \sim 1$. The unit of magnetic induction generally used for geophysical work is the nanotesla (nT) or gamma (γ).

The geomagnetic field of the Earth is composed of three parts:

1. The main field, which varies relatively slowly and is of internal origin.
2. A small field, which varies rapidly and originates outside the Earth.
3. Spatial variations of the main field, which are usually smaller than the main field, are nearly constant in time and place, and are caused by local variations of the magnetic properties in the near-surface crust of the Earth. These are the targets in magnetic prospecting.

Local changes in the main field result from variations in the near-surface rocks of 1) magnetic mineral content, i.e. bulk magnetic susceptibility, or 2) remanent magnetization. Thus, the anomalies can be produced either due to susceptibility contrasts or to the existence of a remanent or residual magnetization. The remanent magnetization is the magnetization shown by ferromagnetic materials as the magnetizing field is removed. This material behaviour constitutes the base of paleomagnetic studies, but is not relevant for this study.

Attending to their magnetic susceptibility, the minerals can be classified as diamagnetic ($k < 0$), paramagnetic ($k > 0$) or ferromagnetic ($k \gg 0$). The susceptibility of the rocks can range between very different values, depending on their composition. Sedimentary rocks have usually a lower susceptibility than crystalline rocks. The latter have a higher susceptibility, the more basic/mafic they are. Thus, ultrabasic rocks, such as peridotites, kimberlites and eclogites, are easily identifiable using magnetic methods.

In this study, measurements of the total intensity were carried out with a GSM neutron precession magnetometer, with a precision of 1nT. Once the magnetic data have been

acquired, they must be processed in order to obtain the magnetic anomaly. The processing usually involves the following steps:

- Some corrections must be undertaken. The so-called spikes are anomalous values caused by instrumental errors or anomalous bodies located next to or at the surface. They must be removed in order to eliminate the superficial noise. Furthermore, the magnitude of the magnetic intensity varies with time at a given location and thus, this variation must be corrected, especially if the anomalies expected are small; the correction can be made by comparing with a reference station or by linear interpolation in measurement cycles of less than 3 hours. Finally, the theoretical intensity value, which is dependent on location and time, must be subtracted from the observed value. This theoretical intensity is given by the International Geomagnetic Reference Field (IGRF) and based on empirical observations. After subtracting the theoretical from the observed magnetic intensity value, the magnetic anomaly is obtained.
- Reduction to the pole. This processing step might be optionally made. Since the flow lines of the geomagnetic field are generally (except at the poles) oblique to the Earth's surface, the changes of the magnetic field intensity produced by an anomalous body are displaced with respect to the vertical of the body. Moreover, the shape of the anomalies is also distorted: for example, an anomalous body with high susceptibility in the northern hemisphere would produce not a simple positive anomaly centered on its vertical, but a pair of anomalies (a dipole), positive and negative, being the positive one more pronounced and located south of the body. The reduction to the pole eliminates this effect by simulating vertical flow lines of the geomagnetic field and restoring the shape of the anomaly to one single maximum.
- Also optionally, the regional variations can be eliminated in a similar way as in gravimetry in order to obtain the anomalies caused by anomalous bodies located in the zone of interest.

Magnetic survey results are displayed as a set of profiles or a magnetic contour map. Because of the erratic and complex character of magnetic maps, the interpretation is often only qualitative, as in the case of the present work.

3.3. Structural inventory of pluton-host rock systems

The ascent and emplacement mechanisms that operated during magma migration, together with the subsolidus evolution of granitoids, may leave their imprint in the shape and structure of plutons, as well as in their relationships with the deformation and metamorphism of the contact aureole. Thus, for the reconstruction of the geological history of plutons it is important to constrain their shape and structure, apart from other petrological, geochemical and structural aspects, such as their absolute age or their relative timing in relation to the observed deformation phases.

The first approximation to a pluton-host rock system is the determination of the cartographic form of the pluton and the characteristics of its contacts. The position and dip of the contact surface places important constraints on the gravimetric models and gives some information about the possible shape of the plutonic body on its uppermost part. Discordant contacts have been usually interpreted as diagnostic for a passive emplacement mode. On the other hand, concordant contacts are supposed to reflect the forceful emplacement of the pluton and the accommodation of the country rocks accompanying the uprise and arrival of the magma. Regarding the thermal effects of the magma, the mineral associations developed next to the contacts provide information about the P-T-conditions governing the intrusion.

The shape of granitic plutons can be only partly constrained using the conventional field techniques, since field observations are limited to their uppermost part or, sometimes, if some crustal tilting occurred, to a limited section of them. Constraining the shape of granitic bodies in depth is only possible by means of geophysical techniques, amongst which gravimetry is the most useful one (Vigneresse, 1990).

The internal structure of a pluton is principally characterized by the shape preferred orientation of planar and elongated crystals, which define foliations and lineations. These can provide information about the dynamics of the magma chamber at the late stages of emplacement and about the subsolidus evolution of the pluton-host rock system. They are sometimes observable and measurable with the aid of a compass, provided that the grains are large enough and the degree of their shape preferred orientation is sufficiently pronounced. In fine grained rocks or in the case of poorly-developed fabrics, they can be studied by means of anisotropy of magnetic susceptibility (AMS). This method has been proved to constitute a useful tool to characterize the fabrics of granitoid bodies (Borradaile, 1988; Bouchez, 1997). Other structural elements to be studied and documented are xenoliths, microgranitic enclaves, dykes, veins, and schlieren.

A key issue is the differentiation of sub- and hypersolidus structures of plutons, as well as their relationship with the structure and metamorphism of the contact aureole. Paterson et al. (1989) proposed a series of criteria to distinguish between magmatic,

sub-magmatic, high-temperature solid-state and medium- to low-temperature solid-state fabrics, which develop during or after the ascent and emplacement. The principal criterion for magmatic flow is the shape preferred orientation of magmatic minerals without any evidence for crystal-plastic deformation or recrystallization. Evidence for solid-state deformation can be easily found under the microscope in form of recrystallized quartz aggregates, fractured feldspars, or *S–C* fabrics, amongst other microstructures.

Finally, the structure of the host rock, especially in thermal and strain aureoles, must be documented in order to develop an emplacement model. It is important to distinguish between pre-, syn-, and post-emplacement cleavages (Fig. 3.3-1) and to establish their relationships with the mineral associations formed during the contact metamorphism.

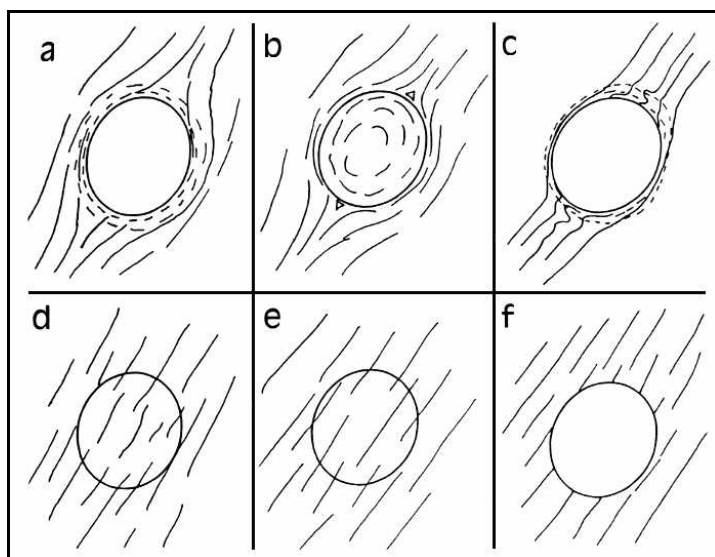


Figure 3.3-1. Hypothetical end-member foliation patterns produced around pre-tectonic (a,d), syn-tectonic (b, e) and post-tectonic (c, f) plutons, after Paterson et al. (1991).

Plutons may intrude prior, during or after the regional deformations and they are commonly used to constrain the age of deformation and metamorphism in mountain belts. Their structure and the one of their contact aureole depend partly on the relative timing of their intrusion. A useful way of viewing contact aureoles is as gradients (of temperature, strain, viscosity, etc.) between a pluton and their wall rocks (Paterson et al., 1991). Foliation patterns in contact aureoles noted as being typical of pre-, syn- and post-tectonic are the following (Paterson et al., 1991; see also Paterson et al., 1998; Fig. 3.3-1). For post-tectonic plutons, the foliations in the host rock are sharply truncated by the pluton or curve into parallelism with the pluton margin, depending on whether the emplacement is passive or forceful, respectively. For syn-tectonic plutons, a regionally developed foliation is continuous with any emplacement-related foliation in the pluton or deflects across the contact because the pluton does not record the same strain as the country rock. For pre-tectonic plutons, a regionally developed foliation either cuts through the granitoid, maintaining its regional strike, or curves around a

non-foliated pluton because of viscosity contrasts, and in both cases postdates all emplacement-related structures.

3.4. Geological mapping

The detailed geology of the Bavarian Forest remained up to now poorly known in some areas. Thank to an EU-project of the Bavarian Environment Agency called "*Schaffung geologischer und hydrogeologischer Informationsgrundlagen*" (generation of geological and hydrogeological basis information), the financial support was provided to perform detailed geological maps at scale 1:25000. The authoress carried out the geological mapping of the topographic sheet number 7246 Tittling (Fig. 3.4-1).

The field work related to this project brought a big amount of information about up to now unknown sheared dykes and stocks, which are the central object of this thesis on its Bohemian Massif section, but also about their country rocks and the structural elements present in the region.

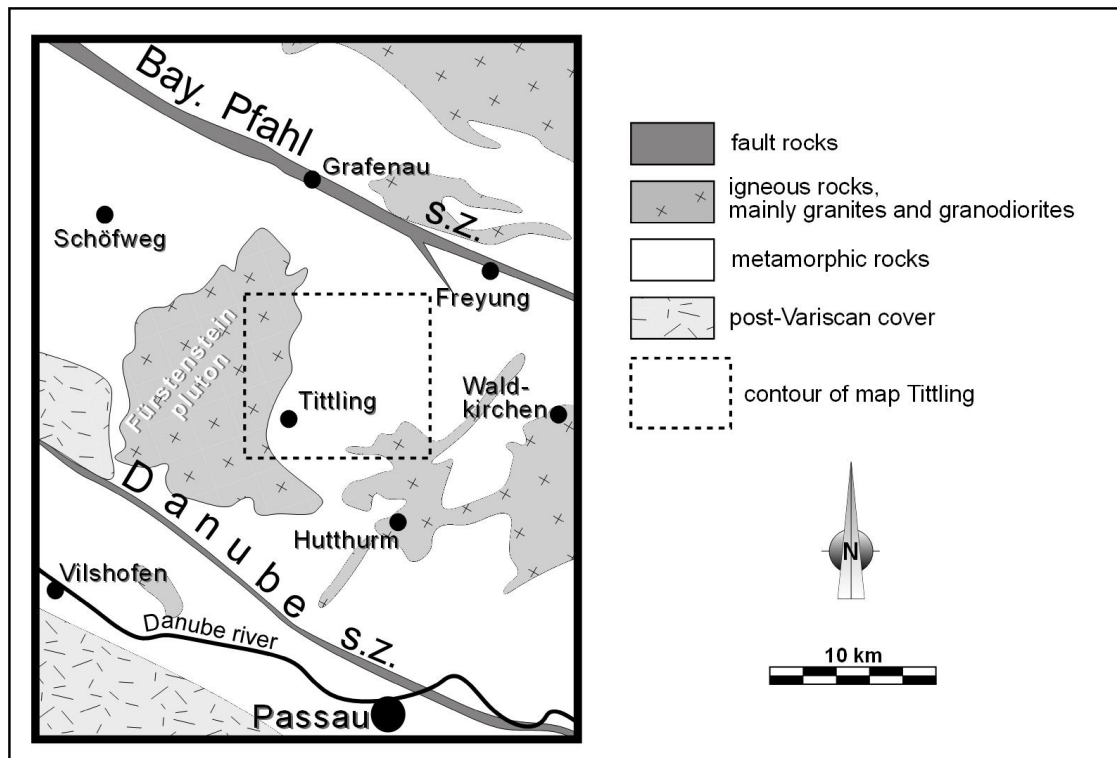


Figure 3.4-1. Location of the topographic sheet 1:25000 number 7246 Tittling.

3.5. Microfabrics and optical microscopy

Several thin sections were studied, some of which were used for the petrographical characterization of the different rock types cropping out in the study area. Some others were prepared for their structural analysis: they were cut parallel to the XZ and YZ -planes of the finite strain ellipsoid in order to (i) describe the microstructural features characterizing each deformation phase that affected the sheared granites and its host rock, (ii) estimate the temperature conditions and the deformation mechanisms governing each phase and (iii) study the changes in intensity and style of deformation inside the sheared granites.

The spatial and geometrical configuration of all those components that make up a rock is referred to as fabric. The fabric of a rock, especially the microfabric, provides information about the deformation mechanisms that operated during its geological history, because each deformation mechanism gives rise to some associated fabric features. For the purpose of the present work the fabrics of quartz and feldspar are especially relevant, most of all those formed under ductile conditions.

The dynamic recrystallization of a rock or mineral aggregate can occur by local migration of grain boundaries and growth of the less deformed crystals or by adding dislocations to subgrain boundaries causing a progressive misorientation of subgrains (Passchier and Trouw, 1996 and references therein; Stipp et al., 2002 and references therein). These recrystallization mechanisms are called grain boundary migration (GBM) and subgrain rotation (SGR), respectively. At natural strain rates and low temperature (lower greenschist facies), quartz recrystallizes by a particular type of grain boundary migration which occurs in a localized fashion at the borders of porphyroclasts. This mechanism is called bulging recrystallization (BLG). At higher temperatures SGR becomes dominant, followed by GBM. The temperature ranges in which each recrystallization mechanism takes place proposed by Stipp et al. (2002) at 2.5 to 3 kbar are: 260-420°C BLG, 380-530°C SGR, 480°C and above GBM. Feldspars typically start to recrystallize at higher temperatures than quartz (Tullis, 1983), at around 450°C.

At high or very high temperatures solid-state diffusion creep may operate. In quartz-feldspar aggregates this deformation mechanism leads to the formation of strongly lobate grain boundaries between both minerals (Gower and Simpson, 1992).

Grain boundary sliding, in combination or not with diffusion creep (superplasticity), typically takes place in fine-grained, equigranular aggregates. This deformation mechanism usually destroys a pre-existing lattice-preferred orientation or prevents the formation of a new one.

3.6. Quartz textures by means of electron backscatter diffraction

Quartz textures

In this work the term "texture" will be used to refer to the geometrical arrangement of the crystallographic directions of the grains in a rock. In deformed rocks, the orientation of the crystallographic axes of the grains is not randomly distributed, but tends to cluster at concrete directions, giving rise to the so-called lattice-preferred orientation (LPO) patterns. In the case of tabular or prismatic grains, such as amphiboles or micas, the LPO is linked to a shape preferred orientation (SPO), which is as easy to identify as a foliation or lineation. In equant grains, such as quartz, the LPO occurs as a result of recrystallization by dislocation creep. Therefore, the configuration of the LPO patterns depends on the slip systems (i.e. crystallographic slip planes and slip directions) that are active during the deformation (Fig. 3.6-1).

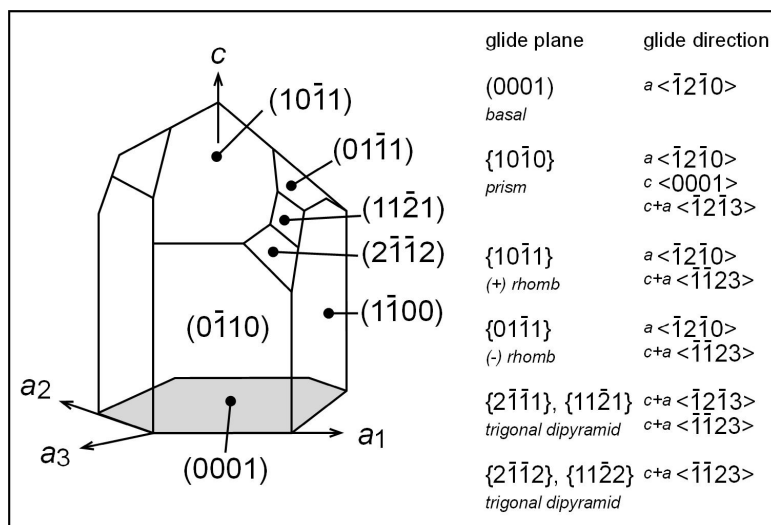


Figure 3.6-1. Quartz crystal showing main crystal faces and principal crystallographic axes. Some of the main slip systems in quartz are listed.

Each slip system has a critical resolved shear stress that changes with temperature and chemical activity of certain components. Thus, the study of the quartz LPO patterns constitutes a good way to estimate the temperature governing the deformation. The quartz textures have been profusely studied, maybe due to the fact that quartz is a mineral present in most of the rocks of the crust and is stable under a wide range of metamorphic conditions.

Fig. 3.6-2 shows the typical LPO patterns formed by coaxial progressive deformation under low to intermediate temperatures in quartz. Small circle girdles are most common, but in plane strain they are connected giving rise to Type I crossed girdles.

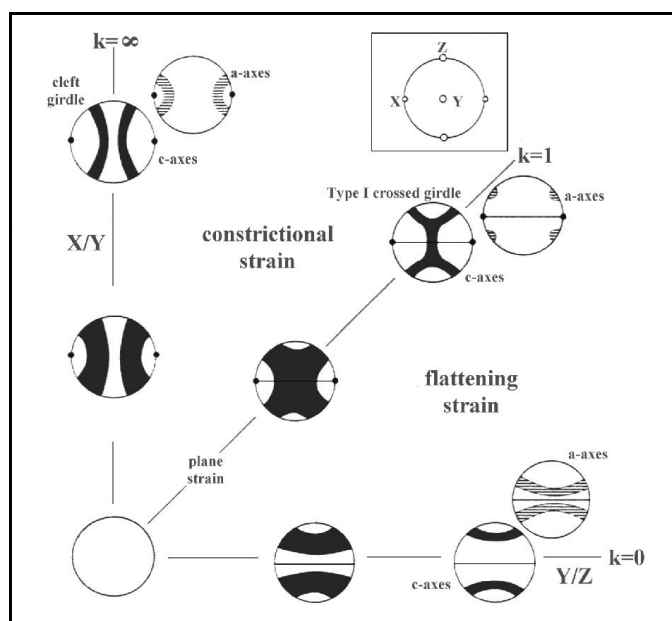


Figure 3.6-2. Flinn diagram showing the relation of geometry of LPO patterns of quartz c -axes (black contours) and a -axes (striped) with strain in the case of coaxial progressive deformation. The inset at the top shows the orientation of the principal strain axes in the pole diagrams. Horizontal lines in pole diagrams indicate reference foliation. Dots indicate reference lineation. Taken from Passchier and Trouw (1996).

Other c -axis LPO patterns that develop in coaxial progressive deformation are Type II crossed girdles, which form under constriction, and point maxima around the Y -axis of the finite strain ellipsoid. Both patterns seem to form at higher temperature than the patterns of Fig. 3.6-2 (Schmid and Casey, 1986).

Under non-coaxial deformation (Fig. 3.6-3) cross girdles become slightly asymmetric (or monoclinic symmetric). Increasing temperature, the following patterns develop progressively: single girdles inclined towards the foliation plane, single maxima around the Y -axis of the finite strain ellipsoid and point maxima close to the direction of the stretching lineation. As for a -axes, they display two maxima parallel and perpendicular to the movement direction on the XZ -plane of strain under low temperatures. Increasing temperature, they cluster first parallel to the movement direction, begin later to scatter on the XZ -plane of strain and become at the end perpendicular to the movement direction.

As mentioned above, the development of the different LPO patterns is due to the activation of given slip systems. Fig. 3.6-4 represents the areas of the stereographic plot in which c -axes concentrate when a given slip system is active: Prism $\langle a \rangle$ slip is active under a wide range of temperatures, whereas basal $\langle a \rangle$ slip is active rather at low-grade conditions and prism $\langle c \rangle$ slip under high temperatures (Mainprice et al., 1986; Masberg et al., 1992; Kruhl, 1996).

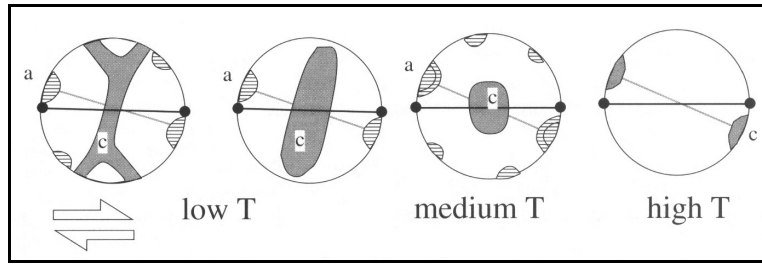


Figure 3.6-3. Pole diagrams showing four types of contoured LPO patterns of quartz *c*-axes (grey) and *a*-axes (striped) such as develop with increasing metamorphic grade in non-coaxial progressive deformation. The variation is due to a change in the dominant slip systems.

Taken from Passchier and Trouw (1996).

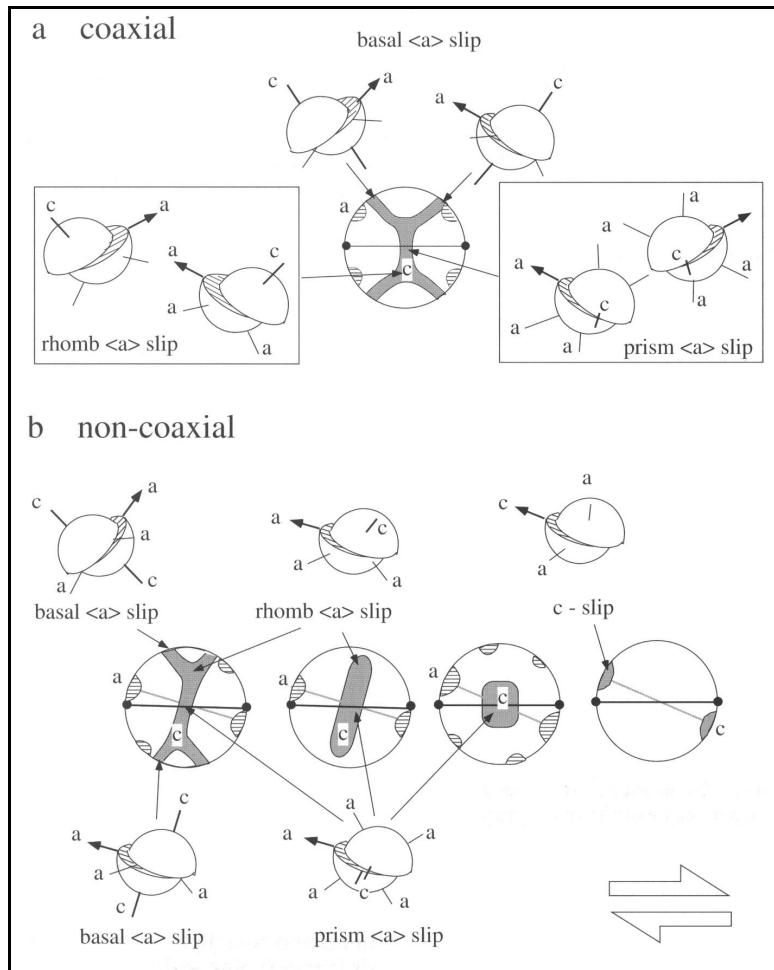


Figure 3.6-4. a) Illustration of the contribution of equidimensional quartz crystals with aligned *a*-axes and basal, rhomb or prism slip planes to a Type I crossed girdle pattern formed in coaxial progressive deformation. *c*-axes in grey, *a*-axes striped. b) The same for several patterns that develop in non-coaxial progressive deformation. Taken from Passchier and Trouw (1996).

Electron backscatter diffraction

Using a U-stage, the measurement of the orientation of *c*-axes is, although time consuming, easily carried out. The application of electron backscatter diffraction (EBSD, e.g. Prior et al., 1999) to the study of quartz microfabrics provides information about the existence of a lattice preferred orientation not only concerning *c*-axes, but also other crystallographic directions which are not easily measured on a U-stage and provide also valuable information, for example *a*-axes.

This technique was applied using a SEM Leo 1530 at the Bayerisches Geoinstitut of the University of Bayreuth (Germany). From different samples of mylonite, deformed granite and diatexite, slabs parallel to the XZ -section of the finite strain ellipsoid were cut and polished in a first step up to a particle size of the medium of 1 μm and finally with a high pH silica solution (SYTON). The samples were coated with carbon up to a thickness of about 4 nm to reduce charging effects and scanned under an accelerating voltage of 30 ke. The beam current was about 4 nA. Rectangular areas of the samples were delimited and scanned with a step width between 170 and 10 μm , depending on the grain size in every case.

3.7. Strain analysis

The strain in the studied sheared granites is typically inhomogeneous. In order to study the geometry of strain and its variations, a strain analysis was performed at different locations of an especially well exposed dyke: the Saunstein granite dyke (chapter 5.3.3.2).

Four samples were selected for the application of the R_f/Φ' method (Peach and Lisle, 1979; Ramsay and Huber, 1983), which allows the calculation of the aspect ratio of the finite strain ellipse (R_s) from initially elliptical markers. As marker we used feldspar mantled porphyroclasts, whose initial form after crystallisation from melt is comparable to an ellipse. Hand specimens were cut parallel to the XZ and YZ principal planes of the finite strain ellipsoid and scanned. For an average of 73 particles per section the elliptical shape of porphyroclasts (R_f) and the orientation of their major axis (Φ') were measured. Making use of the program "STRAIN" (Unzog, 1990), the strain ratios on the above mentioned principal planes ($R_{s,xz}$ and $R_{s,yz}$) were calculated. $R_{s,xy}$ was obtained from $R_{s,xz}/R_{s,yz}$.

The angle between S and C planes was used to estimate the strain in three of the former samples using the formula:

$$\gamma = \frac{2}{\tan 2\theta'}$$

where γ is the shear strain and θ' the angle between S and C (Ramsay and Graham, 1970).

3.8. X-ray fluorescence analysis

Six samples distributed throughout the Saunstein dyke (chapter 5.3.3.2) were selected to be analyzed by means of X-ray fluorescence (XRF) at the Bavarian Environment

Agency (Marktredwitz, Germany). The results were used in the application of the isocon-diagram method and the Zr-thermometry.

3.8.1. Isocon diagram

In order to check a possible mass transfer and volume change during deformation the isocon-diagram method (Grant, 1986) was applied. This method consists in plotting the concentration of components in an unaltered rock (undeformed in our case) against the concentration in an altered (deformed) equivalent. The equation linking the concentration of a component relative to its concentration prior to deformation is:

$$\frac{\Delta C_i}{C_i^O} = \frac{M^A}{M^O} \cdot \frac{C_i^A}{C_i^O} - 1,$$

where C is the concentration and M is the mass of the sample. i , O and A represent a given component, the undeformed state and the deformed state respectively. If deformation carries no change in volume, both mobile and immobile components will plot on a line of slope = 1. If deformation was accompanied by mass loss, which normally takes place by removing the mobile components, then the immobile components would become more concentrated and tend to plot on a line of slope > 1.

3.8.2. Zr-thermometry

From the zirconium content of the samples, the temperature of the granitic melt can be calculated after Watson and Harrison's (1983) zircon solubility model making use of the equation:

$$D = \frac{-3.80 - 0.85 \cdot (M - 1) + 12900}{T},$$

where D represents the solubility of zircon in the melt, T the temperature and M the cation ratio

$$M = \frac{Na + K + 2Ca}{Al \cdot Si}.$$

3.9. Electron microprobe analysis

3.9.1. Phengite barometry

The phengite geobarometer (Massonne and Schreyer, 1987; Massonne and Szpurka, 1997) correlates the number of Si atoms per formula unit (p.f.u.) in white mica with pressure and temperature. The minerals biotite/phlogopite, quartz, K-feldspar and white mica constitute the limiting assemblage for the use of this barometer and are present in most of the studied sinistrally sheared dykes and stocks. The phengite geobarometer can provide information about the emplacement depth and the pressure governing the deformation. White micas found in mylonites and deformed granites were analysed at the Institut fuer Geowissenschaften, Frankfurt am Main University (Germany), using a JEOL JXA-8900RL electron probe microanalyzer with five wavelength-dispersive spectrometers. The operating conditions were 15 kV accelerating voltage, 13 nA specimen current and 5 μm spot size. The results are listed in Appendix 3.

3.9.2. Feldspar composition

Electron microprobe analyses of feldspars were performed with the aim of studying variations in chemical composition between old and dynamically recrystallized feldspar grains. The analyses were performed at the Institut fuer Geologie und Mineralogie, Erlangen-Nuernberg University (Germany), using a JEOL Superprobe JXA-8200 with four wavelength-dispersive spectrometers. Operating conditions were 15 kV accelerating voltage, 15 nA specimen current and 5 μm beam size. The results are listed in Appendix 4.

3.10. Piezometry

Several empirical (Mercier et al., 1977; White, 1979; Christie et al., 1980; Etheridge and Wilkie, 1981; Koch, 1983; Stipp and Tullis, 2003) and theoretical piezometers (Twiss, 1977; Twiss, 1980) have been calibrated, which relate differential stress and the size of dynamically recrystallized quartz grains formed during steady-state dislocation creep. The difference between the piezometers lies in the value of the parameters b and r in an equation of the form:

$$\sigma = \left(\frac{D}{b}\right)^{\frac{1}{r}},$$

where σ is the differential stress, D the diameter of quartz grains and b and r experimentally determined constants (Table 3.10-1).

	b	r
Twiss (1977, 1980) ^a	14500	-1.47
Mercier et al. (1977) ^a	4070	-1.4
White (1979) ^a	12900	-1.43
Etheridge and Wilkie (1981) ^a	14200	-1.47
Koch (1983) ^a	490	-0.59
Christie et al. (1980), wet ^b	1780	-0.9
Stipp and Tullis (2003)	3631	-1.26

Table 3.10-1. Basic parameters for piezometers. ^a taken from Abalos et al. (1996), ^b taken from Ord and Christie (1984).

In order to apply them to the deformation in the Saunstein dyke (chapter 5.3.3.2), quartz grains were traced on photomicrographs. Their area was measured using the image analysis software DIAna. The grain diameter is then calculated as the diameter of a circular particle of equal area.

4. Investigations on granitoids of the Ossa-Morena and Central Iberian Zones, Iberian Massif

4.1. Geographic overview

In the Iberian Massif two areas were studied. The La Bazana Pluton is located in southwestern Spain in the administrative district of Extremadura, at about $38^{\circ}18'N$ $6^{\circ}46'W$. The Nisa-Alburquerque batholith lies between $39^{\circ}13'N$ and $39^{\circ}31'N$ and $6^{\circ}49'W$ and $7^{\circ}49'W$, half of it is found in the same Spanish district, the other half in Portuguese territory. In this area the climate is continentalized Mediterranean, with precipitations from 400 to 600 mm/yr. The landscape is dominated by the western ends of the mountain ranges called Montes de Toledo and Sierra Morena, and also by the valleys of the rivers Guadiana and Tajo (Fig. 4.1-1). Most of the surface of Extremadura is occupied by a vast plain with an average altitude of 350 m AMSL, in which pasture grounds are a very typical way of land use. The lack of a dense vegetal cover eases the geological observation. In some areas, the road coverage is insufficient, so that a part of the geological work must be done on foot.

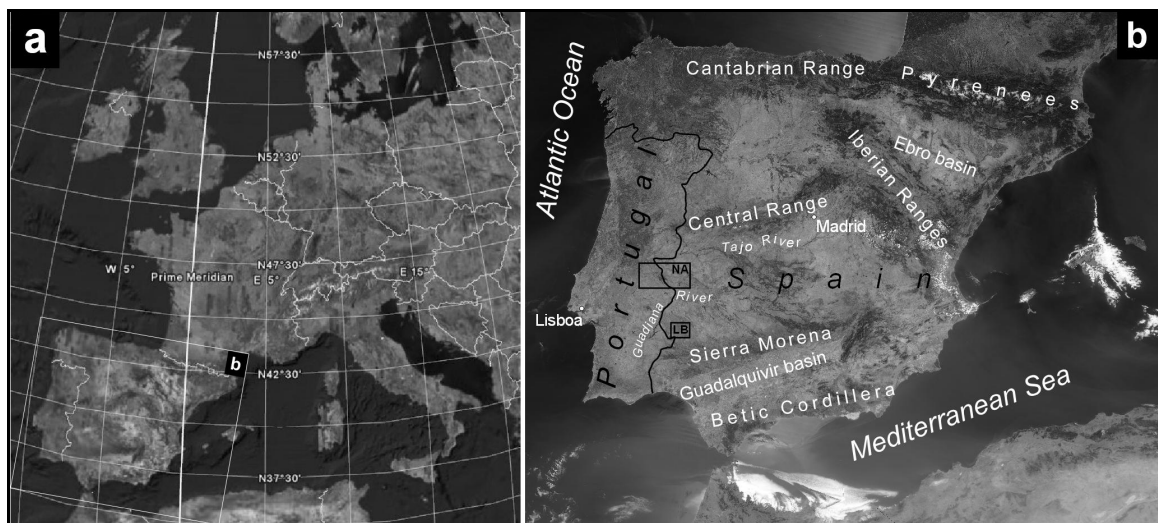


Figure 4.1-1. a) General map of Europe. Source: Google Earth. b) Enlargement of the Iberian Peninsula showing the main geographic features and the location of the Nisa-Alburquerque (NA) and La Bazana (LB) study areas.

4.2. The La Bazana pluton

4.2.1. Introduction

The La Bazana pluton is a late-Variscan pluton intruding Cambrian rocks of the Ossa-Morena Zone, in the south-western part of the Iberian Massif (Fernández-Carrasco et al., 1981; Fig. 4.2.1-1). Magmatism in the Ossa-Morena Zone was abundant, and apart from Late Proterozoic (Cadomian) and Early Palaeozoic (rifting-related) plutonism and volcanism (Sánchez Carretero et al., 1990; Pérez-Estaún and Bea, 2004), there are plutonic and volcanic rocks emplaced at different times during the Variscan Orogeny.

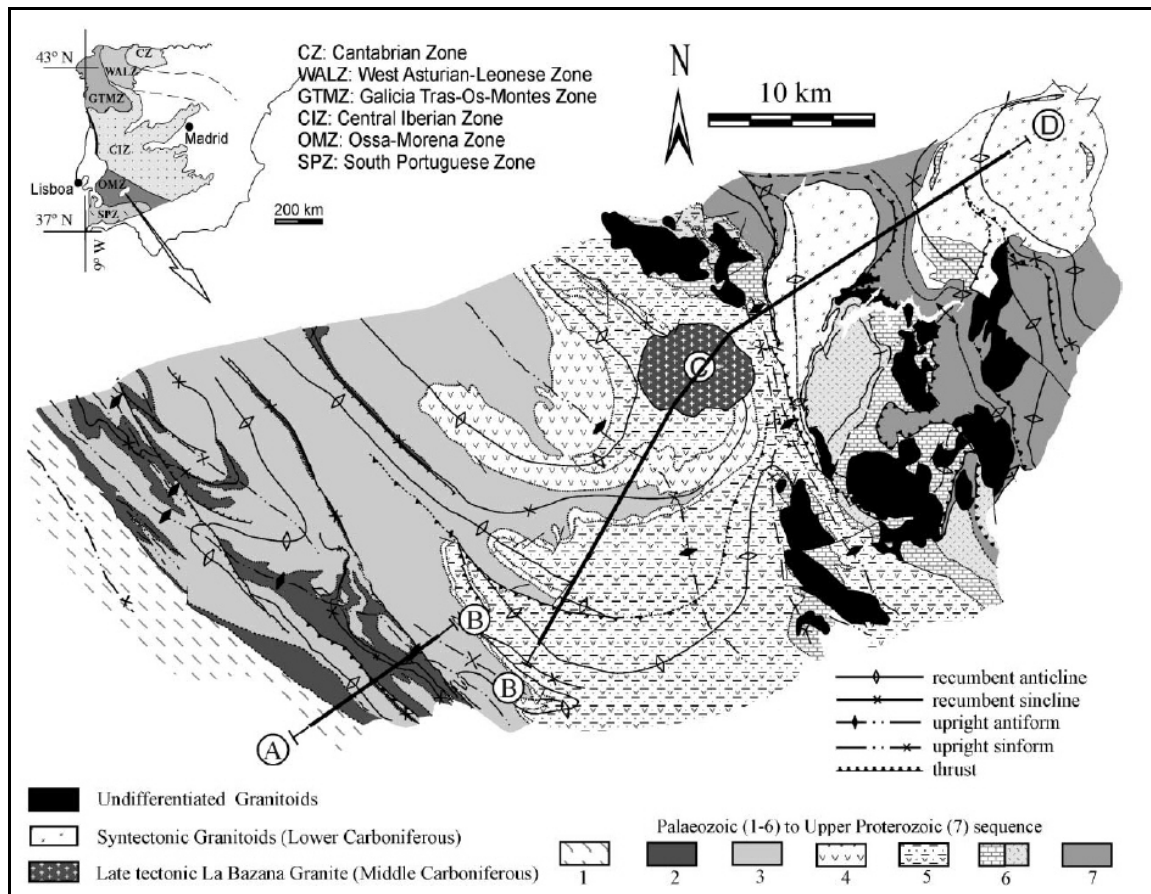


Figure 4.2.1-1. Geological map of the study area, modified after Expósito (2000). A-D indicate the position of the composite cross-section in Fig. 4.2.3-5. (1) Syn-orogenic sediments (Devonian – Lower Carboniferous); (2) siliceous slates and chert (Silurian – Lower Devonian); (3) metasandstones and slates (Cambro-Ordovician); (4) basalts and slates (Middle Cambrian); (5) slates, metagreywackes and volcanics (Lower Cambrian); (6) carbonates, metagreywackes and volcanics (Lower Cambrian); (7) slates, metagreywackes and black quartzites (Upper Proterozoic).

The La Bazana pluton is a late manifestation of the Variscan collisional magmatism (Expósito, 2000). In the area around this pluton, the stratigraphic sequence consists of a pre-orogenic succession ranging from Late Proterozoic to Early Devonian rocks, unconformably covered by syn-orogenic Devonian-Carboniferous sedimentary rocks (Fig. 4.2.1-1). The pre-orogenic rocks are affected, successively, by (Expósito, 2000): (1) Devonian recumbent folding verging to the SW and having developed regional axial plane cleavage, (2) thrusting with top-to-the-south sense of movement, (3) Early Carboniferous normal faulting, and (4) Middle Carboniferous upright folding with irregular development of crenulation cleavage. The La Bazana pluton is located in the core of one of these large late upright antiforms (Fig. 4.2.1-1). As the granite is sub-circular in outcrop and does not seem to record any of the aforementioned regional deformations, its emplacement is likely to have occurred during or shortly after the development of the upright Middle Carboniferous folds. No geochronological data are available for this granite.

4.2.2. Petrography and structure of the La Bazana pluton and its country rocks

The cartographic shape of the La Bazana pluton is approximately circular, 6 km in diameter (Fig. 4.2.1-1). Petrographically, it is remarkably homogeneous, medium-grained and with a monzogranitic peraluminous composition (Fernández-Carrasco et al., 1981). The main primary constituents are quartz (30%), K-feldspar (25–30%), plagioclase (25–30%), biotite (10%) and muscovite (5%). Muscovite has the microstructural appearance of igneous crystallisation: crystals are clean, subidiomorphic and frequently intergrown with biotite, and they impose their own shape to the adjacent quartz (Fig. 4.2.2-1a). Plagioclase is also usually subidiomorphic and shows zoning ranging from oscillatory oligoclase compositions in the core to albite at the rim. Quartz grains are moulded to the shapes of plagioclase and micas, but in contact with (or as inclusions in) K-feldspar, they preserve crystal faces. K-feldspar always has an interstitial appearance and myrmekite is locally developed at the grain margins. From these microstructural relationships, the following order of crystallisation is inferred: (1) plagioclase (though the most external albitic rim is somewhat late), (2) biotite and muscovite, (3) quartz, and (4) K-feldspar. In most samples, the mineral grains do not show any signs of significant strain, although quartz sometimes displays undulatory extinction (Fig. 4.2.2-1a).

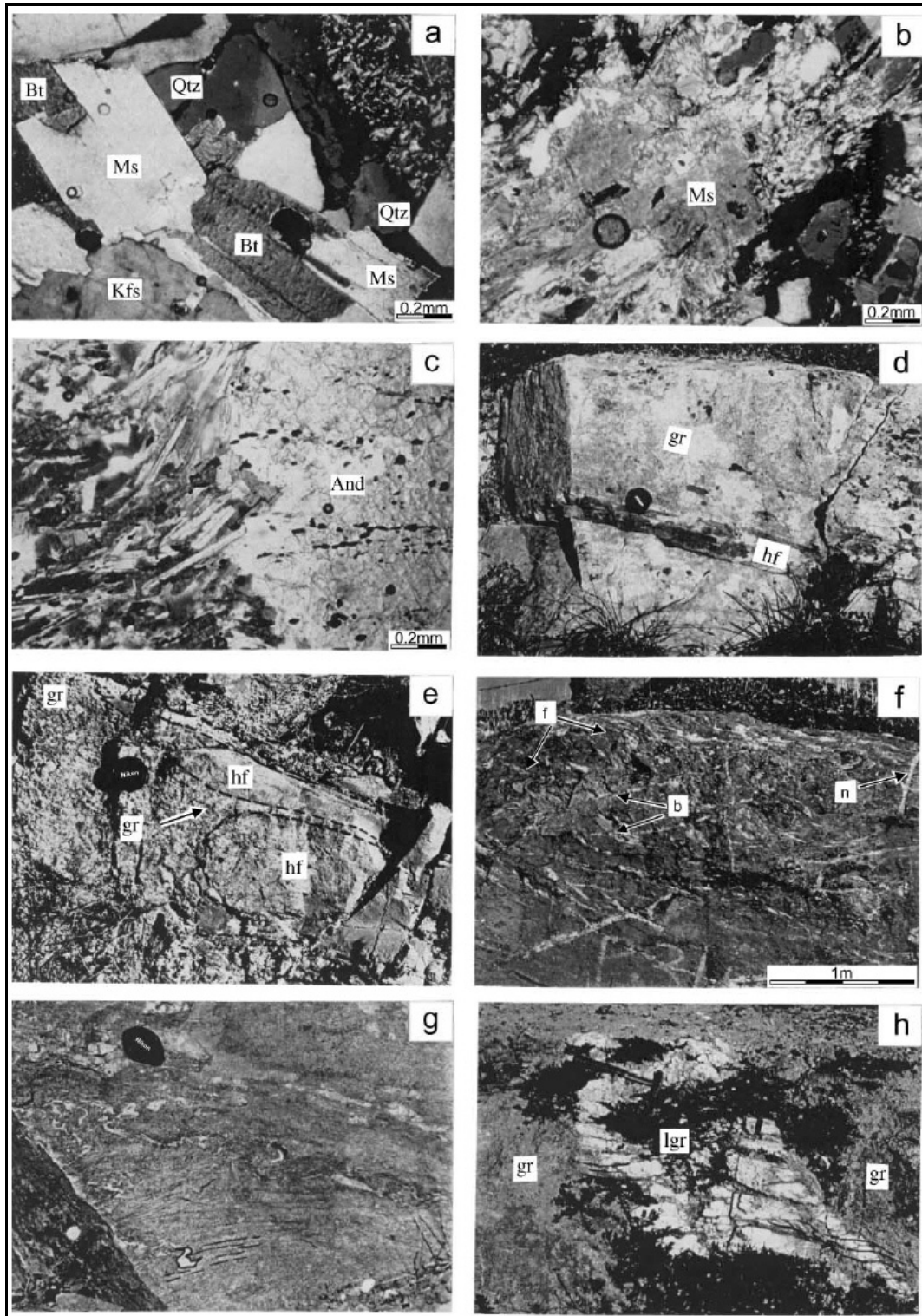
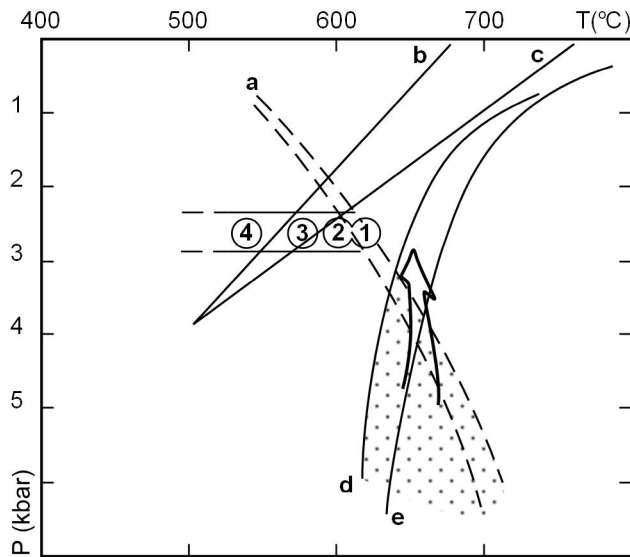


Figure 4.2.2-1. Microscopic and field aspects of the La Bazana granite and its country rocks. a) The La Bazana granite muscovite (Ms) and biotite (Bt), frequently intergrown, impose their crystallographic shape to quartz (Qtz) and K-feldspar (Kfs), which supports the igneous crystallisation of muscovite. b) Ragged appearance of muscovite (Ms) in the innermost zone of the thermal aureole, suggesting that it is out of equilibrium. c) Andalusite porphyroblast including the main regional foliation, which is deflected around the porphyroblast due to a late flattening (see also f, g, h). Continues on next page →

→**Figure 4.2.2-1 (continued). d) Layers of hornfels (hf) can be seen sometimes in the proximity of the top of the granite; they are parallel to the contact with the country rock. e) Outcrop scale view of a lateral contact between the granite (gr) and the hornfelsic country rock (hf), showing small fingers of granite. f) Country rock just on top of the granite, with folded (f), boudinaged (b) or non-deformed veins (n). g) A sub-horizontal spaced foliation in the country rock on top of the granite as a consequence of the subvertical flattening illustrated in the previous photograph. h) Dyke of leucocratic granite (lgr) flattened and foliated, its foliation being continuous with the one in the granite (gr); this constitutes further evidence for flattening undergone by the granite and the country rock on top.**

A distinctive thermal aureole 1–200 m wide developed around the granite (Fernández-Carrasco et al., 1981). Within the first few meters away from the granite contact, the rocks are hornfelses having the following mineral associations (in order of proximity to the granite): (1) Qtz, Bt, Sil, Ms, Crd?; (2) Qtz, Bt, And, Sil, Ms, Crd?; (3) Qtz, Bt, And, Ms, Crd?. In the first association, muscovite has a ragged appearance (Fig. 4.2.2-1b), suggesting that it is not stable in the innermost part of the aureole, where the reaction $Ms + Qtz = Sil + Kfs$ may have just begun to develop. Cordierite is very scarce (a few grains of unclear identification), perhaps because chlorite was depleted in the first reactions and afterwards andalusite is formed consuming cordierite (Yardley, 1989). The andalusite appears as prismatic porphyroblasts with inclusions of opaque grains and sericitic rims. Trails of opaque minerals inside the andalusite prisms demonstrate that the regional foliation associated with recumbent folding existed prior to the growth of andalusite. However, the same foliation is also moulded around the andalusite porphyroblasts (Fig. 4.2.2-1c), constituting the microstructural expression of fabric formation synchronous with blastesis that is also clearly expressed at the outcrop scale (see below). The crystallisation of sillimanite in the innermost part of the thermal aureole starts in the stability field of muscovite, but within a short distance the muscovite seems to be in disequilibrium by microstructural evidence. This observation allows pressure during thermal metamorphism to be estimated at 2–3 kbar (Fig. 4.2.2-2). On the other hand, igneous muscovite in granites seems to imply a minimum of 3 kbar for the pressure of crystallisation, although this matter is still questioned (Zen, 1988). Anyway, bearing in mind that the granite could have ascended somewhat after the muscovite crystallisation, there is no conflict with the metamorphic data, and it is believed that a depth of 7–10 km corresponds to the emplacement of the La Bazana granite (Fig. 4.2.2-2).



4.2.2-2. P-T diagram illustrating the emplacement conditions of the La Bazana granite inferred from mineral assemblages. a) Upper limit for the stability of muscovite in the presence of quartz, after Chatterjee and Johannes (1974) and Chatterjee and Flux (1986). b) and c) Andalusite/sillimanite boundary, after Hemingway et al. (1991) and Holdaway (1971), respectively. d) and e) Water saturated granite solidi, after Wyllie (1977) and Tuttle and Bowen (1958), respectively. Dotted area:

stability field of magmatic muscovite. Arrow: ascent path of the La Bazana granite. Thermal aureole: (4) andalusite, (3) andalusite and sillimanite, (2) sillimanite and muscovite, (1) sillimanite (unstable muscovite).

The axial-plane foliation of Devonian recumbent folds represents a previous marker that helps to determine the deformation produced by the granite intrusion in the host rocks. The dip of the main regional foliation in the nearby country rock defines a gentle dome centred on the granite and imposed over the regional NW—SE strike (Fig. 4.2.2-3). Congruently, the dominant dips of the granite–country rock contact point outward from the granite, as well as do the foliation in the granite (see below). The granite does not show, however, a simple immersion under the country rock: Fingering at different scales has been observed where the granitic magma penetrated along the regional foliation (Fig. 4.2.2-1e and 4.2.2-4). The country rock just on top of the granite is sometimes pervaded by the veins of quartz and feldspar, as a result of hydrothermal fluid flow coming from the granite. These veins (Fig. 4.2.2-1f) show different orientations and strain: Some of them are folded with sub-horizontal axial-plane surfaces, and veins lying sub-horizontally are boudinaged. Locally, a centimetre-spaced sub-horizontal crenulation cleavage is developed (Fig. 4.2.2-1g). Consequently, the country rock on top of the granite has been affected by subvertical shortening and sub-horizontal stretching (see also Fig. 4.2.2-1c), a strain probably related to the granite emplacement. There are also undeformed or less deformed veins whose penetration into the overlying country rock had to be late with respect to the vertical flattening (Fig. 4.2.2-1f).

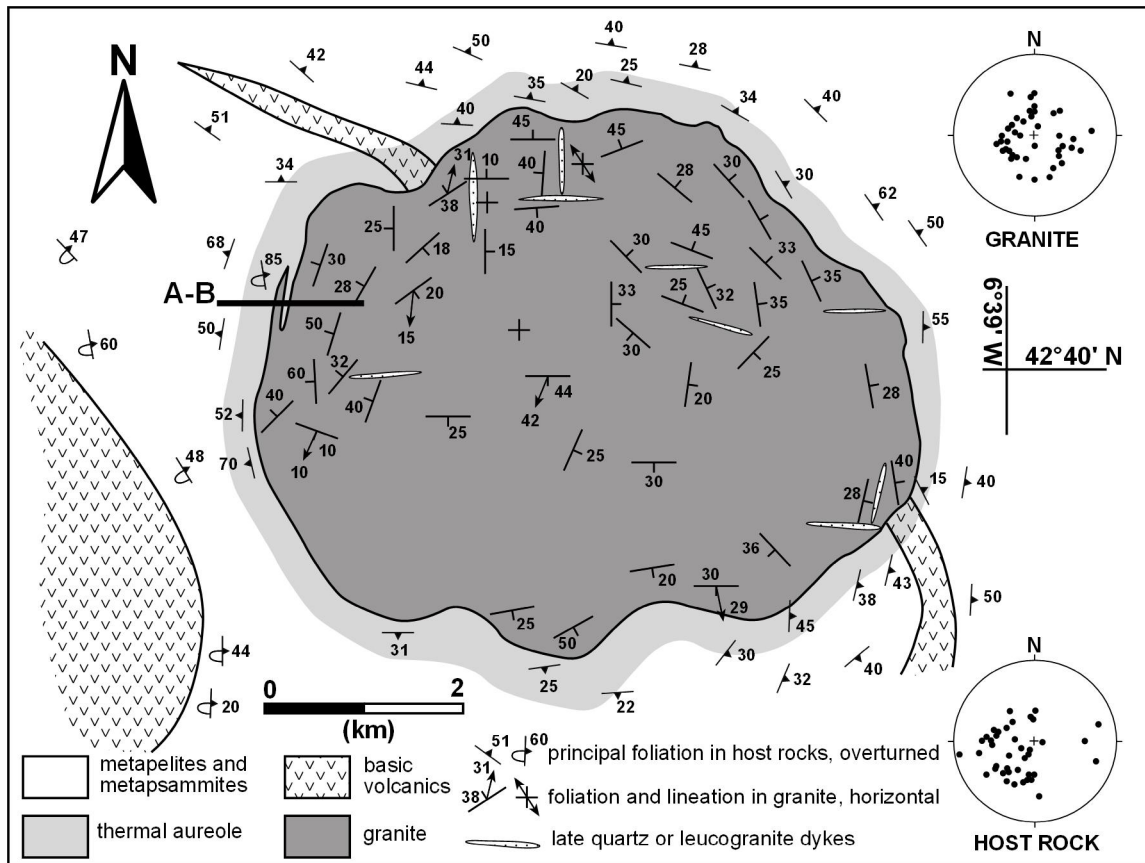


Figure 4.2.2-3. Map of foliations and lineations in the La Bazana pluton and its host rock. Plots of granite and host rock foliation poles (equal area, lower hemisphere projection).

Careful examination of the granite reveals a foliation and, locally, a mineral lineation defined by biotite and feldspar crystals. These are magmatic structures, i.e. they formed while the crystallisation of the magma was not complete, as no tectonic twins or bending in feldspars, no kink folds in micas, and only weakly deformed interstitial quartz is observed. The shape preferred orientation is never strong, so that the foliation and the mineral lineation have a faint appearance. The foliation is distinguishable in most outcrops (not so the lineation); its orientations describe a dome pattern (Fig. 4.2.2-3). In some places, there are N—S and E—W subvertical leucogranitic dykes with a sub-horizontal foliation passing into the foliation of the granite (Figs. 4.2.2-1h and 4.2.2-3), implying that at some point during crystallisation of the granite, tensional sub-horizontal stress-originated fractures immediately replenished with residual magma, after which vertical shortening deformed both the granite and the dykes. This deformation in the granite has an obvious correlation with the flattening observed in the country rock, and with the dome pattern in both the granite and the country rock around it.

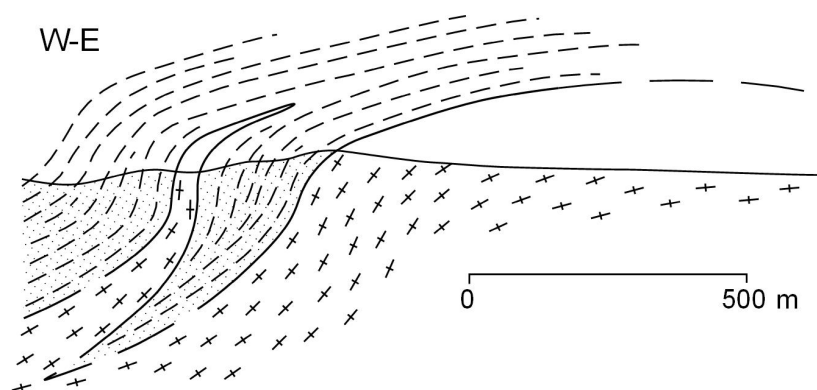


Figure 4.2.2-4. Cross-section through the western border of the La Bazana pluton. Location shown in Fig. 4.2.2-3. Cross pattern: granite. Dashed-dotted pattern: host rocks. Horizontal scale = vertical scale.

4.2.3. Three-dimensional granite geometry

After the field study of the granite and its metamorphic aureole, new gravity data were gathered in order to model the deep geometry of the pluton. Relative gravity measurements were carried out on an irregular grid covering the outcrop and surrounding areas. Relative gravity measurements were calibrated with the absolute gravity value of the base station of the Instituto Geográfico Nacional located in Fuente de Cantos (Badajoz, Spain). The irregular grid of gravity measurements was interpolated using the kriging method in order to draw the Bouguer anomaly map (Fig. 4.2.3-1).

In addition, we had access to an aeromagnetic survey carried out by the Junta de Andalucía and the Instituto Tecnológico Geominero de España in 1997. The recording lines were N—S and spaced 250 m, and the control lines were E—W and spaced 2.5 km. Flight altitude was 80 m above the topography. Magnetic measurements were carried out with a G822 Geometrics magnetometer and positioned by means of differential GPS.

The gravimetric and magnetometric data provided valuable information to constrain the deep shape of the granite. Regional Bouguer anomaly maps (1:1000000 scale, I.G.N., 1976) show the presence of a poorly-defined minimum in the La Bazana granite region, over 20 km in diameter, with anomaly values < 0 mGal, and a regional increase of 0.357 mGal/km towards the SW. The Bouguer anomaly map calculated with the new field data (Fig. 4.2.3-1) offers a more detailed view of the anomaly minimum related to the granite.

The calculated Bouguer anomalies in the study region range from -2 to 17 mGal, compatible with the regional Bouguer anomaly map values (I.G.N., 1976). The gravity minimum is approximately circular in shape, though slightly displaced northeast of the granite outcrop probably as an effect of the basic volcanic rocks located to the south-west. In analysing the main features of the granite shape, two profiles with SW—NE and NW—SE orientations were studied. The granite intrudes into a homogeneous sequence of host rock consisting of metapelites, except at the south-western border where basic

volcanic rocks are also present (Figs. 4.2.1-1 and 4.2.2-3). The regional anomaly was determined taking into account this setting. In the NW—SE oriented B profile, with a most homogeneous host rock near the granite body, the regional anomaly was established mainly by the main asymptotic tendency of the Bouguer anomaly, taking into account that in both extremities of the profile this tendency is well defined (Fig. 4.2.3-2), allowing the calculation of the residual anomaly. However, in the SW—NE oriented A profile, the outcropping host rock is not homogeneous. We have considered for this profile the gradient of the south-westwards regional increase of the Bouguer anomaly obtained from the 1:1000000 scale map (I.G.N., 1976). Both A and B profiles intersect with the same regional anomaly value. The residual anomaly related to the granite body shows values < -8 mGal despite the small size of the granite outcrop.

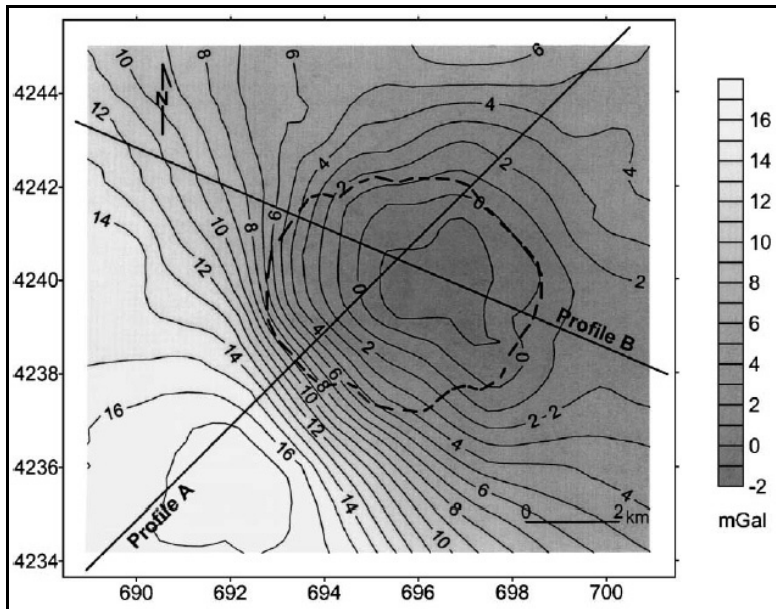


Figure 4.2.3-1. Bouguer anomaly map. The hatched line shows the contour of the outcropping La Bazana granite. UTM coordinates.

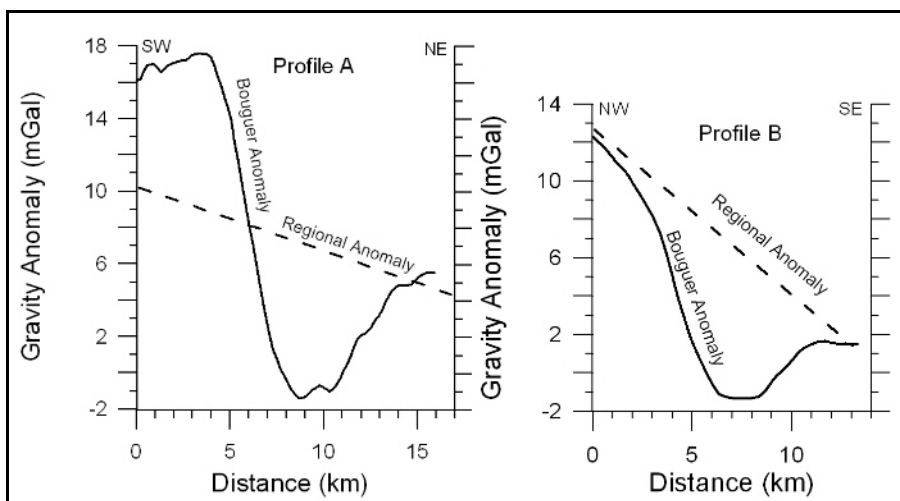


Figure 4.2.3-2. Bouguer and regional anomaly profiles. Location in Fig. 4.2.3-1.

In order to determine the shape of the granite in the subsurface, we constructed gravity models (Fig. 4.2.3-3) of this body along the two profiles A and B located in Fig. 4.2.3-1, also taking into account field data (Figs. 4.2.1-1 and 4.2.2-3) and magnetic data (Fig. 4.2.3-4).

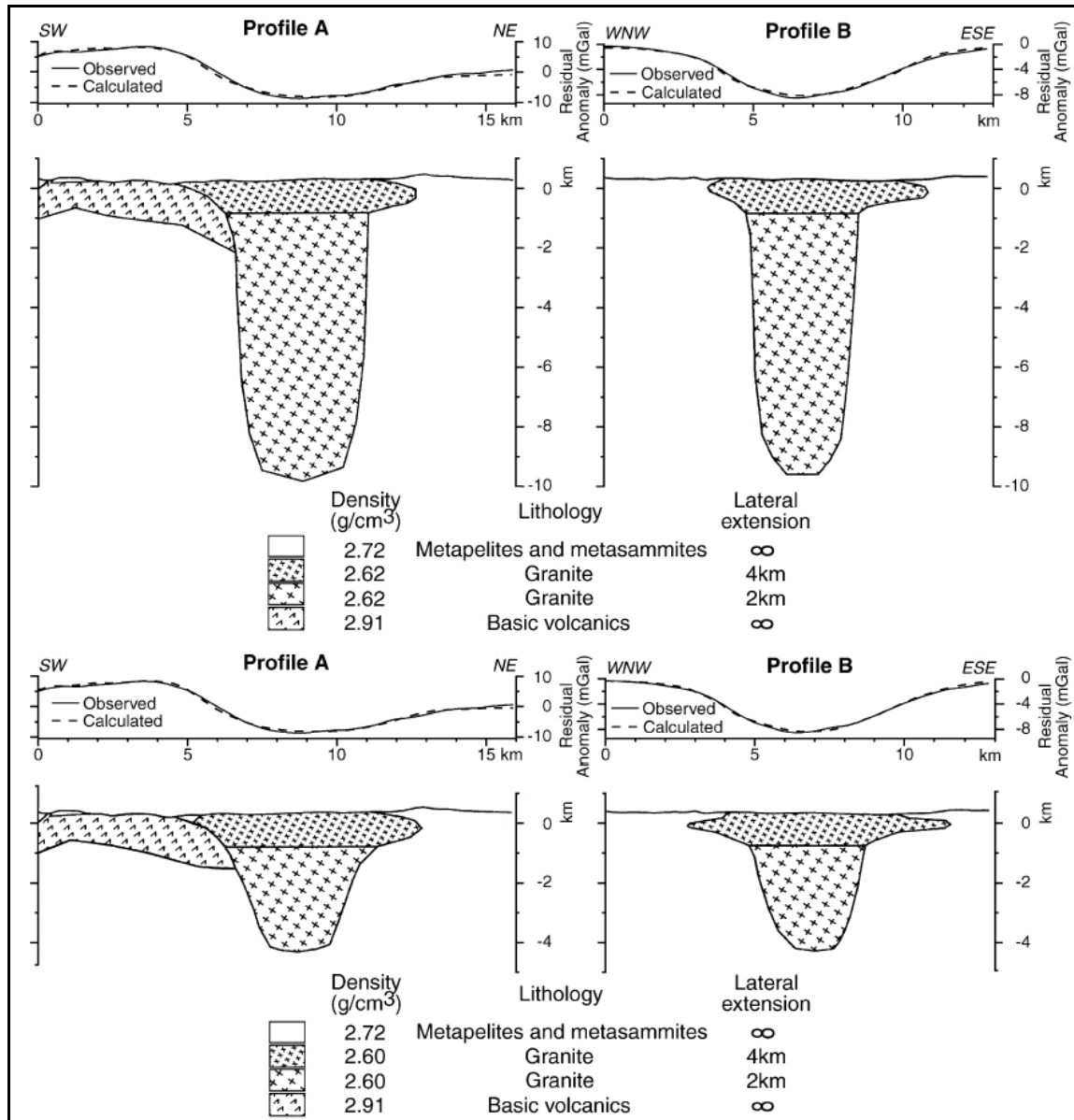


Figure 4.2.3-3. Residual gravity anomaly models. Location in Fig. 4.2.3-1. Two possibilities are presented, considering densities of 2.62 and 2.60 g/cm³ for the granite body. The two patterns in the density represent no different densities, but only different lateral extension in the 2 ½ modelling.

Campos and Plata (1991) determined the mean density of metapelites (2.72 g/cm³) in the region of Albuquerque, similar to those in the host rock of the La Bazana granite. Consequently, we took 2.72 g/cm³ as the value for mean density of the host rock,

except at the south-western border where basic volcanic rocks crop out. The La Bazana granite has a homogeneous composition, as shown by the petrographic observations and its largely constant, low mean magnetic susceptibility values (comprised between 1×10^{-5} and 17×10^{-5} with a mean value of 10×10^{-5} SI) which point to a low density. Specifically, taking into account the modal composition of the granite and the mineral densities (quartz: 30%, 2.65 g/cm³; K-feldspar: 30%, 2.56 g/cm³; oligoclase: 30%, 2.63 g/cm³; mica: 10%, 2.85 g/cm³), it is possible to estimate a mean density of 2.637 g/cm³. However, the true density will be a little lower, as it occurs in other granite bodies (Campos and Plata, 1991) because of weathering and the presence of fractures. Then, we have modelled two possibilities, considering the most probable 2.62 g/cm³ and the extremely low 2.60 g/cm³ densities. In addition, we adopted a 2.91 g/cm³ density for the metabasites located southwest of the granite body, a value well in the range for this lithology (Telford et al., 1990), while justifying the observed anomaly. These basic rocks constitute laterally discontinuous strata of variable thickness (see Figs. 4.2.1-1 and 4.2.3-5). The higher density rocks formed in the aureole have not been considered in our model, since there are no relative positive values of the residual anomaly that we could relate to them. Thus, their thickness must be so small that their influence on the observed gravity values remains unnoticed. Note finally that the strip of basic rocks in the northwest and southeast of the granite (Figs. 4.2.1-1 and 4.2.2-3) just touches the surface and does not penetrate in depth (Fig. 4.2.3-5); its volume is insignificant. Gravity models were built in 2 ½ dimensions (Fig. 4.2.3-3) in order to take into account the limited extent of the bodies orthogonal to the profiles. The shallower part of the granite was considered to have greater lateral extent than the deeper part for the sake of consistency between the two crossing sections.

In the gravity model of profile A (Fig. 4.2.3-3), a positive residual gravity anomaly is observed; it may be related to the basic volcanic rocks, and could produce the north-eastward displacement of the anomaly minimum related to the granite body. The gravity models suggest that the uppermost part of the granite extends laterally below the host rocks, reaching a diameter of up to 8 km at very shallow depths. At deeper levels, however, the granite would have a thinner root. The root depth depends upon the density considered. For a density of 2.62 g/cm³, we obtain a deep root of up to 4 km in diameter and as much as 10 km in depth. However, for a lower density of 2.60 g/cm³, we obtained a shallower root of about 4 km in depth (Fig. 4.2.3-3). Anyway, the granite has a teardrop-pipe geometry, with a larger cap zone. At the south-western border, the lateral spreading of the granite seems to exploit the mechanic anisotropy of the contact between the metapelites and the volcanic rocks (Fig. 4.2.3-5).

Southwest of the granite, there are large aeromagnetic anomalies (Fig. 4.2.3-4) associated with the outcrop of basic volcanic rocks (Fig. 4.2.2-3). The aeromagnetic map shows the dipole centre to be located very near the granite border, suggesting that

the basic volcanic rocks may extend in depth to the SSW of the granite and even below the granite, as it was foreseen from geological studies (Fig. 4.2.3-5; Expósito, 2000).

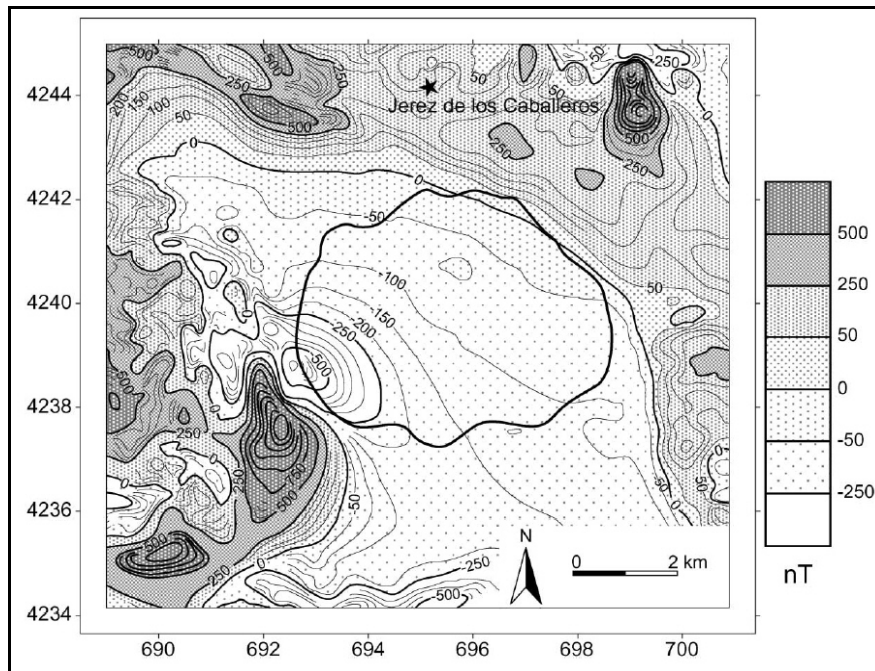


Figure 4.2.3-4.
Aeromagnetic
anomaly map. The
thick line shows the
contour of the
outcropping La
Bazana granite.

The geological cross-section of Fig. 4.2.3-5 shows that the La Bazana granite emplaced at a late stage of the regional tectonic evolution and cuts the recumbent folds. The granite is located in the core of a late antiform. The granite was most likely emplaced during or shortly after the development of this late large antiform since: (1) as indicated by the petrographic data, the top of the granite at the time of emplacement was situated at a maximum depth of 10 km; (2) the geological cross-section of Fig. 4.2.3-5 shows that such an overburden atop the granite is viable, provided it intruded when erosion had not yet removed much of the relief created by late folding; and (3) it was not deformed during the late upright folding. All these considerations suggest the emplacement to have occurred most likely at the end of or shortly after the Middle Carboniferous upright folding.

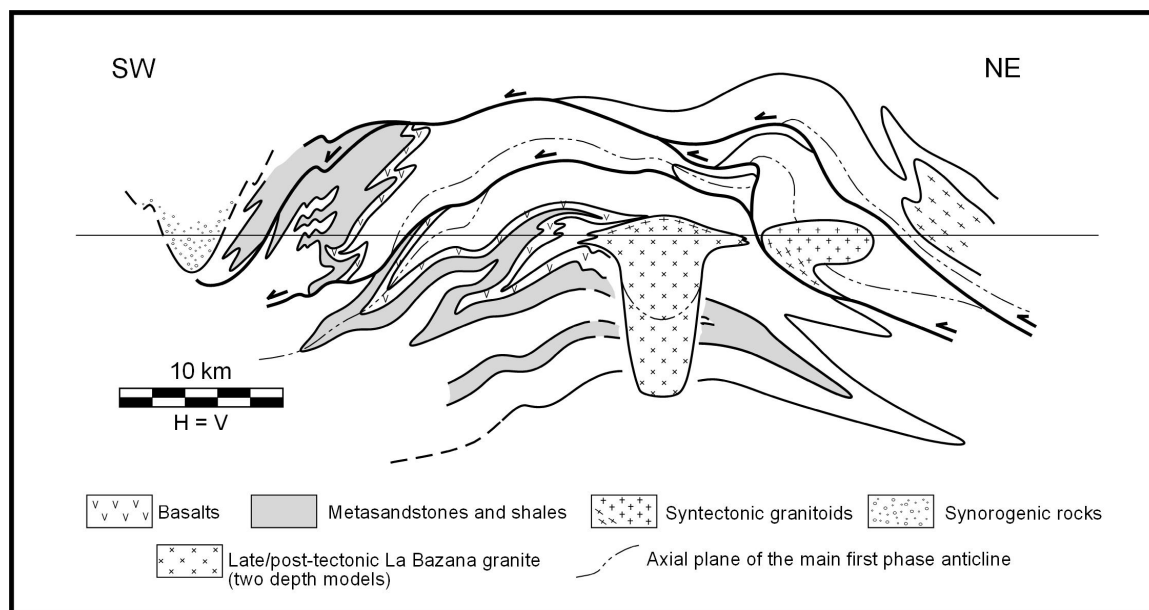


Figure 4.2.3-5. Composite cross-section of the study area, including the geometry of the La Bazana granite as modelled from gravity data. Location in Fig. 4.2.1-1 (A-D). The floor depth of the granite body depends upon the density considered, although the geometry of the top is similar. Host-rock structure after Expósito (2000).

4.2.4. Ascent and emplacement model: discussion

Field observations provide data to determine the shallow structure of granite plutons and gravity measurements help to establish their 3D view, although the size of the bodies determined by gravity modelling depends on the choice of regional and residual anomalies and density contrasts. In our study of the La Bazana granite, the regional and residual gravity anomalies have been determined from the regional gravity data (I.G.N., 1976) and the asymptotic tendency of our Bouguer anomaly data. As the local anomaly is strong, no improvement in the characterization of the residual (granite-related) anomaly is expected with more sophisticated procedures. The density contrast is, of course, essential in gravimetric interpretation. The modal composition of the La Bazana granite gives a mean density of 2.637 g/cm^3 , but a gravity model developed with this density needs a very large body occupying almost the entire crust, and the theoretical anomaly of this model does not fit well with the observed anomaly profile. In fact, the true density of granite massifs is somewhat lower (Telford et al., 1990) than those of fresh samples because granite massifs are more or less altered and fractured. Consequently, models with mean densities of 2.62 and 2.60 g/cm^3 were developed. The shapes obtained in both cases are very similar, of teardrop-pipe, expanded at the top, but the root is greater if we consider a 2.62 g/cm^3 density. The 2.72 g/cm^3 density for the country rock, determined by Campos and Plata (1991) for similar lithologies, is rather on the top of the densities for schists and metagreywackes. If we consider a

lower density for the host rock, it would result in an even deeper root for the granite body. In summary, whatever the densities considered, a teardrop-pipe 3D shape is obtained, with some uncertainty about the maximum depth of the root (Figs. 4.2.3-3 and 4.2.3-5). The geometry of the La Bazana granite strongly suggests diapiric ascent because of its thick root and teardrop-pipe shape. The geometry of its upper part indicates lateral expansion of the diapir during its final emplacement. The strain undergone in the host rock and the magmatic fabric pattern indicate upward pushing producing vertical shortening plus doming, and are compatible with this type of emplacement.

The petrological data of the granite and its metamorphic aureole show that the final emplacement occurred at a pressure between 2 and 3 kbar. The geological cross-section of the region (Figs. 4.2.1-1 and 4.2.3-5) also shows that the level where the granite was emplaced may have been located at depths of up to 10 km. In the same direction points the lens shape of the uppermost part of the intrusion (in contrast to bell shapes), as similar geometries have been also observed in the analogue models of Román-Berdiel et al. (1995), indicating a relatively deep emplacement (deep regarding the upper crust). The La Bazana granite cuts through all the regional structures (Fig. 4.2.3-5). It is not related to any fault; for this reason, we may discard mechanisms of fault-controlled emplacement. Although it is sub-circular in outcrop, its mushroom geometry, its homogeneity and its internal fabric is not compatible with a ballooning emplacement. Indeed, only a gentle dome has been observed in the studied area that is compatible with diapiric emplacement but not with in situ inflation (Fig. 4.2.4-1). The importance of stoping in assisting emplacement is difficult to evaluate: the discordant contacts observed in a few places suggest that some amount of it would have occurred, but the absence of large blocks on top of the granite makes it difficult to confirm.

The final stage of the evolution of the La Bazana diapir is characterized by the widening of its top laterally, exploiting the anisotropy of flat-lying bedding and foliation, as clearly shown by the interfingering with the country rock (Figs. 4.2.2-1d and 4.2.2-4). This evolution is the consequence of still active pushing by buoyancy, though insufficient (it has been diminished by crystallisation) to force the upward migration of the diapir through an increasingly viscous crust. Upward magmatic pressure at this stage is evidenced not only by the upper widening, but also by the dome geometry and the flattening strain in the granite (late-magmatic fabric) and in the overlying country rock.

In salt tectonics, diapiric growth is said to be effected through two end-member mechanisms (Jackson and Talbot, 1994): downbuilding (syn-depositional diapir growth) and upbuilding (post-depositional diapir growth by active piercing through the overburden). The upbuilding of salt diapirs is believed unlikely, yet possible if: (a) the diapirs are tall and the overburden is thin, (b) the overburden is being extended, or (c) the overburden is unusually weak. In contrast to salt tectonics, downbuilding can never be the case for the ascent of granite diapirs. Then, concerning upbuilding, it has been

argued, as in salt tectonics, that magmatic diapirs are unable to penetrate through the rheologically strong upper crust (e.g. Petford, 1996; Clemens, 1998). Natural examples, like the La Bazana granite, provide new data to influence theoretical discussions. The key for the ascent of granite diapirs seems to be the thermal and strain-rate softening of the country rock by the granite (Mahon et al., 1988; Weinberg and Podladchikov, 1995; Weinberg, 1996; Miller and Paterson, 1999), bearing in mind the whole complexity of the crust's behaviour. The La Bazana granite is an example that suggests that some granite bodies may have undergone a diapiric ascent to relatively shallow levels of the crust (7–10 km in depth in the case studied). Clemens (1998) considers that diapiric thermal death by increasing crystallisation carries with it the important implication that diapiric ascent should give rise mainly to diapiric emplacement, since the magma would have little or no potential to migrate further once the diapiric process had finished. Nevertheless, our case study suggests that sometimes other mechanisms may still operate: when the diapiric ascent is blocked, the bodies probably start to develop a lateral expansion. It could be that highly evolved diapirs would reach even tabular shapes (e.g., Goultly et al., 2001) by further evolution of what is observed in the upper part of the La Bazana pluton. In an extreme case, this would lead to the removal of the root zone and the development of a flat floor.

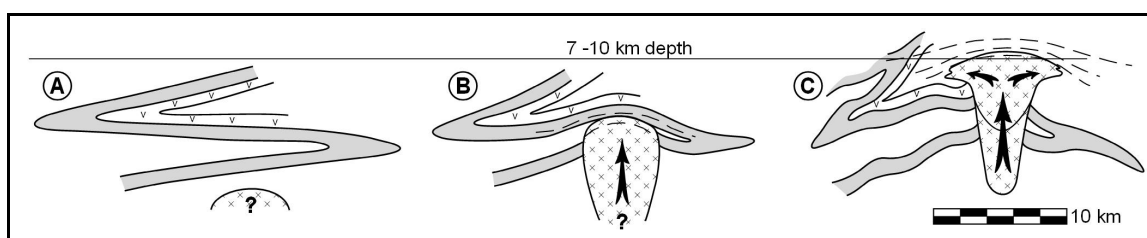


Figure 4.2.4-1. Ascent and emplacement model of the La Bazana granite. A) and B) Two stages of diapiric ascent, probably simultaneous to late regional fold development. C) Emplacement with doming and lateral expansion of the granite at shallow levels. The model is based on the present-day geological cross-section of the area and the data on granite emplacement discussed in the text.

4.3. The Nisa-Alburquerque batholith

4.3.1. Introduction

The Nisa-Alburquerque batholith is a 1000 km² WNW—ESE elongated granitic body (Fig. 4.3.1-1) emplaced during the Late Carboniferous, after the Variscan ductile deformation phases in the SW Iberian Massif, mostly in the Central Iberian Zone and partly in the Ossa-Morena Zone (see chapter 1.2). The Ossa-Morena and the Central Iberian Zones are characterized by intense deformation and coeval metamorphism, with pervasive Carboniferous magmatism resulting in granitoids cropping out at different structural levels.

The Ossa-Morena / Central Iberian Zones boundary is marked by a strongly deformed and metamorphosed NW—SE trending band, namely, the Badajoz-Córdoba Shear Zone or Central Unit (Burg et al., 1981; Matte, 1986; Azor et al., 1994; Simancas et al., 2003). This unit is made up of orthogneisses, metasediments and amphibolites affected by high-pressure metamorphism and an intense shearing responsible for the development of a planar-linear fabric. South of the Central Unit, the northern Ossa-Morena Zone is made up of Upper Precambrian to Silurian metasediments affected by SW-vergent recumbent folding and low-grade regional metamorphism.

The southern Central Iberian Zone is made up of uppermost Precambrian to Carboniferous low-grade, mostly siliciclastic metasediments displaying upright kilometric syn-schistose folds formed in Westphalian times (Martínez Poyatos et al., 1998; Simancas et al., 2001). Next to the Central Unit, in the so-called allochthonous unit, Late Devonian NE-vergent recumbent folds are also observed (Martínez Poyatos et al., 1998; Simancas et al., 2001). The lowest formation is the Schist-Greywacke Complex, a monotonous succession made up of slates with greywacke intercalations of uppermost Precambrian to Lower Cambrian age. Unconformably over the Schist-Greywacke Complex, an Ordovician to Lower Carboniferous succession made up by slates, metaquartzites and metasandstones is present; among the different formations, the Armorican Quartzite, consisting of a several hundred-metre thick sequence of metaquartzites can be used as a regional marker that depicts the different structures. The Nisa-Alburquerque batholith intrudes the southern Central Iberian Zone, the Central Unit and the northern part of the Ossa-Morena Zone (Fig. 4.3.1-1).

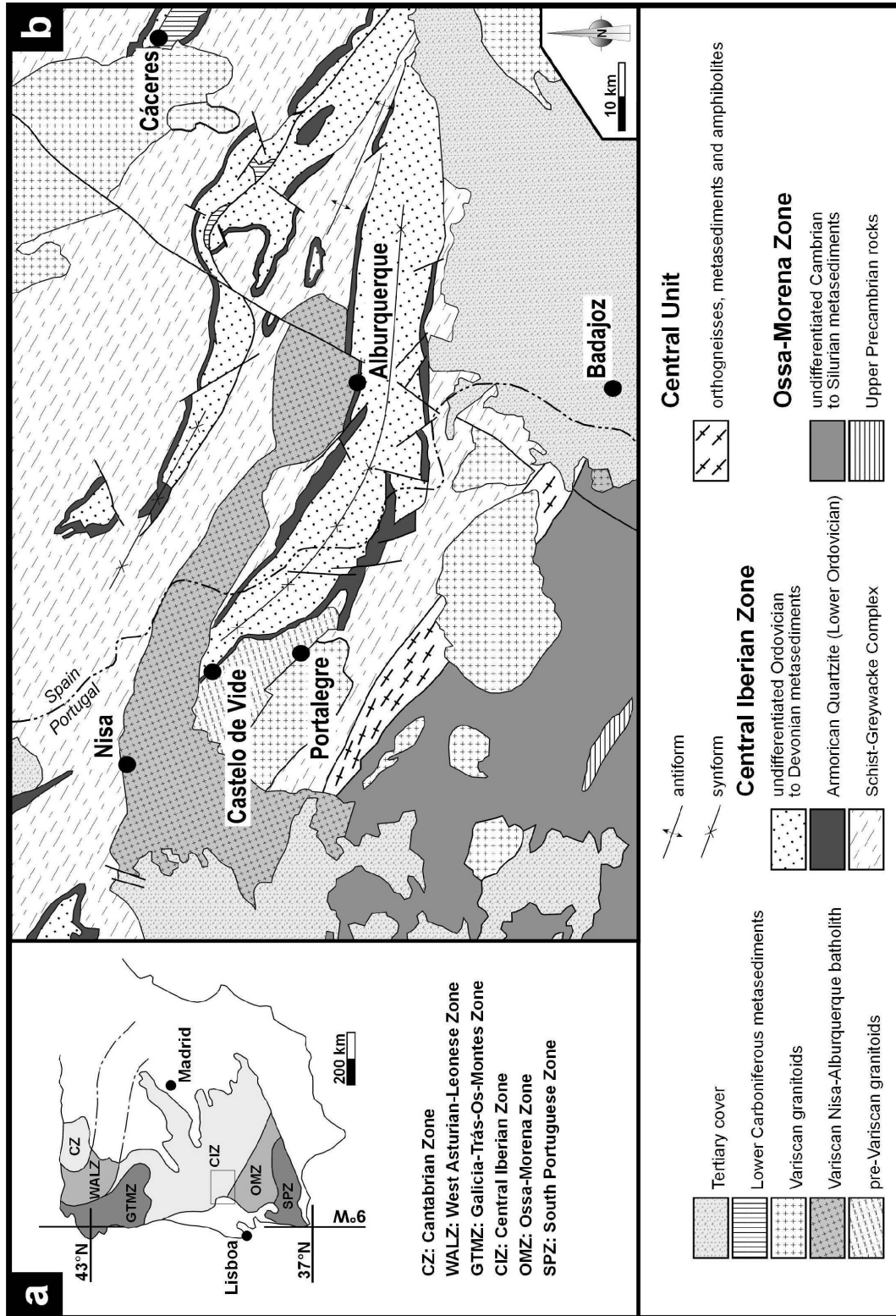


Figure 4.3.1-1. a) Sketch of the Iberian Massif and location of the geological map shown in b (rectangle). b) Geological map of the area surrounding the Nisa-Alburquerque batholith, simplified after Instituto Tecnológico Geominero de España (1994).

4.3.2. Petrography and structure of the Nisa-Alburquerque batholith and its country rocks

The present chapter outlines the main results published by Azor et al. (2000), González Menéndez (2002), González Menéndez and Bea (2004) and González Menéndez and Azor (2006).

The Nisa-Alburquerque batholith is made up of a dominant Coarse-Grained Granite representing 70% of the total outcrop extent, and three subordinate facies, namely a Central Granite A, a Central Granite B and a Fine-Grained Granite (Fig. 4.3.2-1). The Coarse-Grained Granite, Central Granite A and Fine-Grained Granite are two-mica peraluminous S-type granites which were mapped according to their fabrics. The Coarse-Grained Granite is a cordierite, tourmaline and andalusite bearing, usually porphyritic granite that includes monzogranites and leucogranites. The Central Granite A is medium-grained and crops out along the axis of the batholith as a 40 km-long body roughly parallel to the external contacts. This dike-shaped body of biotite-bearing muscovite granite appears in the central and western sectors of the batholith. The Fine-Grained Granite is a medium- to fine-grained, equigranular granite that crops out in the easternmost portions of the batholith (North of Alburquerque) as small stocks scattered throughout the Coarse-Grained Granite; this facies is a cordierite, tourmaline and andalusite bearing granite, very similar to the Coarse-Grained Granite but slightly more leucocratic. The Central Granite B is a medium-grained biotite granite that appears inside the Central Granite A and the Coarse-Grained Granite at the southwest sector; it forms small stocks aligned in the same direction as the Central Granite A band. Compositionally, the Central Granite B includes metaaluminous monzogranites, granodiorites and tonalites, being more mafic towards the W-SW, where it contains amphibole and sphene, and shows local mixing effects with the Coarse-Grained Granite. Giving these features, the Central Granite B is classified as I-type, in clear contrast with all the other granites of the Nisa-Alburquerque batholith, which are regarded as S-type granitoids.

The compositional and geochemical data reveal an E—W zonation in the batholith, being the less differentiated facies in the western part. The main field evidence of this zonation is that the Coarse-Grained Granite becomes more leucocratic to the east. Further evidence is provided by the biotite composition, that shows a zonation in the Coarse-Grained Granite and in the Central Granite A, with a $Fe/(Fe+Mg)$ ratio that decreases toward the crystal rims and also westward parallel to the longest dimension of the batholith. Moreover, the whole rock composition of the Coarse-Grained Granite shows an increasing abundance of MgO, Sr, Ba, V, Zr, Th, and REE from the east-central domains towards the west-southwest region of the batholith. There is also a slight normal zonation consisting in a more leucocratic composition toward the centre of

the batholith and a decrease in MgO, Ba, V, Zr and LREE in the same direction (González Menéndez, 2002).

The dominant Coarse-Grained Granite has been dated in several locations yielding ages between 285 and 310 Ma. In the western part of the batholith, Mendes (1967-68) obtained Rb-Sr isochrons with ages of 290 ± 8 , 309 ± 20 and 301 ± 9 Ma. In the eastern part, Roberts et al. (1991) obtained a Rb-Sr age of 286 ± 3.6 Ma, while González Menéndez (1998) reported Rb-Sr ages of 289 ± 22 and 294 ± 11 Ma. Despite the uncertainties, these ages point to a slightly older age in the western part than in the eastern one. The emplacement pressure has been estimated at 2.3-3 kbar (7-10 km, Rodríguez Suárez, 1985).

The Nisa-Alburquerque batholith is strongly elongated parallel to the main Variscan structures of the southern Central Iberian zone, showing at the outcrop scale sharp contacts parallel to the main foliation in the country rocks, which strikes NW—SE and dips sub-vertically. The south-eastern end displays an E—W elongated sub-rounded shape that joins the rest of the batholith by means of a sort of narrows (Figs. 4.3.1-1 and 4.3.2-1). Towards the west-northwest, the batholith enlarges and is deflected to the south, cutting across the Variscan structures and intruding the Central Unit and the northern part of the Ossa-Morena Zone. The north-western end is covered by Cenozoic sediments. The country rocks are mostly metapelites and quartzites, except along the southern contact close to the Castelo de Vide sector where the batholith intrudes the Ordovician Portalegre orthogneiss. The southern contact of the batholith in the Alburquerque sector is close to the Armorican Quartzite formation belonging to the southern limb of a major antiform; actually, the granite intrudes the Armorican Quartzite formation in the sub-rounded eastern termination while to the west the contact separates from this formation by a north directed deflection. Along the northern contact the batholith intrudes the Schist-Greywacke Complex.

The batholith shows a 1-2 km-wide contact aureole where andalusite grew statically over the previous regional foliation. A strain aureole is not well developed since no penetrative structures attributable to the granite emplacement are recognized. The Armorican Quartzite formation does not modify its regional trend in the proximity of the batholith along the southern external contact.

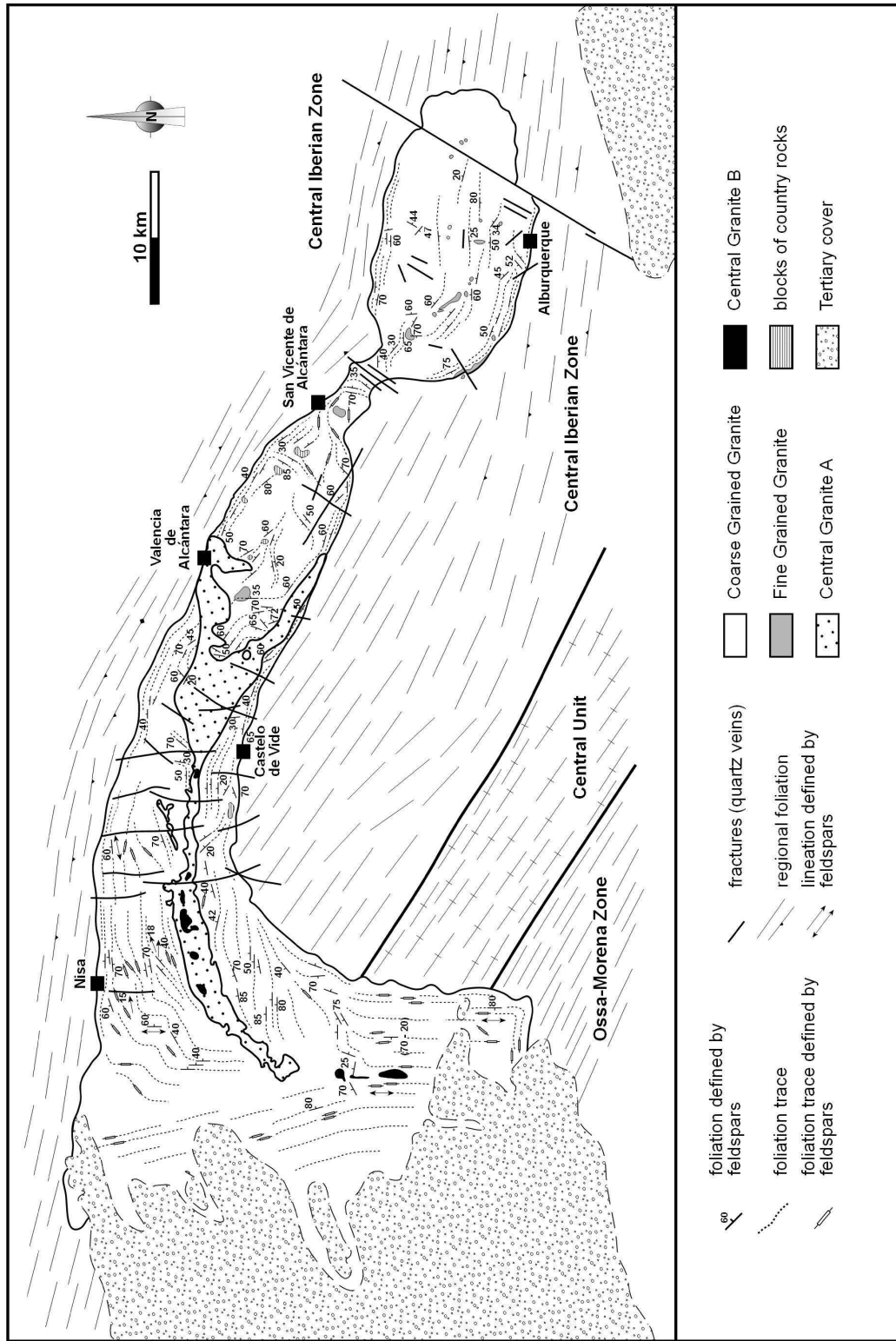


Figure 4.3.2-1. Geological map of the Nisa-Alburquerque batholith showing its internal structure and facies distribution, as well as the foliation trajectories in the country rock, modified after González Menéndez (2002) and González Menéndez and Azor (2006).

The internal fabric of the batholith is defined by the shape preferred orientation of K-feldspar megacrysts of the Coarse-Grained Granite (Fig. 4.3.2-1). This fabric is probably related to magmatic flow since other minerals apart from K-feldspar megacrysts are not oriented and do not show evidence for solid-state deformation. Except for the western part where the batholith enlarges, the magmatic fabric has an average WNW—ESE direction and variable dips (20-80°) mainly to the north; the fabric is therefore roughly parallel to the internal contact with the Central Granite A, the external contacts and the regional foliation in the country rocks. In the western termination, the fabric is mainly N—S oriented and parallel to the longest dimension of the batholith here. The intensity of the fabric generally increases from east to west. In the eastern sub-rounded-shaped sector, the fabric is more often than not isotrope, except close to the external contacts where a planar fabric parallel to the contact is observed. In the central-western sector, the fabric is very intense and homogeneous. In this sector, the orientation of the (010) planes of K-feldspar megacrysts define a planar fabric parallel to the external contact.

4.3.3. Geometry of the Nisa-Alburquerque batholith

To characterize the 3D shape of the Nisa-Alburquerque batholith, 6 gravimetric and magnetic profiles were carried out. Their orientation is approximately perpendicular to its longest dimension and covering its whole cartographic extent and surrounding areas. The obtained relative gravity measurements have been calibrated with the absolute gravity value of the base station of the Instituto Geográfico Nacional located in Badajoz (Spain). The resulting absolute gravity values were interpolated between measurement points using the kriging method in order to draw the Bouguer anomaly map (Fig. 4.3.3-1). As for the magnetic data, the magnetic anomaly was obtained by subtracting the theoretical intensity of the geomagnetic field from the observed values; the theoretical intensity of the geomagnetic field at the time and location of measurement is given by the International Geomagnetic Reference Field (IGRF).

The magnetic profiles show no significant anomalies associated with the batholith (Fig. 4.3.3-2), which can be taken as evidence for its homogeneous character. As for the country rocks, there are no magnetic anomalies, except in the south-westernmost sector, where some rocks with high magnetic susceptibility, such as amphibolites, can be found.

Two-dimensional models of residual gravity anomaly along the 6 profiles were developed in order to infer the geometry of the batholith at depth (Fig. 4.3.3-3). The regional anomaly has been considered to approximate a linear function, which can be drawn in each profile taking into account the asymptotic tendency of the Bouguer anomaly towards and in the host rock (Fig. 4.3.3-2). We have considered the densities provided by Campos and Plata (1991). For the metapelitic-quartzitic country rocks, an

average density of 2.72 g/cm^3 was assumed. For the granite, a density of 2.63 g/cm^3 , slightly lower than the one used by Campos and Plata (1991), has been considered in order to get the best adjustment between the observed and calculated anomalies. As for the Portalegre orthogneiss, we have considered the same density as for the granite, since their compositions are similar.

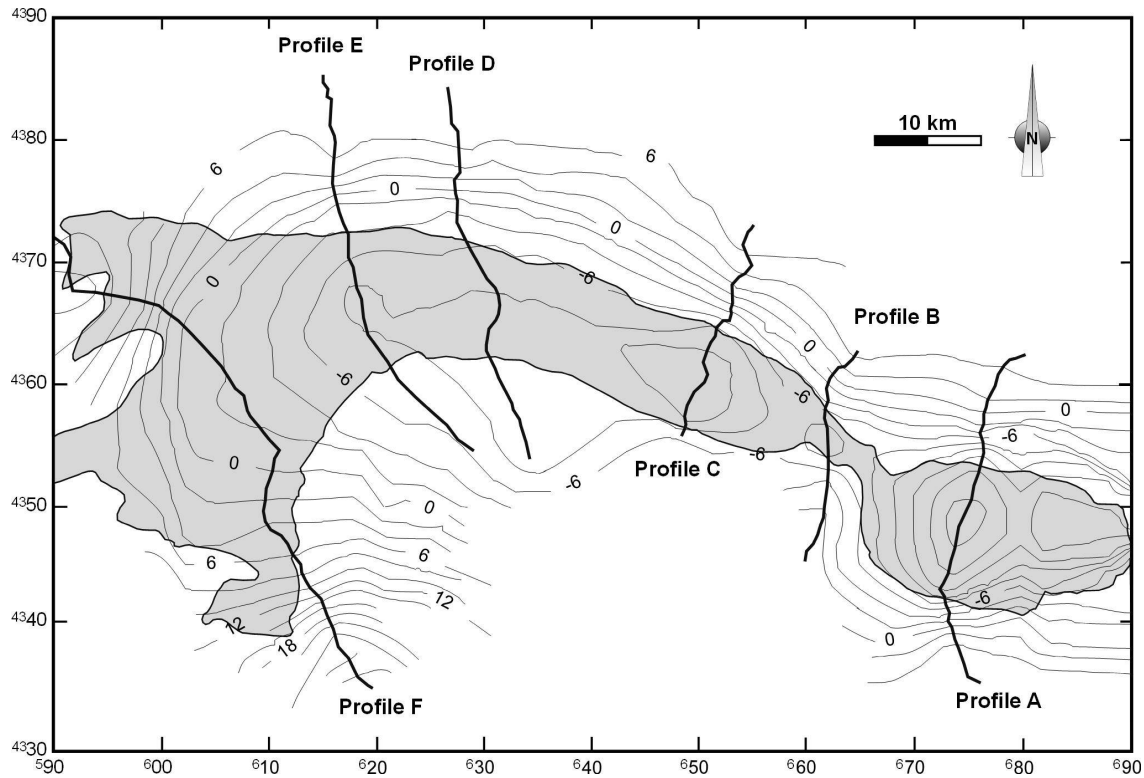


Figure 4.3.3-1. Bouguer gravity anomaly map of the Nisa-Alburquerque batholith and its surroundings. UTM coordinates.

The Bouguer anomaly profiles vary notably from east to west along the batholith. In the easternmost part, the batholith is related to a very pronounced minimum with amplitudes up to -16.4 mGal of Bouguer anomaly, and residual anomaly close to -32 mGal . To the west, the profiles show progressively a less intense anomaly, reaching values of -3 mGal for Bouguer anomaly and between -15 and -18 mGal for residual anomaly. The shape of the profiles also changes notably from east to west. In the eastern and central parts, the batholith intrudes metapelites and quartzites and the anomaly is symmetric. In the western part, the batholith intrudes to the south the Portalegre orthogneiss, resulting in asymmetric profiles with lateral flats at different levels.

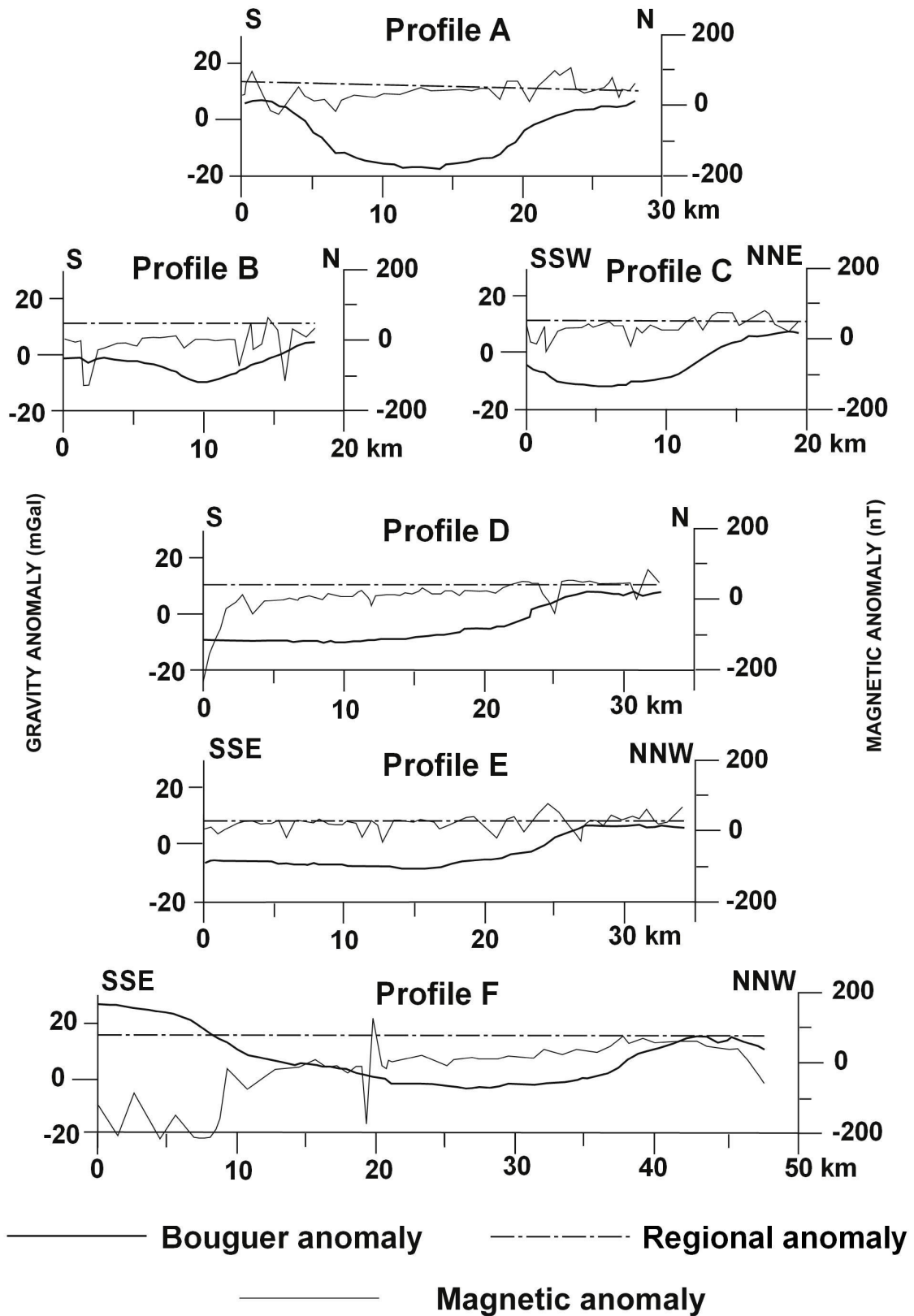


Figure 4.3.3-2. Gravity and magnetic anomaly profiles across the Nisa-Alburquerque batholith (see Fig. 4.3.3-1 for location).

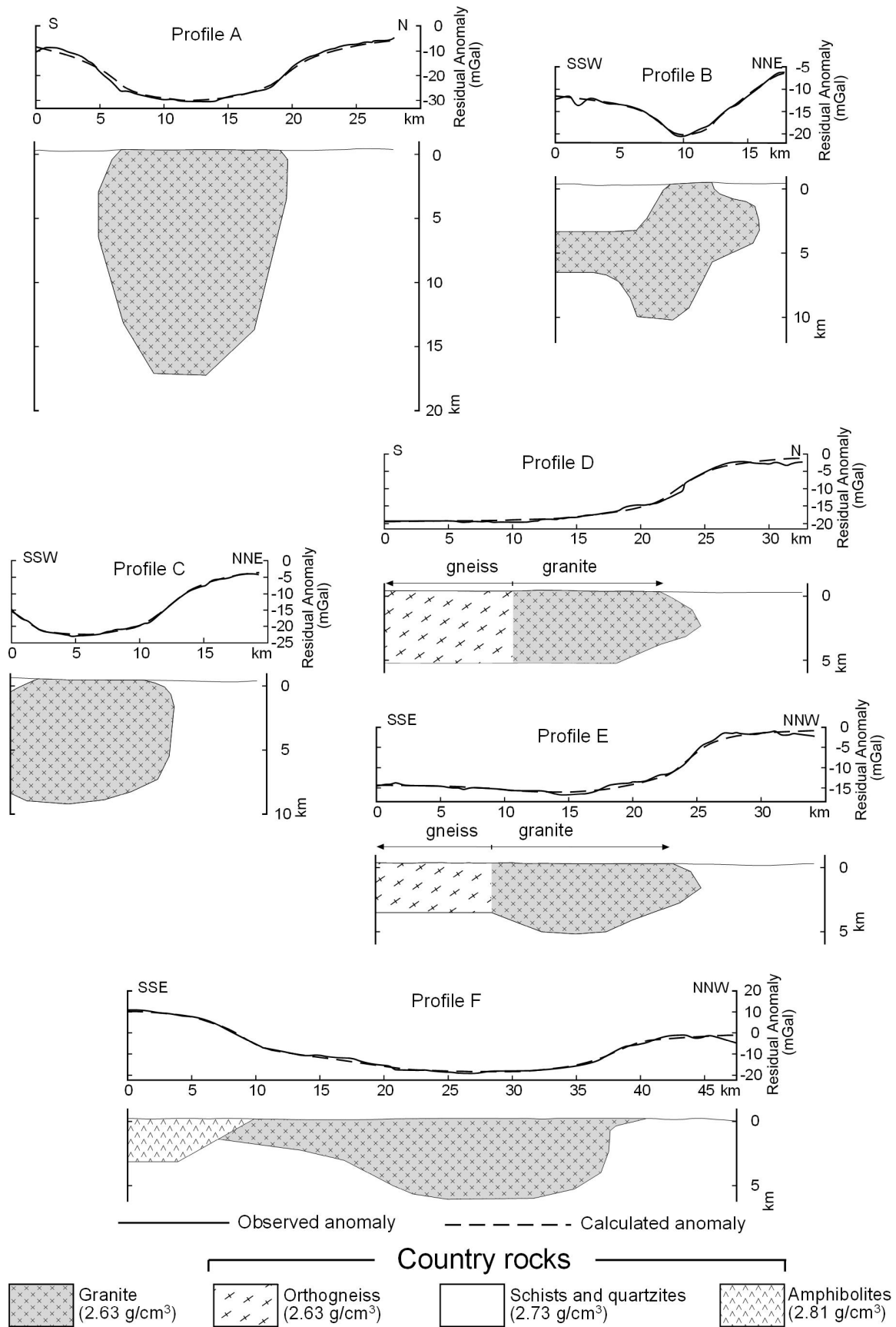


Figure 4.3.3-3. Residual gravity anomaly models of the Nisa-Albuquerque batholith along profiles A to F (see Fig. 4.3.3-1 for location).

The two-dimensional models of the granite (Fig. 4.3.3-3) show that the geometry of the batholith varies notably along the different profiles. In the eastern part, the batholith has the geometry of an irregular cylinder inclined to the ESE, from which at surface one can observe the upper part, being the floor located at a depth close to 15 km in the easternmost part. Moreover, according to Campos and Plata (1991) the batholith prolongs to the ESE underneath the surface, since the gravity anomaly extends in that direction outside the contour of the body at surface. In the profile B, a hidden mass deficit must be considered in the south-south-western part in order to explain the obtained anomaly, suggesting that the granitic body might show some widening and interfingering with the country rock at depth. A similar shape was modelled by Campos and Plata (1991) at this location. To the west, the batholith becomes a more extended body whose floor is irregular and located at a depth of 4-8 km. Slight differences in the assumed densities for country rocks and granite provoke important variations in the depth of the batholith's floor. Nevertheless, the relative differences in the granite shape between the profiles remain unchanged independently of the assumed densities.

4.3.4. Ascent and emplacement model: discussion

An emplacement model for the Nisa-Alburquerque batholith must take into account the deep geometry deduced from gravimetry, together with the petrologic, geochemical and structural data available, and the geotectonic context at the time of intrusion. The whole south-western Iberian Massif underwent transpression during most of the Variscan Orogeny, giving way to left-lateral ductile and brittle shear zones partially coeval with the folding phases (Azor et al., 1994; Simancas et al., 2001). The granite cuts across all the Variscan structures, meaning that it intruded after the Variscan deformation, during a period of post-orogenic tectonic quiescence or extension in Stephanian times (Simancas et al., 2003 and references therein). Sanderson et al. (1991) proposed that the Nisa-Alburquerque batholith intruded in a releasing bend of a left-lateral shear related to the Badajoz-Córdoba shear zone (or Central Unit). However, this hypothesis must be rejected, since no shear zone was found in the area to be spatially related to the batholith and the granite intrudes the ductile and brittle fault rocks of the Central Unit without recording any penetrative deformation.

The gravimetric data indicate that the central and eastern parts of the Nisa-Alburquerque batholith correspond to a WNW—ESE elongated body that tends to be equidimensional in cross section; the body increases in thickness and is rooted in the eastern part. To the west, the batholith becomes a much more superficial, flat-floored body. Thus, it is likely that the main feeding channel of the batholith was located in the east, where the maximum granite thickness is found.

The petrological, geochemical and geochronological data (González Menéndez, 1998, 2002) suggest that from west to east the Coarse-Grained Granite becomes younger and is built up by more differentiated facies. As for the structure (González Menéndez and Azor, 2006), the batholith is elongated parallel to the Variscan structures and is located at the southern limb of a kilometre-scale antiform. In the central-eastern part of the batholith, the external contacts are subvertical and parallel to the regional foliation in the country rocks. The internal fabric of the Coarse-Grained Granite is characterized by magmatic foliations and lineations in WNW—ESE direction. In the western sector the granite cuts across the Variscan structures and its internal fabric is oriented in N—S direction. In the easternmost, sub-rounded termination, the internal structure is not well defined, except next to the borders, where a contact parallel fabric is observed.

Given the above-mentioned characteristics, it is proposed that the Coarse-Grained Granite ascended through the crust along a feeding channel located in the eastern part of the batholith (Fig. 4.3.4-1). The ascent mechanism and the shape of this feeding zone cannot be postulated with confidence, but it is possible that the regional, subvertical cleavage constituted pre-existing, planar anisotropies which were exploited by the magma during ascent. The poorly defined fabric found in the eastern part can be explained by the turbulent flow in a site of continuously incoming magma, whereas the contact parallel fabric is the result of the accommodation of the magma to the chamber shape with more or less contribution of radial chamber expansion (ballooning) or local convection. From the eastern part, the magma flowed towards the west along the southern limb of an antiform. This is congruent with the WNW—ESE fabric, presumably parallel to the magma flow lines, since the flow was here nearly uniform, with an increasing component of non-coaxial flow (or velocity-gradient flow, Paterson et al., 1998 and references therein) towards the margins. Progressive cooling during westward flow increased the viscosity of the magma and caused its blockage at the western termination of the batholith. The deceleration flow, together with successively incoming magma batches pushing former ones aside, caused the fabric to rotate towards a N—S direction and the magma chamber to spread laterally to the south. This southward expansion led to further flow deceleration, thus enhancing the development of the fabric at high angles to the flow direction. This scenario is compatible not only with the structural and gravity data, but also with the younger and more differentiated magma batches being located to the east. A similar situation was found by Vignerresse and Bouchez (1997) in the nearby Cabeza de Araya pluton, in which the root zones, interpreted as feeders, also correlate with the more leucocratic facies.

The space needed by the intrusion might have been created mostly by rigid displacement of the wall rock in NE—SW direction, provided that the tectonic scenario was at this time most probably extensional. The formation of andalusite in the contact aureole post-dates the cleavage formation, suggesting that no ductile shortening was achieved by the country rocks during or after the emplacement. The sub-rounded shape

and the contact parallel fabric at the borders of the eastern lobe can be attributed to some contribution of ballooning. Finally, stoping must have played some role during emplacement, since some fragments of the host rock were found in some areas of the pluton.

The above described emplacement history accounts for the Coarse-Grained Granite. For the existence of the other granitoid facies, namely the Central Granite A and B and the Fine Grained Granite, the intrusion of later magma batches, probably along dykes, must be invoked.

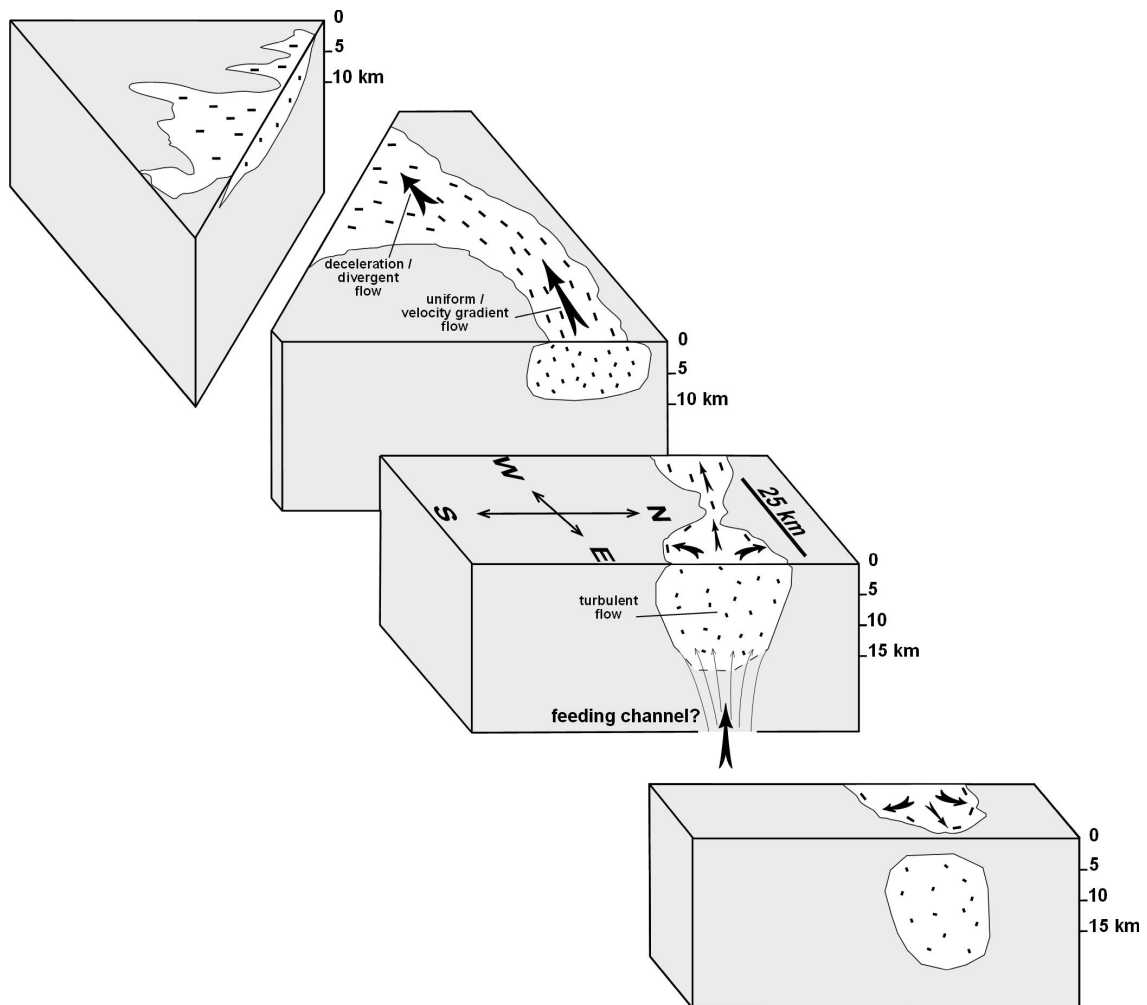


Figure 4.3.4-1. Sketch showing a possible scenario for the emplacement of the Nisa-Albuquerque batholith (Coarse-Grained Granite). Short, thick lines represent the shape preferred orientation of feldspars (linear and planar fabric after Azor et al. (2000) and González Menéndez and Azor (2006)). Arrows symbolize the inferred magma flow direction.

5. Investigations on granitoids of the Moldanubian Zone, Bohemian Massif

5.1. Geographic overview

The area studied in the Bohemian Massif is located in south-eastern Germany and belongs to the region known as Bavarian Forest (Fig. 5.1-1). It is situated between 48°30'N to 48°50'N and 13°10'E to 13°40'E, north of the German city of Passau and the Danube River, next to the border to the Czech Republic and Austria. Very characteristic in this region are the quarries, in which granite and other rocks are mined. The altitude ranges from 300 to 800 m AMSL. The climate in this area is transitional between atlantic and continental with a precipitation of about 800 und 2000 mm/yr, a big amount of it in form of snow. The landscape is the typical one of a hilly, low mountain range and an important portion of the surface is occupied by forests of conifers and broad-leaved trees. The vegetal cover is dense, which makes geological work somewhat difficult. On the other hand, road conditions and coverage are excellent and almost every outcrop can be reached by car.

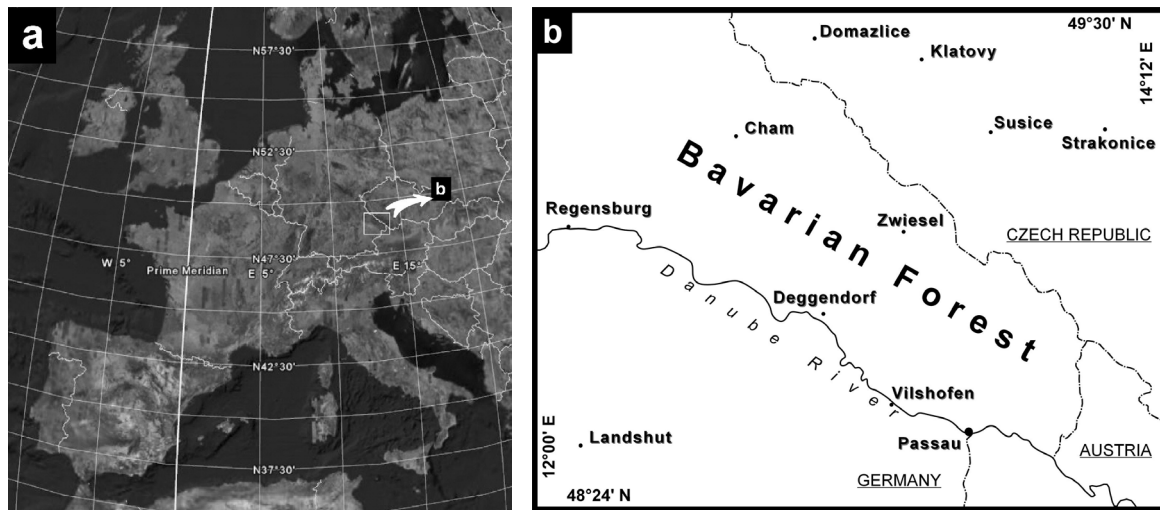


Figure 5.1-1. a) General map of Europe. Source: Google Earth. b) Enlargement of the region known as Bavarian Forest, in which the study area is located.

5.2. Geological setting and previous works

5.2.1. The Moldanubian Zone in the study area

The study area is located at the south-western margin of the Bohemian Massif, where rocks belonging to the Moldanubian Zone crop out (see chapter 1.2 and Fig. 5.2.1-1).

The Moldanubian Zone is a mosaic of different tectonic units with their own tectonometamorphic history, which were assembled during the collision of Laurussia and Gondwana at late Palaeozoic times (Urban and Synek, 1995). The present architecture of the Moldanubian Zone is mainly due to the dominant medium pressure / medium temperature collisional event which led to stacking of all tectonic units at ca. 350-330 Ma. This phase was succeeded by the most important metamorphic event in the study area, which is characterized by high temperature and low pressure and linked to anatexis and extensional processes. It occurred at ca. 330-316 Ma in the neighbourhood of the study area (Blümel, 1995, and references therein; Kalt et al., 2000; Propach et al., 2000; Teipel, 2003) and is responsible for the present appearance of the migmatic rocks. After Kalt et al. (1999) the peak conditions during the HT-LP metamorphism reached 800-850°C and 0.5-0.7 GPa, whereas the last equilibration occurred under 770-846°C and 0.44-0.51 GPa. Finger et al. (2007) postulate the existence of two HT-LP events in the south-western sector of the Bohemian Massif at 345-330 Ma and at 330-315 Ma, respectively. Numerous late- to post-kinematic granitoids intruded between 340 and 280 Ma. The Variscan tectonic activity was terminated by important intracontinental strike-slip movements along two fault sets (NW—SE and NNE—SSW, see chapter 5.2.2) vaning at around 290-260 Ma (Urban and Synek, 1995, and references therein).

The Moldanubian Zone is usually regarded as part of the SE-vergent flank of the bilateral Variscan Orogen (Urban and Synek, 1995, and references therein). In the central part of the Moldanubian Zone the general structure is characterized by thrusts with dominant top-to-SE sense of movement formed during two thrusting phases. These thrusts were folded during a later deformation phase. The Variscan tectonic activity was terminated by ductile to brittle strike-slip faulting. However, the structure of the south-western part of the Moldanubian Zone is strikingly different. Thus, some authors have attempted to distinguish different lithotectonic units based in part on their distinct structural style (Urban and Synek, 1995, and references therein). One of these units is the so-called Bavaricum, which represents an intensely reworked marginal part of the Moldanubian Zone located mostly in German and Austrian territory (Fig. 5.2.1-1). The boundary of the Bavaricum with other Moldanubian units is marked by a gradual change in the foliation trend which is typically NW—SE in the Bavaricum and NE—SW in the central part of the Moldanubian Zone. In the Bavaricum, the intensity of dextral transcurrent movements along NW—SE trending shear zones decreases to the north.

The SW part of the Moldanubian Zone (Bavaricum) can be roughly divided into two parts: (1) the antiformal wedge of the Oberpfalz and Bohemian Forests and (2) the generally monoclinally area of the Bavarian Forest, Mühlviertel, Sauwald, and Sumava Mountains (Fig. 5.2.1-1).

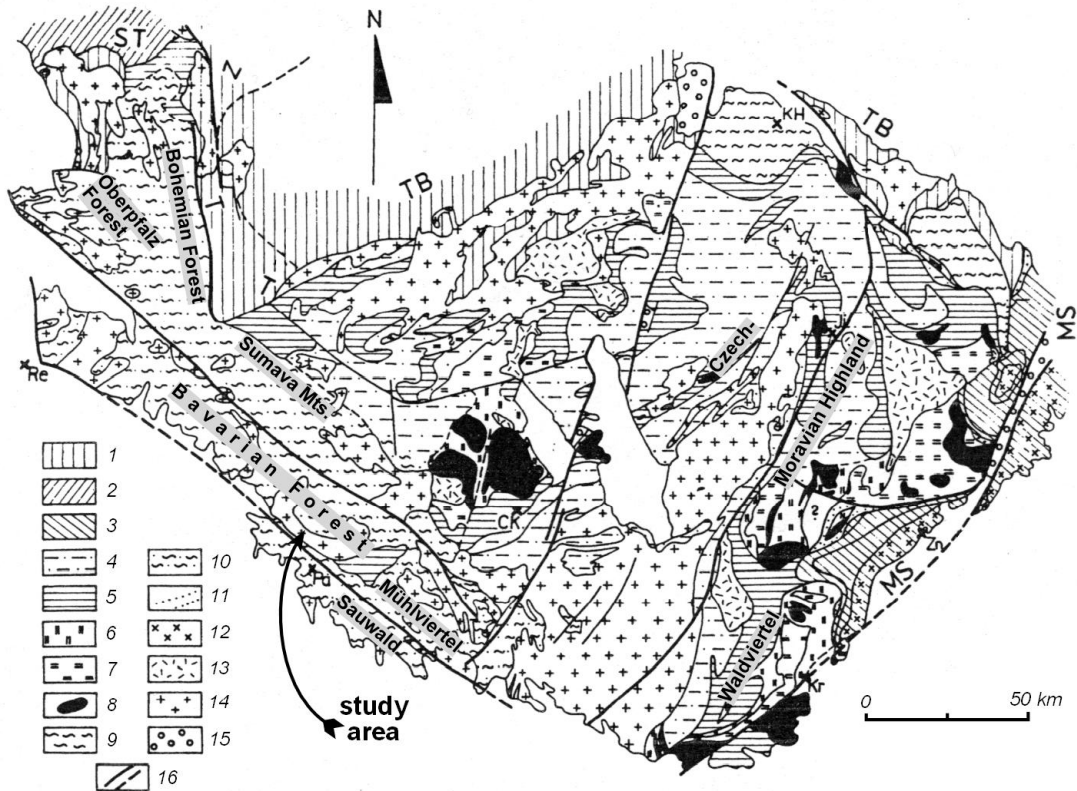


Figure 5.2.1-1. Distribution of the main lithotectonic units of the Moldanubian Zone in the Bohemian Massif, modified after Urban and Synek (1995). 1 Teplá-Barrandian Zone (including the Zone of Erbendorf-Vohenstrauß; ZTT Zone of Teplá-Domažlice (Taus)); 2 Saxothuringian Zone (ST); 3 Moravo-Silesian Zone (MS); 4-10 Moldanubian Zone; 4 Monotonous Group; 5 Variegated Group; 6 Gföhl Group; 7 Gföhl Gneiss; 8 Granulite bodies; 9 Kutná Hora-Svratka Complex; 10 Bavaricum; 11 Moravian Micaschist Zone between the Moldanubian and Moravo-Silesian Zones; 12 Cadomian granitoids; 13-14 Variscan granitoids; 13 durbachites; 14 other granitoids; 15 Permo-Carboniferous basins; 16 important faults; ČK Český Krumlov; Ji Jihlava; KH Kutná Hora; Kr Krems; Pa Passau; Re Regensburg; Zn Znojmo.

As already mentioned in chapter 1.2, Matte et al. (1990) and Franke (2000) distinguished two main tectonostratigraphic units in the Moldanubian Zone: the Drosendorf and the Gföhl units. The above-mentioned Bavaricum is after these authors equivalent to the western part of the Drosendorf Unit (Fig. 1.2-2). Two lithostratigraphic units are traditionally distinguished in the Drosendorf Unit: the Monotonous Group, constituted by migmatic paragneisses with intercalations of metamorphosed igneous rocks and calc-silicate rocks, and the Variegated Group, which is embedded in the

former one and consists of migmatic paragneisses and amphibolites, leucocratic gneisses, marbles and graphite (Rohrmüller et al., 1996).

The study area is located at the south-western margin of the Bohemian Massif, between the Bayerischer Pfahl shear zone, the Danube shear zone, the Hauzenberg pluton and the Fürstenstein pluton (Fig. 5.2.1-2). Consequently, the rocks of the study area belong to the Monotonous Group of the Drosendorf Unit and to the Bavaricum.

In the following lines an overview will be given about the main Variscan ductile deformation phases proposed by some authors in the neighbourhood of the study area.

Stein (1988) found in the Oberpfalz Forest (see Fig. 5.2.1-1 for location) four ductile deformation phases accompanying the HT-LP metamorphism. All of these deformations resulted in the formation of folds with axes parallel to the zone limits (NE—SW), except for D_4 , which produced folds with axes trending NNW—SSE to NW—SE and steeply dipping axial planes under greenschist facies conditions. After Stein (1988), this change in the orientation of fold axes points to a change in the convergence direction between Laurussia and Gondwana at the end of the Variscan Orogeny (Late Westphalian to Early Stephanian) from NW—SE to E—W or NE—SW.

According to Tanner (1995), Tanner and Behrmann (1995), and Behrmann and Tanner (1997) four compressive or transpressive deformation phases (D_3 - D_6) occurred during the Namurian in the Oberpfalz Forest, which in order of decreasing age produced: subvertical foliation striking NW—SE to NNE—SSW (re-folded) with a steep NW-plunging lineation, originated mainly by simple shear with east-side-up shear sense (D_3); large-scale folds with steeply dipping axial planes and 60° NW-plunging axes (D_4); the two younger deformations D_5 and D_6 are only locally observed. D_4 is the result of NE—SW horizontal contraction.

After some other authors (Zulauf et al., 2002a; Zulauf and Vejnar, 2003), the Carboniferous anatexis was linked in time with an extensional process of orogenic collapse that provoked the sinking of the Teplá-Barrandian block in the Moldanubian rocks between approx. 360 and 320 Ma (Upper Devonian to Upper Carboniferous).

Büttner (1999) described two main deformation phases in the Mühlviertel (Austria, see Fig. 5.2.1-1 for location). D_2 led to the development to gently dipping foliations and lineations with top-to-SE shear sense. D_2 affected the Weinsberg granite in hypersolidus state. D_3 led to the formation of the Bayerischer Pfahl conjugate shear-zone system. Both deformation phases took place under a sub-horizontal principal compression in approximately N—S direction.

After Beer (1981) the migmatites south of the Bayerischer Pfahl shear zone show a steep NW—SE striking mylonitic foliation formed during the Carboniferous at high- to medium-grade metamorphic conditions. North of the Bayerischer Pfahl shear zone, the migmatic gneisses display isoclinal folds with axial planes dipping to the NE, which were formed in Ordovician times.

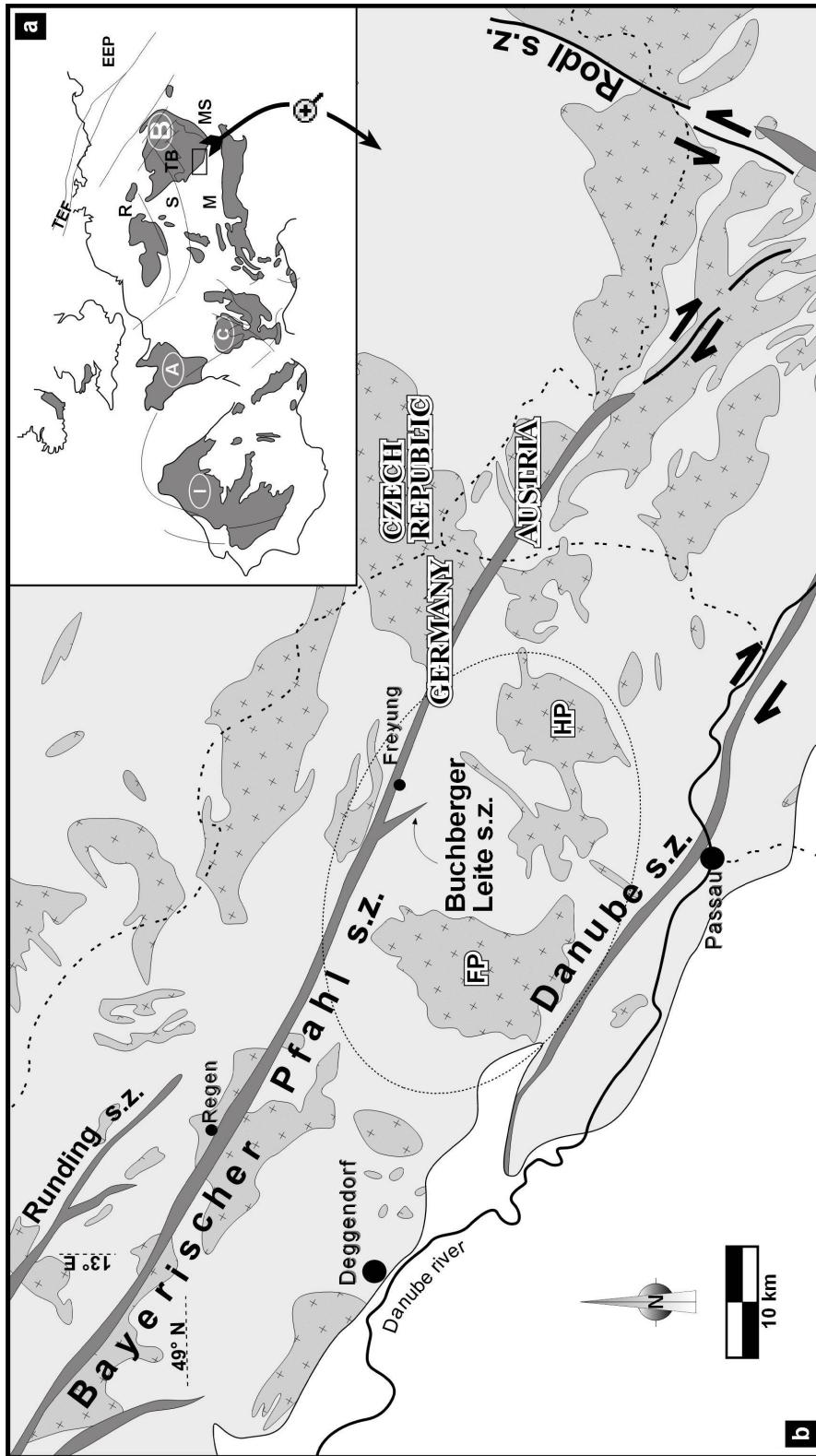


Figure 5.2.1-2. a) Overview of the European Variscides, simplified after Franke (1992). Letters enclosed in ellipses refer to Variscan Massifs: B Bohemian Massif, A Armorican Massif, I Iberian Massif, C Massif Central. Major tectonometamorphic zones in Central Europe: R Rhenohercynian, S Saxothuringian, M Moldanubian, TB Teplá-Barrandian, MS Moravo-Silesian. TEF Transeuropean Fault, EEP East European Platform. b) Geological map of the south-eastern part of the Bohemian Massif, roughly coincident with the extension of the Bavarian Forest, simplified after Bundesanstalt fuer Geowissenschaften und Rohstoffe (1993). White: post-Variscan cover. Light grey: metamorphic rocks. Medium grey with crosses: intrusive rocks, mainly granites and granodiorites. Dark grey and thick lines: major faults and fault rocks. FP Fürstenstein pluton, HP Hauzenberg pluton. The thin, dashed line represents the limits of the study area.

5.2.2. The Bayerischer Pfahl shear zone and the Bayerischer Pfahl shear-zone system

The Bayerischer Pfahl shear zone is, from the geographical point of view, the most prominent shear zone in the Bavarian Forest. This is due to the quartz lode formed by hydrothermal processes during its late history (Horn et al., 1986). The quartz lode is very resistant against meteorization and builds in some areas impressive natural walls of rock.

There are some other shear zones which together with the Bayerischer Pfahl form a strike-slip system of conjugate and subsidiary shear zones. All together will be named in this work "Bayerischer Pfahl shear-zone system". These shear zones are (Fig. 5.2.2-1):

- NW—SE striking: Bayerischer Pfahl shear zone, Runding shear zone, Danube shear zone.
- NNW—SSE striking: Buchberger Leite shear zone and other minor ones.
- NE—SW to NNE—SSW striking: Rodl shear zone, Karlstift shear zone, Vitis shear zone, Diendorf shear zone.

All of them are represented in Fig 5.2.1-2 (except for the last three, which are located further to the east in Austrian territory) and in Fig 5.2.2-1.

The Bayerischer Pfahl shear zone, and probably the whole system, has been active over a wide time and temperature span ranging from amphibolite facies to near-surface conditions (Hoffmann, 1962; Beer, 1981; Brandmayr et al., 1990; Wallbrecher et al., 1990; Masch and Cetin, 1991; Brandmayr et al., 1995, 1999) from pre-Variscan to Miocene times (Freudenberger, 1996, and references therein). The Bayerischer Pfahl shear-zone system was probably active, at least during its ductile history, under compression in N—S to NNW—SSE direction (Brandmayr et al. 1990, 1995). The NE—SW trending shear zones of this system display a sinistral sense of shear and tend to show lower grade conditions than the others (Brandmayr et al. 1990, 1995, 1999). The NW—SE and NNW—SSE trending ones are dextral and reach deformation temperatures up to amphibolite facies conditions. After Beer (1981) the movement at the Bayerischer Pfahl shear zone had a dextral and a NE-side-down vertical component. Reaching progressively lower temperatures and brittle conditions, the regime of the Bavarian Pfahl shear zone might have changed (Mattern, 1995).

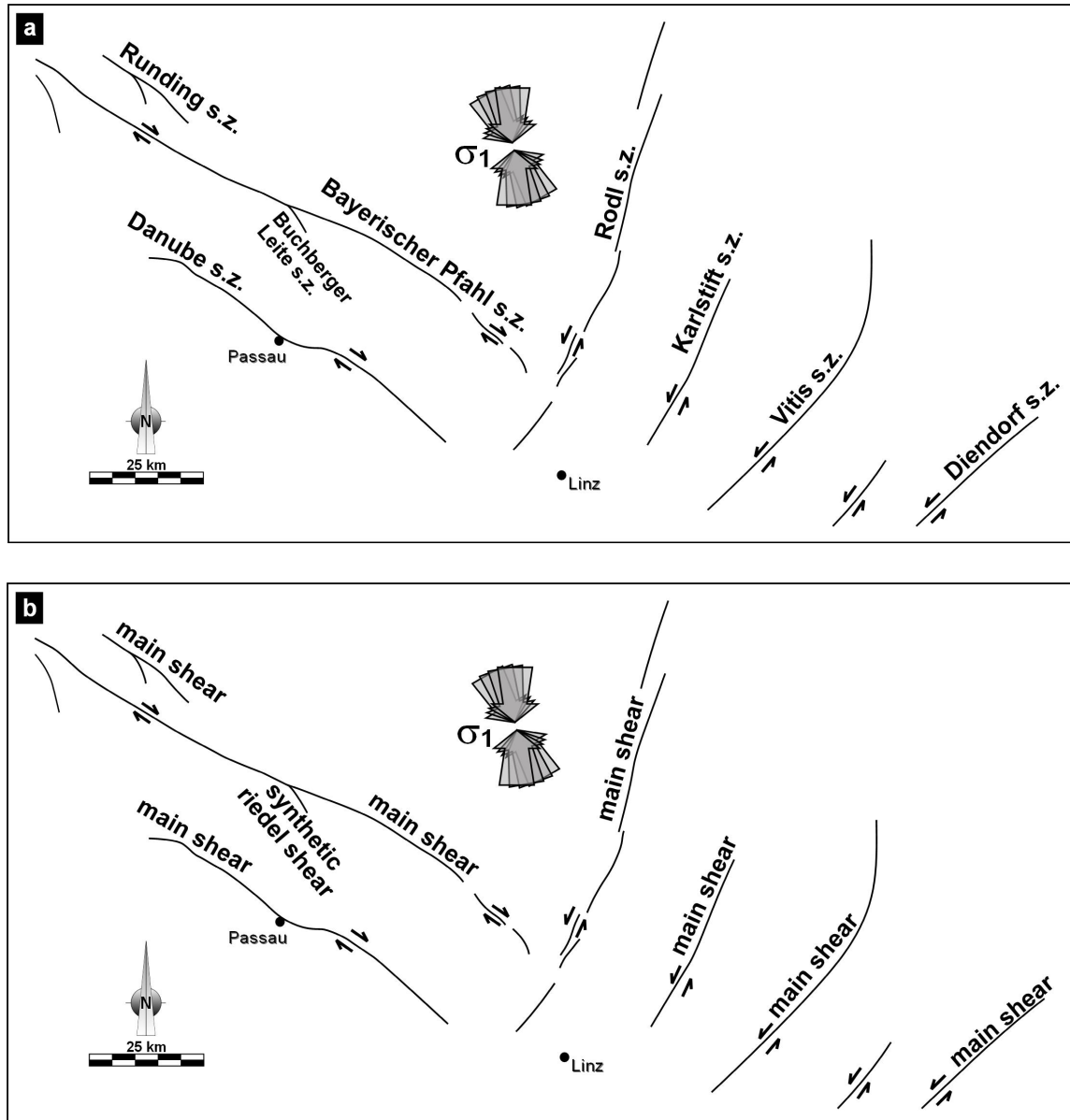


Figure 5.2.2-1. a) Sketch of the Bayerischer Pfahl shear-zone system and b) its tectonic interpretation.

The conclusions of previous investigations about the temperature conditions governing the deformation at the Bayerischer Pfahl shear-zone system can be summarized as follows. It must be born in mind that the boundaries between high, intermediate and low temperature are not sharp and may be different for each author:

Beer (1988). At the Runding shear zone quartz c -axes patterns show a maximum parallel to the stretching lineation combined with small circle girdles around the Z -axis of the finite strain ellipsoid, pointing to a combination of pure and simple shear under high temperatures. The shear sense is not clearly defined. The c -axes patterns at the Bayerischer Pfahl shear zone show single girdles inclined towards the foliation plane indicate dextral simple shear under intermediate to low temperatures.

Masch and Cetin (1991). At the Buchberger Leite shear zone took place a dextral movement and a relative sinking of the western block. They interpret the recrystallization of feldspars and the existence of the association Bt-Kfs-Pl-Qtz-Hbl as indicative of high deformation temperature. At the Bayerischer Pfahl shear zone (Reschbach/Wolfsteiner Ohe) the paragenesis Chl-Ab-Ep-Qtz-Ser and the c -axes mostly parallel to the Y -axis of the finite strain ellipsoid are (after these authors) indicative of low temperature conditions during dextral shearing.

Brandmayr et al. (1990), Handler et al. (1991), Brandmayr et al. (1995, 1999). Their conclusions are based on quartz c -axes patterns and microfabrics. Temperatures above 650 °C were reached in the Bayerischer Pfahl and the Danube shear zones, whereas shearing under greenschist facies conditions took place in the Rodl and Karlstift shear zones. The Vitis and Diendorf shear zones are characterised by essentially brittle deformation. The high and medium temperature fabrics observed at the Bayerischer Pfahl, Danube, Rodl and Karlstift shear zones were subsequently overprinted during younger deformation stages.

Büttner (1999). The deformation at the Bayerischer Pfahl and related shear zones started under amphibolite facies and continued during cooling to greenschist facies conditions. The conditions during the deformation at the shear-zone system were around 3.3-4.0 kbar and 650-700°C at the high-T stages and 1.8-3.1 kbar and 472-510°C at the greenschist-facies stages.

It is important to remark that the temperatures deduced by these authors neither represent an upper limit, nor governed deformation at the same point in time. Two facts must be born in mind: (i) the deformation was polyphase, that is, younger events might have completely overprinted former fabrics and (ii) even considering the existence of parts of the shear-zone rock which are representative for the early stages of deformation, i.e. that have undergone little or no overprint during later stages, it is a question of luck whether the sampling sites coincide exactly with these zones. Therefore, it should not be forgotten that the deformation temperatures deduced from microfabric and textural analysis always provide a minimum estimation for the maximum temperature reached during the deformation at the shear zone considered as a whole.

5.2.3. The intrusive bodies

Variscan and late-Variscan intrusives are ubiquitous in the Moldanubian Zone. Focusing in our study area, a succession of magmatic bodies is observed, which intruded at different stages of the Variscan Orogeny. Attending to their age, composition, deformation and geometry, the following classification of the intrusives cropping out in the study area can be made (see some examples of each group in Fig. 5.3.1-1 and Appendix 1). It is important to remark that some bodies might show transitional

characteristics. Although this classification oversimplifies the regional variability of intrusive rocks, this simplification fits the scope of the present work. For more general discussions about the Variscan intrusives of the Bohemian Massif the reader is referred to the existing literature (e.g. Finger et al., 1997; Siebel, 1998):

Group 1: Old dioritic to granodioritic bodies

The diatexites of the study area are very often cut by dioritic to granodioritic/tonalitic stocks of different sizes. The ages available for these rocks suggest that they intruded prior to the peak of the HT-LP metamorphism. One of the varieties of dioritic to granodioritic rocks included in the Fürstenstein pluton (granodiorite with titanite spots) has been dated at 334-332 Ma (Pb-Pb evaporation and U-Pb on zircon, Chen et al., 2002; Chen and Siebel, 2004).

One special type of this group of rocks is the traditionally called "Palit" (Frentzel, 1911): this rock is dark coloured, biotite and amphibole rich, with a granodioritic to dioritic matrix and often bearing large crystals of K-feldspar (see detailed description later in chapter 5.3.1.1). In recent works (e.g. Galadí-Enríquez and Zulauf, 2006; Galadí-Enríquez, in press) these rocks are considered to have been affected by Variscan anatexis. Consequently they are called dark-coloured diatexites. Siebel et al. (2005) consider dark-coloured diatexites to have evolved from a plutonic protolith, which intruded at 334 ± 3 Ma (Pb-Pb evaporation and U-Pb on zircon).

Dioritic to granodioritic stocks may be tectonically foliated or nearly undeformed, depending on the considered outcrop.

Group 2: Small granitic stocks and dykes

In the migmatites also intruded granitic magmas in form of small stocks and dykes, very often spatially coinciding with older, more basic intrusions. Siebel et al. (2005) dated some small granitic dykes ranging between 322 ± 5 and 331 ± 9 Ma (U-Pb on zircon). One of them, the Saunstein granite dyke (see chapter 5.3.3.2), intruded at 324.4 ± 0.8 Ma (U-Pb on monazite, Galadí-Enríquez et al., 2005). Like the dioritic to granodioritic intrusions, the granitic ones can show variable deformation intensities, which vary from one body to another, but also within the same one. Judging from the characteristics of these bodies in the field, showing mostly sharp but lobate contacts at the outcrop scale, it seems most probable that their intrusion took place just after the regional anatexis.

Group 3: Large stocks (main facies in plutons)

Mainly after the intrusion of the former small granitic bodies, the igneous activity concentrated in two domains, which nowadays constitute roughly the flanks of our study area: the Fürstenstein Pluton to the west and the Hauzenberg Pluton to the east.

The Fürstenstein Pluton (Troll, 1964) is composed of many different magmatic batches. The first one is constituted by granodioritic to dioritic rocks, which can be included in the aforementioned group 1. After that, more acid facies intruded, for example the Tittling granite, dated at 323-321 Ma (Chen et al., 2002; Chen and Siebel 2004), which could be included in the group 2. The youngest facies dated up to now is also the one which occupies most of the surface area of the pluton: the Saldenburg granite, which intruded at 318-312 Ma (Chen et al., 2002; Chen and Siebel, 2004), almost contemporaneously with the Eberhardsreuth granite (a fine- to medium-grained facies located at the northern margin of the pluton on topographic sheet 1:25000 No. 7146 Grafenau) and shortly after the two-mica granite (see Appendix 1 and chapter 5.3.1.5). The initial ϵ_{Nd} values and initial $^{87}Sr/^{86}Sr$ ratios of the more basic facies suggest a mantle contribution to the melts or melting of a young mafic lower crust. The values of the same parameters in the granitic facies indicate the involvement of crustal material in their genesis.

The Hauzenberg Pluton is made up of three magmatic facies (Dollinger, 1967): a granodiorite, a fine-grained granite (Hauzenberg granite I) and a coarse-grained granite (Hauzenberg granite II). The Hauzenberg granite II has been dated at 320 ± 3 Ma and 329 ± 7 Ma (U-Pb on zircon and monazite, respectively, Klein et al., 2007). As for the Hauzenberg granite I, K-Ar datings of Harre et al. (1967) yielded 284 ± 3 and 313 ± 3 Ma for muscovite and 293 ± 3 Ma for biotite, whereas Rb-Sr datings of biotite yielded 310 ± 3 Ma. The same author obtained an age of 284 ± 4 and 294 ± 5 by means of K-Ar dating on biotite and 302 ± 13 by means of Rb-Sr dating on biotite for the Hauzenberg granodiorite.

All of the facies of the group 3 are rarely affected by ductile deformation.

The Bouguer gravity anomaly map 1:500000 of Germany (Plaumann, 1995) reveals a negative anomaly of about 8 mGal (approximate residual) centered on the Fürstenstein Pluton, and a similar one centered on the Hauzenberg Pluton. We could make a simple calculation to obtain a rough estimation of the geometry of the Saldenburg granite, which builds up most of the volume of the Fürstenstein pluton. In a simple scenario, we can imagine the form of the Saldenburg granite to resemble a vertical cylinder. After the equation $g_{max} = 2\pi G\rho [L+R-(L^2+R^2)^{1/2}]$ (Telford et al., 1995), in which g_{max} is the residual anomaly, G the gravitational constant, ρ the density contrast, L the cylinder thickness and R the cylinder radius, and using the values of $g_{max} = 8 \cdot 10^{-5} \text{ m s}^{-2}$, $G = 6.672 \cdot 10^{-11} \text{ m}^3 \text{ kg}^{-1} \text{ s}^{-2}$, $\rho = 10^2 \text{ kg m}^{-3}$ and $R = 3000 \text{ m}$, results in a thickness of 3600 m.

Dietl et al. (2005) postulate for the Fürstenstein Pluton a combination of active and passive emplacement mechanisms. The main intrusion phase took place at 14-17 km (Massonne, 1984; Dietl et al., 2005). The Hauzenberg granite II intruded into its country rocks at about 550°C and 16-18 km depth (Massonne, 1984; Klein et al., 2007).

Group 4: Post-granitic dykes (young sub-volcanic rocks)

The last magmatic episode ascribed to the Variscan Orogeny in the study area is represented by sub-volcanic rocks of rhyolitic to basaltic andesitic composition (von Gümbel, 1868; Frentzel, 1911; Scholtz, 1927; Voll, 1960; Troll, 1964; Dollinger, 1967; Ohst and Troll, 1981; Troll and Ohst, 1984; Bayer, 1997; Propach et al., 2007). In the new geological maps 1:25000 of the Bavarian Environment Agency they are grouped under the rubric of "post-granitic dykes". They are always found in form of subvertical dykes striking NNW—SSE to WNW—ENE, showing very sharp and straight contacts to the country rock. Their thickness rarely exceeds 5 m, except for a few ones in the area west of Waldkirchen (east of sheet Tittling, see Fig. 3.4-1 and Appendix 2 for location). Dacitic varieties have been dated at 302 ± 7 (Rb-Sr on apatite-biotite, Christinas et al., 1991b) and 299.0 ± 2.3 Ma (U-Pb on zircon, Propach et al., 2007). Their composition can be explained by mantle melting with more or less contribution of crustal material. Their emplacement occurred 4-6 km deep (Propach, 2002) in a country rock at a temperature of $200 \pm 50^\circ\text{C}$. These rocks are, except for some brittle overprint, always undeformed.

5.2.4. The sheared granites

The recent mapping survey at scale 1:25000 undertaken by the Bavarian Environment Agency in the Bavarian Forest led to the discovery of several small dykes and stocks of granitic composition, which belong to the group 2 of Variscan intrusives of the study area. Many of these bodies are affected by subvertical, ENE—WSW to WNW—ESE trending sinistral shear zones. In well exposed examples it is possible to realize that the deformation concentrates preferentially in the intrusions, affecting the host rock (diatexites and granodiorites to diorites) in rare cases. As we will analyze in the next chapters, the existence of these sheared granitic bodies has opened new research lines and new questions that need to be answered. They constitute the main object of investigation of the study area.

5.2.5. Deformation phases in the Moldanubian Zone: open questions

Up to now, a tectonic model concerning all Carboniferous structures present in Moldanubian rocks is lacking. From the results of some authors, a N—S to NNW—SSE compression seems to explain many of the ductile Variscan structures found in migmatites, gneisses and pre- to syn-orogenic intrusives (Stein, 1988; Tanner, 1995; Tanner and Behrmann, 1995; Behrmann and Tanner, 1997; Büttner and Kruhl, 1997; Büttner, 1999). In the same way, such a compression direction is compatible with the

kinematics of the Bayerischer Pfahl shear-zone system (Brandmayr et al., 1990; Wallbrecher et al., 1990; Brandmayr et al., 1995) during its ductile deformation. The frontal convergence between Laurussia and Gondwana during most of the Carboniferous represents the geotectonic framework, in which this compression took place.

However, some structural elements remain to be difficult to integrate in this geotectonic framework. As reported by Stein (1988), Tanner (1995), Tanner and Behrmann (1995), and Behrmann and Tanner (1997), some of the observed structures need a rearrangement of the principal stresses. Thus, the existence of NW—SE to NNW—SSE trending, open folds in the Oberpfalz Forest would be easier to understand under NE—SW compression.

An important question is whether the studied sinistrally sheared granites (Fig. 5.2.5-1) might have developed coevally with the Bayerischer Pfahl shear-zone system under N—S to NNW—SSE compression. Platt (1984) presented a model regarding different foliation types developed in ductile shear zones (Fig. 5.2.5-1c), which can be useful in our case to visualize the geometrical relationships between the different shear zones found in the Bavarian Forest. Comparing the orientation of shear planes in sinistrally sheared granites with the foliations of Platt (1984), it would be possible to correlate some of the sinistrally sheared granites (some of the ones located to the east striking ENE—WSW) with extensional crenulation cleavages (ecc2) related to the Bayerischer Pfahl shear-zone system. However, many other sinistrally sheared granites with shear planes striking E—W to WNW—ESE cannot be explained by this model.

Therefore, we concluded that the sinistrally sheared granites presented and studied in this work are not compatible with a N—S to NNW—SSE compression and cannot develop contemporaneously with the Bayerischer Pfahl shear-zone system under normal conditions.

In the following chapters we will evaluate the importance of the sheared granites in supporting the rearrangement of the directions of principal stresses in the Bavarian Forest in late-Carboniferous times.

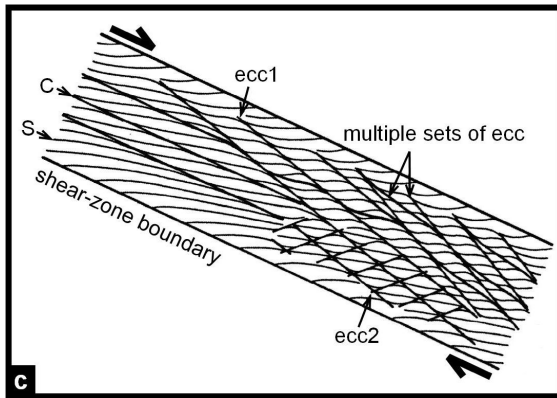
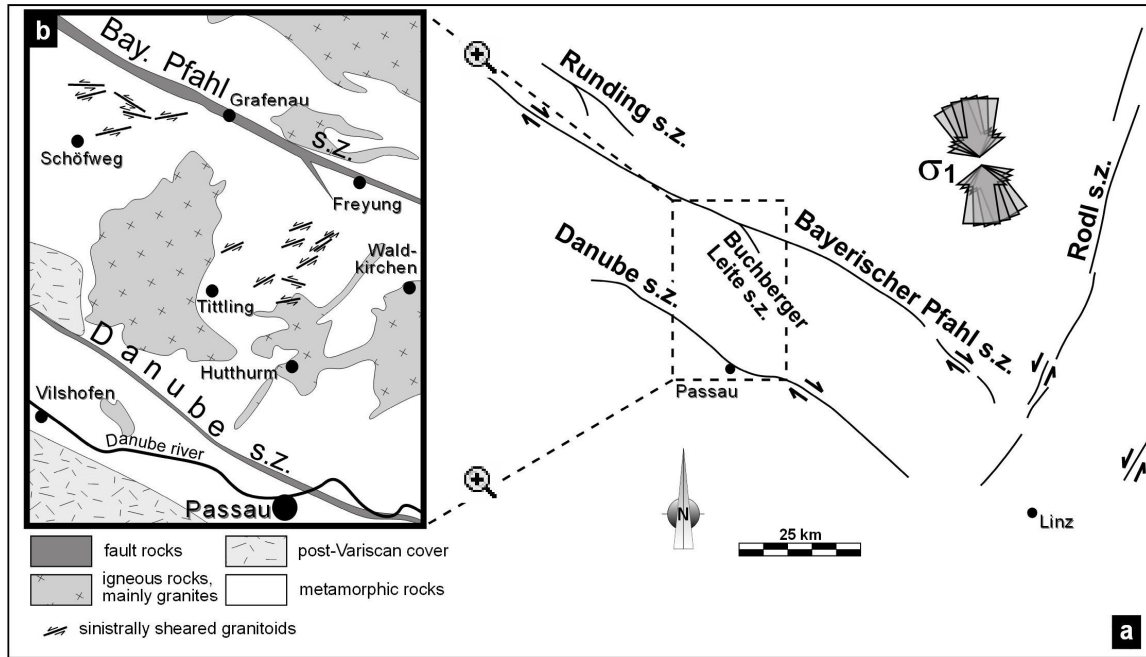


Figure 5.2.5-1. a) Tectonic sketch of the Bayerischer Pfahl shear-zone system. b) Simplified geological map of the study area showing the orientation of shear planes in sinistrally sheared granites, modified after Bundesanstalt fuer Geowissenschaften und Rohstoffe (1993). c) Diagram illustrating the orientations and mutual relationships of foliations in shear zones: S, shape fabric; C, shear bands, ecc1 and ecc2, conjugate sets of

extensional crenulation cleavage, redrawn after Platt (1984). The shear-zone boundaries of the diagram (c) were drawn parallel to the Bayerischer Pfahl and Danube shear zones in order to allow an easier comparison. Note that ecc2 planes are parallel to some of the sinistrally sheared granites of (b), but oblique to some others.

5.3. Results

5.3.1. Geological mapping in the Passau Forest

In this chapter an overview about the different rock types present in the topographic sheet 1:25000 number 7246 Tittling will be given (see Appendix 1). The information contained in some previous works was taken into account, reviewed and in part included in the resulting geological map. The most important contribution is the work of Troll (1964, 1967), who mapped the whole Fürstenstein Massif and made also some studies about its country rock (Troll, 1966; Troll and Winter, 1969) and other intrusives (Troll and Ohst, 1984). His results were included in the geological map nearly unchanged. Three diploma theses were also considered: the one of Koch (1998) occupying the central area surrounding the Miocene deposits, the one of Schmidl (2000) in the SE corner of the map and the one of Weiss (1981) in the north-eastern margin of the Fürstenstein Pluton. Steiner (1968, 1969, 1972) focused on the rocks formerly called "Palit", which crop out in the north-eastern corner of the map and will be called "dark-coloured diatexites" from now on. For the version of the geological map provided in the present work, the Cenozoic units were grouped under the general term "post-Variscan cover". A more detailed version of the map can be found in Galadí-Enríquez and Zulauf (2006). Fig. 5.3.1-1 shows schematically the main lithologies found in the map and a tentative reconstruction of their temporal relationships.

host rocks	age	protoliths: Neoproterozoic to Early Palaeozoic main metamorphism: Carboniferous			
	lithology	migmatites (diatexites) metamorphosed magmatic and sedimentary rocks			
intrusives	age	Carboniferous to Permian			
		older	←————→		younger
	group (chapter 5.2.3)	1 diorites to granodiorites	2 small granitic stocks and dykes	3 large stocks (main facies in plutons)	4 post-granitic dykes (sub-volcanic)
	lithology	diorite quartz diorite granodiorite* tonalite*	granite (fine to medium grained) Tittling granite* granite to granodiorite (fine grained)*(?)	two-mica granite* Saldenburg granite*	andesite dacite rhyolite
* included in Fürstenstein pluton					

Figure 5.3.1-1. Chart summarizing the principal rock types present on the Tittling map and a tentative reconstruction of their temporal relationships.

5.3.1.1. Migmatic rocks

In the special case of this map, the partial melting of the rocks reached an advanced stage, in which the dark-coloured minerals were also involved in melting: the darker and lighter parts of the rock form schlieren and nebulitic structures which merge into one another. Consequently, they are called diatexites (Wimmenauer and Bryhni, 2002).

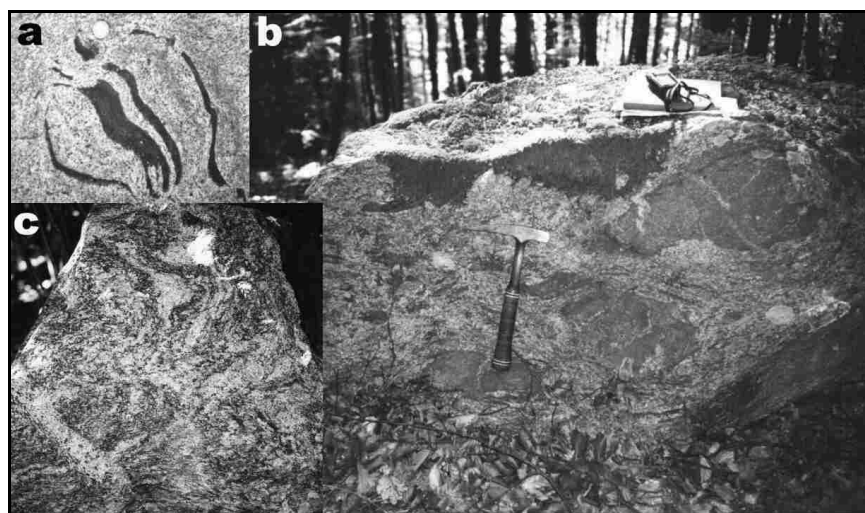


Figure 5.3.1.1-1. a) Schollen structure south of Tittling. b) Schollen structure north of Neureut. c) Schlieren structure near Poxreut.

The diatexites in the Tittling map show different deformation intensities and, therefore, different macro- and microfabrics: Granofelsic as well as intensively foliated varieties were found.

The variability of the appearance of the diatexites is not only due to the deformation intensity and type of migmatic structure, but also to the mineral composition, which was used as a criterion to subdivide the diatexites in varieties. The differences in the quartz, K-feldspar and plagioclase content between light-coloured and dark-coloured diatexites can be viewed in a diagram for the classification of plutonic rocks (Le Maitre et al., 1989, 2002), although it must be born in mind that these rocks are in their present form no plutonic, but metamorphic rocks. Both varieties can be described as mainly granitic in composition, whereas the dark-coloured diatexites show a tendency towards granodiorite and a wider compositional range (Fig. 5.3.1.1-2).

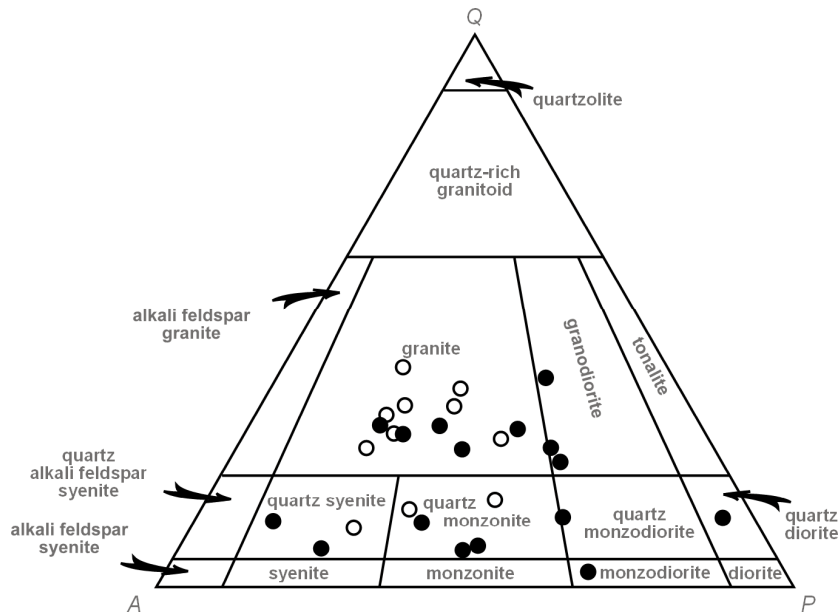


Figure 5.3.1.1-2. QAP modal classification of light- (white circles) and dark-coloured (black circles) diatexites

Light-coloured diatexite

Macroscopic features

The appearance of this rock is granitoid-like. A detailed observation leads to the discovery of numerous, dark-coloured, unmelted parts. At the outcrop scale pegmatoid pockets and aploid veins are usually found. The weathering product of the rock, made of angular grains of sand to fine gravel grain size, is often mined and used as a fill material (e.g. small sand pits northeast of Pfefferhof and between Adlmühle and Pötzersdorf). Melanosomes result typically in a finer weathering product with a grain size between fine sand and silt. The rock is medium to coarse grained, finer in melanosomes. Its colour is white to greyish, sometimes pinky in leucosomes and black in melanosomes. Some amphibole grains may be present, but the greenish colour of some mineral aggregates used to be due rather to the secondary biotite that grows from them as to the amphiboles themselves.

In some areas, in which the pervasive intrusion of granite in diatexite makes it impossible to map single bodies, "light-coloured diatexite crosscut by granite veins" was mapped. In a few outcrops the alternance of diatexite and granite at the cm to dm scale is observable.

The size of the K-feldspar crystals can vary strongly. Large specimens, about 1.5 cm long or even larger, can be found in the whole region. The porphyritic variety of the light-coloured diatexite was mapped only there, where the length of the K-feldspars exceeds 2 cm within a mappable area. These large crystals occur in more or less discrete bands and are usually scattered, that is they are embedded in the matrix of the rock, rarely in touch with each other.

Garnet is a rare mineral on the Tittling map and, when present, it is not easily identifiable with the naked eye. The mapping of the garnet-bearing variety is based on a few outcrops south-west of Perlesreut and some observations under the microscope.

Microscopic features

Major constituents: K-feldspar 60—30%, with cross-hatched and carlsbad twinning, often as microperthite, the size of the crystals can locally exceed the size of the crystals of other minerals (porphyritic fabric); quartz 40—10%, shows depending on the thin section undulose extinction, dynamic or static recrystallization; plagioclase 45—15%, normally with a stronger alteration than K-feldspar, with pericline and albite twins and myrmekites at the contact to K-feldspar.

Major to minor constituents: biotite 15—1%, pleochroism from reddish brown to yellow, rarely from greenish brown or brownish red to yellow, sometimes deformed as kink folds and mica fishes.

Minor to accessory constituents: pale amphibole 3—0%.

Accessory constituents — most of them appear also in the rest of the diatexite varieties and will therefore be described only once, later only mentioned: zircon, mostly in biotite, in which it builds pleochroic haloes, and nearly always with several distinguishable growth episodes; chlorite, light green with blue anomalous interference colour, rarely green, secondary from biotite; opaque phases (ilmenite?) and titanite occur very often together in form of aggregates next to biotite and sometimes as large opaque grains surrounded by titanite coronas; allanite, with pleochroism in pink colours, zoned and twinned, as very well developed crystals, sometimes with epidote corona; apatite, sometimes as minor constituent, often in form of aggregates together with biotite, shows characteristic hexagonal basal sections; rutile as tiny needles (max. 0.05 mm long) in quartz and biotite; white mica, secondary from feldspars.

Microfabric: granoblastic to lepidoblastic, porphyritic in some areas.

The pale amphibole occurs in form of aggregates of tabular crystals, sometimes mixed with opaque phases. These aggregates replace a former mineral (probably pyroxene) which has been completely corroded. Sometimes, most of all at the rims, the aggregates show a greenish colour (hornblende?). In most cases they are surrounded by green biotite ± chlorite.

The growth of titanite and opaque phases next to biotite can be explained as a result of the crystallisation of biotite at high temperatures and the expulsion of titanium out of the biotite lattice during temperature drop.

Hornblende diatexite

Macroscopic features

In several areas the relationship between the occurrence of hornblende diatexite and metabasite enclaves is patent: they both are found often spatially related. At the outcrop scale light-coloured and hornblende diatexites look pretty much similar, but a closer look on the hand specimens of hornblende diatexites reveals a mosaic-like pattern of green and milky white grains, which are hornblende and plagioclase, respectively, accompanied by varying amounts of biotite.

Microscopic features

Major constituents: plagioclase 70—40%, sericitized, with pericline and albite twins; green amphibole (hornblende) 30—5%, pleochroism yellow - light green - light bluish green, in some samples as well developed hypidiomorphic crystals, in some others as patchy transformation product from clinopyroxene, in some others as transformation product from an older pale amphibole; biotite 15—5%, most of it is primary with pleochroism yellow - reddish brown, a minor part of it is secondary growing from amphibole and showing pleochroism yellow - light green.

Major to minor constituents: pale amphibole 15—0%, in form of aggregates of long prismatic to fibrous crystals; quartz ~ 5%.

Minor constituents: pyroxene, most of it is certainly clinopyroxene (diopside), but the presence of a low amount of orthopyroxene is also possible.

Accessory constituents: K-feldspar (microcline); zircon; epidote, secondary from amphibole; chlorite, light green, pleochroic, secondary from amphibole and biotite; sericite; opaque phases; apatite; titanite, mostly next to biotite and amphibole in form of very fine-grained aggregates; rutile, as tiny needles in quartz and biotite.

Microfabric: granoblastic to lepidoblastic, depending on the considered domain.

The reactions that took place in relationship with the formation and destruction of amphiboles can be summarized as follows:

The oldest mineral is a clinopyroxene. It has been semi-quantitatively analysed at the Institut fuer Geologie und Mineralogie in Erlangen by means of energy dispersive spectroscopy (EDS) (sample from the area around Dießenstein—Unteranschiessing), obtaining a diopsidic composition. In the course of the observation under the light microscope it was not possible to definitively clarify, whether orthopyroxene is present in the sampled hornblende diatexites. The pyroxene transforms into hornblende, being the transformation either direct or over an intermediate step involving the crystallisation of pale amphibole. The pale amphibole is after Steiner (1968) cummingtonitic (Mg-rich) or actinolite-edenitic after our semi-quantitative analysis (see chapter "Hypersthene-

bearing diatexite" for more information), i.e. with magnesium and low amounts of calcium and sodium (Leake et al. 1997). The amphiboles transform later into biotite at the borders, sometimes giving way to a late chlorite growing.

Further EDS analyses point to the plagioclase having an intermediate composition (andesine-labradorite). The bulk composition of hornblende diatexites can be described as dioritic to quartz dioritic, since the rock is relatively poor in quartz and K-feldspar was found only in very small amounts.

Dark-coloured diatexite

Macroscopic features

This diatexite variety shows a relatively dark colour, since it contains a higher percentage of mafic minerals, mainly biotite, amphibole and clinopyroxene. Under the microscope, these mafic minerals can be found dispersed everywhere in the rock, in contrast to the light-coloured diatexite, in which pyroxene is found only in restitic parts, amphibole is rarely present and biotite represents only a low volume percentage.

The appearance in hand specimens is dominated by the pink K-feldspars and the black, biotite-rich matrix. These colours are found to form bands and augen structures in foliated specimens, but granofelsic varieties can be found as well. Lens-shaped biminerally, K-feldspar-hornblende pockets were observed at the cm to dm scale, bounded by biotite-rich bands. The exposed surface of the rock is typically much lighter than in fresh sections due to meteorization processes. Clinopyroxene and amphibole appear as mm long, rusty brown and green spots, respectively. Zonations, macroperthites and twins are identifiable in feldspars with the unaided eye.

The porphyritic variety of the dark-coloured diatexite differs from the porphyritic variety of the light-coloured diatexite in two aspects. On the one hand, the K-feldspar crystals are much bigger in dark-coloured diatexites, reaching up to 4 cm in the Tittling map, but being even larger in neighbouring areas, e.g. sheets 7145 Schöfweg (Blaha and Siebel, 2006; Blaha, in press) and 7147 Freyung (Ott, 1988). On the other hand, K-feldspar crystals are much more densely packed in dark-coloured diatexites, i.e. they are often in close contact to each other, making the rock locally exceptionally pale.

Microscopic features

Major constituents: plagioclase 75—10%; K-feldspar 65—3%, with typical cross-hatched and carlsbad twinning, often as microperthite, the crystals are sometimes bigger than the crystals in the matrix (porphyritic structure); quartz 35—1%; biotite 20—10%, pleochroic in reddish or greenish brown and yellow colours, rarely brownish green or brownish red to yellow, also as secondary phase with pleochroism in light green colours.

Major to minor constituents: clinopyroxene 10—0%, not always present, corroded by amphibole; green amphibole (hornblende) and pale amphibole 10—1%.

Minor to accessory constituents: apatite, frequently as aggregates together with biotite; titanite, mostly as fine-grained aggregates next to biotite, but also as large, idiomorphic crystals; opaque phases, often next to biotite and amphibole, sometimes surrounded by titanite.

Accessory constituents: zircon; rutile, as tiny needles in quartz and biotite; chlorite, secondary from biotite and amphibole; white mica, as sericite from feldspars and rarely from biotite.

Microfabric: lepidoblastic to granoblastic, in parts porphyritic.

Clinopyroxene is probably diopsidic, since it shows the same appearance as in other rock types (hornblende diatexite and metabasites), in which EDS analyses were performed. The pale, fibrous amphibole might be similar to the one found in hypersthene-bearing diatexites, i.e. actinolite-edenitic after our EDS analyses, or cummingtonitic after Steiner (1968). The bulk composition of the rock can vary largely, but it can be described as mostly granitic to granodioritic. The dioritic varieties represent the transition to the amphibole-pyroxene-plagioclase-biotite gneisses.

Hypersthene-bearing diatexite

Macroscopic features

Its appearance is still more variable as in the other diatexite varieties. Some characteristics of this rock type can be observed uniformly along its whole extension. One of them is the equigranular fabric, i.e. porphyritic fabrics are hardly found. Another one is the existence of up to 3 mm long, leather brown to ochre brown hypersthene crystals and up to 7 mm long hypersthene aggregates. Hypersthene crystals and aggregates are not uniform in size and abundance: To the SE they become smaller and rarer, in such a way that in the area of Reisersberg they might be difficult to identify with the naked eye. The maximum size is reached in the most mafic members (Waldbrunn, northwest of Perlesreut and in some areas of the Lindberg). Since the boundaries between the different diatexite varieties are not sharp but rather progressive, some hypersthene can be found beyond the limits of the mapped hypersthene-bearing diatexite.

The light-coloured hypersthene-bearing diatexite is characterised by the occurrence of hypersthene and the scarcity of amphibole and biotite. The hypersthene grains are smaller and more difficult to identify as in the rest of the hypersthene-bearing diatexites, but the rock itself is much easier to identify instead, due to its characteristic appearance. The rock can be granofelsic (e.g. southeast of Poxreut) or gneissose (e.g.

northeast of Poxreut at the map boundary), its colour is milky and it has relatively few metabasitic fragments.

Garnet-hypersthene-bearing diatexite was found in a small area northeast of Hammermühle. The red garnets reach a diameter of 8 mm. Towards the north (Wittersitt quarry) the garnet crystals become smaller and can be identified only under the microscope.

Microscopic features

Major constituents: plagioclase 70—20%; quartz 5—5%, not necessarily in big amounts, but always present.

Major to minor constituents: K-feldspar 30—0%, with myrmekites at the contact to plagioclase, sometimes lacking; biotite 25—0%, pleochroic in yellow to reddish brown.

Minor constituents: orthopyroxene (hypersthene, Fig. 5.3.1.1-3) 5—1% is a characteristic mineral in this rock, appears in form of long prismatic, hypidiomorphic crystals, shows pleochroism from light pink to light green and displays a corona structure together with its transformation products (see later for further explanations); amphibole 5—1% in different generations; rutile, as tiny needles in quartz, chlorite and biotite.

Accessory constituents: zircon; chlorite; opaque phases (ilmenite), not only next to biotite, but also in cleavage planes of hypersthene and as aggregates together with amphibole in coronas around hypersthene crystals; titanite; apatite; rutile; white mica, secondary.

Microfabric: granoblastic, rarely lepidoblastic.

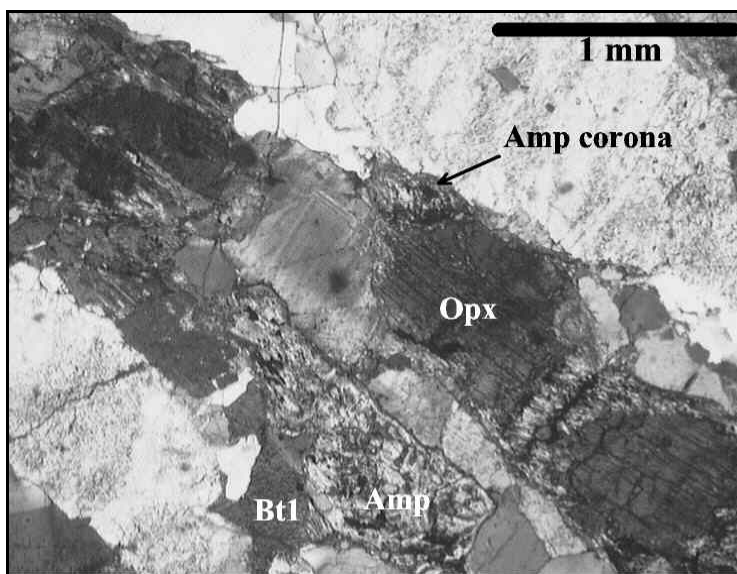


Figure 5.3.1.1-3. Hypersthene-bearing diatexite under the microscope, crossed polarizers. Around the hypersthene grows a fibrous, pale amphibole. The crystal at the bottom of the photomicrograph is completely transformed. Further transformations into hornblende, biotite and chlorite are not visible in this black and white version of the original photograph.

The hypersthene is a relic mineral that grew under granulite facies conditions. During the retrograde path undergone by the rock, the hypersthene became unstable, giving way to the formation of the corona structure that can be found under the microscope. Together with opaque phases, a fibrous, pale amphibole grows from hypersthene (Fig. 5.3.1.1-3). This amphibole was semi-quantitatively analysed by means of EDS in a sample taken 300 m west of Hirtreut and another one taken between Poxreut and Wittersitt. After our results and the nomenclature of amphiboles of Leake et al. (1997), it is probably a clinoamphibole of actinolite-edenitic composition. Alternatively, the amphibole may be cummingtonitic, as proposed by Steiner (1968). The fibrous, pale amphibole becomes greenish towards the borders of the corona, which is the result of a progressive transformation into hornblende that can be observed at different stages depending on the sample. The youngest minerals found at the borders of the coronas are light green biotite and sometimes chlorite.

The transformation processes of pyroxenes into amphiboles proceeds in a similar way in all diatexite varieties. An important and remarkable difference is, however, the resulting fabric. Whereas in hypersthene-bearing diatexites the characteristic transformation pattern gives rise to a corona structure, that in general is made up of orthopyroxene and two amphiboles, the other diatexite varieties show a patchy transformation of clinopyroxene into one or two amphiboles.

Some EDS analyses on plagioclase resulted in a composition from oligoclase to labradorite. The bulk composition of hypersthene-bearing diatexites is extremely variable, but tends to fall into the tonalite and quartz diorite fields of the QAP classification diagram for plutonic rocks (Le Maitre et al. 1989, 2002).

5.3.1.2. Metamorphosed magmatic rocks

Metabasite (undifferentiated)

The metabasites of the Bavarian Forest have been studied by many authors (e.g. Frenzel, 1911; Steiner, 1968; Troll, 1966; Troll and Winter, 1969; Weiss, 1981). These studies are often dealing with very small bodies like the „Essexite“ of Trautmannsdorf (Frenzel, 1911), the metabasite of Anschuessing (Troll and Winter, 1969) or the metabasite of Mauthäusl (Troll, 1966). Sometimes these studies describe larger bodies, like in Galgenreiter (Troll, 1966). Most of these rocks have been usually called amphibolites or biotite amphibolites. In most cases, these names do not match the modern definition of “proper” amphibolites (Coutinho et al., 2002).

The composition of the metabasites on the Tittling map is anything but uniform. Two principal types, the Amp-Px-Pl-Bt gneiss owing to its ubiquitousness and the amphibolite

owing to its popularity as a rock type, were distinguished from the rest of metabasites. They will be described in the corresponding chapter.

The metabasites are hardly found as large bodies, but rather in form of small intercalations of a few decimetres in diameter in the diatexite. Their composition is very variable. Even inside one and the same body, we can see fluctuations in the mineral composition, e.g. between biotite- and amphibole-rich layers in the outcrop Dießenstein. The metabasite bodies are found to be tabular, ellipsoidal or angular. As a general tendency, the macrofabric correlates with the biotite content. Thus, the specimens richer in biotite tend to show a better developed foliation. The rest of metabasites show very often a granofelsic fabric, which is probably inherited from the protolith, i.e. it formed during the freezing of a mafic magma (Steiner, 1986), largely lacking later overprints. Most of the metabasites are fine to medium grained. Some of the factors controlling the variation of the fabric and composition of these rocks could be the metamorphic grade, the protolith, the deformation intensity and the activity of fluids.

The rocks mapped as "metabasite (undifferentiated)" are those, whose composition matches neither the definition of amphibolites (Coutinho et al., 2002), nor the one of Amp-Px-Pl-Bt gneisses. These rocks can be named, depending on the particular case, for example diopside-plagioclase granofels or gneiss, amphibole-biotite gneiss or pyroxene-hornblende metanorite. It is difficult to list the volume per cent limits, in which any mineral appears in the undifferentiated metabasites. Common minerals are pyroxene, amphibole, plagioclase and biotite in different amounts. In the following lines we will describe three outcrops that will help to exemplify the variability of the undifferentiated metabasites.

The outcrop Spitzendorf-Fürsteneck

Macroscopic features

The rock cropping out here can be classified locally as a proper amphibolite, but not the whole body. In some areas, the rock can be better described as hypersthene-hornblende metanorite or hypersthene-hornblende-plagioclase granofels. At first glance, the appearance is very similar to that of the amphibolites. A closer observation leads to the discovery of brown hypersthene grains.

Microscopic features

Major constituents: plagioclase ~ 60%, zoned and with broad albite-twins; hornblende ~ 25 %, pleochroism in yellow - light brownish - green - brownish green, often as skeletal crystals which are diablastic intergrown with hypersthene; hypersthene ~ 15 %, pleochroism light pink to light green.

Accessory constituents: opaque phases; quartz; pale amphibole as transformation product of hypersthene.

Microfabric: granoblastic, nearly unchanged after freezing of the melt (Fig. 5.3.1.2-1)

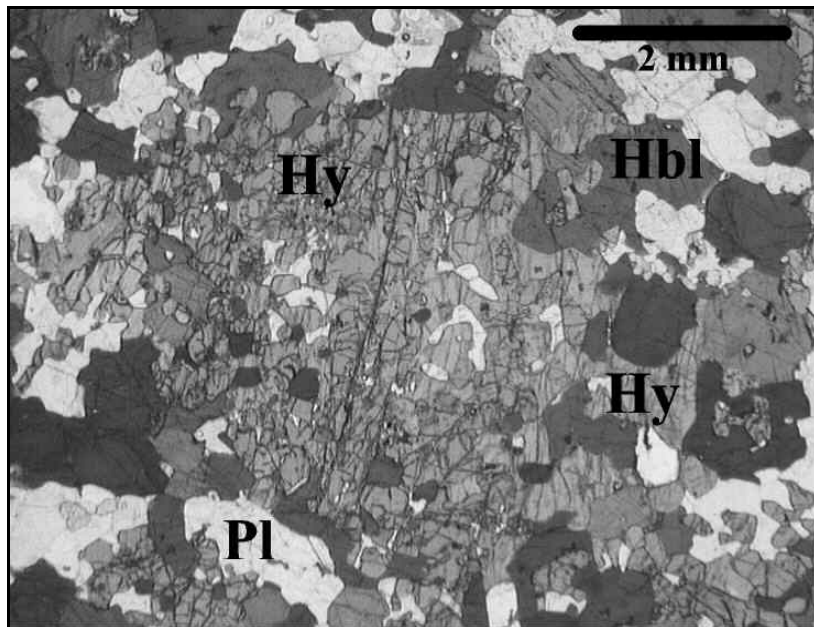


Figure 5.3.1.2-1. Hy-Hbl-Pl granofels under the microscope, parallel polarizers. Two intergrown hypersthene crystals in the centre are surrounded by hornblende and plagioclase.

The outcrop near Dießenstein

Macroscopic features

This metabasite body shows strong variations in its composition. It contains gold-coloured grains of sulphides at the millimetre to centimetre scale. There is a tendency to become richer in biotite to the NE, where the rock fits in the group of the Amp-Px-Pl-Bt gneisses. The south-western sector can be denominated Pl-Px granofels, Amp-Pl-Px granofels or gneiss, depending on the considered point. The following microscopic description is based on one single sample, and is therefore not necessarily representative for the whole metabasite body.

Microscopic features (one sample from the south-western part of the outcrop)

Major constituents: clinopyroxene ~ 70%; plagioclase ~ 20%.

Minor constituents: biotite; amphibole, mainly pale-coloured growing from pyroxene; chlorite, secondary from pyroxene and biotite.

Accessory constituents: quartz; epidote, secondary from amphibole; sulphides (pyrite?); apatite; opaque phases.

Microfabric: granoblastic.

The outcrop at the Ilz River south of Fürsteneck

Macroscopic features

This metabasite body is too small to be mappable (coordinates R 46 07 670 H 53 98 58) and can be referred to as a Amp-Px-Pl gneiss. The rock is dark-coloured, hard and heavy and shows a weak banding.

Microscopic features

Major constituents: plagioclase ~ 50%; clinopyroxene ~ 30%; green amphibole (hornblende) ~ 20%, grows from pyroxene.

Minor constituents: biotite; minerals of the epidote group.

Accessory constituents: titanite; quartz; apatite; opaque phases.

Microfabric: granoblastic to lepidoblastic.

One sample of this outcrop was used for EDS analyses. The clinopyroxene shows a diopsidic composition (with calcium, magnesium and iron) and the plagioclase is An-rich.

Amphibolite

Macroscopic features

It is not easy to find „proper“ amphibolites (after the definition of Coutinho et al., 2002) in the Tittling map. The rock is in general weakly foliated and shows a dark-green colour. The well crystallised hornblende grains are surrounded by a matrix of plagioclase. At their borders, the amphibolite fragments contained in diatexite display a biotite-rich zone. Due to meteorization processes, the amphibolites develop a light-coloured crust on their surface.

Microscopic features

Major constituents: plagioclase 60—50%; green amphibole (hornblende) 40—30%, pleochroism yellow – light green – light bluish green.

Minor to accessory constituents: pale amphibole, as aggregates together with opaque phases and displaying coronas of green biotite; titanite, especially abundant in the area north-northeast of Reisersberg; chlorite, secondary from biotite and amphibole, with pleochroism in green colours.

Accessory constituents: biotite, both primary (brown) and secondary (green) from amphibole; opaque phases, often at the borders of amphibole crystals; epidote, secondary from amphibole; zircon; quartz; apatite; white mica, as secondary sericite from plagioclase.

Microfabric: granoblastic, rarely lepidoblastic.

Chlorite can appear in large amounts, most of all in foliated areas, in which a more intense fluid activity took place. The hornblende occurs often, but not always, in form of well developed, short prismatic crystals. Sometimes it builds aggregates of rod-like to fibrous crystals. This fact, together with the presence of fibrous, pale amphibole, points to at least a part of the amphiboles growing from a former phase (pyroxene?).

Amphibole-pyroxene-plagioclase-biotite gneiss

It is possible to find transitional rocks with hybrid characteristics not only between different diatexite varieties, but also between diatexites and metabasites. In fact, at least from a descriptive point of view, we can consider the Amp-Px-Pl-Bt gneiss as a dark-coloured diatexite with a higher concentration of mafic minerals (more than around 40% of mafic minerals) and less K-feldspar as usual. A pervasive mingling between both end members is ubiquitously visible in the field.

Steiner (1968) called this rock „K-feldspar metablastite from gabbro“ and analyzed the outcrop of Söldtrümmer. From his point of view, it is about a gabbroic rock that suffered during the last metamorphism some transformations leading to the growth of biotite, hornblende and K-feldspar. Troll (1966) interpreted the metabasite of Galgenreiter as a diabase which suffered transformations due to an input of alkalis and phosphorus. The Amp-Px-Pl-Bt gneiss can also be found in form of small intercalations and fragments everywhere in the diatexites.

Macroscopic features

The rock is black and brittle. The macrostructure is mainly gneissose, sometimes schistose or granofelsic. Every now and then the rock is crosscut by quartzofeldspathic veins. There are two important differences between the rock of the outcrops Galgenreiter and Söldtrümmer. On the one hand, the K-feldspar is found in Galgenreiter only as accessory mineral, while in Söldtrümmer it is in parts present even as major constituent. On the other hand, the rock in Söldtrümmer contains ortho- and clinopyroxene, whereas in Galgenreiter only clinopyroxene was found.

Microscopic features

The following list describes the composition of the rock in both principal outcrops (Galgenreiter and Söldtrümmer).

Major constituents: biotite 50—25%, pleochroism reddish brown - yellow; plagioclase 60—30%; clinopyroxene 20—5%, probably diopsidic; green amphibole (hornblende) and pale amphibole 10—5%, the hornblende can be found either in form of well developed crystals or as patches on pyroxene, the pale amphibole appears as aggregates together with opaque phases, often with coronas of green biotite.

Minor to accessory constituents: apatite, as aggregates together with biotite; K-feldspar.

Accessory constituents: quartz; titanite, mostly as aggregates next to biotite; orthopyroxene; opaque phases; rutile; epidote; zircon.

Microfabric: lepidoblastic.

The transformations suffered by pyroxenes and amphiboles can be explained in the same way as in former chapters.

Metaultramafic rock, serpentinite

von Gümbel (1868) found a serpentinite body cropping out in the Tittling map. He located this body in the hamlet of Neureut, but it was not found in the course of the present investigation.

5.3.1.3. Metamorphosed sedimentary rocks

Quartz-biotite-cordierite-feldspar granulite

Macroscopic features

At the road between the hamlets Stadl and Ebersdorf, an uncommon rock crops out. It is a very hard rock, bluish in colour. Red garnets around 1-2 mm in diameter can be distinguished in a matrix of feldspar, biotite and cordierite. The tectonic foliation is poorly developed.

Microscopic features

Major constituents: feldspar ~ 35%, with albite and carlsbad twins; cordierite ~ 20%, as prismatic or rounded crystals with patches or coronas of white mica and chlorite; biotite ~ 20%, pleochroism red - yellow; quartz ~ 15%.

Minor constituents: garnet, pink (almandine), with inclusions of quartz, biotite, opaque phases and not identifiable needles around 0,02 mm in length; white mica, secondary from biotite, feldspar and cordierite, possibly in part grown from former sillimanite; chlorite, pleochroism in light green colours, secondary from biotite and white mica.

Accessory constituents: zircon; opaque phases.

Microfabric: granoblastic (Fig. 5.3.1.3-1).

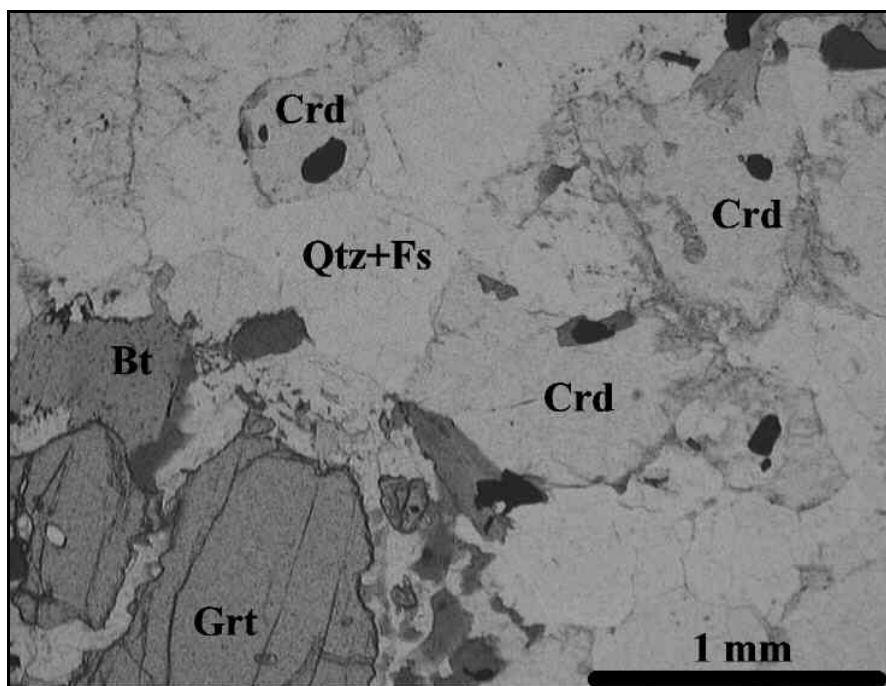


Figure 5.3.1.3-1.
Qtz-Bt-Crd-Fs
granulite under
the microscope,
parallel polarizers.

Calc-silicate granofels

Only a few fragments of this rock type were found in the south-western part of the map. The calc-silicate rocks lied originally as lenses or fine bands intercalated in diatexite. Their protoliths are supposed to be marls, which were intercalated in a psammopelitic series that was subsequently metamorphosed.

Macroscopic features

At the first glance the light grey-blue colour and the splity fracture of the rock are very characteristic. Loose fragments develop a reddish colour at the surface due to the meteorization. At the hand-specimen scale the rock is fine grained and granofelsic. A poorly developed banding is identifiable only under the microscope.

Microscopic features

Major constituents: plagioclase ~ 50%; quartz ~ 20%; diopside ~ 20%.

Accessory constituents: opaque phases; titanite; minerals of the epidote group; apatite.

Microfabric: granoblastic.

5.3.1.4. Magmatic rocks out of the Fürstenstein pluton

Diorite

Macroscopic features

Only some few blocks of this rock were found at the Steinhügel east of Tittling. The rock is dark grey, fine- to medium-grained and undeformed. The black, idiomorphic, long prismatic hornblende crystals are very noticeable.

Microscopic features

Major constituents: plagioclase ~ 60%; hornblende ~ 30%, with pleochroism in brown colours, as idiomorphic rods, sometimes zoned; opaque phases 10—5%.

Minor constituents: chlorite, secondary; epidote, secondary; quartz.

Accessory constituents: apatite; zircon; white mica (sericite).

Microfabric: hypidiomorphic equigranular, poorly developed fluidal structure.

Quartz-biotite diorite

This rock is almost always associated with fine- to medium-grained granite. When both appear together, the quartz diorite is crosscut by the granite, which is an important fact to deduce their relative age. No outcrops were found showing the contact between the diorite and the diatexite. Diorites and quartz-diorites belong to the group 1 of intrusives, as defined in chapter 5.2.3.

Macroscopic features

The rock forms always small bodies, often coinciding with topographic highs due to its resistance against the weathering. It is sometimes tectonically foliated. The foliation is easy to recognize in the varieties containing flattened or stretched aggregates of biotite ± hornblende. These aggregates are very sensible to the weathering, giving way to the occurrence of characteristic holes in the surface of the rock. It is fine or very fine grained and is bluish dark grey.

Microscopic features

Major constituents: plagioclase 60—40%, either fine grained in the matrix or as large crystals or aggregates; biotite 45—20%, with pleochroism green brown to yellow, sometimes in form of aggregates with or without hornblende; quartz 20—5%, small crystals dispersed in the matrix; hornblende 15—0%, pleochroism in bluish green colours.

Accessory constituents: titanite; opaque phases; apatite; epidote; chlorite, secondary from biotite; white mica, as sericite from plagioclase.

Microfabric: hypidiomorphic inequigranular (magmatic structure), lepidoblastic (with tectonic overprint).

The modal composition of this rock cannot be accurately determined due to its very fine grain size, but it plots most probably in the field of the quartz diorites, and in some cases in the granodiorite and tonalite fields of the QAP diagram (Blaha and Siebel, 2006; Galadí-Enríquez and Zulauf, 2006). The hornblende is very often lacking and is therefore not considered to be typical for this rock. The most important mafic mineral, which is always present, is biotite.

Fine- to medium-grained granite

In the diatexites we can find a myriad of small granitic intrusions in form of stocks and dykes (group 2 of intrusives, as defined in chapter 5.2.3). At least in part, these intrusions can be considered to be older than the granites of the Fürstenstein pluton, since the later often crosscut the former, as seen in map view (see Appendix 1). Nevertheless, the contact between both of them was not found in any outcrop. The lower limit for the age of these granite bodies is given by the quartz dioritic rocks, since the later are usually crosscut by the younger granitic intrusions. Most of the described sinistrally sheared granite bodies described in later chapters belongs to this group of rocks.

The fine- to medium-grained granite was mined principally in the Schlossberg quarry north of Tittling, but also in many small quarries all over the study area. Many of them constitute good outcrops, some others are unfortunately inaccessible due to the dense vegetation or to the bad state originated by anthropogenic fillings.

Macroscopic features

As already mentioned, the fine- to medium-grained granite can be found all over the study area, but it tends to be more abundant and build larger bodies to the SSE. The granite is more resistant to the meteorization than the hosting diatexite; that is why we can find much more granite than diatexite fragments resting on cultivated fields. The granite usually builds summits and crests. The fractures found in granite are more even and penetrative than in diatexites: This feature makes the granite easy to identify even at some distance. The contact to the host rock, i.e. diatexite or quartz diorite, is always sharp.

At the hand-specimen scale the appearance of the granite can vary regarding colour and intensity of deformation. It can be bluish grey, orange, yellowish or even reddish if it is strongly altered. It is mostly fine to medium grained. Most of the bodies are

undeformed, but some of them can be slightly or moderately deformed or even ultramylonitic.

To the ESE, the granite contains more and more diatexite fragments and blocks (Fig. 5.3.1.4-1), not only in the areas mapped as such, but also sometimes in other small areas. North of Wilhelmsreut, the diatexite fragments reach several meters in size.



Figure 5.3.1.4-1. Diatexite fragment in fine- to medium-grained granite east of Wilhelmsreut.

The fine- to medium-grained granite intrudes very often into quartz diorite. As a result, the quartz diorite is crosscut and divided in several fragments that are completely enclosed by granite. The size of the quartz diorite fragments typically reaches some dm.

Microscopic features

Major constituents: K-feldspar 65—20%, with typical cross-hatched twinning and often as microperthite, sometimes with myrmekites at the contact to plagioclase; quartz 60—28%, often deformed and recrystallized; plagioclase 25—8%, twinned and sometimes zoned, in general stronger sericitized than K-feldspar; biotite 7—1%, with pleochroism from brown, greenish brown or rarely red to yellow.

Minor to accessory constituents: white mica, as primary, hypidiomorphic crystals and as secondary sericite from feldspars as well; chlorite, secondary from biotite, often intergrown with opaque phases and titanite.

Accessory constituents: titanite; zircon, with several growth phases; opaque phases.

Microfabric: granoblastic, mylonitic.

In the QAP diagram, the modal composition of the fine- to medium-grained granites plots in the field of the granites, in some cases in the field of the K-feldspar granites. Biotite is always present, but not necessarily as a major constituent. Primary white mica

was found in about a half of the sampled specimens. Therefore, the rock can be called biotite granite or two-mica granite, depending on the case.

5.3.1.5. Magmatic rocks of the Fürstenstein pluton

The Fürstenstein Pluton is partly located on the Tittling map and continues on the topographic sheets 7245 Schöllnach, 7145 Schöfweg, 7146 Grafenau, 7346 Hutthurm and 7345 Vilshofen. Most of the results of Troll (1964, 1967) were included in the present work with minor modifications. One of the most important changes presented here concerns not that much the map extension of the different facies but rather their nomenclature, which has been modified to match the modern recommendations of the IUGS (Le Maitre et al., 1989, 2002; see Fig. 5.3.1.5-1). The rocks referred to as "quartz dioritic" by Troll are in fact granodiorites and tonalites.

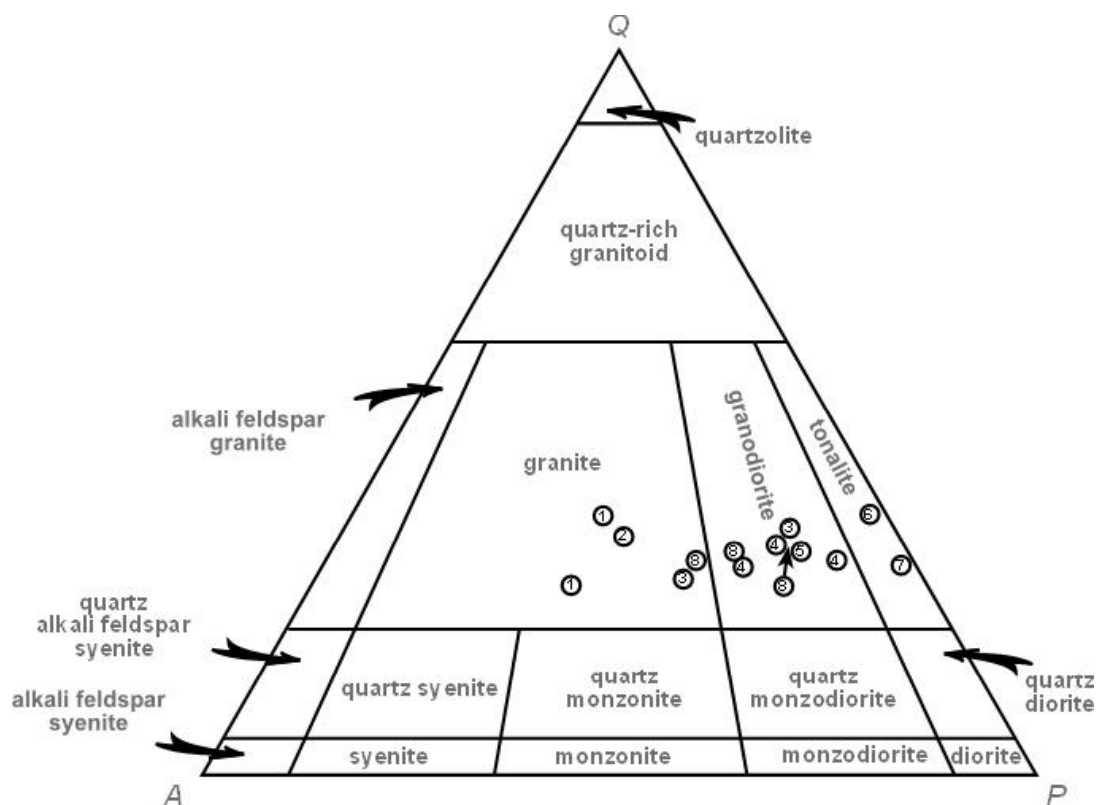


Figure 5.3.1.5-1. QAP diagram showing the composition of the facies of the Fürstenstein Pluton contained on the Tittling map, using modal data reported by Troll (1964), 1 = medium- to coarse-grained porphyritic granite (Saldenburg granite), 2 = fine- to medium-grained two-mica granite, 3 = medium-grained granite to granodiorite (Tittling granite), 4 = medium-grained granodiorite, 5 = fine-grained granodiorite with titanite spots, 6 = fine-grained biotite tonalite, 7 = medium-grained biotite tonalite, 8 = fine-grained granite to granodiorite.

Fine-grained granite to granodiorite

This magmatic facies groups the ones referred to as „very fine-grained biotite granite“ and „old fine-grained granite dykes“ by Troll (1964), since no important petrographic criteria to treat them as separate facies were found. These rocks are found in form of large blocks enclosed in younger facies.

Macroscopic features

Good outcrops showing this rock type were not found. The rock suffered an intensive weathering together with the neighbouring two-mica granite, which is responsible for its reddish colour. Representative for the whole unit are the relatively dark colour and the fine grain size.

Microscopic features

Major constituents: plagioclase 46—38%, twinned, zoned, sericitized; quartz 27—26%; K-feldspar, mostly microcline 22—12%; biotite 13—10%, with pleochroism in brown colours.

Minor to accessory constituents: muscovite.

Accessory constituents: titanite; opaque phases; apatite; epidote; allanite; zircon; monazite; white mica, as secondary sericite from feldspars.

Microfabric: hypidiomorphic equigranular.

Medium-grained biotite tonalite („Unterpolling granodiorite“ after Troll, 1964)

Macroscopic features

A single block of this rock was found at the south-western corner of the map. It is surrounded by two-mica granite. Plagioclase, biotite and hornblende crystals confer this medium-grained rock the appearance of a chessboard, in which some rare titanite crystals are distinguishable with the naked eye.

Microscopic features

Major constituents: plagioclase 54—48%, An-content 43—20% (andesine-oligoclase); biotite 24—19%, with pleochroism in red or greenish brown colours; quartz 22—19%.

Minor constituents: hornblende, pleochroism yellow - light green - light bluish green; titanite, primary or secondary from biotite.

Minor to accessory constituents: K-feldspar; apatite.

Accessory constituents: opaque phases (ilmenite, magnetite and pyrite); zircon; epidote; allanite; apatite; white mica, as secondary sericite from feldspars; chlorite, secondary from biotite.

Microfabric: hypidiomorphic equigranular.

Fine-grained biotite tonalite („Fürstenstein quartz-mica diorite" after Troll, 1964)

Macroscopic features

Some small blocks of this rock can be found in the neighbourhood of Fürstenstein, surrounded by porphyritic granite or two-mica granite. The rock is fine-grained and dark coloured. Some larger plagioclase and biotite crystals or aggregates are found in a biotite-rich matrix. Some biotite aggregates are interpreted by (Troll, 1964) as rests of not completely assimilated gneiss fragments.

Microscopic features

Major constituents: plagioclase 49—45%, An-content 50—15% (andesine-oligoclase), zoned, twinned, sericitized; quartz 28—23%; biotite 25—19%, with pleochroism in brown or green colours.

Minor constituents: K-feldspar.

Minor to accessory constituents: opaque phases (ilmenite); apatite.

Accessory constituents: titanite; allanite; zircon; white mica, as secondary sericite from feldspars; chlorite, secondary from biotite; epidote.

Microfabric: hypidiomorphic inequigranular.

Fine-grained granodiorite with titanite spots („Englburgit" after Troll, 1964)

This is one of the best-known rocks of the Fürstenstein Pluton. The Tittling granite intruded at approximately the same location of the granodiorite with titanite spots, which caused the fragmentation of the latter (Fig. 5.3.1.5-2). After Troll (1964) the titanite spots grew after the cooling of the granodiorite as a result of the heat provided by the Tittling granite. At their contact, both facies partially mingled with each other producing an intermediate facies, which is called medium-grained granodiorite in the present work. The fine-grained granodiorite with titanite spots was dated at 334-331 Ma (Chen et al., 2002, Chen and Siebel, 2004). At the time of research this rock was being mined in the quarry Kusser at the Kühberg (1.3 km east-southeast of Fürstenstein). Some more information about this rock and the enigmatic origin of its fabric can be found in Frenzel (1911), Osann (1923), Fischer (1926), Drescher (1930), and Troll (1964).

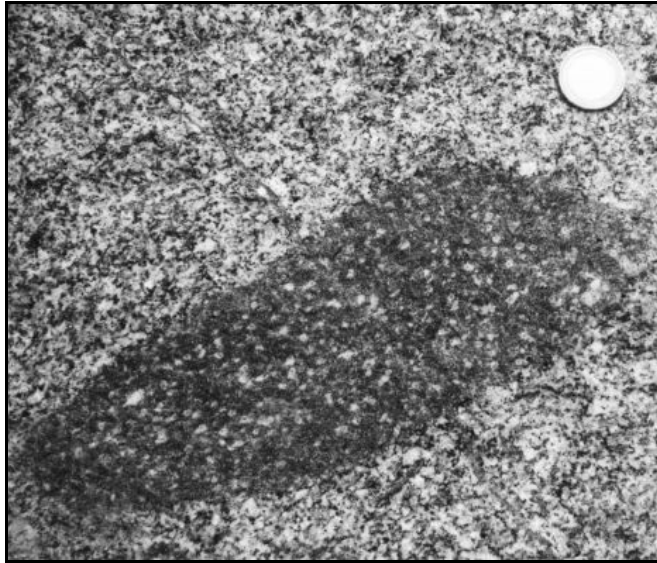


Figure 5.3.1.5-2. Fragment of fine-grained granodiorite with titanite spots enclosed in Tittling granite.

Macroscopic features

At the outcrop scale the rock can be found in form of blocks and fragments enclosed in Tittling granite or in medium-grained granodiorite. The fragments are from some cm to a few meters in size. The spots are aggregates of quartz and feldspar with a diameter of 3 to 5 mm containing a titanite crystal in the centre (Fig. 5.3.1.5-3). Some spots reach even 1 cm in diameter. They use to be elongated. The spots are contained in a dark-coloured matrix which is rich in biotite and contains some hornblende. Some of the spots contain allanite instead of titanite.

Microscopic features

Major constituents: plagioclase 48—37%, An-content 49—15% (andesine-oligoclase), twinned, zoned; quartz 25—21%; biotite 28—18%, pleochroism in green colours; alkali feldspar (orthoclase and microcline) 15—2%, heterogeneously distributed, with myrmekites.

Minor constituents: hornblende, pleochroism yellow - light green - light bluish green, mostly transformed into biotite, sometimes in form of aggregates; titanite, as idiomorphic crystals up to 3 mm in length.

Accessory constituents: opaque phases; apatite; epidote; zircon; allanite, zoned, twinned, sometimes completely transformed into epidote; chlorite, secondary from biotite; white mica, as secondary sericite from feldspars.

Microfabric: hypidiomorphic inequigranular (titanite crystals are larger than the matrix grains), poikilitic (we can find often large microcline crystals containing other crystals), usually banded by magmatic flow or tectonically foliated.

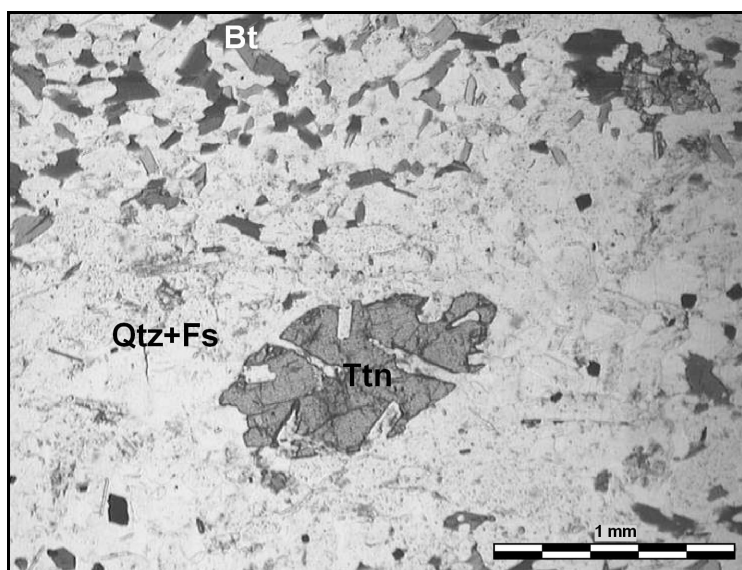


Figure 5.3.1.5-3. This photomicrograph shows a titanite spot, i.e. a titanite crystal surrounded by a biotite-free halo.

Medium-grained granite to granodiorite („Tittling granite" after Troll, 1964)

The medium-grained granite to granodiorite or “Tittling granite” crops out at the easternmost part of the Fürstenstein Pluton. The sharp contact between it and the younger porphyritic granite is shown in some outcrops (Fig. 5.3.1.5-6). On the other hand, the contact to the two-mica granite is poorly known. As documented in the neighbouring topographic sheet 7346 Hutthurm, a block of Tittling granite is enclosed in two-mica granite, which determines the relative age of these facies (Troll, 1964). The contact to the granodiorite with titanite spots is described in the former and next chapters. The contact between the Tittling granite and the hosting diatexite was found only in the quarry Krenn south of Matzersdorf. The Tittling granite was dated at 323-321 Ma (Chen et al., 2002; Chen and Siebel, 2004). Together with the “quartz dioritic” rocks (sensu Troll, 1964), the Tittling granite is the most appreciated material by the rock industry in the Fürstenstein Massif. It is mined in the quarries „Hötzendorfer Granitwerke Merkschlager” west of Hötzendorf, „Kusser am Höhenberg” north of Rothau and „Krenn” south of Matzersdorf.

Macroscopic features

The bluish grey colour is typical for the Tittling granite. It is equigranular and medium grained. In parts (Steinhügel) some bigger microcline crystals can be identified. Brown titanite and allanite grains are dispersed in the rock. Primary muscovite is lacking.

Microscopic features

Major constituents: plagioclase 50—33%, An-content 38—18% (andesine-oligoclase), twinned, zoned; quartz 34—21%; K-feldspar (mostly microcline) 32—10%, myrmekites; biotite 15—8%, pleochroism in brownish green colours.

Accessory constituents: titanite; opaque phases; apatite; epidote, often as corona around allanite crystals; allanite, brownish, zoned and twinned, sometimes isotropic; zircon; xenotime; white mica, secondary from biotite and feldspars; chlorite, greenish, secondary from biotite.

Microfabric: hypidiomorphic equigranular.

Medium-grained granodiorite

The medium-grained granodiorite represents the zone in which the Tittling granite and the granodiorite with titanite spots mingle (Fig. 5.3.1.5-4). After Troll (1964), the Tittling granite is chemically more active than the younger facies, that is the reason why it reacted with the older granodiorites at the contact zone giving rise to an intermediary product: the medium-grained granodiorite ("*Tittlinger Mischdiorit*" after Troll, 1964).

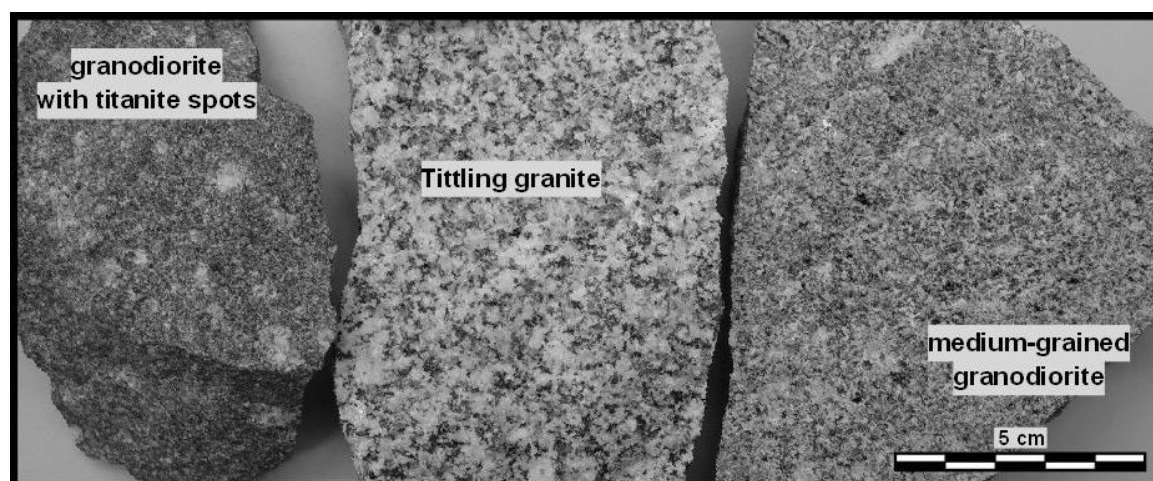


Figure 5.3.1.5-4. This photo shows the appearance of the granodiorite with titanite spots, the Tittling granite and the mixing product of both of them: the medium-grained granodiorite.

The variety containing gneiss fragments can be best observed in a small, old quarry south of Enlburg. Unfortunately, the observations in the quarry are hindered by the vegetation, but some gneiss rests and fragments can still be found.

Macroscopic features

The medium-grained granodiorite fills the voids and veins between the blocks of granodiorite with titanite spots. The granodiorite with titanite spots is usually surrounded by a more or less thick band of medium-grained granodiorite. The boundary between the medium-grained granodiorite and the Tittling granite is anything but sharp. At the scale of hand specimens, the rock is intermediary between both Tittling granite

and granodiorite with titanite spots in terms of colour and fabric (Fig. 5.3.1.5-4). Some titanite spots are also present.

Microscopic features

Major constituents: plagioclase 50—41%, An-content 35—20% (andesine-oligoclase), twinned, zoned; quartz 31—23%; biotite 19—12%, pleochroism in brownish green colours; K-feldspar (orthoclase and microcline) 18—5%, with some impressive myrmekites at the contact with plagioclase.

Minor to accessory constituents: hornblende; titanite, as well developed crystals or as secondary aggregates growing from biotite, sometimes transformed into ilmenite.

Accessory constituents: opaque phases (ilmenite and magnetite); apatite, often associated with biotite; epidote; allanite, zoned, twinned; zircon; white mica, as secondary sericite from feldspars.

Microfabric: hypidiomorphic equigranular.

Fine- to medium-grained two-mica granite

This rock is rarely mined due to the fact that weathering reaches relatively deep levels of it. The outcrops in which we can find it are normally quarries of other rocks where the two-mica granite either appears in form of dykes (Fig. 5.3.1.5-5) or encloses a mined stoped block (e.g. in the Unterpolling quarry in the SW corner of the map). The contacts to the older facies of the Fürstenstein pluton are sharp. However, this is not the case of the contact to the younger facies, i.e. the porphyritic granite (see below), that probably intruded while the two-mica granite was not completely frozen. The two-mica granite contains often blocks of "quartz dioritic" rocks (sensu Troll, 1964), gneiss, diatexite and fine-grained granite to granodiorite.

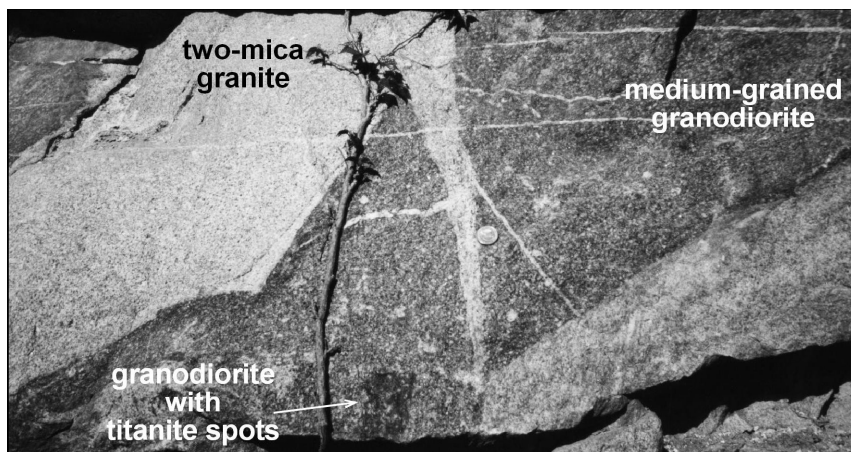


Figure 5.3.1.5-5.
Medium-grained granodiorite containing fragments of granodiorite with titanite spots and crosscut by two-mica granite. The photograph was taken at the Bahnhof quarry south of Fürstenstein.

Macroscopic features

This rock is predominantly fine to medium grained and pale yellow. Biotite and muscovite crystals shine under the sunlight. Troll (1964) distinguished a fine-grained, a medium-grained and a porphyritic variety. In the present work all of them were integrated in the same facies. A possible origin for the big K-feldspar crystals of the porphyritic variety is the potassium supply by the younger Saldenburg granite.

Microscopic features

Major constituents: plagioclase 43—33%, An-content 19—7% (oligoclase-albite), zoned, twinned; quartz 32—24%; K-feldspar (microcline and orthoclase) 28—21%, with myrmekites; biotite 11—8%, pleochroism in brown and reddish brown.

Minor constituents: muscovite, partially secondary from biotite.

Accessory constituents: apatite; opaque phases (mostly magnetite); zircon; monazite; xenotime; sillimanite.

Microfabric: hypidiomorphic equigranular, sometimes porphyritic.

Medium- to coarse-grained porphyritic granite („Saldenburg granite" after Troll, 1964)

This rock type can be found in areas which are most densely covered with forest and in the highest areas of the map. It is the youngest facies of the Fürstenstein Pluton and therefore crosscuts any older facies. U-Pb dating on zircon of this intrusion yielded 318-312 Ma (Chen et al., 2002; Chen and Siebel, 2004). The contact to the Tittling Granite is very well exposed in two quarries (Krenn south of Matzersdorf and Kusser at the Höhenberg, see Fig. 5.3.1.5-6), in which the contact surface between both facies dips around 30—35° to the E or SE.

The porphyritic granite contains stopped fragments of "quartz dioritic" rocks (sensu Troll, 1964), gneiss and diatexite, the former being found only in the marginal zone. The variety containing fragments of two-mica granite was mapped at the north-western corner of the map. These fragments are supposed to belong to the group of fine- to medium-grained granites that can be found almost everywhere scattered in the region out of the limits of the plutons.

Macroscopic features

The porphyritic granite is mostly found in a strongly weathered state. The thickness of the weathered rock may reach several meters above the fresh rock. Taking a closer look to the rock, large, pink K-feldspar crystals are prominent. The latter can be up to 5 cm long and are surrounded by a matrix of white plagioclase, bluish transparent quartz and biotite. The carlsbad twins of the K-feldspars can be seen with the naked eye.

There are all possible intermediary varieties between the dominant porphyritic one and a medium-grained, muscovite-bearing facies, the latter being mostly found as a marginal facies.



Figure 5.3.1.5-6. In the Kusser am Höhenberg quarry the contact between the Saldenburg granite (bottom left) and the Tittling granite (top right) can be seen. The Tittling granite contains fragments of „quartz dioritic“ rocks and diatexite (left of hammer). Line of sight pointing to the north.

Microscopic features

Major constituents: K-feldspar (microcline) 41—31%, with carlsbad twins, often with myrmekites; plagioclase 30—28%, An-content 23—9% (oligoclase-albite), zoned, twinned, saussuritized und sericitized; quartz 34—24%; biotite 6—5%, with pleochroism in brown colours, greenish in weathered specimens.

Accessory constituents: muscovite, primary only in marginal areas; opaque phases; apatite; zircon, with several growth phases; xenotime; monazite; allanite; epidote, secondary; white mica, as secondary sericite from feldspars.

Microfabric: porphyritic, rarely hypidiomorphic equigranular (mostly at the margins).

5.3.1.6. Dykes

Aplite

Macroscopic features

Together with the pegmatites, with which they are often spatially associated, and with the post-granitic dykes, these rocks are the youngest ones on the Tittling map. Aplites can be found either in the Fürstenstein pluton or in the neighbouring country rock. Normally, they are not mappable due to their small thickness, with the exception of a few examples. Aplite dykes are generally straight and crosscut the country rock with very sharp contacts.

Microscopic features

Major constituents: quartz; K-feldspar; plagioclase; muscovite.

Minor constituents: biotite.

Accessory constituents: chlorite, secondary from mica.

Microfabric: hypidiomorphic equigranular.

Pegmatite

Though the pegmatites of the study area are in general considered to be younger than the facies found as stocks, most of them intruded actually prior to the Saldenburg granite, and some of them even prior to the two-mica granite (Troll, 1964).

Macroscopic features

As well as the aplites, they can be found in the Fürstenstein pluton and in the neighbouring country rocks as well. The contacts with the host are sharp. Characteristic for this rock is its coarse grain size.

Microscopic features

A thin section was prepared from a specimen taken in the outcrop east-southeast of Rettenbach at the Ilz River. The typical major constituents quartz, K-feldspar plagioclase and biotite were found. Regarding the microfabric, the rock is panallotriomorphic to hypidiomorphic and equigranular.

Tennyson (1960, 1981) distinguished two major pegmatite generations. One of them is associated with the Tittling granite and contains apatite, fluorite, garnet (spessartine), epidote and zeolithes. The other one, associated with the two-mica granite, contains tourmaline, beryl and mica. Other minerals that can be found in the pegmatites of the area are molybdenite, zircon, monazite, titanite, allanite and chlorite.

Post-granitic dyke, intermediary to acid („Porphyrite“)

These rocks have been studied by many authors since the beginning of the century. That is the reason why they have received several different names (“porphyrite” amongst others). They are found everywhere in the whole Bavarian Forest. In the Tittling map they can be observed in the Fürstenstein pluton as well as in its host rock.

The post-granitic dykes represent the final records of Variscan magmatic activity. Dacitic varieties have been dated at 302 ± 7 (Rb-Sr on apatite-biotite, Christinas et al., 1991b) and 299.0 ± 2.3 Ma (U-Pb on zircon, Propach et al., 2007).

These rocks show an aphanitic fabric, which means that, after the recommendations of the IUGS (Le Maitre et al., 1989, 2002), they should be named after the nomenclature of volcanic rocks. Due to their small grain size and strong late-magmatic alteration, it is difficult, if not impossible, to calculate their modal composition under the microscope. Consequently, we will not use the QAP, but the TAS diagram for their classification (Le Maitre et al., 1989, 2002), i.e. the rocks are classified attending to their chemical composition (sodium, potassium and silicon content). The differentiation between types of dykes is based on chemical analyses of Propach et al. (2007) or on the appearance of the rocks in hand specimens, since some macroscopic characteristics (colour, mineralogy of phenocrysts) correlate roughly with the bulk chemical composition. In some cases, the strong post-magmatic alteration or the untypical macroscopic features shown by the rocks made their classification as rhyolite, dacite or andesite impossible.

General macroscopic features

The post-granitic dykes strike WNW—ESE to NNW—SSE and are subvertical. They are always undeformed. Their thickness ranges between a few dm and 6 m on the Tittling map. Some thicker dykes can be found on sheet Waldkirchen, east of Tittling. The contacts to the host rock are always sharp and sometimes a marginal facies free of phenocrysts develops. The primary magmatic minerals are often transformed due to a late- to post-magmatic fluid activity. Fragments of the host rock are rarely found enclosed in the sub-volcanic dykes. Since these rocks are harder than the country rock, they can be usually found in topographic highs. All post-granitic dykes are aphanitic. They are mostly porphyritic, in some rare cases aphyric.

Post-granitic dyke, andesitic

Macroscopic features

Hornblende phenocrysts are embedded inside a dark green coloured matrix. The arrangement of the phenocrysts is often controlled by magmatic flow. Plagioclase phenocrysts, when present, appear as light coloured spots (Fig. 5.3.1.6-1).

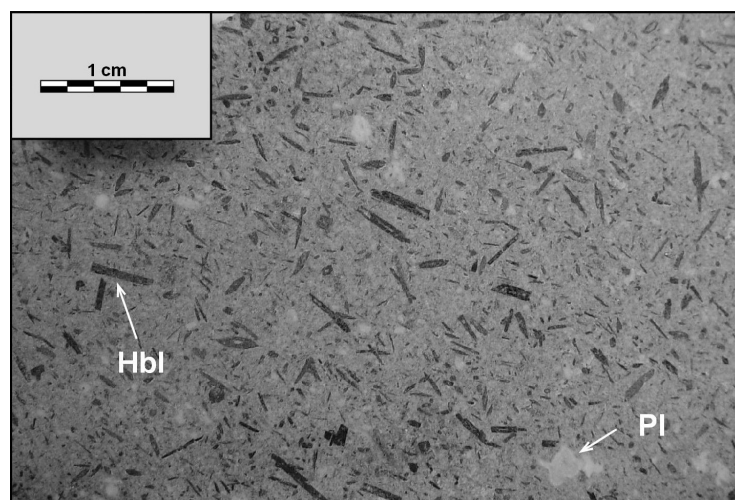


Figure 5.3.1.6-1. Hand specimen of andesite, taken north of Schneidermühl. Phenocrysts of hornblende and plagioclase are embedded in a very fine-grained matrix.

Microscopic features

Major constituents: plagioclase is an important constituent of the matrix, sometimes also found as phenocrysts, zoned, strongly sericitized and saussuritized; hornblende, as phenocrysts, with pleochroism in brown or greenish colours, twinned, completely or partially transformed into biotite or chlorite; quartz.

Minor to accessory constituents: biotite, primary or secondary from hornblende; chlorite, secondary from hornblende or biotite; K-feldspar; epidote, secondary; opaque phases; titanite, secondary; calcite, secondary; apatite; zircon; white mica, secondary.

Microfabric: porphyritic, pilotaxitic, rarely aphyric.

After Propach et al. (2007), in the most mafic end members phenocrysts of olivine and orthopyroxene can be found.

Post-granitic dyke, dacitic

Macroscopic features

In comparison to the andesitic ones, the dacitic varieties have a lighter, greyish green colour. The most typical phenocrysts are of plagioclase, whereas phenocrysts of mafic minerals recede.

Microscopic features

Major constituents: plagioclase, in the matrix and as phenocrysts, zoned, sericitized and saussuritized; chlorite, secondary from biotite or hornblende; K-feldspar; quartz.

Minor to accessory constituents: biotite; hornblende, not always present, transformed into biotite and chlorite; titanite, secondary, often intergrown with chlorite; epidote,

secondary; opaque phases; calcite, secondary; apatite; zircon; white mica, secondary; allanite.

Microfabric: porphyritic, pilotaxitic, rarely aphyric.

Post-granitic dyke, rhyolitic

Macroscopic features

The lack of phenocrysts is the most typical feature of the rhyolites of the Tittling map. The two existing outcrops show different characteristics. The rock south of Fürsteneck shows a grey-bluish colour and intrudes into both the diatexite and the pre-existing dacite (Propach, pers. comm.). The rock found north of Auggenthal was called alkali aplite by Troll (1964) and is accompanied by some veins of micro- to cryptocrystalline quartz. The rock is here light brownish yellow. Both dykes show a rhyolitic composition (Propach et al., 2007).

Microscopic features

The analysis of one thin section obtained from the outcrop south of Fürsteneck provided less information due to its extremely fine grain size and strong late-magmatic alteration. The identified minerals are: quartz; feldspar, strongly altered, presumably plagioclase and K-feldspar; sericite; epidote; chlorite; apatite; opaque phases.

Microfabric: aphyric, trachytic.

5.3.1.7. Mineralisations

Quartz lode

The most popular quartz lode in the Bavarian Forest is represented by the natural rock wall of Weißenstein, at the Bayerischer Pfahl shear zone. The quartz mineralisation occurred not only at this shear zone, but everywhere in the Bavarian Forest, which led to the formation of more or less thick veins and dykes of quartz, often associated with brittle faults or fault zones. The quartz lode was dated at 247 ± 21 Ma (Rb-Sr whole-rock age, Horn et al., 1986). Its origin is supposed to be related with a high fluid activity in post-Variscan times.

In the Tittling map, quartz veins are normally found in form of small blocks and fragments distributed along straight lines across the cultivated fields and forests. Very rarely, the veins or dykes can be observed in good outcrops: This is the case of one outcrop at the Ilz River southeast of Allmunzen, in which a thickness of 1.60 m and an orientation N120E/80SW were measured.

5.3.1.8. Fault rocks

Mylonite

The protolith of most of the mylonites is a fine- to medium-grained granite. This influences the colour of the mylonite, which is mostly light yellow or milky white. Two different groups of mylonites can be distinguished attending to their kinematics and the orientation of their foliation planes:

- NNW—SSE, dextral.
- WSW—ENE to WNW—ESE, sinistral.

The second group is constituted by the so-called sinistrally sheared granites and will be studied in detail in the next chapters.

5.3.2. Deformation phases in migmatites of the study area: D₁ and D₂

In the study area the following deformation phases were inferred from field and microscopic observations:

5.3.2.1. D₁

This is the oldest deformation phase recognizable in the diatexites south of the Bayerischer Pfahl shear zone and is identifiable only under the microscope. It is recorded by very high temperature microfabrics (Fig. 5.3.2.2-1a). Amoeboid contacts between quartz and feldspar are the result of diffusion creep indicating high-grade conditions (Gower and Simpson, 1992). Quartz grains show subgrains with boundaries parallel to both prism and basal planes, defining a so-called chessboard pattern. The latter is thought to be diagnostic for prism $\langle c \rangle$ slip, which is active at temperatures higher than 600°C in the β -quartz stability field (Mainprice et al., 1986; Masberg et al., 1992; Kruhl, 1996). This deformation phase produced a weak foliation defined by the shape-preferred orientation of minerals (mainly quartz, feldspar and biotite). D₁ is found as a relict in areas with no or a very weak D₂ overprint. The D₁ kinematics is unknown.

5.3.2.2. D₂

D₂ is characterized by a variously, usually poorly developed, steep NW—SE striking tectonic foliation resulting from dextral simple shear (Fig. 5.3.3-1b). It can be found in diatexites and igneous bodies of the groups 1 and 2 (see chapter 5.2.3) and reaches its maximum intensity in the vicinity of major shear zones like the Bayerischer Pfahl shear zone. Photomicrographs of diatexites affected by D₂ are presented in Fig. 5.3.2.2-1b-d. Quartz forms aggregates of new grains, in which relict old grains are abundant. New grains appear to be nearly strain free, whereas old grains present chessboard patterns. The chessboard pattern might be to some extent inherited from D₁, since subgrain boundaries may be very stable microstructures in quartz (Kruhl, 1996), but this possibility is difficult to evaluate. Grain boundaries are strongly lobate or serrated due to grain boundary migration recrystallization, often with crystallographically controlled squared contours that constitute the so-called reticular or mosaic-like pattern (Gapais and Barbarin, 1986).

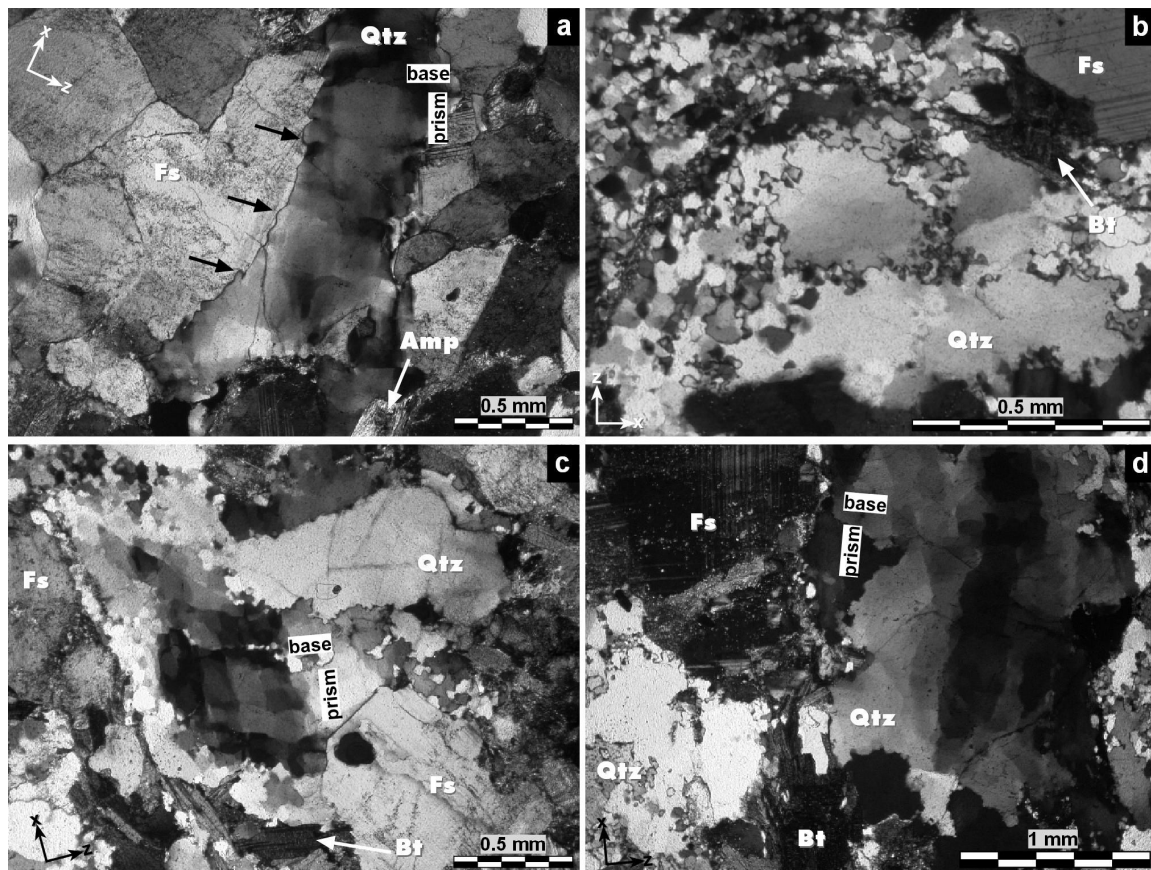


Figure 5.3.2.2-1. Photomicrographs of diatexites affected by D_1 and D_2 , XZ -sections (for D_2), crossed polarizers. a) D_1 in sample Tit 141 (see Appendix 2 for location). D_1 is recorded by amoeboid contacts between quartz and feldspar (indicated by black arrows) and chessboard patterns in quartz (orientation of prism and basal planes indicated by labels). b) D_2 in sample Grf 599 (see Appendix 2 and Fig.5.3.3.1-1 for location), mosaic-like pattern in quartz. c) and d) D_2 in sample Frg 92 (see Appendix 2 for location), chessboard pattern in relictic old quartz grains (orientation of prism and basal planes indicated by labels) surrounded by recrystallized quartz.

Feldspar started to recrystallize at grain boundaries and cracks. Although the temperature seems to have been high enough, the amount of strain was probably not sufficient to produce pervasive feldspar recrystallization, as proposed by Tullis and Yund (1977). Feldspar shows also patchy undulose extinction and microcracks and is in a few cases boudinaged or broken. Plagioclase is mechanically twinned and sometimes zoned. Lobate grain boundaries between feldspar and quartz are rare. Most of the mobile contacts between different phases were probably formed during D_1 and destroyed during D_2 , since they represent a rather unstable microfabric element (Gower and Simpson, 1992). Amphibole, often containing a diopsidic core in dark-coloured diatexites, displays patchy undulatory extinction and subgrains. Biotite plates define the tectonic foliation. Biotite grains are always accompanied by a large number of tiny ($\sim 10 \mu\text{m}$) titanite and/or ilmenite crystals at the borders or at mineral cleavage planes,

suggesting crystallisation of Ti-rich biotite at high temperature and Ti exsolution during temperature decrease. Dextral shear sense is deduced from σ -type mantled porphyroclasts (Fig. 5.3.3-1b).

5.3.3. D_3 and sinistrally sheared granites: the D_3 shear-zone system

D_3 is characterized by a well-developed, ENE—WSW to WNW—ESE trending mylonitic foliation and a sub-horizontal stretching lineation resulting from sinistral simple shear. It occurs in a localized fashion, mostly in granitic dykes and stocks of the group 2 (see chapter 5.2.3), rarely in the country rock (diatexites and dioritic to granodioritic rocks). A rare case of diatexite affected by D_3 is found in the Saunstein quarry (see below). Apart from the orientation of the foliation, the sinistral sense of shear of this phase, as clearly indicated by σ -type mantled porphyroclasts and other kinematic criteria, also differs from the kinematics of D_2 . It is important to note that dextral displacement along NW—SE trending planes (D_2) and sinistral displacement along ENE—WSW to ESE—WNW trending planes (D_3) cannot result from one single deformation phase (see chapter 5.2.5). Therefore we consider sinistral shearing as a result of a post- D_2 event, which will be referred to as D_3 and is the central object of the present work. The shear zones formed during D_3 constitute the D_3 shear-zone system.

The fabric associated to D_3 in granites will be described in the following chapters. When observed in diatexites, D_3 is accompanied by a considerable grain size reduction (compare Fig. 5.3.3-1a and b).

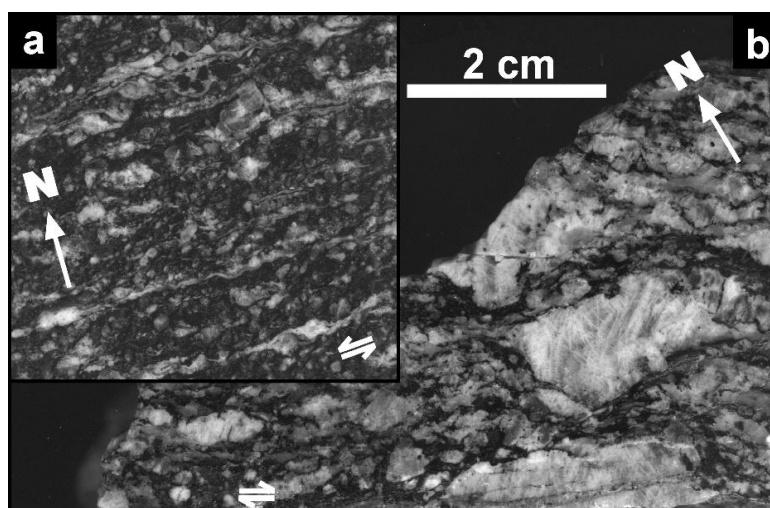


Figure 5.3.3-1. Hand specimens of dark-coloured diatexite, XZ-sections, same scale for both specimens. a) Sample Grf 598 (see Appendix 2 and Fig. 5.3.3.1-1 for location) is affected by D_3 ; sinistral shear sense is deduced from σ -type mantled porphyroclasts. b) Sample Frg 92 (see Appendix 2 for location) is affected by D_2 ; dextral shear sense is deduced from σ -type mantled porphyroclasts.

Quartz forms lenticular aggregates and ribbons of equant new grains of strain-free appearance (Figure 5.3.3-2). Grain boundaries are mostly regular and straight, but some show also serrated or sutured geometries. A well-developed LPO is present, but no shape-preferred orientation. Chessboard patterns are lacking. Attending to these microfabric features, a combination of subgrain rotation and grain boundary migration are proposed as active recrystallization mechanisms. Feldspars are partially recrystallized forming core-and-mantle structures, σ -type mantled porphyroclasts and fine-grained polycrystalline ribbons. Local brittle behaviour is also documented by some broken crystals. There is no evidence for diffusion creep at quartz/feldspar boundaries. Amphibole can be found as porphyroclast, often with a diopsidic core, and also forming part of the foliation planes together with biotite. New, small biotite grains grow in strain shadows and parallel to the foliation. The amount of titanite and ilmenite accompanying biotite is even higher than described for D_2 .

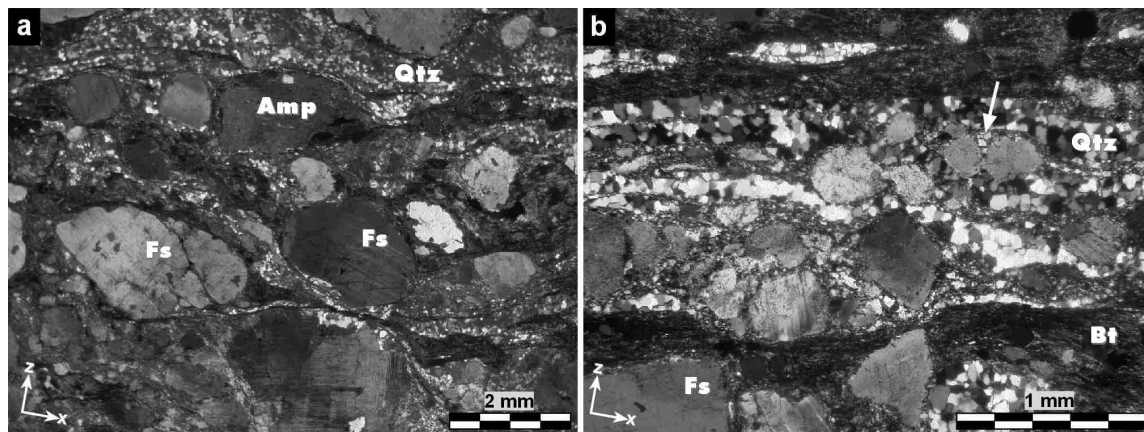


Figure 5.3.3-2. Microfabrics of dark-coloured diatexite affected by D_3 , sample Grf 598 (see Appendix 2 and Fig. 5.3.3.1-1 for location). a) Quartz is completely recrystallized and feldspar is partly recrystallized. Amphiboles are found as porphyroclasts. b) Local brittle behaviour is shown by some feldspars (see white arrow pointing to a fracture).

EBSD analyses were performed on two diatexite samples in order to compare the quartz textures resulting from D_2 and D_3 . Quartz in diatexites shows a weak lattice preferred orientation, probably due to the low quartz content, which leads to a stronger interaction between quartz and other minerals and prevents quartz grains from recrystallizing without obstacles. Whereas the lattice preferred orientation patterns of sample Frg 92, which is representative for D_2 , are hardly interpretable (Fig. 5.3.3-3), the ones of sample Grf 598, representative for D_3 , are fairly well developed and show a similar appearance as in sheared granites (see following chapters), i.e. a concentration of c -axes around the Y -axis of the finite strain ellipsoid. We will discuss the meaning of

the quartz textures after presenting the patterns obtained from sinistrally sheared granites.

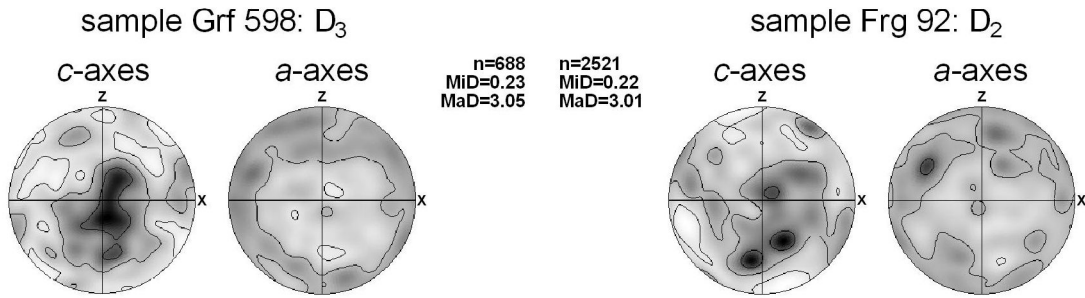


Figure 5.3.3-3. Quartz *a*- and *c*-axes patterns of diatexites affected by D_2 and D_3 (see Appendix 2 for sample location).

5.3.3.1. Geographic distribution of sinistrally sheared granites

The sites which have been sampled and studied (Fig. 5.3.3.1-1) constitute the best exposed examples, but they are not the only existing sheared granites in the region. More information about the sampling sites can be found in Appendix 2.

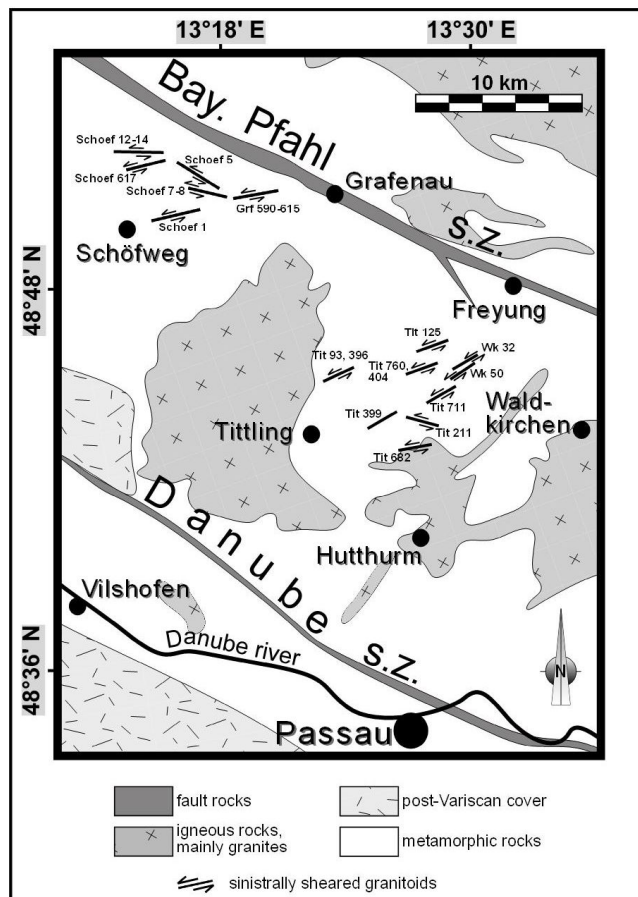


Figure 5.3.3.1-1. Geographic distribution of sampling sites of sinistrally sheared granites (see also Appendix 2).

5.3.3.2. The case study of the Saunstein granite dyke

Introduction and previous data

The Saunstein granite dyke is the best exposed one amongst all of the sinistrally sheared granites. It is about 50-100 m thick, but only the northern half of it is well exposed in the quarry of the same name, which is located 4 km west of the town Grafenau (Fig. 5.3.3.2-1, 5.3.3.2-2). This outcrop has raised the interest of many workers. A good documentation of it can be found in Artmann (2001). Christinas et al. (1991a) dated cooling age $T < 500 \pm 50^\circ\text{C}$ at 316 ± 6 Ma (Rb-Sr on muscovite) and $T < 300 \pm 50^\circ\text{C}$ at 310 ± 7 Ma (Rb-Sr on biotite). Siebel et al. (2005) provided an age of 326 ± 9 Ma (U-Pb on zircon). Dr. W. Dörr (University of Giessen, Germany) carried out a U-Pb dating of monazite separated from this dyke and obtained an emplacement age of 324.4 ± 0.8 Ma (Galadí-Enríquez et al., 2005).

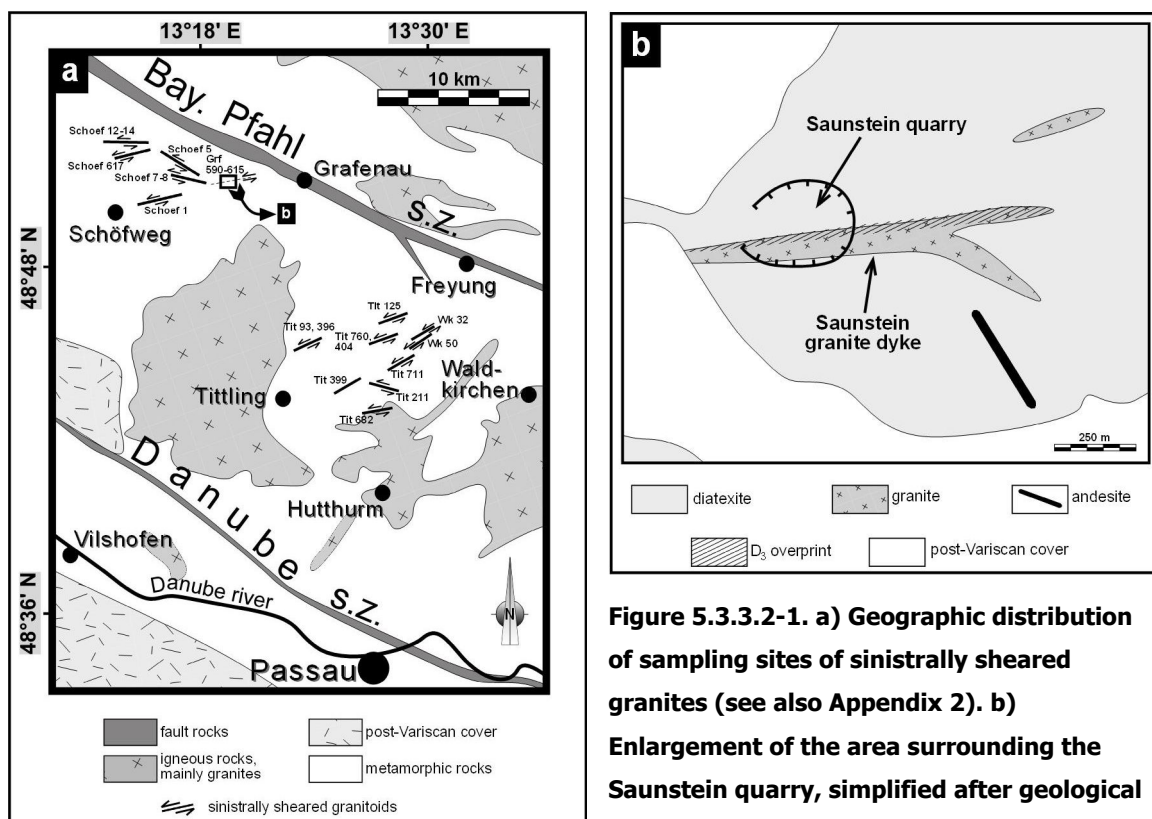


Figure 5.3.3.2-1. a) Geographic distribution of sampling sites of sinistrally sheared granites (see also Appendix 2). b) Enlargement of the area surrounding the Saunstein quarry, simplified after geological maps at scale 1:25000 of Blaha and Siebel (2006) and Teipel et al. (in press).

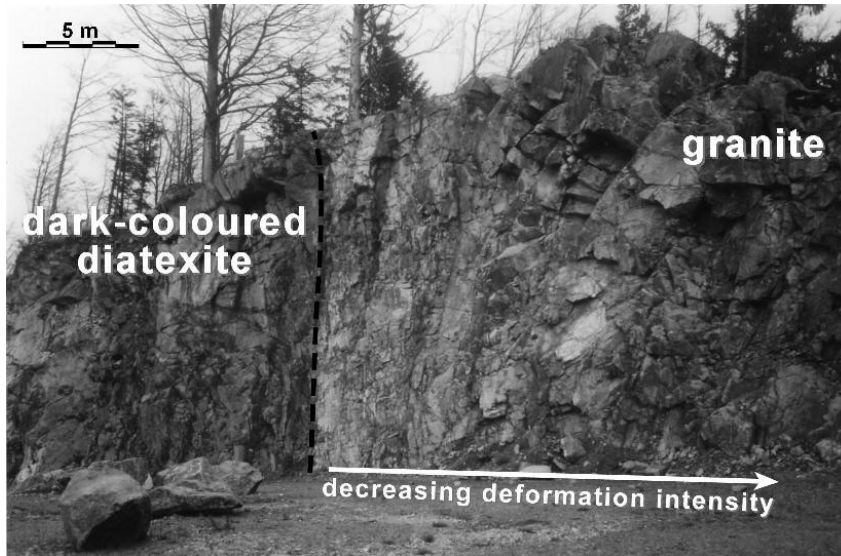


Figure 5.3.3.2-2.
Overview of the upper level of the Saunstein quarry, in which an impressive sinistrally sheared dyke crops out.

Outcrop description and sampling mode

The Saunstein dyke belongs to the group 2 of intrusive bodies (see classification in chapter 5.2.3). D_3 transformed the granite into proto-, meso- or ultramytonite, depending on the considered location across the dyke. The deformation is heterogeneous: The increase in strain intensity towards the contact to the hosting diatexite is reflected by the reduction in grain size, the increasing intensity of the foliation and the lineation and the decreasing angle between C and S planes (Fig. 5.3.3.2-3, 5.3.3.2-4).

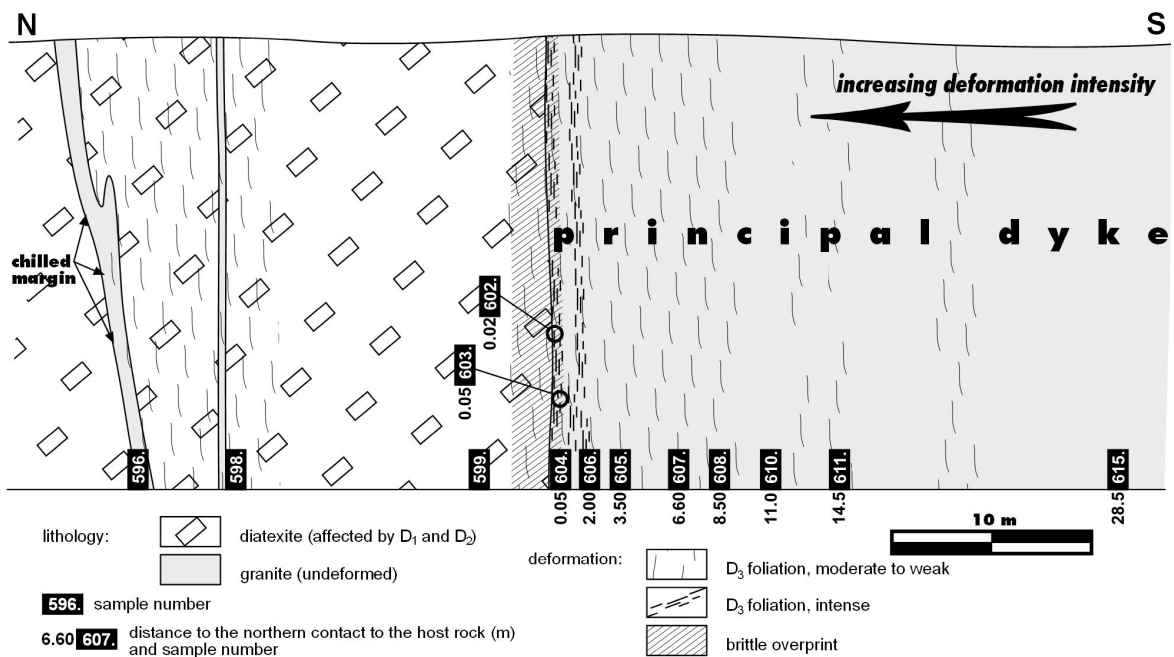


Figure 5.3.3.2-3. Geological section along the eastern wall of the Saunstein quarry. The location of the samples used in this study is indicated (see also Appendix 2).

Looking at the different samples in detail, we can realize that the decrease of the deformation intensity does not take place in a strictly progressive fashion, but rather changes back and forth on a meter scale with a generally decreasing trend on the outcrop scale. The most fine-grained specimens are found in two bands, one of them between 0 and 2 cm away from the contact to the host rock and the second one between 0.5 and 2 m away from the contact (schematically represented in Fig. 5.3.3.2-3).

The dyke was sampled at intervals from a few centimetres in highly deformed parts up to two meters in less deformed parts. *XZ* and *YZ*-sections at hand specimen and thin section scale were prepared for structural analysis.

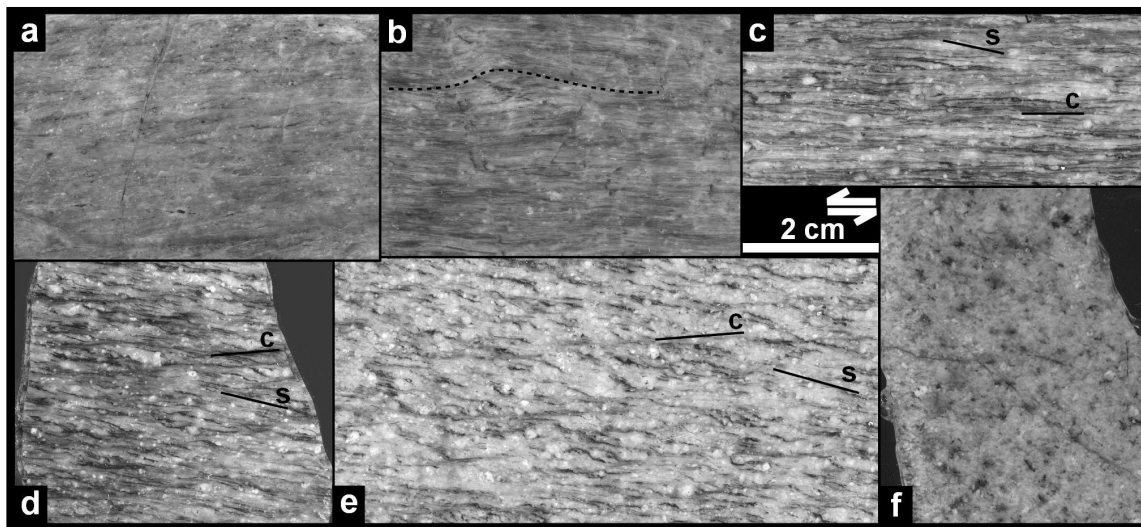


Figure 5.3.3.2-4. Hand specimens of granite in order of increasing distance to the host rock and decreasing intensity of D_3 , *XZ*-sections. a) Sample Grf 603, *S* and *C* planes are parallel to each other. b) Sample Grf 606, *S* and *C* planes are parallel to each other, an asymmetric fold is observable (indicated by dashed line). c) Sample Grf 605, *S* and *C* planes at an angle of 12° , d) Sample Grf 607, *S* and *C* planes at an angle of 18° . e) Sample Grf 608, *S* and *C* planes at an angle of 20° . f) Sample Grf 615, nearly undeformed.

A detailed geologic profile along the eastern wall of the quarry allows the recognition of two more dykes north of the principal one (Fig. 5.3.3.2-3). One of them is 0.15 m thick and presents a very strong D_3 mylonitic foliation. The other one is 0.5 m thick and is affected by D_3 at the southern part and practically undeformed at the northern contact, where a not strongly marked but visible chilled margin is present (Fig. 5.3.3.2-5). The internal characteristics of these two smaller dykes are similar to those of the principal dyke and will therefore not be the focus of further studies. Nevertheless, there is an important fact accompanying these dykes: the host rock at their southern part is

affected by D_3 . The host rock at the contact to the main dyke is also likely to have been affected by D_3 (Fig. 5.3.3.2-3), but structures related to D_3 cannot be unequivocally identified due to a late cataclastic overprint.

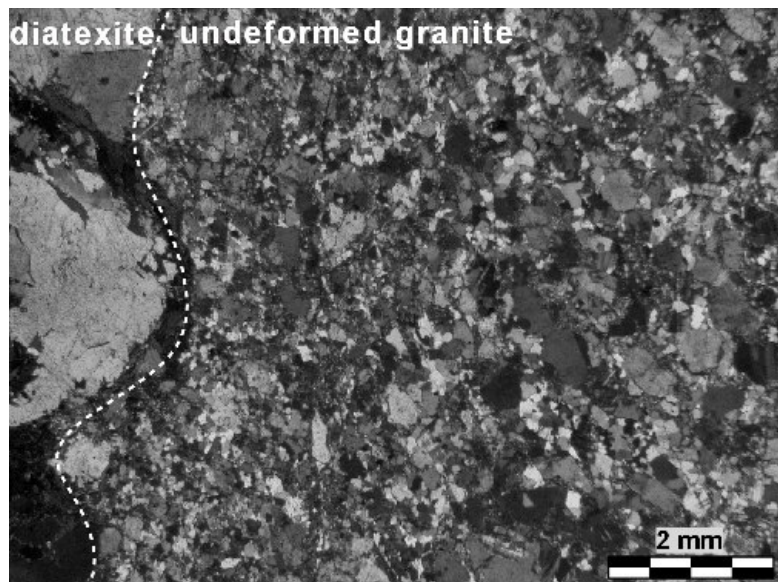


Figure 5.3.3.2-5.
Photomicrograph of sample Grf 596 (see Fig. 5.3.3.2-3 for location), showing a slight decrease in grain size in undeformed granite towards the contact to the host rock. Crossed polarizers.

Microfabrics

Under the microscope the most fine-grained samples are constituted by a very fine-grained quartz-feldspar matrix in which some cleavage domains of newly formed white mica are recognizable (Fig. 5.3.3.2-6a and c). Quartz and feldspar grains are completely mixed, with the exception of some rare bands of pure quartz. Some porphyroclasts of feldspar and igneous white mica are present. The configuration of asymmetric folds is compatible with a sinistral sense of shear (Fig. 5.3.3.2-4b).

In moderately to weakly strained areas (Fig. 5.3.3.2-6b, d, e, f and g) a fine banding of quartz and feldspar layers becomes visible, whereas white mica is more homogeneously distributed and does not form separate domains. Quartz and feldspar domains are easily identified due to the difference in grain size.

Quartz occurs in form of equigranular polycrystalline ribbons. Grain boundaries are straight and regular as well as irregular and serrated. A lattice preferred orientation is present. Most of the grains appear to be strain-free; a few of them show prism-parallel subgrain boundaries or deformation bands. The quartz microfabrics present no differences compared to those described for D_3 in the host rock (chapter 5.3.3). Grain boundary migration and subgrain rotation seem to have been likewise the dominant recrystallization mechanisms.

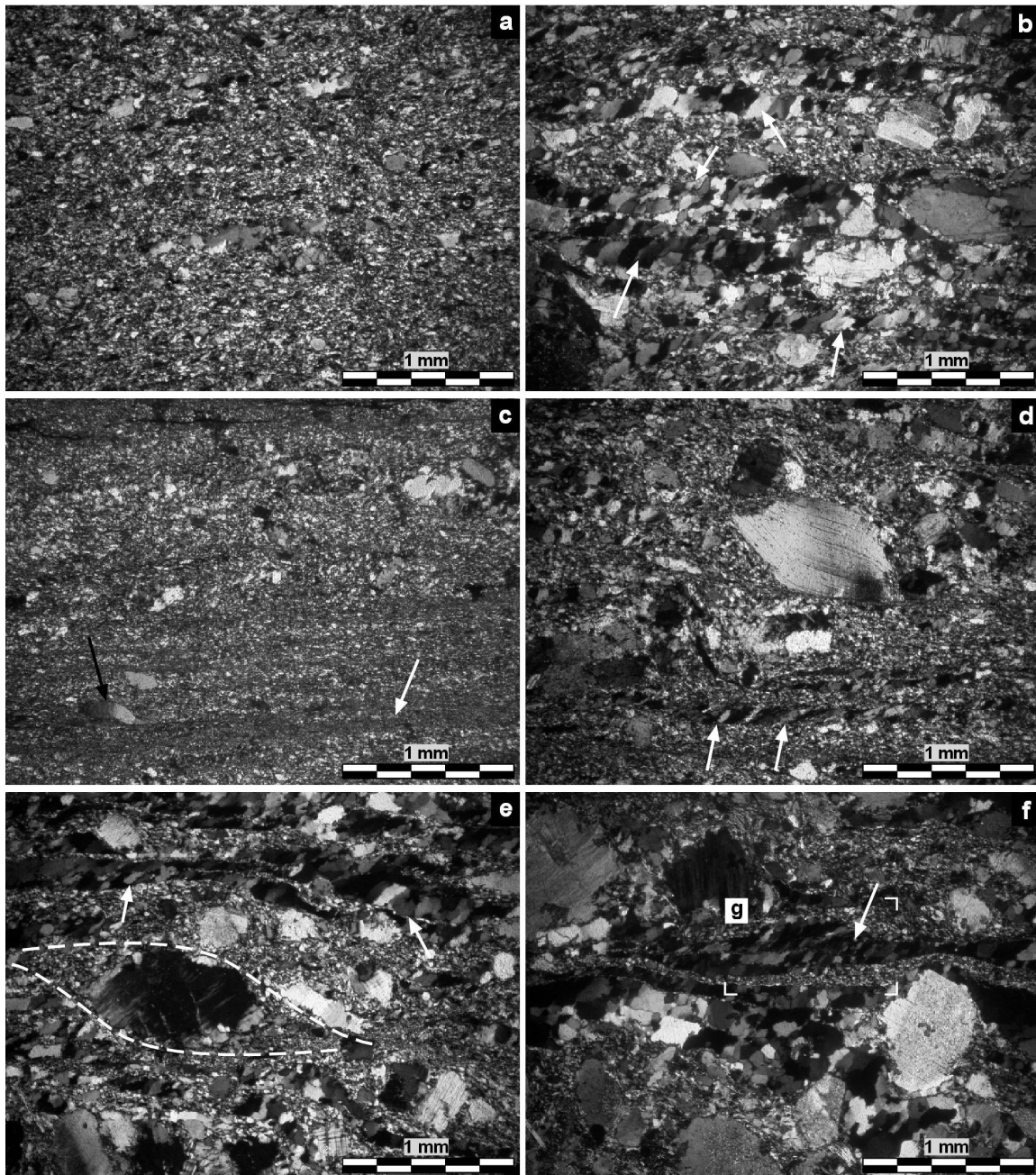


Figure 5.3.3.2-6. Photomicrographs of granite samples affected by D_3 and D_4 in order of increasing distance to the host rock, XZ -sections, crossed polarizers. a) Sample Grf 602 and b) Grf 603. D_4 quartz SPO (white arrows) indicates dextral shear sense. c) Sample Grf 606. The white arrow indicates a cleavage domain constituted by synkinematic white mica. The black arrow points to a white mica crystal showing kinking. d) Sample Grf 605. Mica-fish and angular relationship between S and C planes point to a sinistral sense of shear (D_3), whereas quartz SPO results from dextral simple shear (white arrows, D_4). The fine-grained matrix consists of recrystallized feldspar. e) Sample Grf 607. White mica and feldspar porphyroclasts embedded in a matrix of alternating fine-grained feldspar layers and polycrystalline quartz ribbons. Note the sinistral sigmoidal fabric (white dashed lines, D_3) and dextral quartz SPO (white arrows, D_4). f) Sample Grf 608. The arrow indicates a band along which D_4 concentrates, resulting in dextral quartz SPO. Below this band there are some other quartz layers which are practically not affected by D_4 and show no SPO.

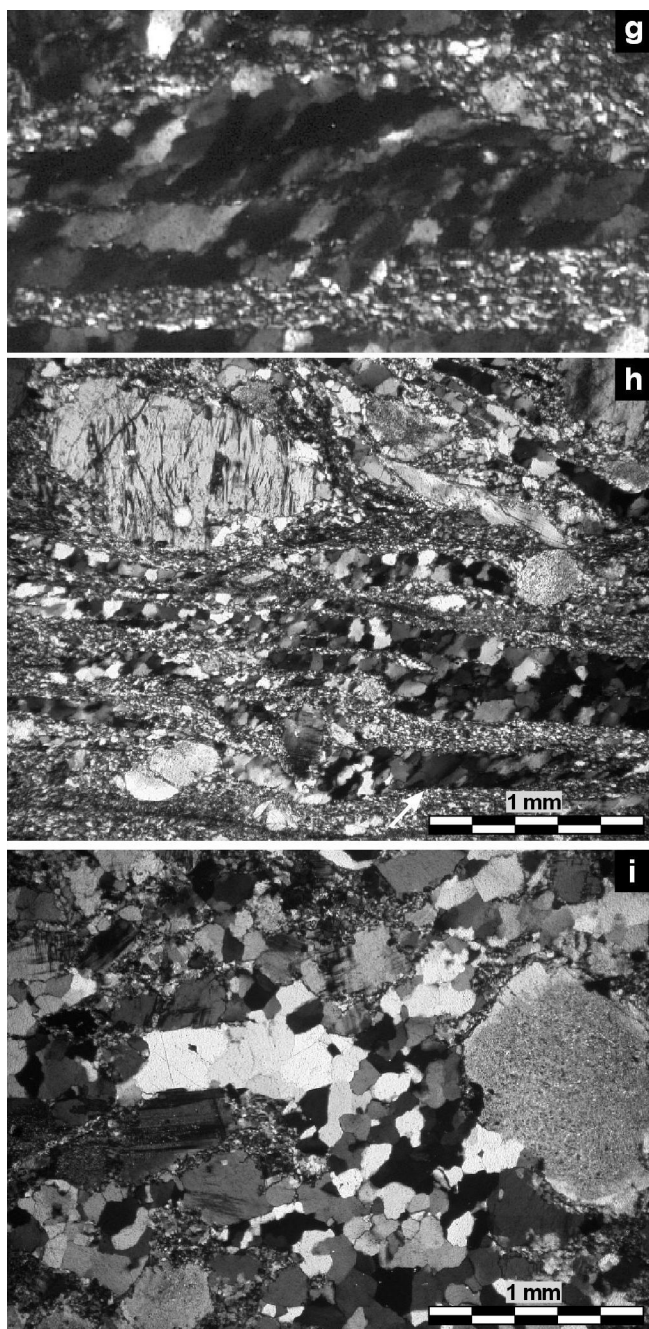


Figure 5.3.3.2-6 (continued). g) Enlargement of the former picture showing a quartz aggregate affected by D_4 . Grain boundaries are intensely sutured and fuzzy. **h) Sample Grf 611.** Quartz ribbons are slightly affected by D_4 , more intensively at the bottom right corner of the photograph (white arrow). **i) Sample Grf 615.** Nearly undeformed granite.

Feldspar is partially recrystallized, forming fine-grained layers and σ -type mantled porphyroclasts, rarely δ -type ones. K-feldspar was replaced by albite at the margins (see below under feldspar composition), which points to a fluid-assisted deformation. Some porphyroclasts are transected by synthetic or antithetic microfaults. Primary igneous feldspars were partially transformed into white mica during grain-size reduction. Fine-grained white mica and biotite grow principally in strain shadows or at foliation surfaces. Igneous white mica typically forms mica-fishes (Fig. 5.3.3.2-6d) and shows kinking (Fig. 5.3.3.2-6c). Igneous biotite is found as inclusions in feldspar or dispersed in the matrix. Sinistral shear sense is reported by σ -type mantled

porphyroclasts, mica fishes, monomineralic sigmoidal bands and the angular relationship between *S* and *C* planes.

Considering all microfabric aspects of D_3 both in this granite dyke and in the adjacent diatexite, some constraints on the deformation temperature can be made: (i) the transition from dominant subgrain rotation recrystallization to dominant grain boundary migration recrystallization is proposed by Stipp et al. (2002) to be approximately between 480 and 530°C ($P \sim 2.5\text{-}3$ kbar); (ii) after Kruhl (1996) the absence of chessboard patterns in quartz does not allow any major constraint in our case, since the pressure during the deformation is unknown, but even assuming middle crust pressures, the maximum deformation temperature is above or around the wet granite solidus, which represents in fact no constraint at all; (iii) the lack of mobile boundaries between different phases indicates that diffusion creep did not play an important role in deformation; thus, the deformation must have taken place well under solidus conditions; (iv) feldspar deforms by dislocation creep at temperatures above 450-500°C, the presence of fluids can have contradictory effects (microcracking and recrystallization favoured by a chemical free energy term (Tullis, 1983)), which are difficult to evaluate in terms of deformation temperature. In summary, assuming a deformation temperature around 500-550°C seems to be reasonable.

A further deformation phase D_4 can be inferred from the study of the Saunstein granite dyke. While σ -type porphyroclast systems and other monoclinic fabric elements (e.g. mica fishes, sigmoidal bands and ribbons) indicate clearly a sinistral sense of shear during D_3 in the granite dyke, the oblique foliation defined by the SPO in many quartz aggregates displays a dextral shear sense (Fig. 5.3.3.2-6b, d, e, f and g). This phenomenon could be explained in three ways:

1. The quartz SPO is older than the whole D_3 fabric. A pre- D_3 dextral event produced the quartz shape-preferred orientation, which remains preserved as a relict.
2. The quartz SPO formed during D_3 , i.e. there is some unknown mechanism producing "anomalous" SPO of quartz grains under certain conditions.
3. The quartz SPO is younger than the whole D_3 fabric. A new deformation phase (D_4) of very low intensity overprinted not the whole fabric, but only the SPO of quartz.

The first possibility is improbable: D_3 produced a very strong monoclinic symmetry and a considerable amount of strain; feldspar recrystallized and formed well-developed σ -type mantled porphyroclasts and fine-grained bands; thus, the strain magnitude and the temperature were too high for the preservation of pre-existing structures in quartz during D_3 and resetting of its fabric is to be expected.

The second hypothesis lacks experimental support. Such a phenomenon has not been described up to now. Moreover, the fact that many but not all quartz ribbons present

this “anomalous” SPO (Fig. 5.3.3.2-6f) does not support a common development of SPO and D_3 fabric, but rather a separate formation of the D_3 fabric and the quartz SPO.

Thus, the third option seems the most probable. As a microstructural evidence for the quartz SPO being post- D_3 , we observed that even in polycrystalline quartz ribbons, whose sigmoidal form displays clearly a sinistral shear sense, the SPO shows a dextral shear sense (Fig. 5.3.3.2-6d and e): The opposite temporal succession would have destroyed the dextral SPO of quartz. Quartz grain boundaries are not squared and sharp as observed in D_3 (Fig. 5.3.3.2-6), but intensively sutured and fuzzy (Fig. 5.3.3.2-6g) indicating grain boundary migration recrystallization and a deformation temperature slightly lower to that during D_3 . The amount of quartz aggregates displaying dextral SPO increases towards the contact to the host rock, suggesting that during D_4 this contact continued to play an important role.

Feldspar composition

Microprobe analyses of feldspars of sample Grf 605 were performed in order to detect changes in the composition between old, magmatic porphyroclast cores and their dynamically recrystallized mantles. The results can be found in Appendix 4.

The analyses revealed a strong contrast between the composition of porphyroclast cores and mantles. The average composition of feldspars is $An_0 Ab_5 Or_{95}$ in cores and $An_9 Ab_{90} Or_1$ in mantles. K-feldspar was replaced by albite at the margins, which points to a fluid-assisted deformation.

The variations in composition are also reflected in the backscattered electrons image of Fig. 5.3.3.2-7. The minerals shown are, in order of increasing brightness, quartz, albite, K-feldspar and phengite.

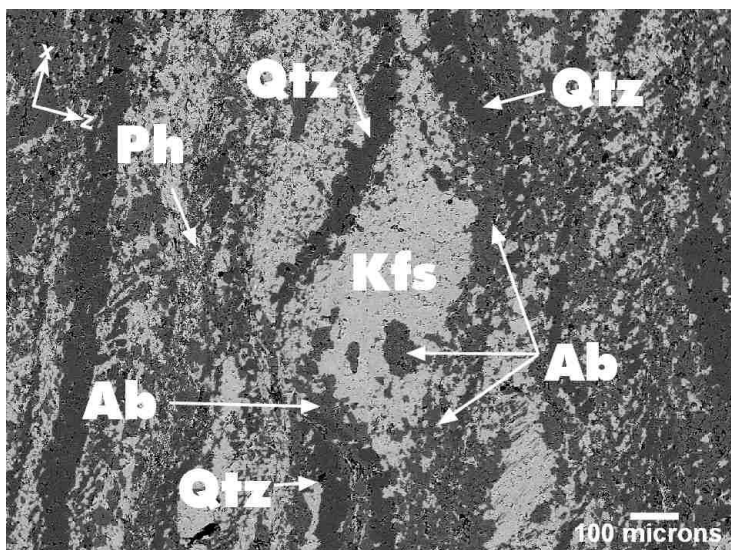


Figure 5.3.3.2-7. Backscattered electrons image showing the chemical variations between feldspar core and mantle in sample Grf 605.

Quartz texture

Six granite samples located at different distances to the contact, and therefore variously deformed, were selected and scanned by means of EBSD on XZ -sections. The obtained a and c -axes patterns are represented in Fig. 5.3.3.2-8. In the diagrams shown, a clustering of quartz c -axes parallel to the intermediate Y -axis of the finite strain ellipsoid is obvious. a -axes patterns develop three maxima: two secondary maxima on the XZ -plane and one principal maximum on the XZ -plane parallel to C . The latter is deviated with respect to the X -axis of the finite strain ellipsoid indicating sinistral sense of shear (Simpson and Schmid, 1983; Schmid and Casey, 1986). This LPO pattern is diagnostic for prism $\langle a \rangle$ slip in quartz, which is known to be dominant at middle to high temperature conditions, that is, at upper greenschist to amphibolite facies conditions (Bouchez and Pêcher, 1981; Schmid and Casey, 1986; Jessell and Lister, 1990; Law, 1990). After Stipp et al. (2002) this pattern is diagnostic for grain boundary migration recrystallization and its transition towards subgrain rotation recrystallization, which corroborates the results of our microfabric analyses (see above) and is in good agreement with a deformation temperature of 500-550°C. The homogeneity of the quartz texture across the dyke indicates no temperature gradient and, therefore, the dyke and the host were thermally equilibrated during the deformation.

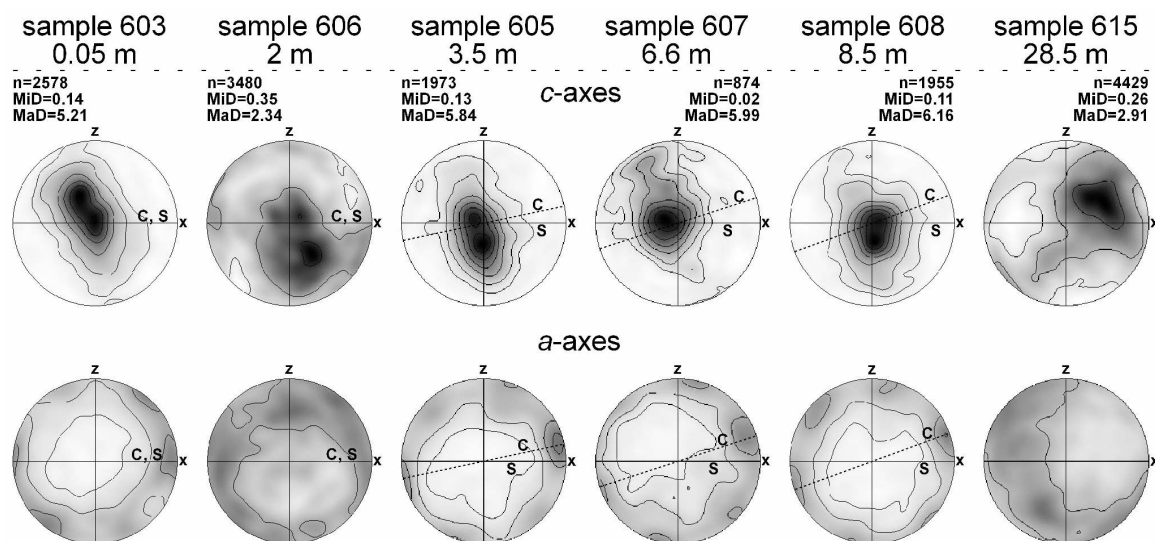


Figure 5.3.3.2-8. Quartz a - and c -axes patterns obtained by means of EBSD in a profile across the deformed dyke indicating sinistral simple shear component. Equal area projection, lower hemispheres. n = number of data points, MiD = minimum density, MaD = maximum density. Density contours at 0.5; 1; 1.5; 2; 2.5; 3; 4; 5; 6. Black represents the maximum density. Data points were smoothed with a Gaussian of 10° full width half maximum.

It is not possible to infer a shear sense from the a -axes pattern of sample Grf 603, in which S and C surfaces are parallel. In the most fine-grained sample (sample Grf 606, Figs. 5.3.3.2-4b and 5.3.3.2-8) the texture is more poorly developed than in the other samples. This phenomenon has already been observed by other authors (Berthé et al., 1979) and could be a result of operating deformation mechanisms that do not promote or even prevent the development of lattice preferred orientation, such as grain boundary sliding with more or less contribution of diffusion creep, since grains slide past each other more easily in fine-grained aggregates than in coarser-grained ones (Boullier and Gueguen, 1975; Behrmann, 1985; Behrmann and Mainprice, 1987). Sample Grf 615 is macroscopically nearly undeformed but shows some weak crystallographic fabric. Maxima are in this case displaced with respect to the principal strain axes due to the uncertainty about their position during sample preparation, since foliation and lineation are lacking.

The effect of D_4 on the LPO patterns is impossible to quantify. In relation to this deformation phase, we should emphasize that both temperature and shear sense inferred from LPO patterns are compatible with D_3 and therefore i) D_4 must have been very weak and/or ii) the averaging effect of the method results in patterns showing predominantly D_3 .

Quartz in diatexites shows a much weaker LPO (Fig. 5.3.3-3), probably due to the lower quartz content, which leads to a stronger interaction between quartz and other minerals and prevents quartz grains from recrystallizing without obstacles. Whereas the LPO patterns of sample Frg 92, which is representative for D_2 , are hardly interpretable, the ones of sample Grf 598, representative for D_3 , are fairly well developed and show a similar appearance as in the granite dyke. Thus, it is corroborated that D_3 observed in granite and host rock took place under similar temperatures.

Finite strain of the principal dyke

Four samples were selected for the application of the R_f/Φ' method (see chapter 3.7). The results obtained are represented in Table 5.3.3.2-1 and Fig. 5.3.3.2-9. It is important to note that R_s is an underestimation of the real strain, since feldspars exist in the deformed granite not only as porphyroclast, but also as completely recrystallized, fine-grained aggregates in the matrix, which could not be taken into account in our measurements due to their small thickness at hand specimen scale. Moreover, feldspar crystals contribute to the bulk strain not only by ductile behaviour but also by rotation. Finally, the strain measured in feldspar porphyroclasts is surely lower than the bulk strain, since the matrix contains a large amount of quartz, which was likely weaker and is expected to have suffered a higher strain than the porphyroclasts.

Two aspects of our results are notable:

- The magnitude of strain increases towards the contact to the host rock.

- The shape of the finite strain ellipsoid in different points of the dyke was plotted in a Flinn graph (Fig. 5.3.3.2-9): Oblate ellipsoids ($S > L$) are obtained, with the flattening being most pronounced near the contact. This result is visually corroborated by the fact that the planar fabric of the deformed granite dyke is best developed next to the contact to the host rock.

In Table 5.3.3.2-1 the strain calculated from the angle between S and C planes is shown.

sample	distance to contact (m)	after Peach & Lisle (1979)				after Ramsay & Huber (1983)				after Ramsay & Graham (1970)	
		R_s			k	R_s			k	θ'	γ
		$R_{S,XZ}$	$R_{S,YZ}$	$R_{S,XY}$		$R_{S,XZ}$	$R_{S,YZ}$	$R_{S,XY}$			
606	2.0	2.94	2.24	1.31	0.25	3.37	2.57	1.31	0.20	-	-
605	3.5	2.59	1.79	1.45	0.45	2.66	1.86	1.43	0.50	12°	4.5
607	6.6	2.33	1.76	1.32	0.43	2.58	1.85	1.39	0.46	18°	2.7
608	8.5	1.99	1.61	1.24	0.39	2.16	1.72	1.26	0.36	20°	2.4

Table 5.3.3.2-1. Finite strain data calculated by the R_f/Φ' method using the computer program "STRAIN" (Unzog, 1990) and by the angle between S and C planes. R_s = ellipticity of the strain ellipse.

As obtained from the R_f/Φ' method, the finite strain ellipsoid plots in the flattening field and therefore the plane-strain requirement for the strain calculation from the angle between S and C planes is not fulfilled. Therefore, the reported γ values must be considered only as an approximation.

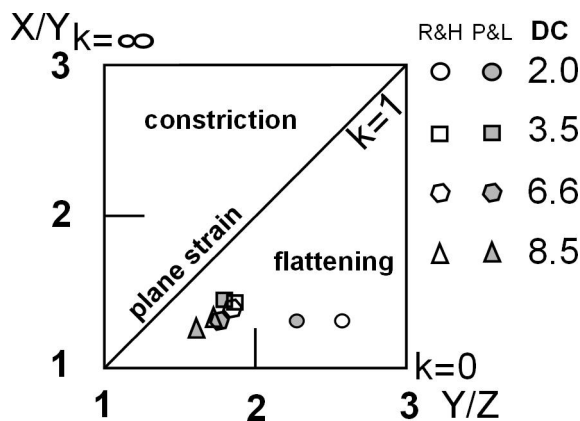


Figure 5.3.3.2-9. Flinn graph showing the finite strain geometry calculated by the R_f/Φ' method at different locations of the principal dyke. White and grey symbols represent the strain calculated after Ramsay and Huber (1983) and Peach and Lisle (1979), respectively. DC = distance to the contact (m).

Mass transfer, volumetric strain and Zr-thermometry

There is some evidence for the presence of a fluid phase during D₃. Electron microprobe analyses (Appendix 4) show a change in feldspar composition: K-feldspar (An₀ Ab₅ Or₉₅) is substituted by plagioclase (An₉ Ab₉₀ Or₁) during dynamic recrystallization (Fig. 5.3.3.2-7). The second evidence is constituted by the fine-grained white mica growing parallel to the mylonitic foliation, whose formation, probably at the expense of igneous feldspar, needs the presence of a fluid phase. At this point, the question arises whether this fluid phase played an important role in transferring mass away from or into the deformed rock.

The isocon-diagram method (see chapter 3.8.1) was applied in order to evaluate the mass transfer effect of the fluids present during D₃. Six samples were chemically analyzed by means of X-ray fluorescence. The results are shown on Table 5.3.3.2-2 and depicted in Fig. 5.3.3.2-10.

sample	DC (m)	Total	SiO ₂	Al ₂ O ₃	Fe ₂ O ₃	MnO	MgO	CaO	Na ₂ O	K ₂ O	TiO ₂	P ₂ O ₅	
603	0.05	99.93	76.12	13.15	0.93	0.023	0.16	0.75	3.86	4.54	0.06	0.02	
604	0.5	99.89	76.79	13.00	0.74	0.033	0.12	0.63	3.50	4.61	0.06	0.02	
605	3.5	100.02	76.97	13.40	0.89	0.044	0.12	0.66	3.28	4.03	0.07	0.02	
608	8.5	100.78	76.47	12.94	1.06	0.041	0.18	1.00	3.15	4.96	0.07	0.02	
610	11	100.47	76.78	12.95	0.97	0.037	0.14	0.35	3.28	5.38	0.06	0.02	
615	28.5	100.80	76.42	13.23	0.86	0.025	0.17	0.42	3.42	5.70	0.07	0.03	
sample	DC (m)	Ce	Cr	Ga	La	Nb	Nd	Ni	Pb	U	V	Zr	
603	0.05	55	18	16	21	51	16	41	23	11	6	44	
604	0.5	75	4	16	10	46	27	18	30	14	3	50	
605	3.5	80	2	14	27	29	28	12	33	11	5	68	
608	8.5	67	10	16	20	29	27	23	32	15	2	69	
610	11	71	13	15	23	28	17	12	28	4	5	68	
615	28.5	66	5	15	15	31	14	19	25	5	5	72	
sample	DC (m)	As	Ba	Co	Cs	Cu	Rb	Sn	Sr	Th	Y	Zn	LOI (%)
603	0.05	5	192	37	15	6	326	9	107	30	78	1	0.23
604	0.5	6	26	55	21	2	462	11	28	26	108	5	0.33
605	3.5	6	27	83	20	6	455	14	32	34	115	10	0.47
608	8.5	6	39	66	12	2	430	14	41	37	116	9	0.83
610	11	6	34	95	14	1	498	13	31	35	107	4	0.43
615	28.5	6	206	91	13	2	392	6	92	42	85	-	0.37

Table 5.3.3.2-2. X-ray fluorescence analyses of different granite samples in order of increasing distance to the host rock. Oxides in weight per cent, elements in ppm. DC = distance to the contact. These data were used for the application of the isocon-diagram method (Fig. 5.3.3.2-10) and for Zr-thermometry.

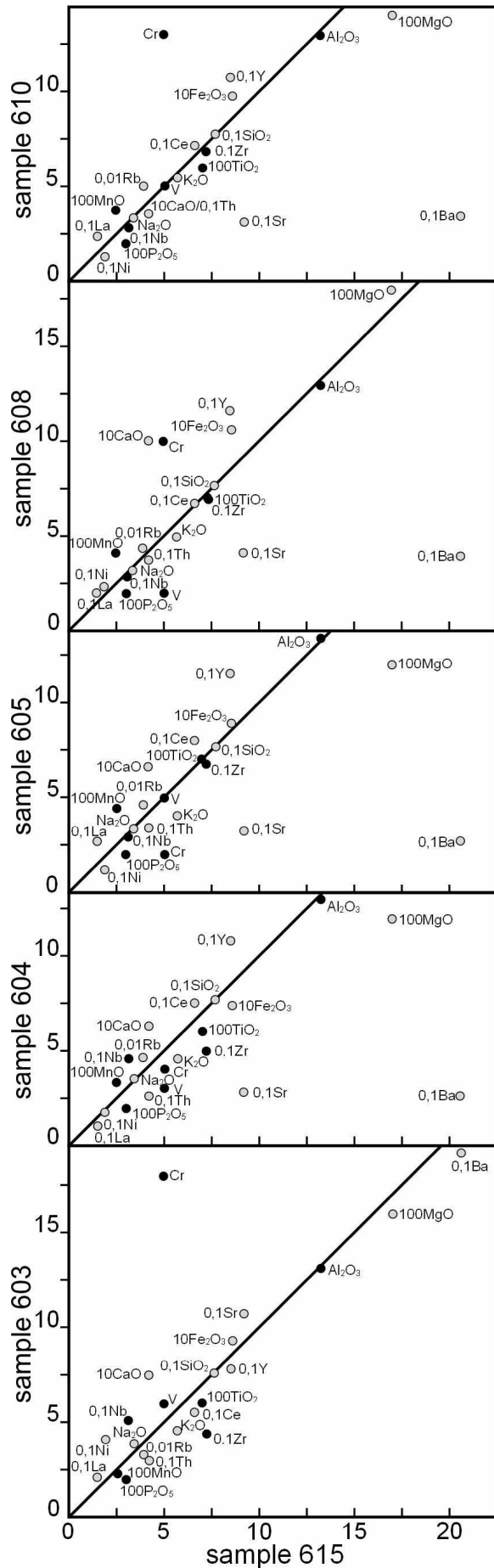


Figure 5.3.3.2-10. Isocon diagrams plotting deformed sample vs. undeformed sample in order of increasing deformation intensity (see Fig. 5.3.3.2-3 for sample location). In all diagrams the X-axis represents the concentration in sample 615 (undeformed). Oxides in weight per cent, elements in ppm. Grey and black points represent mobile and immobile components, respectively.

Fig. 5.3.3.2-10 shows most of the mobile and immobile components plotting next to or on a line of slope = 1. We can therefore conclude that deformation did not lead to an important mass exchange between the sheared granite and the surrounding rocks, despite a fluid being present and enhancing the mobility of some components. Thus, no significant volume change took place during deformation. Nevertheless, some K and Ba loss is observed, maybe due to the transformation of K-feldspar into white mica. The higher Ca content in strained areas is coupled with the aforementioned transformation of K-feldspar into plagioclase during deformation. The required additional Ca might have been supplied by the host rock.

Since no significant volume change took place during the deformation, the strain geometry presented in Fig. 5.3.3.2-9 is therefore a real geometry and not the result of volumetric strain: The dyke constituted a closed chemical system at the outcrop scale, in which the mineral transformations visible at the microscope scale remained nearly isochemical. Flattening strain suggests transpression during the main phase of shearing (e.g. Sanderson and Marchini, 1984; Tikoff and Fossen, 1999).

From the zirconium content of the samples a temperature of $716 \pm 18^\circ\text{C}$ was calculated. After Siebel et al. (2005), the granitic dyke is peraluminous; zircons display magmatic zoning and show no clear evidence for the presence of inherited cores. Therefore, the conditions for the application of the zircon-solution model by Watson and Harrison (1983) are fulfilled. However, it is important to remark that this Zr-thermometer is based upon experiments above 860°C , so that the obtained temperature might be relatively imprecise.

Differential stress

We calculated the differential stress using piezometers from several authors (Table 5.3.3.2-3, Fig. 5.3.3.2-11). Although D_4 had an important effect on quartz oblique orientation, this deformation affected quartz grain size and shape significantly only in some identifiable discrete bands. These overprinted bands were excluded from our analysis and only quartz grains included in monomineralic bands without SPO were used. In these monomineralic bands the size of quartz grains remains nearly constant and steady-state dislocation creep was presumably reached during dynamic recrystallization. The obtained differential stress should therefore approximate the stress governing D_3 . All piezometers show similar tendencies, with the differential stresses increasing towards the contact to the host rock, that is, towards more strained areas. Differential stresses range between ~ 10 und 60 MPa in the analyzed specimens.

	sample 606		sample 605		sample 607		sample 608	
	D = 48 ± 18 μm		D = 86 ± 25 μm		D = 122 ± 37 μm		D = 130 ± 42 μm	
	N = 61		N = 60		N = 87		N = 84	
	σ (MPa)	error	σ (MPa)	error	σ (MPa)	error	σ (MPa)	error
Twiss (1977, 1980) ^a	49	+19, -10	33	+9, -5	26	+7, -4	25	+8, -4
Mercier et al. (1977) ^a	24	+10, -5	16	+4, -3	12	+4, -2	12	+4, -2
White (1979) ^a	50	+20, -10	33	+9, -5	26	+7, -4	25	+8, -4
Etheridge and Wilkie (1981) ^a	48	+19, -10	32	+9, -5	25	+7, -4	24	+8, -4
Koch (1983) ^a	52	+67, -22	19	+15, -7	11	+9, -4	10	+9, -4
Christie et al. (1980), wet ^b	56	+40, -17	29	+14, -7	20	+10, -5	18	+10, -5
Stipp and Tullis (2003)	31	+15, -7	20	+6, -4	15	+5, -3	14	+5, -3

Table 5.3.3.2-3. Differential stresses calculated using the piezometers listed in Table 3.10-1. D = particle diameter, N = number of particles measured. Basic parameters ^ataken from Abalos et al. (1996), ^btaken from Ord and Christie (1984).

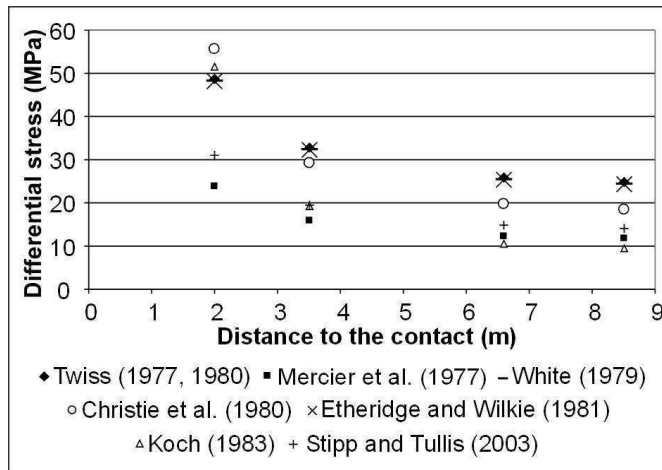


Figure 5.3.3.2-11. Differential stress calculated from quartz piezometers calibrated by different authors. Error bars were omitted for simplicity. See errors on Table 5.3.3.2-3 and Table 3.10-1 for further details.

Phengite barometry

The phengite geobarometer (Massonne and Szpurka, 1997) was applied to one sample of deformed granite (Grf 605, see Fig. 5.3.3.2-3 for location in the profile and Fig. 5.3.3.2-6 for details about the fabrics). This geobarometer correlates the number of Si atoms p.f.u. with pressure and temperature. The minerals biotite/phlogopite, quartz, K-feldspar and phengite constitute the limiting assemblage for the use of the thermobarometer and are present in the granite dyke. The composition of igneous white mica crystals, which can be called porphyroclasts after the deformation, was analysed in cores and rims in order to detect zonation. Fine-grained white mica constituting cleavage domains, which grew syn-kinematically after the emplacement, was also analysed. The results of the analyses are listed in Appendix 3.

	porphyroclasts, core	porphyroclasts, rim	cleavage domains
Si p.f.u. (mean \pm std. dev.)	3.135 \pm 0.015	3.147 \pm 0.022	3.196 \pm 0.039
Pressure (GPa)	0.59 \pm 0.04	--	0.51 + 0.07 - 0.09
Depth (km)	21.7 \pm 1.4	--	18.8 + 2.9 - 3.3

Table 5.3.3.2-4. Si content data used for geobarometry. The listed values were plotted in the PT diagram of Fig. 5.3.3.2-12.

The porphyroclasts show a weak tendency to increase their Si content towards the rim. In comparison with the porphyroclasts, the fine-grained white mica is clearly richer in Si. After Massonne and Schreyer (1987) "...homogenization and re-equilibration of phengitic micas are extremely sluggish processes even within geologic times". Our data support this statement and show that newly grown white micas have a composition different to that of primary igneous white micas in which a zonation is present and, therefore, equilibrium was not reached.

As representative for the conditions during emplacement and freezing of the dyke we considered the Si content p.f.u. in the core of white mica porphyroclasts. The intersection between the granite solidus line and the 3.135 isopleth is assumed to approximately provide a maximum emplacement depth since i) emplacement and reaching of the solidus temperature are thought to occur nearly simultaneously and ii) crystallisation of igneous mica might have taken place to some extent before the magma reached its final emplacement level. The Si content in white mica of cleavage domains is thought to represent the conditions during deformation. The deformation temperature is given by the microfabric inferred from the microfabrics and the *c*-axis patterns, i.e. around 500-550°C. Plotting this information of temperature and Si content (Fig. 5.3.3.2-12) allows the constraining of pressure for each event and sheds some light on the PT path followed between emplacement and deformation of the dyke. Pressure is inferred to have been around 0.59 \pm 0.04 GPa during emplacement and around 0.51 (+ 0.07, - 0.09) GPa during deformation (for a deformation temperature of 525°C), which corresponds to a depth of about 22 km and 19 km, respectively.

Since the analysed white micas contain a larger amount of components than those regarded in the KMASH system, in which the applied geobarometer was calibrated, the pressure results obtained might be somewhat imprecise. The Fe content is relatively high compared to the Mg content. After Massonne and Schreyer (1987), the introduction of Fe in white mica reduces its Si content and might therefore derive in underestimated pressures. The effect of Na might be similar, but the Na content of the analysed white mica is anyway relatively low. Fluorine might have the opposite effect, i.e. it might lead to the overestimation of pressures, but its concentration in the analysed micas is very low. Zen (1988) pointed out that magmatic muscovites are

characterised by a relatively high Ti content. However, it is interesting that the Ti content of all analysed white mica populations is very similar, although their origin is different: magmatic in some cases and metamorphic in others.

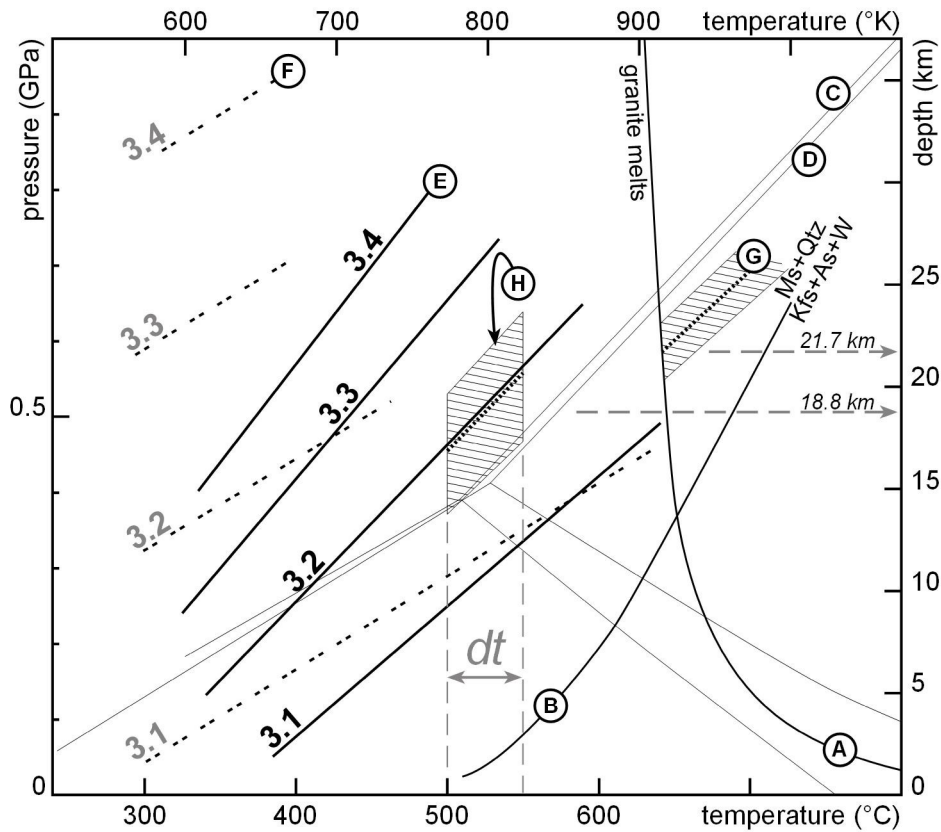


Figure 5.3.3.2-12. PT diagram showing the results of the application of the phengite geobarometer of Massonne and Szpurka (1997) on the Saunstein dyke. **A)** Solidus of water-saturated haplogranite after Johannes and Holtz (1996). **B)** Stability of white mica in presence of quartz after Chatterjee and Flux (1986), see mineral abbreviations in Appendix 5. Stability fields of aluminium silicate polymorphs are shown for reference **C)** after Hemingway et al. (1991) and **D)** after Bohlen et al. (1991). **E)** Phengite geobarometer: Si-content isopleths after Massonne and Szpurka (1997). Number of Si atoms p.f.u. are indicated on each isopleth. **F)** Phengite geobarometer: Si-content isopleths after Massonne and Schreyer (1987), not used for calculations. **G)** The dotted line represents the 3.135 isopleth after the barometer of Massonne and Szpurka (1997), corresponding to the mean Si content of porphyroclast cores, whereas the hatched area was constructed taking into account the standard deviation of all analyses. The hatched area represents the PT window in which white mica might most probably have crystallised. **H)** The same for fine-grained white mica of cleavage domains, using a temperature window of 500-550°C. dt = deformation temperature.

5.3.3.3. The case study of the Untermitteldorf dyke

Introduction

The Untermitteldorf dyke is situated 5 km north of the town Schöfweg and 600 m north of the village Untermitteldorf (Fig. 5.3.3.3-1). It intrudes into diatexite and a granodiorite body (Blaha and Siebel, 2006) belonging to the group 1 of Variscan intrusives of the study area (see chapter 5.2.3).

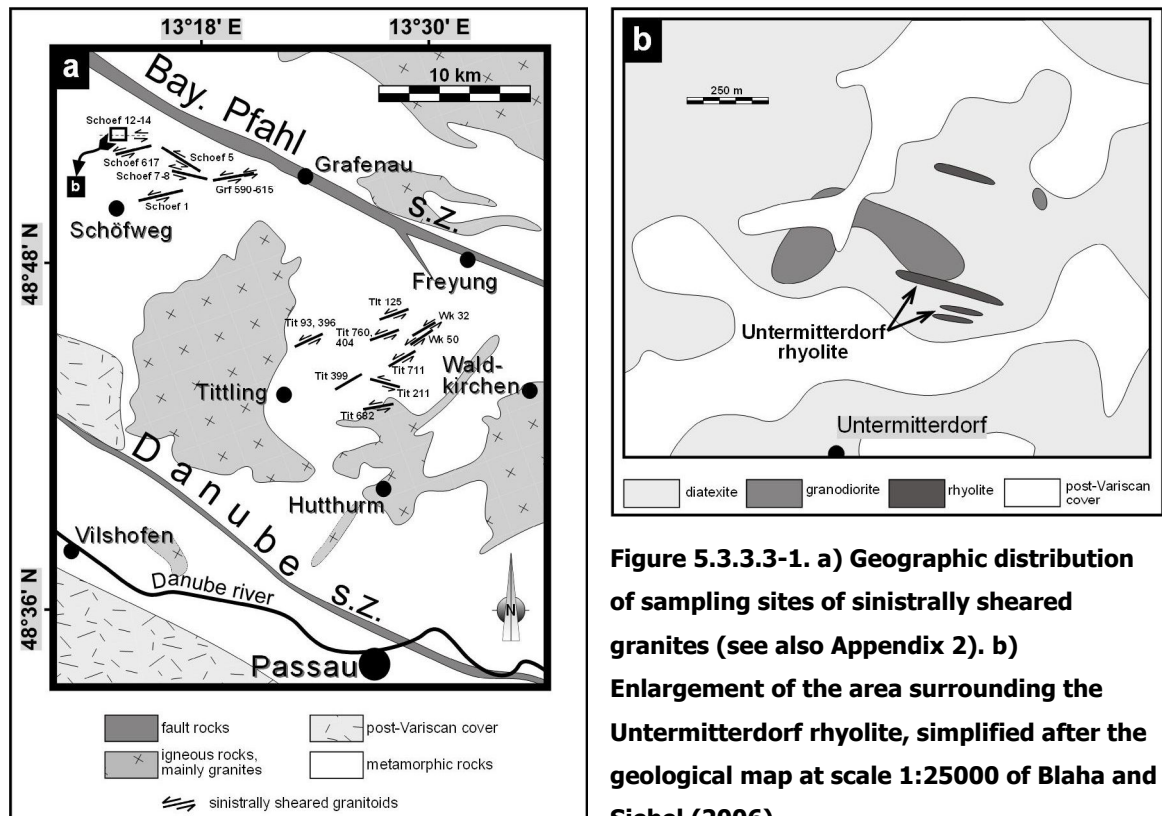


Figure 5.3.3.3-1. a) Geographic distribution of sampling sites of sinistrally sheared granites (see also Appendix 2). b) Enlargement of the area surrounding the Untermitteldorf rhyolite, simplified after the geological map at scale 1:25000 of Blaha and Siebel (2006).

The granodiorite builds an irregular stock, around 150 m wide and 300 m long. It has been dated by Dr. W. Siebel and co-workers (University of Tübingen) at 315-325 Ma (U-Pb on zircon, Galadí-Enríquez et al., in prep.). The rock is fine-grained and dark-coloured due to the high biotite content. It is composed of plagioclase (40–55 %), biotite (20–40 %), quartz (10–20 %), amphibole (5–15 %), opaque phases (1–10 %) and K-feldspar (0–5 %). Secondary chlorite grows from biotite and amphibole. Rutile, titanite, zircon, apatite and allanite occur as accessory minerals. In some areas it is possible to identify a subvertical, NW–SE striking tectonic foliation. In other areas, an evidence for deformation is lacking.

The Untermitteldorf dyke is WNW–ESE striking and granitic in composition (Blaha, in press). It is a few meters thick, building a main dyke and several apophyses and

incorporating stoped blocks (Figs. 5.3.3.3-1, 5.3.3.3-2). It has been dated by the investigation group of Dr. W. Siebel (University of Tübingen) at 315.0 ± 1.0 Ma (Galadí-Enríquez et al., in prep.). Attending to its age and fabric, it can be classified as belonging either to the group 2 or 4 of Variscan intrusives of the study area (see chapter 5.2.3). Its structure is aphanitic and porphyritic; hence it will be referred to as "rhyolite" regardless of its assumed plutonic nature and following the recommendations of Le Maitre et al. (1989, 2002).

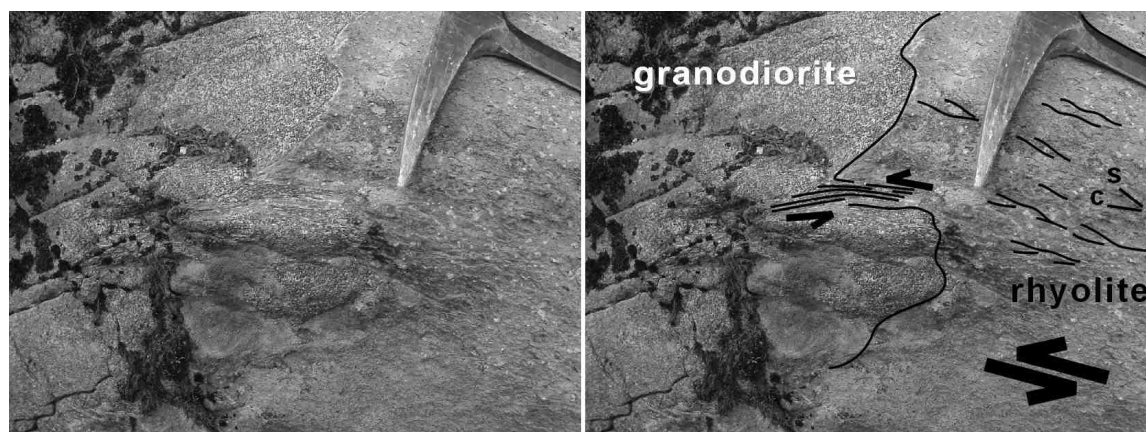


Figure 5.3.3.3-2. One very well exposed stoped block of granodiorite was found in the porphyritic rhyolite. The strain partitioning is strongly controlled by the rheological contrasts between different lithologies: The granodioritic stoped block is, except for one narrow band, almost undeformed and surrounded by deformed rhyolite. Note the large, light phenocrysts in the rhyolite.

Quartz, K-feldspar and biotite phenocrysts are embedded in a very fine-grained, bluish grey-coloured matrix, presumably made of quartz, feldspar and mica (Fig. 5.3.3.3-3). Some plagioclase crystals were also found, but they are scarce and more intensively sericitized than K-feldspar. Aggregates made of white mica, partly transformed into light green chlorite and mixed with biotite, are shiny and greenish in hand specimens. Zircon, apatite, titanite and opaque phases occur as accessory minerals. The intensity of the deformation in the porphyritic dyke is variable. Some more or less discrete bands show a steeply N dipping mylonitic foliation, the latter displaying a sub-horizontal stretching lineation. A well developed *S*–*C* structure (Berthé et al., 1979; Lister and Snoke, 1984) points to a sinistral shear sense (Figs. 5.3.3.3-2, 5.3.3.3-3, 5.3.3.3-5).

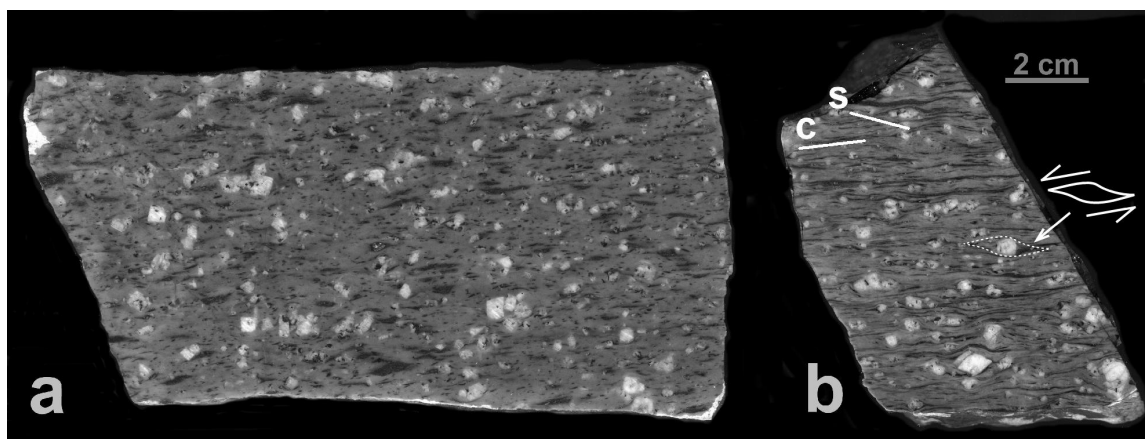


Figure 5.3.3.3-3. Hand specimens of Untermitterdorf rhyolite, XZ -sections, north direction approximately to the top of the picture. a) Slightly deformed rhyolite (sample Schoef 14), where light feldspar phenocrysts and dark, elliptical white mica \pm chlorite aggregates are visible in a very fine-grained, greyish matrix. b) Strongly deformed rhyolite (sample Schoef 12). White mica \pm chlorite aggregates are strongly deformed (elongate dark bands). The sinistral shear-sense can be inferred from σ -type mantled porphyroclasts and the angular relationship between S and C planes.

Microfabrics

The hosting granodiorite is partly deformed. The subvertical tectonic foliation striking NW—SE parallels that of the migmatites. The kinematics is difficult to determine because of the very small grain size of the rock. Similar to the country rock and other dioritic to granodioritic bodies, the deformation might result mainly from dextral simple shear under upper greenschist to amphibolite facies conditions (D_2). D_3 rarely overprints the primary fabric in the granodiorite, except in narrow bands in contact with rhyolitic material (Fig. 5.3.3.3-2).

The porphyritic rhyolite is variably deformed by D_3 , i.e. it was sinistrally sheared along planes striking N079E to N103E and dipping steeply to the north (S_3) with a sub-horizontal stretching lineation (L_3). Sinistral shear sense is inferred from σ -type mantled porphyroclasts, the angular relationship between S and C planes and mica fishes with stair-stepping of trails of mica fragments (Fig. 5.3.3.3-5).

Feldspars (mainly K-feldspar, but also zoned plagioclase) occur as euhedral to subhedral crystals (average diameter 2-2.5 mm) and do not show any evidence for mechanical fragmentation and recrystallization (Fig. 5.3.3.3-5).

White mica was found as stretched, cm-long polycrystalline aggregates, accompanied by biotite and locally replaced by chlorite (Fig. 5.3.3.3-4). The long side of single crystals is usually $< 100 \mu\text{m}$ in length. In rare cases, normally coinciding with strain shadows behind large feldspar grains, these mica aggregates are found in a nearly undeformed

state, constituting sub-spherical, chlorite-free aggregates of subhedral crystals. Thus, white mica is supposed to be of igneous origin. It built spherical aggregates together with biotite before deformation and was partially transformed into chlorite during deformation. The igneous origin of white mica is supported by the fact that it can be found as inclusions inside quartz and feldspar porphyroclasts. The deformation changed the shape of the mica aggregates, but caused no significant recrystallization on them. The fine-grained fraction ($< 5 \mu\text{m}$) of the matrix might partly result from alteration of feldspar in a late magmatic phase and during deformation.

Biotite can be found as aggregates together with white mica (see above), but is also present as larger tabular crystals (length $\sim 600 \mu\text{m}$), usually displaying mica fishes. It is possible that both grain sizes represent two different biotite generations. It is sometimes accompanied by opaque phases (ilmenite?), the latter growing at the margins or at mineral cleavage planes of biotite, suggesting crystallisation of Ti-rich biotite under high temperature and Ti exsolution during temperature drop. Zircon inclusions are commonly found in biotite.

Titanite is, although accessory, abundant in comparison with other samples. It is found in form of bands of boudinaged grains.

Quartz can display very different fabrics (Figs. 5.3.3.3-4b and 5.3.3.3-5, Table 5.3.3.3-1):

i) Euhedral to subhedral quartz grains, not recrystallized (diameter $\sim 1 \text{ mm}$). These grains are nearly undeformed or show evidence for crystal plastic deformation and recovery like undulose extinction, deformation bands and subgrains with boundaries parallel to the prism planes. Subgrains with boundaries parallel to the basal planes are found in less deformed crystals and, together with the prism-parallel planes, define a so-called chessboard pattern. This pattern is thought to be diagnostic for prism $\langle c \rangle$ slip, which is active at temperatures higher than ca. 600°C in the β -quartz stability field (Mainprice et al., 1986; Masberg et al., 1992; Kruhl, 1996). Since the chessboard patterns tend to disappear by increasing strain of the quartz porphyroclasts of the rhyolite, they are considered to be a relic of early, weak deformation at temperatures close to the granite solidus prior to or at early stages of D_3 .

ii) Monocrystalline ribbon-grains of quartz are abundant. Some of them are very elongated, have a strain-free appearance and in extinction position under crossed polarizers in XZ -sections, i.e. their c -axis parallels the Y -axis of the finite strain ellipsoid. Other grains show evidence for crystal plastic deformation and recovery like undulose extinction, deformation bands and prism-parallel subgrain boundaries.

iii) Polycrystalline ribbon-grains or lenticular aggregates of quartz are partially or completely dynamically recrystallized. They are usually equigranular and made

up of equant or slightly elongated new grains (diameter ~ 45 µm) with serrated or polygonal boundaries, sometimes showing crystallographically controlled squared contours. The latter constitute the so-called reticular or mosaic-like pattern (Gapais and Barbarin, 1986). The recrystallized quartz shows a strong LPO and a poorly developed SPO. Relicts of old grains show prism-parallel subgrain boundaries parallel to the long axis of the new grains. Subgrains are similar in size to recrystallized grains. The dominant recrystallization mechanism most probably was subgrain rotation accompanied by grain boundary migration. The recrystallization of quartz by these mechanisms requires temperatures of 480-530°C (Stipp et al., 2002).

not recrystallized:	<ul style="list-style-type: none"> - not deformed - deformed, monocrystalline ribbons with strain-free appearance - deformed, monocrystalline ribbons with: <ul style="list-style-type: none"> undulose extinction deformation bands prism-parallel subgrains
recrystallized:	<ul style="list-style-type: none"> - partially, by subgrain rotation and grain boundary migration: relicts of old grains with prism-parallel subgrain boundaries and some recrystallized grains similar in size to subgrains - completely (rare), by subgrain rotation and grain boundary migration: equigranular aggregates made up of equant or slightly elongated new grains with serrated or polygonal boundaries, strong LPO, poorly developed SPO

Table 5.3.3.3-1. Summary of quartz microfabrics found in the Untermittlerdorf rhyolite.

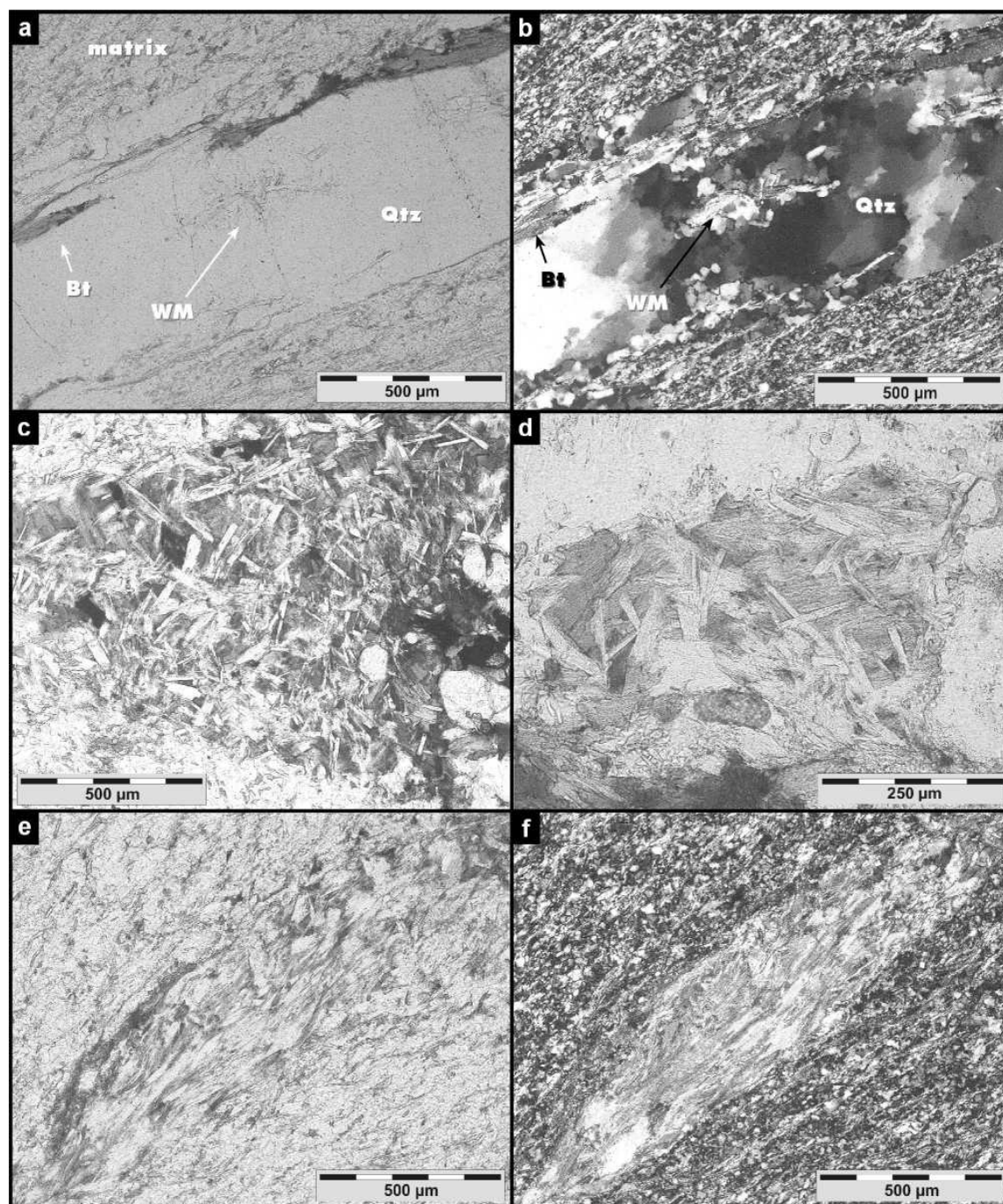


Figure 5.3.3-4. Photomicrographs of rhyolite, all of them belonging to a slightly deformed specimen (sample Schoef 14). a) Parallel polarizers. Inclusions of white mica and biotite in quartz porphyroclast, suggesting magmatic origin of mica. b) Crossed polarizers. Same as (a). This quartz porphyroclast shows subgrains with boundaries parallel to the basal and prism planes. c) Parallel polarizers. Sub-rounded aggregate of white mica, biotite, apatite and opaque phases located at a strain shadow. d) Parallel polarizers. Sub-rounded aggregate of white mica and biotite located at a strain shadow. e) Parallel polarizers. Elliptical aggregate of white mica and biotite, slightly deformed. f) Crossed polarizers. Same as (e).

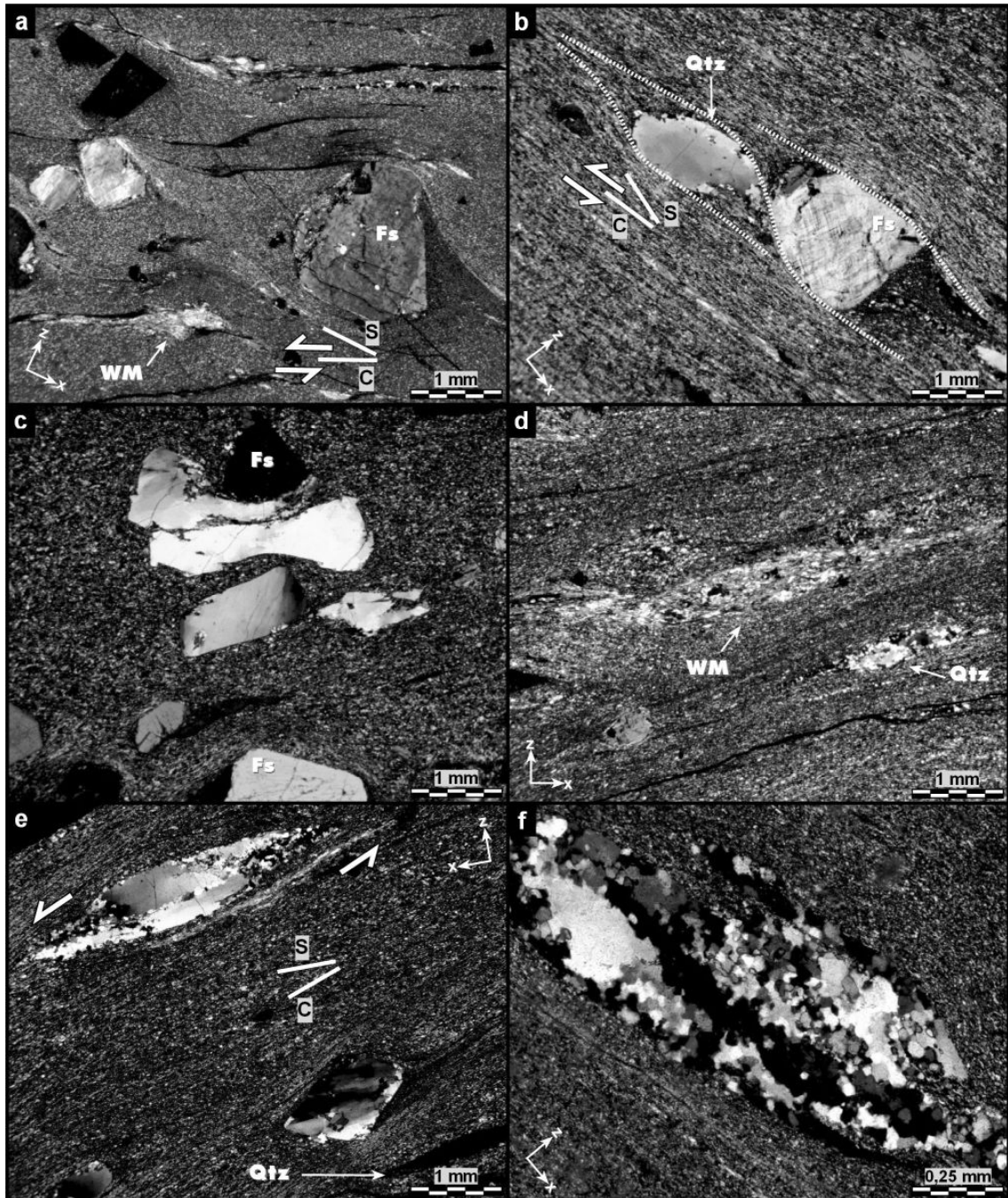


Figure 5.3.3.3-5. Photomicrographs of rhyolite, all of them belonging to a strongly deformed specimen (sample Schoef 12), except for c (sample Schoef 14). Crossed polarizers. The position of the X and Z axes of the finite strain ellipsoid is indicated. X is parallel to S . In most of the pictures the monoclinic symmetry of the fabric (σ -clasts and S - C structures) points to a sinistral sense of shear. a) σ -clasts of feldspar embedded in a very fine-grained matrix. An aggregate of white mica (WM) is found at the bottom left corner. b) Weakly deformed quartz grain at the strain shadow of a feldspar σ -clast. c) The photomicrograph shows several quartz grains situated between two large feldspar phenocrysts. The feldspar crystal at the top acts as an indenter and pierces the quartz crystals in the surroundings, which are flattened by intracrystalline deformation, whereas the quartz grain in the centre is nearly undeformed. Continues on next page →

→Figure 5.3.3.3-5 (continued). d) In the centre there is a stretched aggregate of white mica with stair-stepping of trails of mica fragments. Below the mica aggregate on the right there is a polycrystalline quartz ribbon, presumably resulting from the recrystallization of a former phenocryst. e) Three different forms in which we can find quartz in this rock. Large grain at the top-left part of the picture: partly recrystallized porphyroblast. Large grain at the bottom-right part of the picture: not recrystallized grain with prism-parallel deformation bands. Grain at the bottom-right corner, indicated by an arrow: monocrystalline ribbon-grain in extinction position. f) Lenticular aggregate of quartz, almost completely recrystallized. New grains show serrated or polygonal boundaries.

Quartz texture

For the EBSD analyses of quartz, three rectangular areas of the sample were delimited. Two of them enclosed polycrystalline quartz ribbons and were scanned with a step width of 10 μm . The third rectangle enclosed fine-grained quartz of the matrix and was scanned with a step width of 15 μm . The resulting texture is shown in Fig. 5.3.3.3-6.

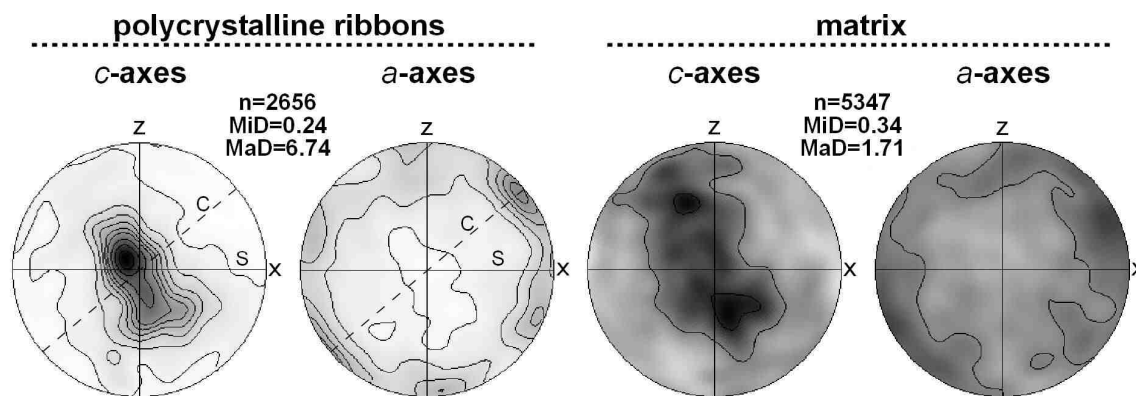


Figure 5.3.3.3-6. Stereographic representation of quartz *c* and *a*-axes obtained by means of EBSD (sample Schoef 12). Equal area projection, lower hemispheres. *n* = number of data points, *MiD* = minimum density, *MaD* = maximum density. Density contours at 0.5; 1; 1.5; 2; 2.5; 3; 4; 5; 6. Black represents the maximum density. Data points were smoothed with a Gaussian of 10° full width half maximum.

Recrystallized quartz ribbons display a very well developed LPO. *c*-axes are clustered in the direction parallel to the *Y*-axis of the finite strain ellipsoid. The *a*-axes pattern shows two weak sub-maxima on the *XZ*-plane and a main strong maximum on the *XZ*-plane parallel to *C*-planes of *S*–*C* structures, pointing to a sinistral shear sense. This LPO pattern is typically developed when intracrystalline slip takes place along the prism planes of the quartz crystal lattice in $\langle a \rangle$ direction. The LPO patterns of the Untermittlerdorf rhyolite suggest a similar or slightly lower temperature than in the other sinistrally sheared granites (compare Figs. 5.3.3.2-8, 5.3.3.3-6, 5.3.3.4-4, and 5.3.3.4-

5): The fact that a -axes tend to concentrate in one single maximum instead of three and that the c -axes maximum shows a slightly stretched shape might be the result of some contribution of rhomb $\langle a \rangle$ slip and a slightly lower deformation temperature. The very fine-grained matrix does not display a well-developed LPO pattern, suggesting that grain boundary sliding was the main deformation mechanism.

Phengite barometry

The phengite geobarometers of Massonne and Schreyer (1987) and Massonne and Szpurka (1997) were applied to the white micas of the rhyolite. Three populations of white mica were distinguished: i) igneous grains, appearing as elliptical aggregates in deformed specimens, ii) crystals enclosed in feldspar porphyroclasts, which could be either magmatic (real magmatic inclusions) or late- to post-magmatic (replacing feldspars) and iii) very fine-grained white mica that grew syn-kinematically parallel to the mylonitic foliation constituting cleavage domains in the deformed rhyolite. The result of the analyses of the Si content in different mica populations can provide a rough estimation about the PT path followed by the rocks in the study area. The results of the microprobe analyses on sample Schoef 12 are listed in detail in Appendix 3 and depicted in Fig. 5.3.3.3-7. Some igneous grains were analysed along profiles, but no remarkable zonation tendency was observed, meaning that no significant chemical overprint occurred in the white mica due to the deformation. Therefore, all analyses performed on igneous grains were listed together in Appendix 3 regardless of their spatial position. The Si content p.f.u. in igneous grains averages 3.080 with a standard deviation of 0.007.

The graphic solution provided by Massonne and Schreyer (1987) and Massonne and Szpurka (1997) comprises the range between 3.8 and 3.1 Si atoms p.f.u.. The approximate position of the isopleth at 3.08 Si atoms p.f.u. was estimated by linear extrapolation for both barometers. The hatched areas G and H in Figure 5.3.3.3-7 represent the estimated PT range, in which igneous white mica may have crystallised. The intersection between the granite solidus line and the 3.08 isopleth is assumed to approximately provide a maximum emplacement depth since i) emplacement and reaching of the solidus temperature are thought to occur nearly simultaneously and ii) crystallisation of igneous mica might have taken place to some extent before the magma reached its final emplacement level. This maximum emplacement depth is then 16.6 ± 0.7 km (0.45 ± 0.02 GPa) or 15.5 ± 0.7 km (0.42 ± 0.02 GPa), depending on the barometer used.

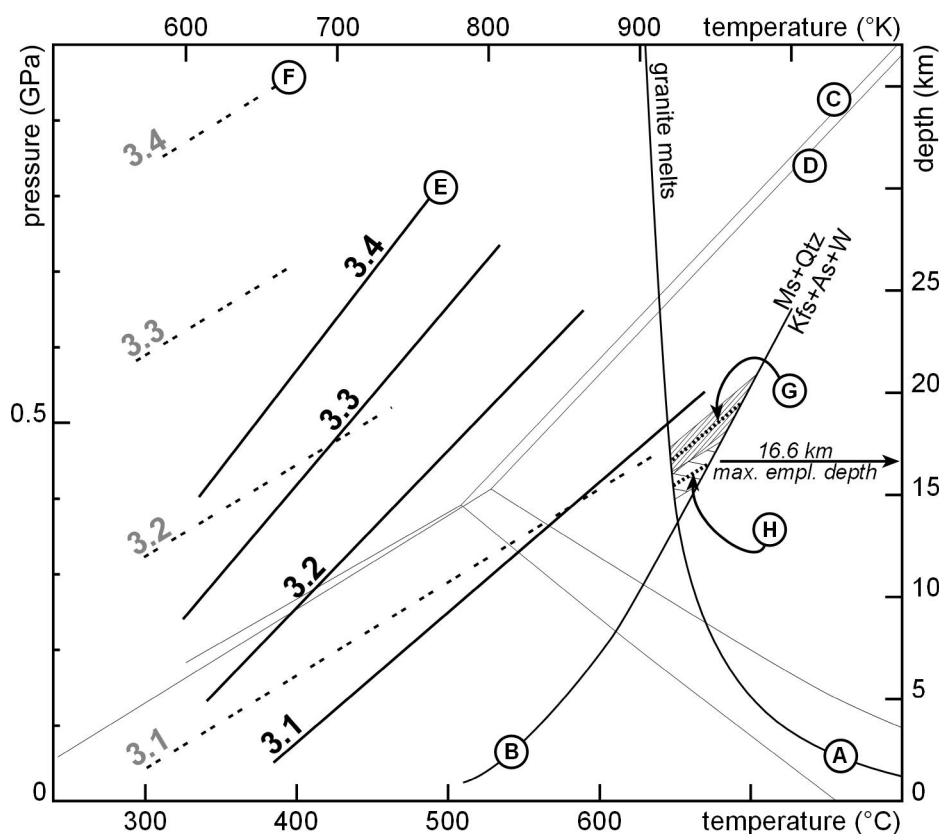


Figure 5.3.3-7. PT diagram showing the results of the application of the phengite geobarometer on the Untermittlerdorf rhyolite. A) Solidus of water-saturated haplogranite after Johannes and Holtz (1996). B) Stability of white mica in presence of quartz after Chatterjee and Flux (1986), see mineral abbreviations in Appendix 5. Stability fields of aluminium silicate polymorphs are shown for reference C) after Hemingway et al. (1991) and D) after Bohlen et al. (1991). E) Phengite geobarometer: Si-content isopleths after Massonne and Szpurka (1997). Number of Si atoms p.f.u. are indicated on each isopleth. F) Phengite geobarometer: Si-content isopleths after Massonne and Schreyer (1987). G) The dotted line represents the extrapolated 3.08 isopleth after the barometer of Massonne and Szpurka (1997), whereas the hatched area was constructed taking into account the standard deviation of all analyses. The hatched area represents the PT window in which white mica might most probably have crystallised. H) A slightly different result delivered by the barometer of Massonne and Schreyer (1987).

Due to the reduced size of white mica crystals of the other two populations, only a few microprobe analyses were successful (see Appendix 3). Unfortunately, these few analyses cannot be presented as evidence, but barely as a clue of a decompression taking place between freezing and deformation, since the Si content tends to decrease in the population of synkinematic white mica. At least some of the white mica grains contained in feldspars seem to be of magmatic origin; this is suggested by their high Ti content. On the other hand, the grains of white mica which have been categorised as igneous based on their fabric features show a very low Ti content. This can be due to

the presence of other phases which incorporate Ti in their lattice, such as biotite, ilmenite and, most of all titanite.

It must be emphasized that the applied geobarometer was calibrated for the KMASH system. However, the analysed white mica shows a high Fe content. After Massonne and Schreyer (1987), the introduction of Fe and Na in white mica reduces its Si content and might therefore derive in underestimated pressures. Fluorine, which is present in the analysed white mica, might have the opposite effect, i.e. it might lead to the overestimation of pressures.

The fabric of the Untermittlerdorf rhyolite remains somewhat enigmatic. Our results point to a relatively deep intrusion inside a warm country rock, so why did it develop an aphanitic structure? It is possible that there are, apart from the cooling rate, other factors (maybe chemical ones) controlling the grain size of magmatic rocks.

5.3.3.4. Other sinistrally sheared granites

The outcrops of Saunstein and Untermitteldorf are the most impressive examples of sinistrally sheared dykes found in the study area. The complete area between Schöfweg and Waldkirchen is crosscut by further sinistrally sheared granite stocks and dykes, some of which are also well exposed (see Fig. 5.3.3.1-1 and Appendix 2 for location). In the following lines we will offer an overview about the characteristics of these rocks.

Macroscopic features

A location map and a list of the most relevant samples of sinistrally sheared granites including coordinates and structural information can be found in Appendix 2. The sinistrally sheared granites are not always, but very often, dykes. In exceptionally good outcrops, such as the Saunstein and the Schneidermühl ones, it is possible to observe contacts sub-parallel to the shear planes. Nevertheless, it is important to remark that the contacts are more often than not lobate, and by far not as straight as in the case of younger subvolcanic dykes. The detailed geometry of most of the sinistrally sheared dykes is at best only roughly mappable, so that a general relationship between the orientation of shear planes and contacts cannot be definitely stated: This is the case of the Untermitteldorf dyke and most of the sampled bodies. The thickness of these dykes ranges between a few cm (Fig. 5.3.3.4-1a) and 50-100 m (Saunstein dyke). Some other sheared bodies are rather irregular stocks; this is the case for the intrusions in Goggersreut (samples Wk 32 and Wk 50) and Hochholz (sample Tit 711). In a few cases it is not possible to infer the shape of the intrusions due to the poor quality of the outcrops, like for example in Loizersdorf (sample Tit 211) or Steinberg (sample Tit 125).

With the only exception of the Untermitteldorf dyke, all of the studied sheared granites are faneritic, i.e. they are "real" granites in the sense of the IUGS nomenclature (Le Maitre et al., 1989, 2002). The Untermitteldorf dyke, as mentioned above, shows an aphanitic structure. The Abersberger Holz dyke (samples Schoef 7 and 8, see Figs. 5.3.3.1-1, 5.3.3.4-1c, 5.3.3.4-2c, and Appendix 2) is very fine grained, partly due to the grain-size reduction undergone during deformation, but also due to a primary smaller grain size, i.e. this dyke shows intermediary characteristics between the Saunstein and the Untermitteldorf end-member types.

Sometimes D_3 affects the whole volume of these intrusions, but it is also very typical to find nearly undeformed parts adjacent to strongly foliated ones. Especially remarkable is the fact that the strongly sheared bands are often found next to the contact to the host rock. This case has been studied in detail in the Saunstein dyke.

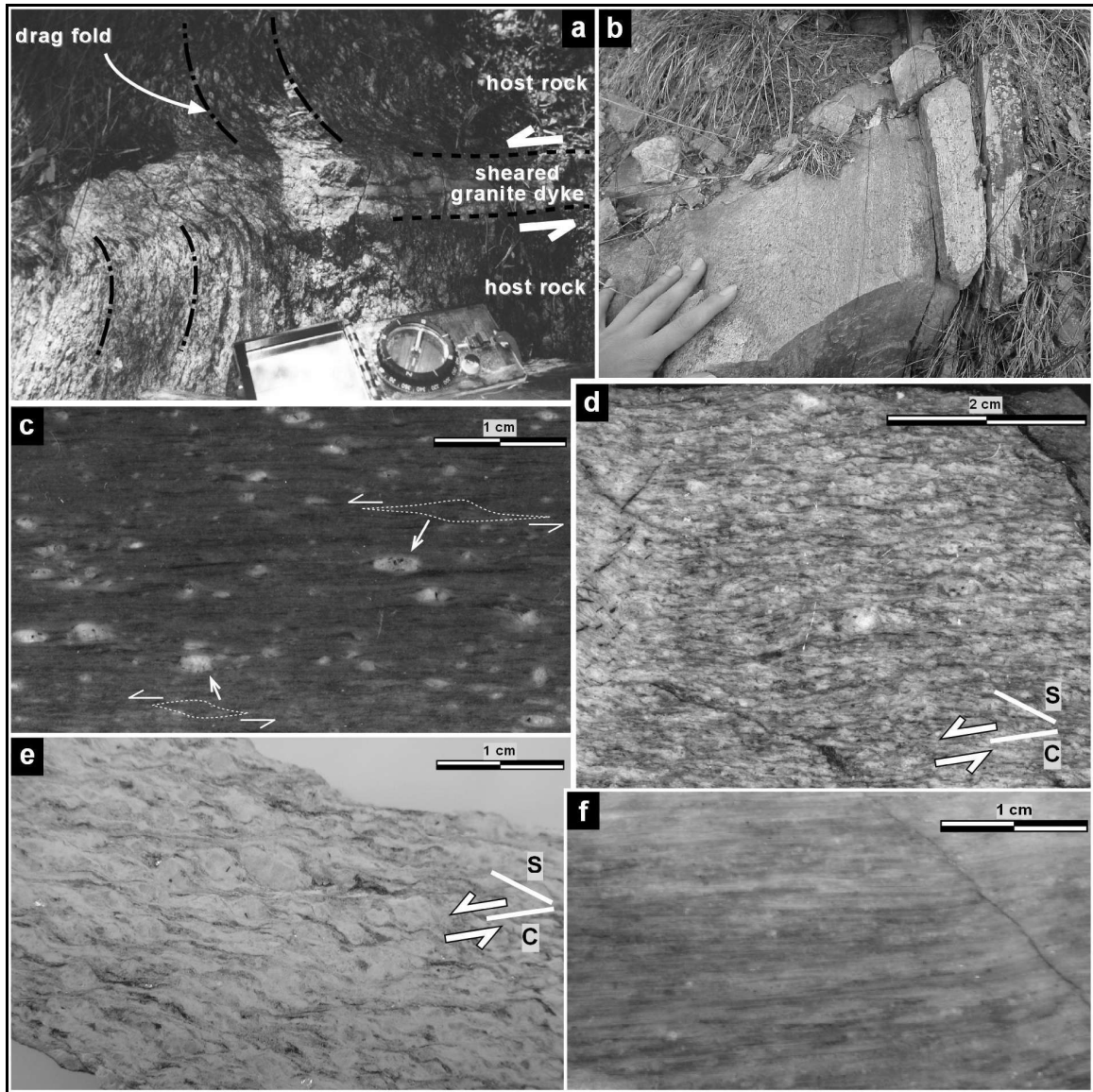


Figure 5.3.3.4-1. a) This thin granitic dyke clearly underwent sinistral shearing. The host rock (hypersthene-bearing diatexite) shows drag folds, meaning that the temperature during deformation was not very high. The photograph was taken at R 4607200 H 5405375 (Gauss-Krüger coordinates). The mylonitic foliation of the dyke strikes N065E and is subvertical. b) This photo shows the outcrop Goggersreut 1, sampling site of Wk 32 (see Fig. 5.3.3.1-1 and Appendix 2 for location). The photo was taken looking to the east. c) Hand specimen of Schoef 7, σ -type mantled porphyroclasts point to a sinistral sense of shear. d) Hand specimen of Schoef 1, the angular relationship between *S* and *C* planes indicates sinistral shear sense. e) Hand specimen of Tit 125, showing a well-developed augen structure. *S-C* fabric shows sinistral sense of shear. f) Hand specimen of Tit 396, D_3 converted the rock into a very fine-grained ultramylonite.

Microfabrics

Microfabrics are in all sinistrally sheared granites similar. They can be described as type I S—C mylonites after Lister and Snoke (1984; see also Berthé et al., 1979). The deformation intensity varies from one specimen to another, comparing different bodies, but also comparing different locations inside one and the same body. Independently of the deformation intensity, the following characteristics apply to most of the studied specimens:

The mylonites which result from the sinistral shearing of granitic bodies are made up of alternating quartz and feldspar layers enclosing feldspar and mica porphyroclasts. Many of them have well-developed cleavage domains of synkinematic white mica.

The quartz is usually completely recrystallized and forms equigranular polycrystalline ribbons. Straight or slightly serrated grain boundaries are commonly found. Some rare old grains show prism-parallel subgrains of the same size as the recrystallized grains. A LPO is identifiable by inserting a gypsum plate under crossed polarizers. This fabric features suggest recrystallization to have occurred by grain boundary migration together with subgrain rotation. In sample Tit 125 (Figs. 5.3.3.4-1e and 5.3.3.4-2h), polygonal crystals with contacts displaying triple points with interfacial angles of 120° and a relatively large grain size point to some static recrystallization by grain boundary area reduction taking place after shear.

The feldspar grains are partially recrystallized and are typically found either as fine-grained layers or σ -type mantled porphyroclasts. The boundaries between cores and mantles are more or less pronounced depending on the sample considered. Some porphyroclasts show evidence for brittle behaviour documented by rare microfaults. The mica grains display a SPO with the long axes oriented parallel to the foliation.

Most of the samples show one or more of the following kinematic indicators pointing to a sinistral sense of shear: σ -type mantled porphyroclasts of feldspar, S-C structures, mica fishes with stair-stepping of trails of mica fragments, asymmetric folds, monomineralic sigmoidal bands.

The cited microstructural features are practically identical to those described for the Saunstein dyke. The only remarkable difference is that the deformation referred to as D₄ can be clearly identified only in the Saunstein dyke and, although in a much weaker way, in sample Schoef 5.

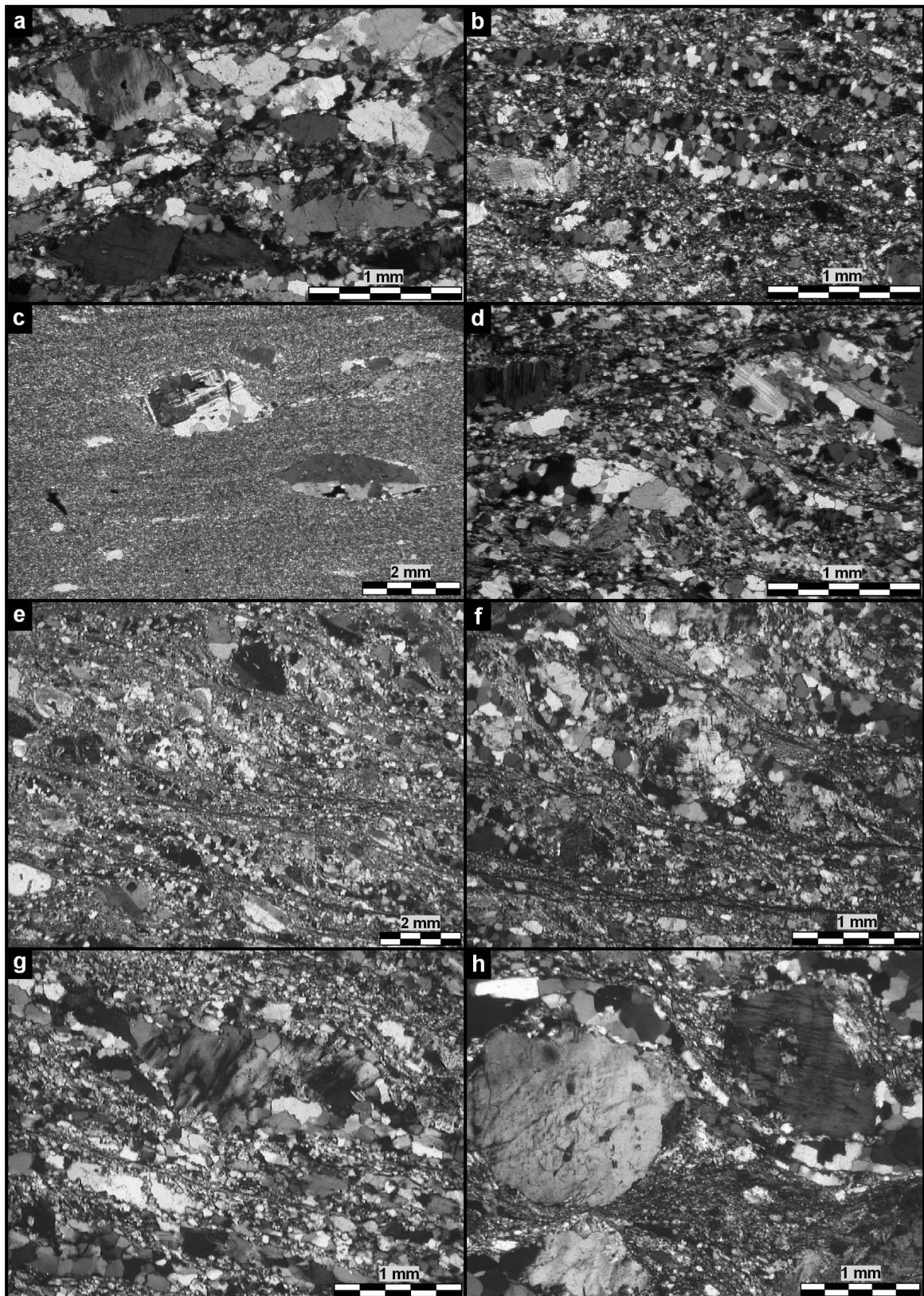


Figure 5.3.3.4-2. Some of the sinistrally sheared granites under the microscope, *XZ*-sections, crossed polarizers. σ -clasts, *S-C* structures and stair-stepping of trails of mineral fragments point to a sinistral sense of shear. a) Sample Schoef 1 shows low deformation intensity, quartz and feldspar are incipiently recrystallized. b) Sample Schoef 5, with the typical alternance of quartz (coarse grained) and feldspar (fine grained) bands. Continues on next page →

→ **Figure 5.3.3.4-2 (continued). c) Sample Schoef 7, only a couple of feldspar porphyroclasts survived the intense deformation. d) Sample Schoef 8, sigmoidal monomineralic bands of quartz and feldspar. e) Sample Schoef 617, typical *S-C* structures and mica grains oriented parallel to the foliation. f) Sample Schoef 617, enlargement of the former picture. g) Sample Tit 760, showing the typical banding of quartz and feldspar. h) Sample Tit 125, showing relatively large feldspar mantled porphyroclasts and sigmoidal polycrystalline quartz ribbons.**

Feldspar composition

In the same way as in the Saunstein dyke, the partially recrystallized feldspars of the samples Tit 125 and Tit 711 were analyzed. The results can be found in Appendix 4.

The analyses corroborate the pattern observed in the Saunstein dyke, in which K-rich feldspar cores are mantled by recrystallized Na-rich grains. The average composition of feldspars is $An_0 Ab_5 Or_{96}$ in cores and $An_4 Ab_{95} Or_1$ in mantles in Tit 125, $An_0 Ab_5 Or_{95}$ in cores and $An_9 Ab_{90} Or_1$ in mantles in Tit 711. K-feldspar was therefore replaced by albite at the margins, which points to a fluid-assisted deformation.

Quartz texture

Apart from the Saunstein and Untermittlerdorf dykes, the quartz textures were analyzed on two further examples of sinistrally sheared granites by means of EBSD.

The granite dyke of the outcrop Schneidermühl was strongly sheared during D_3 . The rock is foliated and shows a couple of milky white, almost monomineralic bands of quartz embedded in a light brown mass of mixed quartz and feldspar. Both areas of the rock were sampled: The quartzitic one is represented by the sample Tit 93 and the quartzofeldspathic one by the sample Tit 396 (see Figs. 5.3.3.4-1f, 5.3.3.4-3, 5.3.3.4-4). In sample 93, poorly-developed *S* and *C* planes are traced by some alternating sigmoidal bands of quartz and feldspar. The angle between both planes is around 10° - 15° . No SPO is shown by quartz grains. In sample Tit 396, *S* and *C* planes are parallel to each other.

At the Heiblmühle locality, sample Tit 760 (Fig. 5.3.3.4-2g, 5.3.3.4-5) has a similar appearance as Schoef 1 (see Fig. 5.3.3.4-1d) at the hand specimen scale, although with a slightly better developed mylonitic foliation. The angle between *S* and *C* planes averages 15° .

The resulting texture is defined in both localities by a strongly developed single maximum around the *Y*-axis of the finite strain ellipsoid, in the same manner as in the Saunstein and the Untermittlerdorf dyke. *a*-axes are clustering in three maxima, being the strongest one sub-parallel to the direction of the stretching lineation, pointing to a

sinistral sense of shear. After Stipp et al. (2002) this pattern is diagnostic for grain boundary migration recrystallization and its transition towards subgrain rotation recrystallization, which is in good agreement with a deformation temperature of 500-550°C. As already observed in other cases, the fine-grained, quartzofeldspathic specimen of Tit 396 tends to show a much weaker texture than the coarser-grained ones, in which monomineralic domains occur. This is supposed to be due to the activation of grain boundary sliding as deformation mechanism.

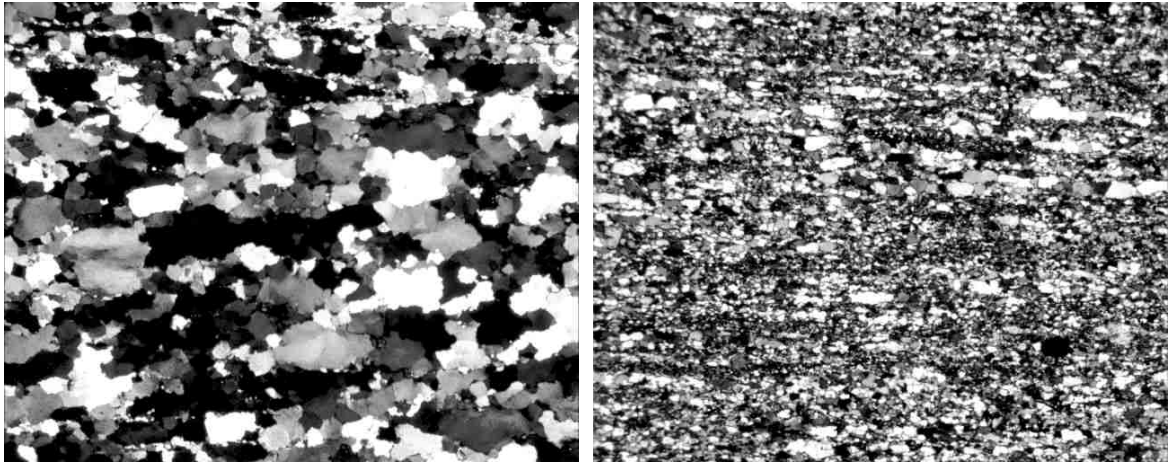


Figure 5.3.3.4-3. Left: Sample Tit 93, recrystallized quartz grains with sutured boundaries and similar size. Right: Sample Tit 396, very fine banding of quartz and feldspar. Both pictures have a total width of 5.5 mm.

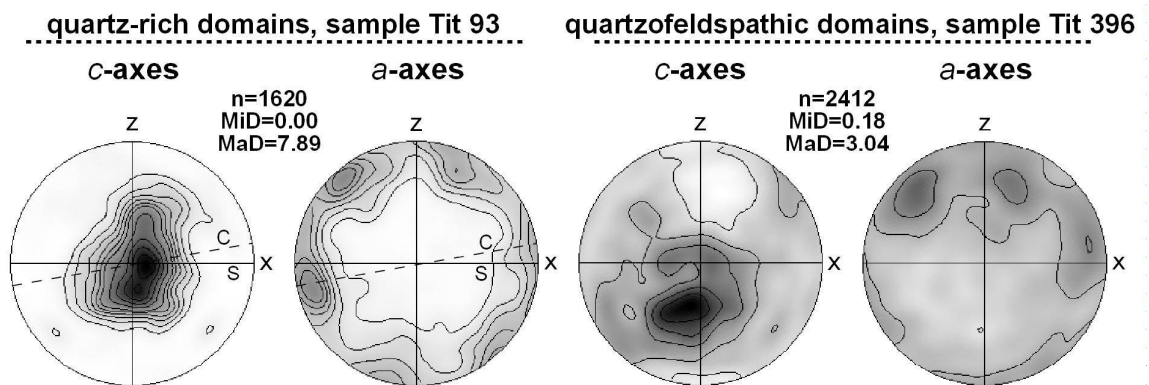


Figure 5.3.3.4-4. Quartz *c* and *a*-axes patterns of two samples of the Schneidermühl dyke obtained by means of EBSD. Equal area projection, lower hemispheres. *n* = number of data points, *MiD* = minimum density, *MaD* = maximum density. Density contours at 0.5; 1; 1.5; 2; 2.5; 3; 4; 5; 6; 7. Black represents the maximum density. Data points were smoothed with a Gaussian of 10° full width half maximum.

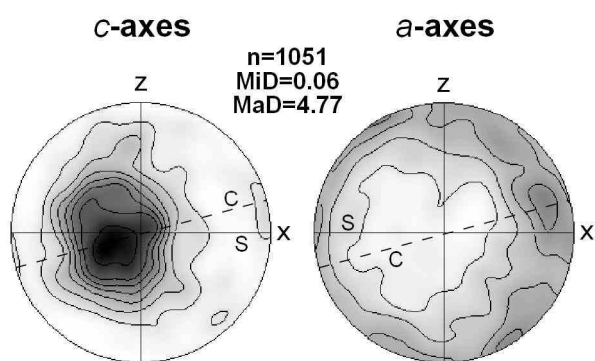


Figure 5.3.3.4-5. Quartz *c* and *a*-axes patterns of Tit 760 obtained by means of EBSD. Equal area projection, lower hemispheres. *n* = number of data points, *MiD* = minimum density, *MaD* = maximum density. Density contours at 0.5; 1; 1.5; 2; 2.5; 3; 4. Black represents the maximum density. Data points were smoothed with a Gaussian of 10° full width half maximum.

Phengite barometry

Many of the sheared granites bear white mica and have the limiting assemblage needed for the application of the phengite geobarometer of Massonne and Szpurka (1997). Three of them were chosen to analyse their white mica crystals.

The analyzed samples contain igneous and synkinematic white mica, whose composition can provide some clues about the intrusion depth of the granitic body that contains them and the conditions during the deformation, respectively. Table 5.3.3.4-1 summarizes the results obtained by the electron microprobe (see full results in Appendix 3). These were plotted in the PT diagram of Fig. 5.3.3.4-6, in which also the barometry results of the Saunstein and the Untermittlerdorf dyke are depicted for comparison.

	Schoef 617, core	Tit 711, average	Tit 125	
			core	cleavage domains
Si p.f.u. (mean ± std. dev.)	3.176 ± 0.016	3.189 ± 0.022	3.097 ± 0.011	3.137 ± 0.021
pressure (GPa)	0.69 ± 0.04	0.72 ± 0.05	0.49 ± 0.03	0.38 ± 0.05
depth (km)	25.5 ± 1.5	26.7 ± 2.0	18.2 ± 1.0	13.9 ± 0.7

Table 5.3.3.4-1. Si content data used for geobarometry. The listed values were plotted in the PT diagram of Fig. 5.3.3.4-6.

In sample Tit 711 (Hochholz locality) two populations of white mica were analyzed. The first one is constituted by large porphyroclast, in which the composition at rim and core positions was measured. The second one consists of small porphyroclasts, in which only the composition in the core was measured. All analyses provided similar results independently of the population or the position in the crystal. Thus, the Si content of these white mica crystals is supposed to reflect the conditions during the emplacement in all cases. The Ti content is high in all cases, pointing to a magmatic origin of the mica.

In sample Tit 125 (Steinberg locality), the difference in the Si content at cores and rims of magmatic grains is noticeable. A second population of very fine-grained white mica of cleavage domains was also analysed. This population has a clearly higher Si content than the magmatic generation. The Ti content is, as expected, higher in magmatic grains.

As already discussed in chapters 5.3.3.2 and 5.3.3.3, the analysed white micas contain a larger amount of components than those regarded in the KMASH system, in which the applied geobarometer was calibrated. Therefore, the pressure results obtained might be somewhat imprecise. The Fe content is relatively high compared to the Mg content, which might derive in underestimated pressures. Na has a similar effect, whereas the presence of fluorine (relatively high in sample Tit 125) might lead to the overestimation of pressures.

5.3.4. Deformation at the Bayerischer Pfahl shear-zone system: some new results

In order to allow a better interpretation of the results obtained for the sinistrally sheared granites, some complementary investigations were carried out on rocks of the Bayerischer Pfahl shear-zone system, and more concretely of the Bayerischer Pfahl and Buchberger Leite shear zones. The locations of the sampling sites are shown in Fig. 5.3.4-1 (for more information see Appendix 2).

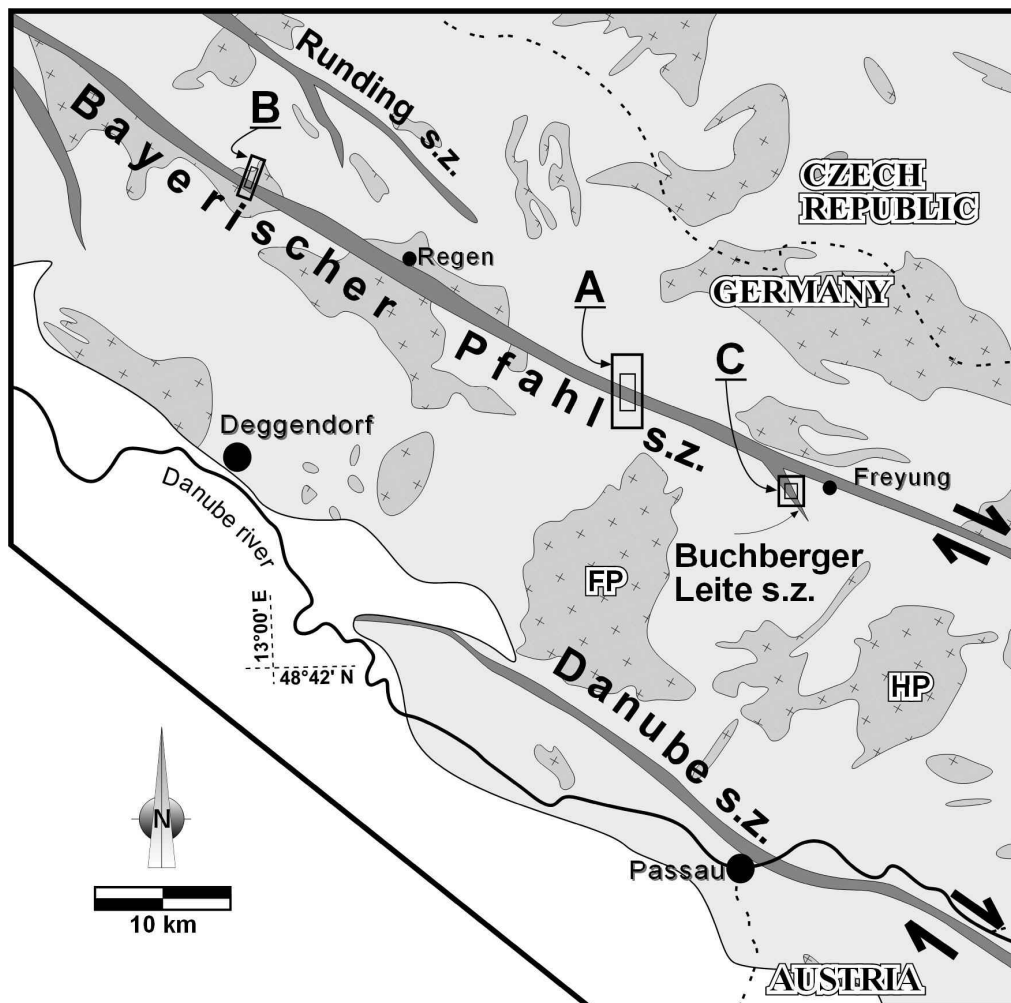


Figure 5.3.4-1. Geological map of the south-eastern part of the Bohemian Massif, simplified after Bundesanstalt fuer Geowissenschaften und Rohstoffe (1993). White: post-Variscan cover. Light grey: metamorphic rocks. Medium grey with crosses: intrusive rocks, mainly granites and granodiorites. Dark grey and thick lines: major faults and fault rocks. FP Fürstenstein pluton, HP Hauzenberg pluton. The locations of the sampling sites at the Bayerischer Pfahl shear-zone system are marked with rectangles and capital letters. A: Große Ohe, samples Grf 4 to 13. B: Patersdorf, samples Pat 10 to 12. C: Buchberger Leite, sample Frg 91.

5.3.4.1. The Bayerischer Pfahl shear zone at the Große Ohe

Introduction

At this locality (Fig. 5.3.4-1 A) a complete profile across the Bayerischer Pfahl shear zone was studied (Fig. 5.3.4.1-1). Here the shear zone separates gneisses to the north from dark-coloured diatexites to the south. Judging from the minerals present in the mylonites found in this area, the protolith is supposed to be a two-mica granite, apart from gneiss and diatexite. From north to south, the following samples were taken (Fig. 5.3.4.1-1, 5.3.4.1-2, more details in Appendix 2):

- Sample Grf 6, gneiss.
- Samples Grf 8, 9, 13, 5, mylonite.
- Sample Grf 4, diatexite.

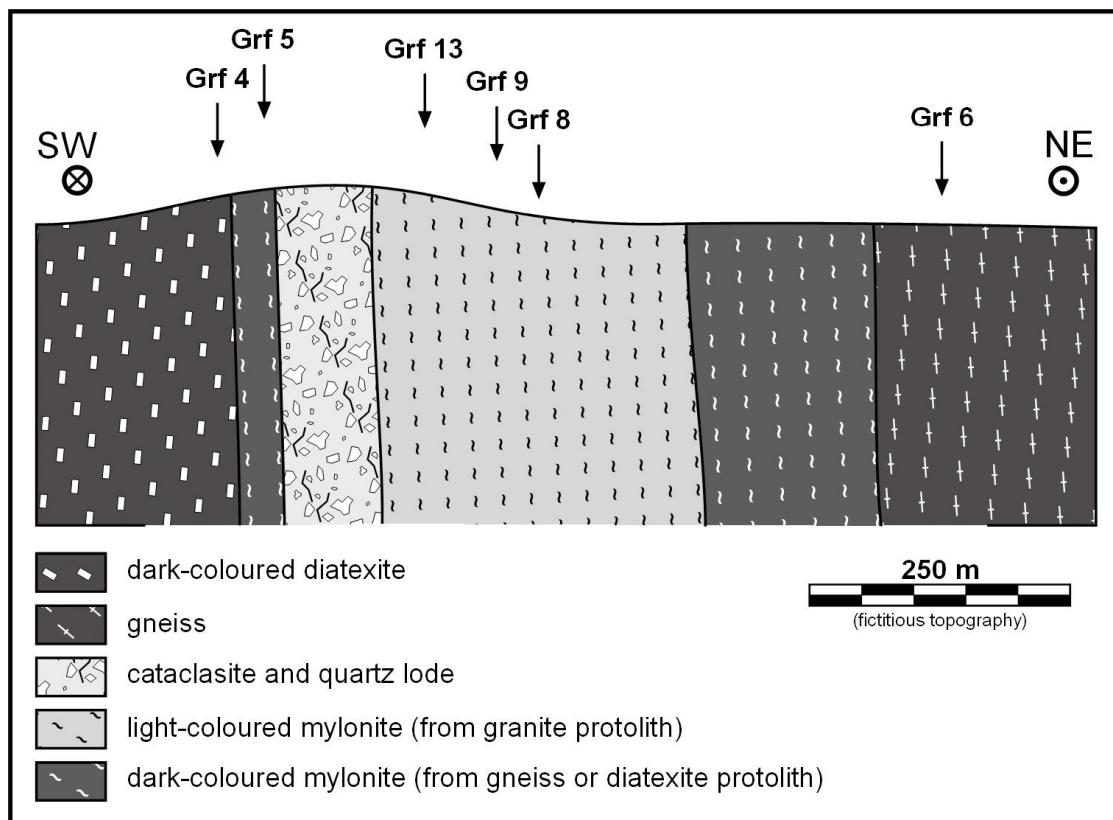


Figure 5.3.4.1-1. Geological cross section across the Bayerischer Pfahl shear zone at the Große Ohe locality, based on geological map 1:25000 of Teipel et al. (in press). Location of sampling sites was projected in the cross-section plane.

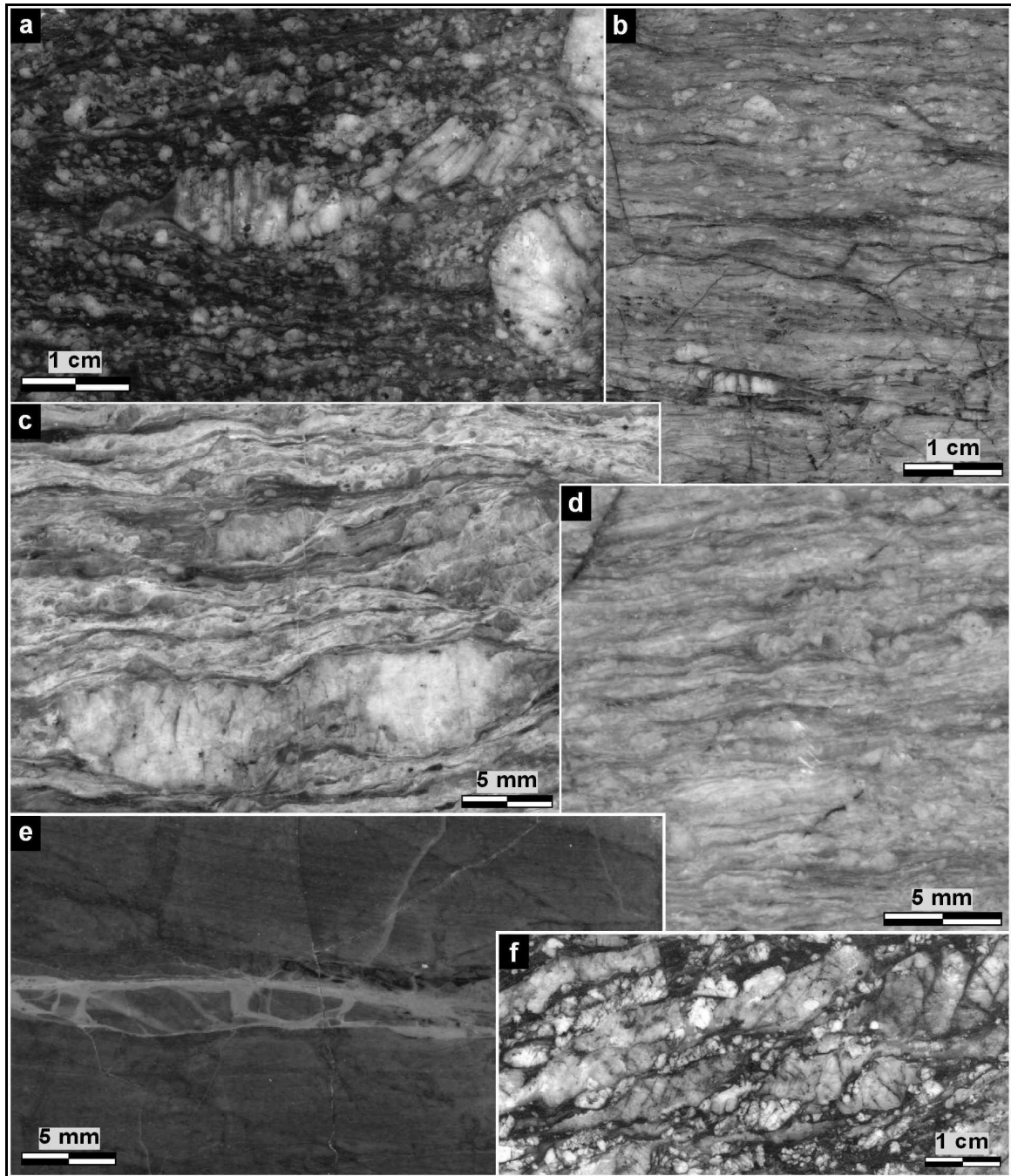


Figure 5.3.4.1-2. Samples of mylonites of the Bayerischer Pfahl shear zone at the Große Ohe locality shown from north to south, XZ-sections. a) Grf 6, gneiss (protomylonite). b) Grf 8, mesomylonite with a relatively strong brittle overprint in the lower half of the photo. c) Grf 9, mesomylonite with a pronounced *S-C* structure. d) Grf 13, meso to ultramylonite. e) Grf 5, ultramylonite with late quartz-epidote veins. f) Grf 4, dark-coloured diatexite (protomylonite), feldspars show here a dominant brittle behaviour.

As typically observed everywhere along the Bayerischer Pfahl shear zone, the shearing during a long time span and, consequently, under a progressively dropping temperature, has caused a rough zonation across the shear zone. Thus, we can imagine

a high-strain domain along the central axis of the shear zone, where the deformation concentrated in space and in time. Brittle deformation tends to concentrate in narrower bands than ductile deformation. Therefore, diverging from this imaginary axial zone, we will progressively find rocks which show less strain and higher-tempered fabrics. The reality in the field is, of course, not that simple and a well developed, symmetrical zonation of the deformation intensity, whether ductile or brittle, is rarely found.

We are interested in the ductile evolution of the Bayerischer Pfahl shear-zone system. From now on, the brittle component of the deformation will be therefore not treated in depth.

Based on the ideal zonation pattern described above, it is expectable to find high-strain domains approximately at the central plane of the shear zone. Thus, at the central zone it is usual to find ultramylonites, whereas heading to the north or to the south, we will find meso- and protomylonites, and finally the country rocks, i.e. gneisses and diatexites, which can be considered to be protomylonites themselves near the shear zone.

Macroscopically, these rocks are similar to the sinistrally sheared granites described above. The orientation of shear planes and the shear sense are the most important differences. The shear planes strike approximately N110E at the Große Ohe locality, although fluctuations can occur (see Appendix 2). Vertical or strongly dipping foliations are most common. The stretching lineation is normally sub-horizontal or plunges gently to the WNW or ESE. The sense of shear is always dextral.

Microfabrics

The quartz is usually completely recrystallized, building equigranular, elongated aggregates. The grain boundaries are serrated, sometimes displaying deflections at 90°. The boundaries tend to be finer serrated and fuzzier than in sinistrally sheared granites. An oblique foliation is usually found, although not strongly developed (Fig. 5.3.4.1-3). Small misorientations between adjacent grains and transitions between subgrains and recrystallized grains can be found in some areas, pointing to a more important contribution of SGR recrystallization than in sinistrally sheared granites. If present, subgrains are oriented parallel to the prism planes.

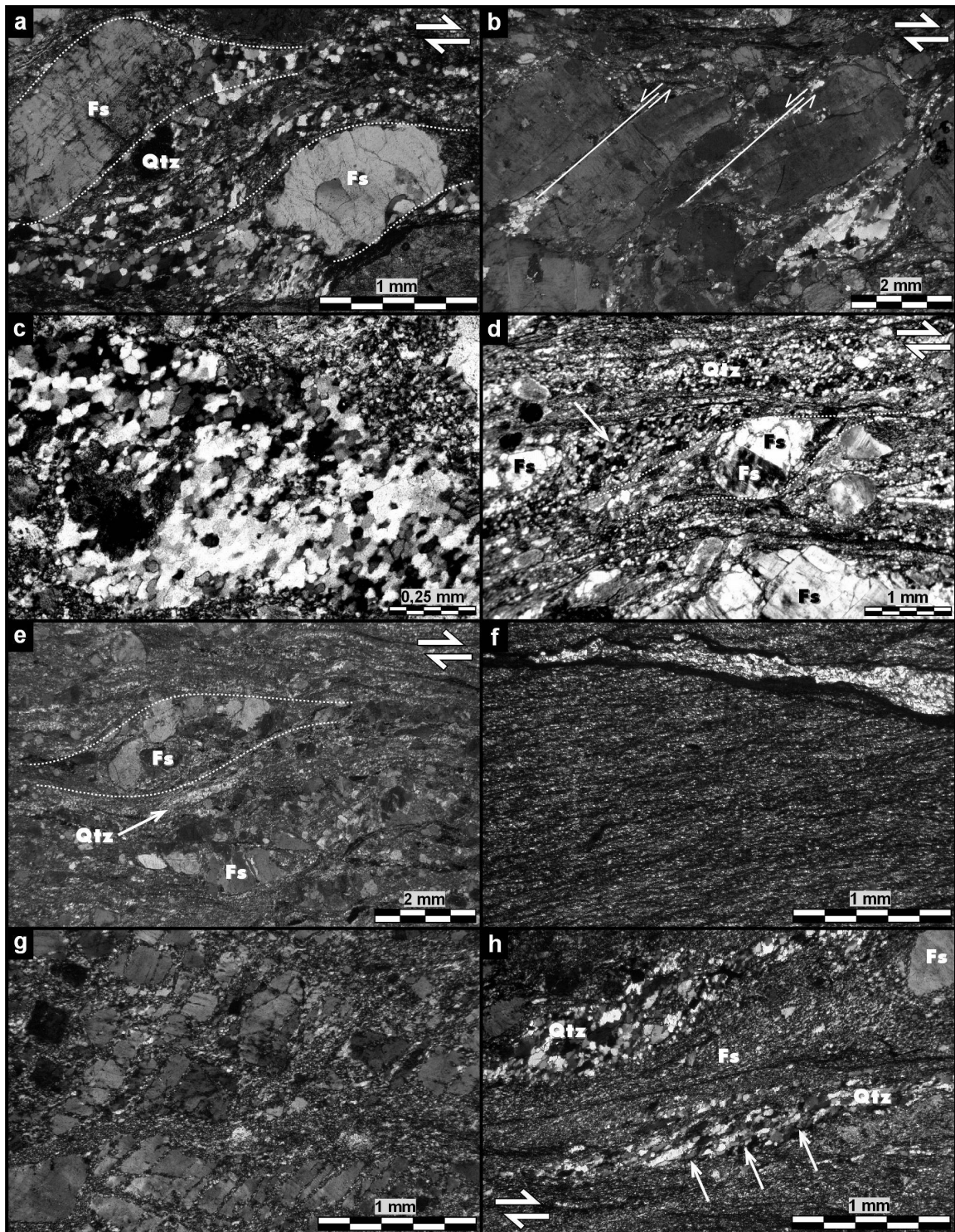


Figure 5.3.4.1-3. Microstructures at the Große Ohe profile, XZ-sections, crossed polarizers. a) Sample Grf 6, σ -clasts of K-feldspar surrounded by sigmoidal bands of quartz. The K-feldspar is generally not recrystallized or only locally, whereas the quartz builds recrystallized, equigranular aggregates. b) Sample Grf 6, K-feldspar porphyroclast showing antithetic microfaults. c) Sample Grf 8, this aggregate of recrystallized quartz shows evidence for SGR being the main recrystallization mechanism: Note the transitions between zones of subgrains (lower central part of the picture) and zones of new grains (upper left and lower right parts of the picture), all of them showing similar sizes. Continues on next page →

→ **Figure 5.3.4.1-3 (continued). d) Sample Grf 9, the quartz here is completely recrystallized displaying sigmoidal bands of grains with a weak SPO (arrow). The feldspar is essentially brittle (note the large clast at the lower part of the picture). Though some fine-grained bands made of feldspar are observed, it is not always easy to determine, what kind of role played recrystallization and cataclasis in their formation. e) Sample Grf 13, *S-C* structures pointing to a dextral shear sense. The quartz forms recrystallized bands and the behaviour of the feldspar has an important brittle component. f) Sample Grf 5, very fine-grained ultramylonite with quartz vein at the upper part of the picture. g) Grf 4, a large K-feldspar porphyroclast showing a mixture of microcracking and localized recrystallization. h) Grf 4, alternating bands of recrystallized quartz (coarser grained) and feldspar (finer grained). The borders of the quartz grains are fine serrated and a SPO (arrows) is present.**

Feldspar shows a transitional brittle/ductile behaviour. Feldspar porphyroclasts are normally broken and recrystallized at borders and cracks. Some of the porphyroclasts developed a core-and-mantle structure with a very sharp boundary between core and mantle, i.e. without a transition zone in between in which subgrain structures occur. In general, the fine-grained feldspar bands may be produced by recrystallization but, especially in the specimens where the feldspar behaviour tends to be more brittle, the cataclastic flow can also play a role in their formation.

The dextral shear sense can be inferred from oblique foliations, σ -clasts, mica fishes, *S-C* structures and monomineralic sigmoidal bands (Fig. 5.3.4.1-3).

Quartz texture

The determination of the quartz texture on samples of the Große Ohe profile involves an important problem: Since the deformation took place in a wide time and temperature span, old deformation stages were subsequently overprinted. For the study of the quartz texture, we delimited and scanned the areas of the samples with the weakest brittle overprint, trying to avoid late quartz veins and cataclastic bands. As we will see, even when selecting only suitable areas of the sample, caution is required when interpreting the resulting patterns (Fig. 5.3.4.1-4).

There is no well-defined texture in sample Grf 13, possibly due to the small grain size that promotes the deformation by means of grain boundary sliding and prevents the texture development. The texture of sample Grf 5 seems to result rather from a late quartz fill in voids than from deformation by dislocation creep. The samples 6, 9 and 4 show a *c*-axes maximum around (or next to) the *Y*-axis of the finite strain ellipsoid. As already mentioned for the sinistrally sheared granites, this texture points to slip along prism planes in $\langle a \rangle$ direction, which is diagnostic for medium grade deformation temperatures. The maxima are shifted off the centre of the stereographic plot, maybe because the movement direction, and therefore the orientation of the stretching

lineation, fluctuated slightly in the course of deformation. Unfortunately, a -axes do not build well-defined patterns. The a -axes in the samples 9 and 4 seem to scatter in all directions perpendicular to Y , which points to a higher temperature as in the sample 6, where the a -axes tend to concentrate preferentially in one maximum (Passchier and Trouw, 1996).

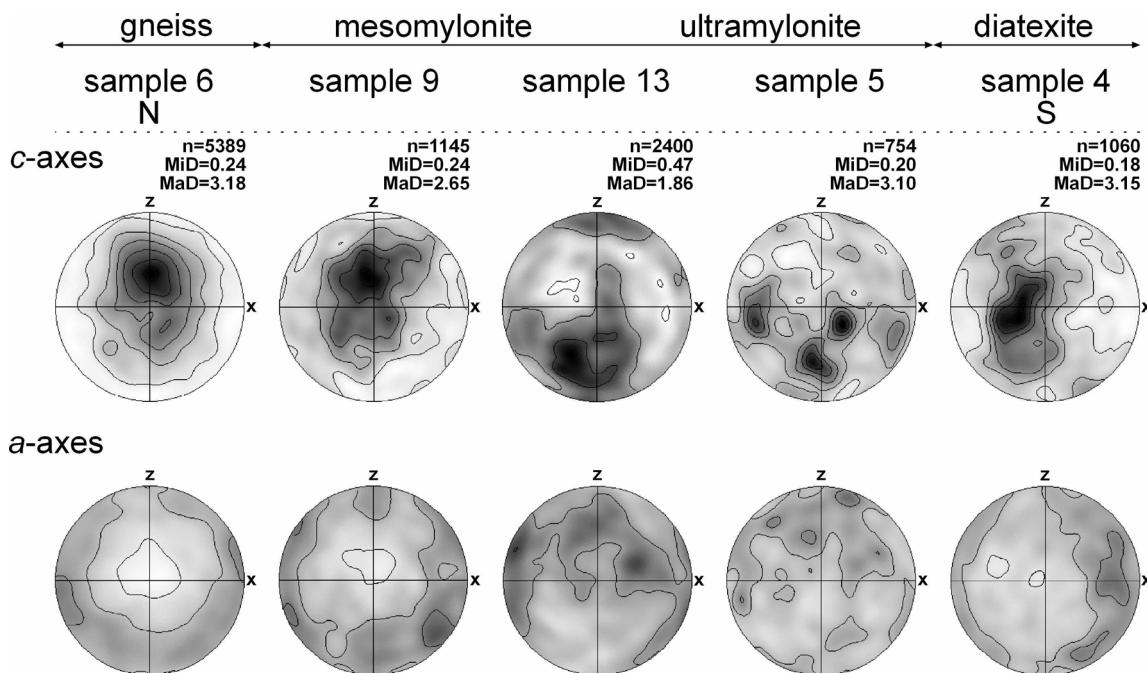


Figure 5.3.4.1-4. Quartz c - and a -axes patterns obtained at the Große Ohe profile by means of EBSD. Equal area projection, lower hemispheres. n = number of data points, MiD = minimum density, MaD = maximum density. Density contours at 0.5; 1; 1.5; 2; 2.5; 3. Black represents the maximum density. Data points were smoothed with a Gaussian of 10° full width half maximum.

A well developed, symmetrical zonation of the textures, in which lower-tempered patterns substitute the higher-tempered ones towards the axial zone of the shear zone, is not observed. Furthermore, towards the axial zone the patterns do not tend to be lower-tempered, but they rather tend to simply disappear.

Phengite barometry

As already mentioned, most of the mylonites found in this profile are supposed to have developed from a granite protolith. This is so due to its mineralogy, which is different from that of the country rocks and similar to that of typical granites, with quartz, K-feldspar, plagioclase and white mica. The phase biotite/phlogopite is normally not present, and thus the limiting assemblage for the application of the geobarometer of Massone and Szpurka (1997) is not available. Only in the sample Grf 9 we could find

some small amounts of biotite; however it is not clear whether their origin is magmatic or post-magmatic.

In the sample Grf 9, the white mica is available in two different generations: magmatic crystals (porphyroclasts) and very fine synkinematic crystals. We analyzed both of them in order to obtain an estimation for the pressure governing the emplacement of the protolith and its later deformation. The analyses provided a Si content of 3.049 ± 0.011 atoms p.f.u. in magmatic crystals, as depicted in Fig. 5.3.4.1-5.

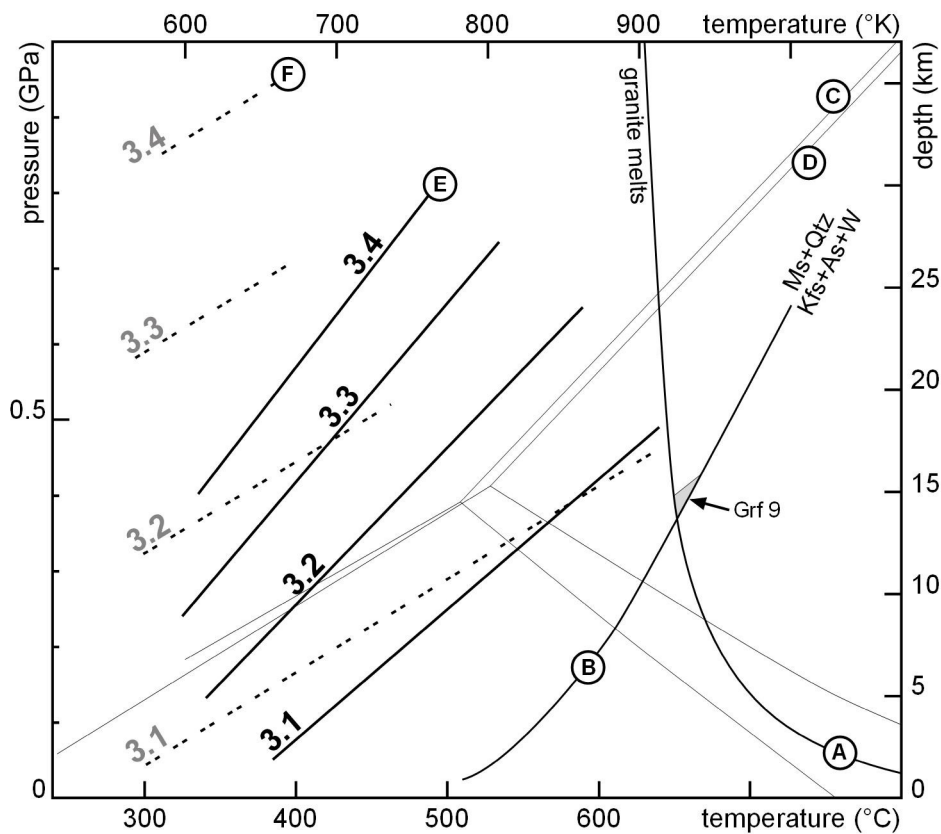


Figure 5.3.4.1-5. PT diagram showing the results of the application of the phengite geobarometer of Massonne and Szpurka (1997). A) Solidus of water-saturated haplogranite after Johannes and Holtz (1996). B) Stability of white mica in presence of quartz after Chatterjee and Flux (1986), see mineral abbreviations in Appendix 5. Stability fields of aluminium silicate polymorphs are shown for reference C) after Hemingway et al. (1991) and D) after Bohlen et al. (1991). E) Phengite geobarometer: Si-content isopleths after Massonne and Szpurka (1997). Number of Si atoms p.f.u. are indicated on each isopleth. F) Phengite geobarometer: Si-content isopleths after Massonne and Schreyer (1987), not used for calculations. The shaded area was constructed taking into account the standard deviation of all analyses as maximum limit and the crossing point between A and B as minimum limit. This area represents the PT window in which white mica might have crystallised.

The synkinematic crystals show a large standard deviation and their Si content has therefore no defined tendency. The extrapolated 3.049 isopleth falls next to the crossing point between the granitic solidus and the Ms-out line. Since the PT field in which white mica crystallised must be above this crossing point, the pressure corresponding to the obtained Si content must be $0.37 +0.03/-0.00$ GPa. This would mean that the protolith of the mylonites found in the Große Ohe profile intruded at around $13.8 +1.0/-0.1$ km.

This emplacement depth clearly differs from the one obtained for the sinistrally sheared dykes and it would suggest in principle that the present rock intruded later in the crust, which is compatible with the lower-tempered fabrics observed here. However, since the requirements for the application of the geobarometer are not surely given, the results cannot be regarded as conclusive.

Both white mica generations have contrasting Ti contents, the higher one belonging to the magmatic population, in agreement with the general tendency pointed out by Zen (1988). Again, it must be emphasized that the analysed white micas contain a larger amount of components than those regarded in the KMASH system, in which the applied geobarometer was calibrated (see discussion about the effects of Fe, Na and F in chapters 5.3.3.2, 5.3.3.3, 5.3.3.4). Therefore, the pressure results obtained might be somewhat imprecise.

5.3.4.2. The Bayerischer Pfahl shear zone and the Patersdorf granite

Introduction

The medium-grained Patersdorf granite is exposed in the surroundings of the town Patersdorf, 11 km north-west of Regen (see Fig. 5.3.4-1B and Appendix 2). After Ott (1983) this granite body is crosscut by the Bayerischer Pfahl shear zone. Since it is a muscovite-bearing granite containing the critical assemblage necessary for the application of the phengite geobarometer (Massonne and Szpurka, 1997), the first intention of the analysis in this locality was to compare fabrics and emplacement depth between the blocks at both sides of the shear zone across a profile. Unfortunately, the study of the rocks under the microscope revealed that white mica is only present in the Patersdorf granite north of the shear zone. This can be explained in two ways:

- The Bayerischer Pfahl shear zone had a vertical component that sank the southern block. Thus, today we find deeper parts of the Patersdorf granite in the north, in which white mica is stable, and shallower parts in the southern block that were at a maximum depth of about 13 km at the time of intrusion, where white mica is not stable.
- The granites that crop out north and south of the shear zone constitute different magma batches with different geochemical characteristics.

The second explanation seems more plausible, since the paragneisses north of the Bayerischer Pfahl shear zone are supposed to belong to shallower crustal levels than the migmatites south of it. Furthermore, Beer (1981) proposed the Bayerischer Pfahl shear zone to have a NE-side-down vertical component. The discussion of this matter is out of the scope of this work and must be kept in mind as a perspective for new investigations.

Due to the aforementioned unexpected eventuality, and together with the fact that no suitable outcrops of deformed granite were found south of the shear zone, the study was restricted to the sampling sites north of the shear zone.

Three samples were studied (Figs. 5.3.4.2-1, 5.3.4.2-2): two samples of deformed granite (Pat 10 and Pat 11, 200 and 150 m northeast of the shear-zone axis, respectively) and one mylonite sample (Pat 12, immediately north of the shear-zone axis). The granite is composed mainly of quartz, plagioclase, K-feldspar, biotite, white mica and chlorite.

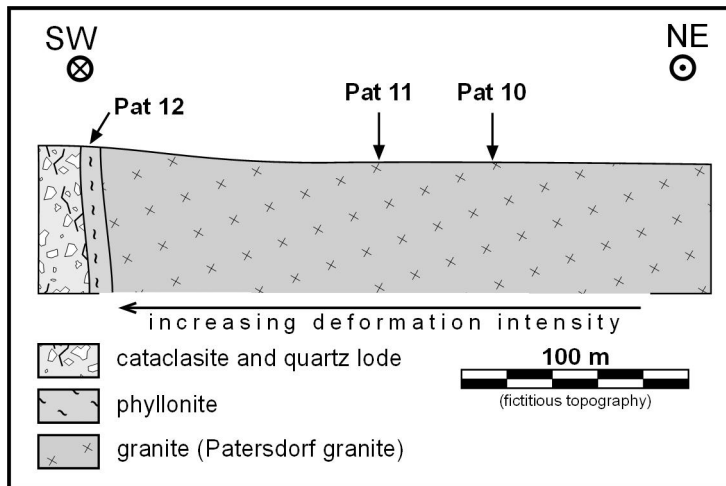


Figure 5.3.4.2-1. Geological cross section across the northern part of the Bayerischer Pfahl shear zone at the Patersdorf locality. Location of sampling sites was projected in the cross-section plane.

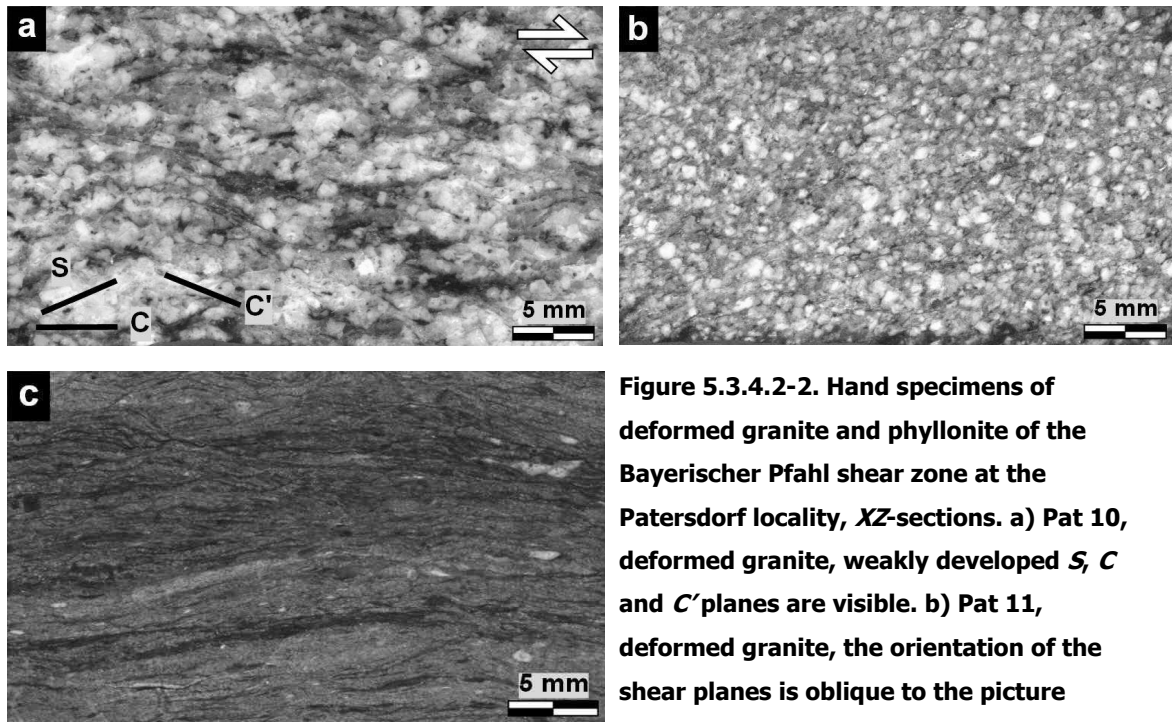


Figure 5.3.4.2-2. Hand specimens of deformed granite and phyllonite of the Bayerischer Pfahl shear zone at the Patersdorf locality, XZ-sections. a) Pat 10, deformed granite, weakly developed *S*, *C* and *C'* planes are visible. b) Pat 11, deformed granite, the orientation of the shear planes is oblique to the picture margins (top right to bottom left). c) Pat 12, phyllonite.

Microfabrics

Sample Pat 10 is more weakly deformed than Pat 11, which is to be expected since Pat 11 was taken closer to the Bayerischer Pfahl shear zone. Apart from the intensity of the deformation, both samples share a common fabric. The mylonitic foliation is poorly developed, strikes NW—SE and dips steeply or is vertical. The stretching lineation is also poorly developed and lies sub-horizontal or gently dipping. *S-C* structures are present, although not strongly developed. As shown in Fig 5.3.4.2-3, the deformation is weak in both samples. Most of the quartz is recrystallized, building aggregates of recrystallized

grains similar in size with serrated boundaries, some of them with deflections at 90°. In some areas of the thin sections it is possible to recognize triple points indicating some late static recrystallization. All grains, even old, large ones, have a strain-free appearance. The feldspar crystals are sometimes recrystallized at the borders, but this is rather the exception, since most of the grains remained unchanged by the deformation, maybe not due to a low temperature, but maybe rather to the low strain (Tullis and Yund, 1977). Myrmekites are often found. The plagioclase crystals are strongly sericitized. White mica and biotite, the latter partially transformed into chlorite, are arranged parallel to the foliation planes. The deformation is clearly stronger in the sample 12, in which the feldspars were transformed into white mica for the most part; thus, we can speak in this case about a phyllonite, i.e. a mylonite that is rich in phyllosilicates.

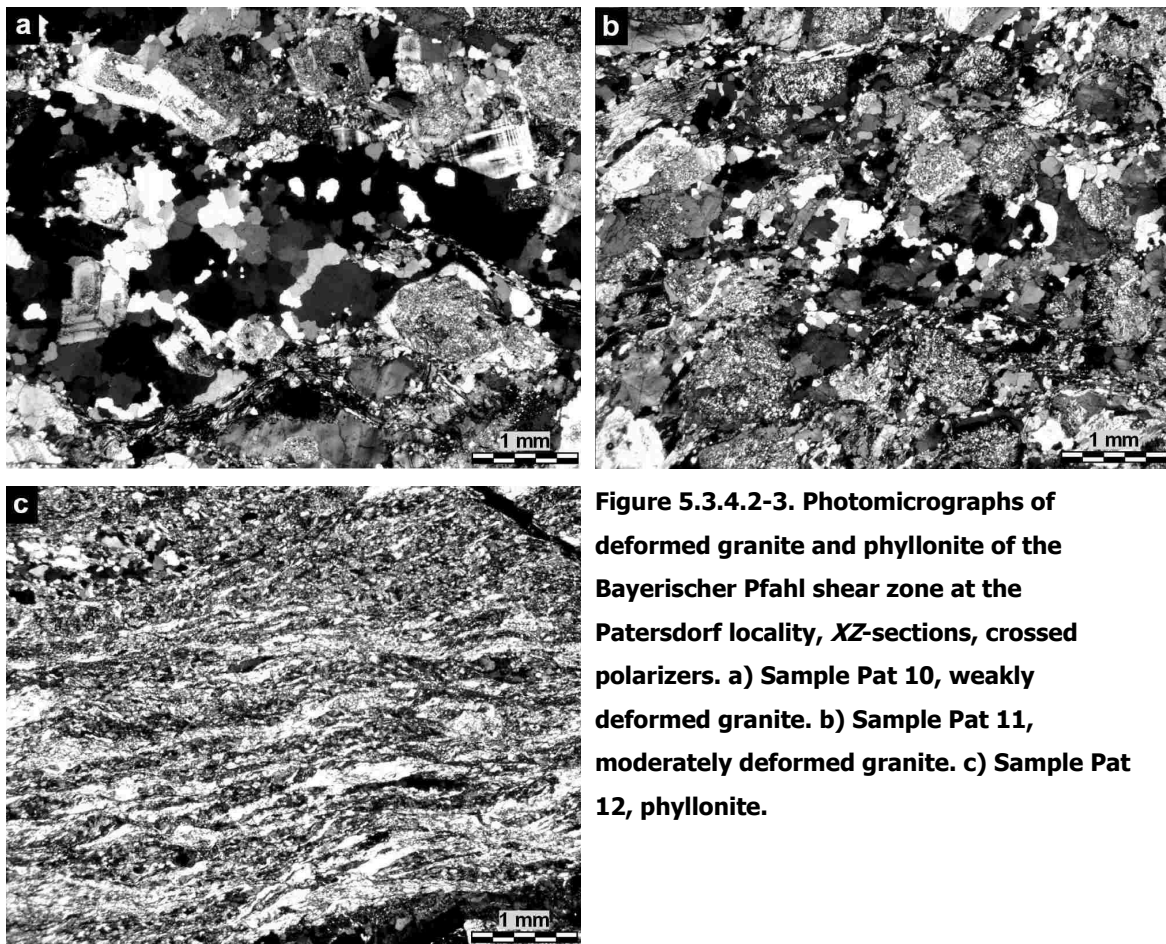


Figure 5.3.4.2-3. Photomicrographs of deformed granite and phyllonite of the Bayerischer Pfahl shear zone at the Patersdorf locality, XZ-sections, crossed polarizers. a) Sample Pat 10, weakly deformed granite. b) Sample Pat 11, moderately deformed granite. c) Sample Pat 12, phyllonite.

Quartz texture

Samples Pat 10, Pat 11 and Pat 12 were scanned by means of EBSD in order to obtain their quartz textures. The resulting *c*- and *a*-axes patterns can be viewed in Fig. 5.3.4.2-4. Sample Pat 12, located at the axis of the shear zone, displays no well defined LPO

pattern. The other two samples show a concentration of c -axes around (or next to) Y . Here again, the maxima are shifted off the centre of the plot, but this time it is probably due to the fact that the foliation and the lineation are not well developed and the sample was probably not exactly cut parallel to the XZ plane of the finite strain ellipsoid. The a -axes build three maxima perpendicular to Y .

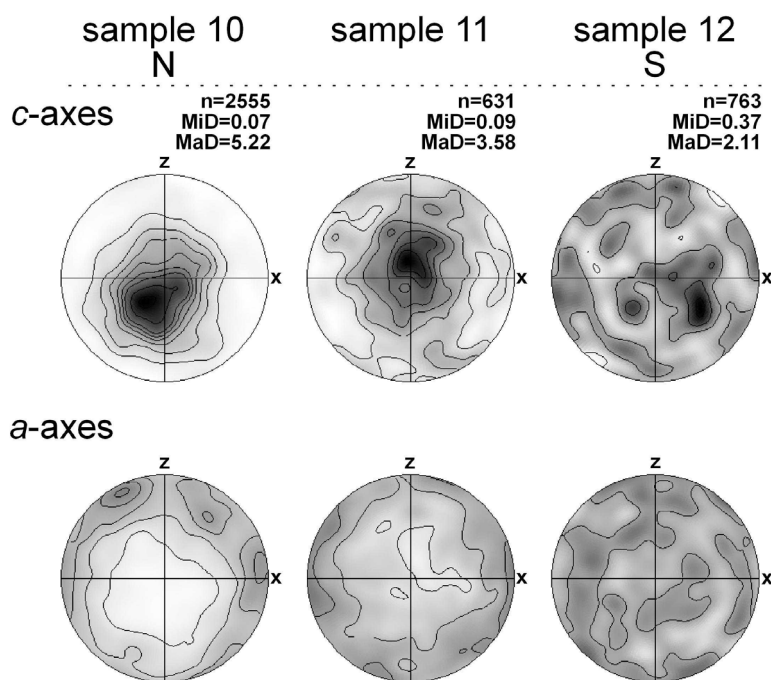


Figure 5.3.4.2-4. Quartz a - and c -axes patterns of samples Pat 10, 11 and 12 obtained by means of EBSD. Equal area projection, lower hemispheres. n = number of data points, MiD = minimum density, MaD = maximum density. Density contours at 0.5; 1; 1.5; 2; 2.5; 3; 4; 5. Black represents the maximum density. Data points were smoothed with a Gaussian of 10° full width half maximum.

Judging from the observed patterns, it seems that the sample Pat 10 is stronger deformed than Pat 11, since the texture is much better developed in the first one. This is just the opposite as observed on the hand specimens and under the microscope. A possible explanation for this is that the deformation lasted for a longer time in Pat 11 and, therefore, the last increment of the deformation occurred under a slightly lower temperature involving some rhomb $\langle a \rangle$ slip, dealing to a partial destruction of the former, higher-tempered texture and originating a slight redistribution of c -axes towards an inclined single girdle. Another possible explanation is a progressively bigger contribution of grain boundary sliding during grain size reduction in sample Pat 11. The continuous deformation towards and under greenschist facies conditions and the formation of big amounts of white mica where probably the causes that destroyed the texture in sample Pat 12.

Phengite Barometry

The critical assemblage for the application of the phengite geobarometer of Massonne and Szpurka (1997) is present in Pat 10 and Pat 11, but not in Pat 12, where the biotite was probably consumed during the deformation. The results of some white mica

analyses in sample Pat 12 are, however, listed in Appendix 3. In Pat 10 and Pat 11 we analyzed:

- medium-sized crystals, which are supposed to be of igneous origin,
- small-sized crystals, which are also of igneous origin, but can change their composition more easily than the larger ones during deformation, and
- white mica included in feldspar, which might in part have grown from feldspar in a late- to post-magmatic stage.

Taking into account the standard deviation of the measurements, the different groups of white mica are indistinguishable from each other regarding the Si content. Thus, the only information that we can extract from the results is the Si content representative for the maximum emplacement depth. The crystals that are supposed to have suffered the minimum post-magmatic overprint are the medium-sized ones in the sample Pat 10. Therefore, their Si content was used to be plotted in the P-T diagram of Fig 5.3.4.2-5. We obtained 3.106 ± 0.018 Si atoms p.f.u. (see Appendix 3). The crossing point between the solidus line and the 3.106 isopleth gives as a result a pressure of 0.51 ± 0.05 GPa and a maximum emplacement depth of 19.0 ± 1.7 km.

No synkinematic white mica was found in aggregates big enough to be analyzed, except in the sample Pat 12, where the geobarometer cannot be applied because of the lack of biotite. An estimation of the pressure governing the deformation can therefore not be made.

It is interesting that the white mica of Pat 12 shows a high Ti content. After Zen (1988) white mica with more than 0.6 wt% TiO₂ are candidates for magmatic origin. However, the white mica of Pat 12 is without any doubt metamorphic and not igneous. The mean TiO₂ content of igneous white mica in Pat 10 and Pat 11 is also above 0.6 wt%.

Once more, it must be emphasized that the analysed white micas contain a larger amount of components than those regarded in the KMASH system, in which the applied geobarometer was calibrated (see discussion about the effects of Fe, Na and F in chapters 5.3.3.2, 5.3.3.3, 5.3.3.4). Therefore, the pressure results obtained might be somewhat imprecise.

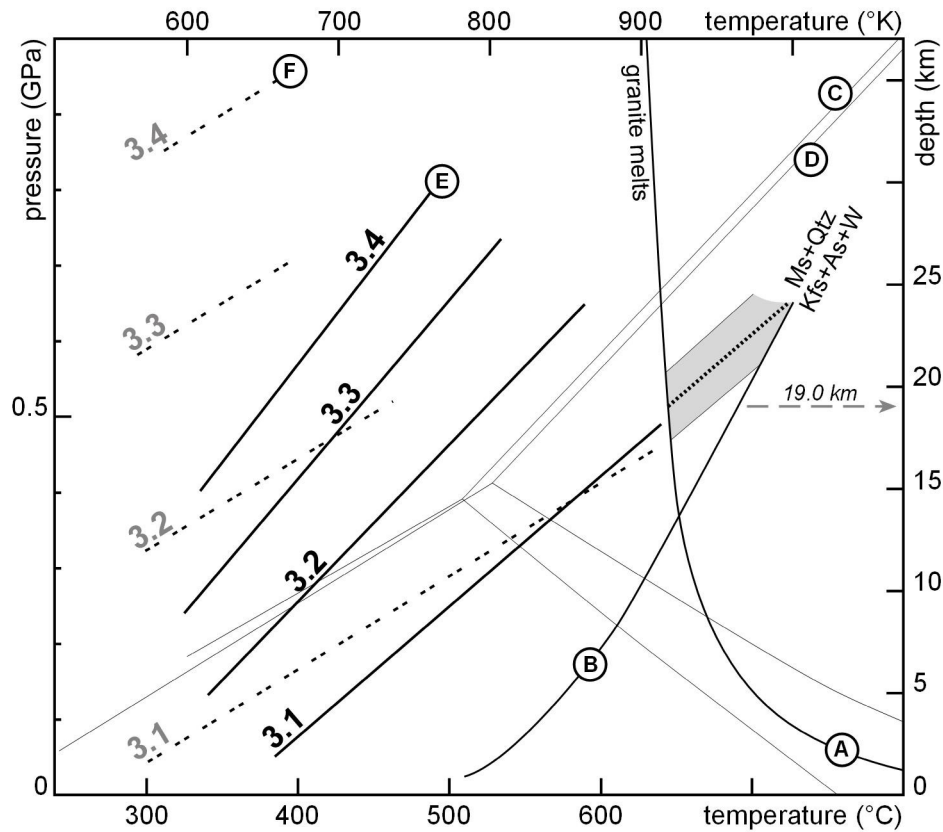


Figure 5.3.4.2-5. PT diagram showing the results of the application of the phengite geobarometer of Massonne and Szpurka (1997). A) Solidus of water-saturated haplogranite after Johannes and Holtz (1996). B) Stability of white mica in presence of quartz after Chatterjee and Flux (1986), see mineral abbreviations in Appendix 5. Stability fields of aluminium silicate polymorphs are shown for reference C) after Hemingway et al. (1991) and D) after Bohlen et al. (1991). E) Phengite geobarometer: Si-content isopleths after Massonne and Szpurka (1997). Number of Si atoms p.f.u. are indicated on each isopleth. F) Phengite geobarometer: Si-content isopleths after Massonne and Schreyer (1987), not used for calculations. The shaded area was constructed taking into account the standard deviation of all analyses. This area represents the PT window in which white mica might have crystallised. A maximum emplacement depth of 19 km is obtained.

5.3.4.3. The Buchberger Leite

Introduction

The Buchberger Leite shear zone strikes approximately NNW—SSE and is supposed to be a subsidiary Riedel shear of the Bayerischer Pfahl shear zone, although no connection is found in the field between both shear zones. Masch and Cetin (1991) studied the mylonites of the Buchberger Leite shear zone and interpreted the recrystallization of feldspars and the existence of the association Bt-Kfs-Pl-Qtz-Hbl as indicative of high deformation temperature.

The mylonites cropping out at the power station on the Wolfsteiner Ohe river shore are very dark, fine grained and developed from a dark-coloured diatexite protolith (Fig. 5.3.4.3-1). The foliation is very well developed and its orientation is N170E/90, with a stretching lineation plunging gently to N170E.

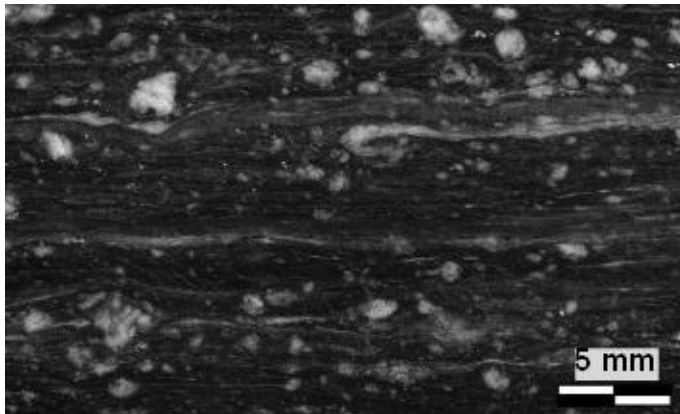


Figure 5.3.4.3-1. The appearance of a polished hand specimen (sample Frg 91) from the Buchberger Leite shear zone, XZ-section. Light feldspar grains are embedded in a dark, fine-grained matrix rich in biotite. Shear-sense criteria are hardly applicable at the scale of hand specimens on this rock.

Microfabrics

The rock contains biotite, quartz, K-feldspar and plagioclase. Titanite, allanite and opaque phases are present in relatively big amounts. The studied sample contains no amphibole. The quartz is found in form of sigmoidal bands of recrystallized grains. Grain boundaries are polygonal or slightly serrated. The feldspars are largely recrystallized, building fine-grained bands. Relic feldspar grains show subgrains and a core-and-mantle structure, in which transitions between subgrains and new grains are common. The feldspars can show sometimes microfractures, in which incipient recrystallization is observed. The biotite crystals are very small; they are oriented parallel to the foliation planes and display also sigmoidal forms. The shear sense is dextral as indicated by the monoclinic symmetry of mantled σ -porphyroclasts and sigmoidal bands (Fig. 5.3.4.3-2).

The microfabric is very similar to the one described for D₂ in diatexites (see chapter 5.3.2.2), with the particularity that the strain seems to have been higher at the Buchberger Leite shear zone.

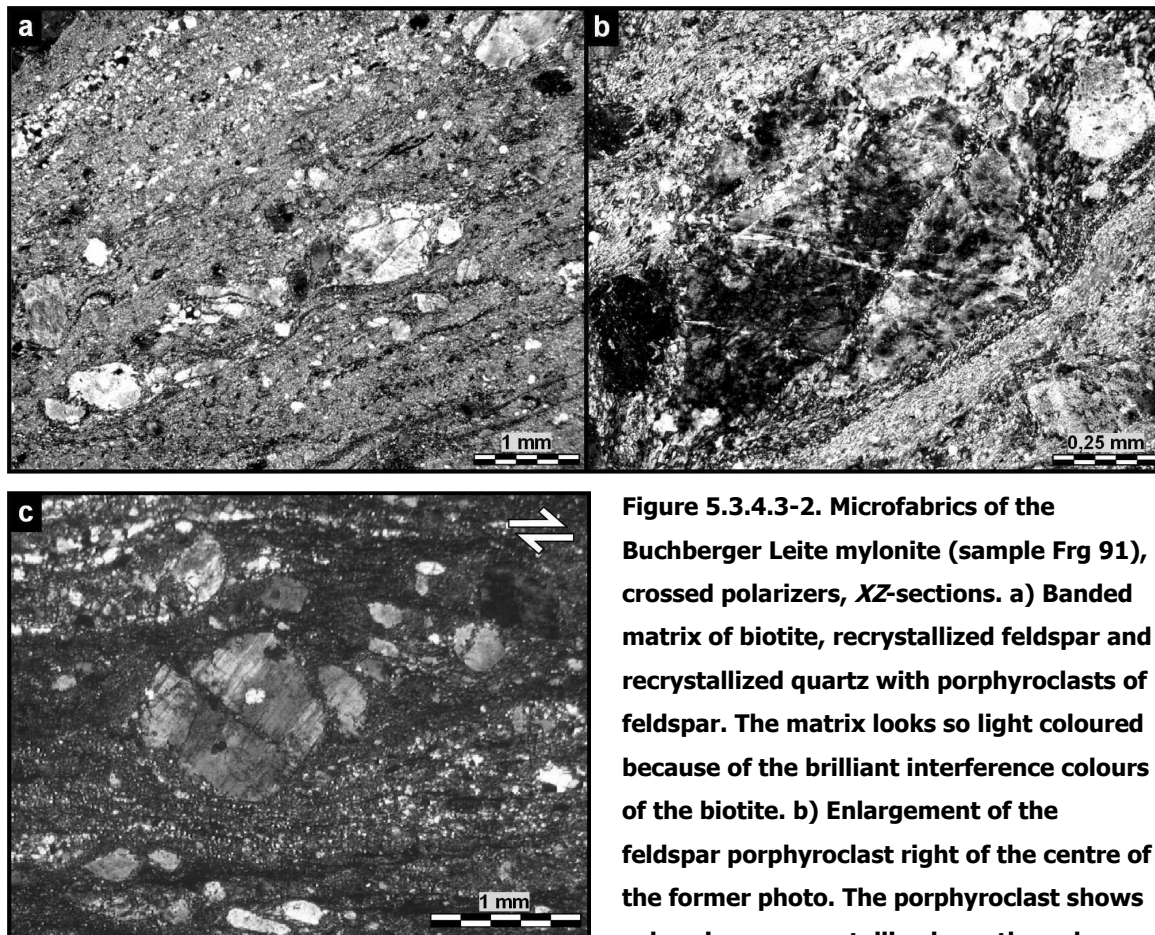


Figure 5.3.4.3-2. Microfabrics of the Buchberger Leite mylonite (sample Frg 91), crossed polarizers, XZ-sections. a) Banded matrix of biotite, recrystallized feldspar and recrystallized quartz with porphyroclasts of feldspar. The matrix looks so light coloured because of the brilliant interference colours of the biotite. b) Enlargement of the feldspar porphyroclast right of the centre of the former photo. The porphyroclast shows subgrains, a recrystallized mantle and microfractures at which incipient recrystallization takes place. c) Feldspar σ -porphyroclast showing dextral sense of shear, embedded in a matrix of biotite, recrystallized feldspar and recrystallized quartz. The porphyroclast is transected by some microfaults along which incipient recrystallization takes place. Subgrains are not well developed in this crystal.

microfractures at which incipient recrystallization takes place. c) Feldspar σ -porphyroclast showing dextral sense of shear, embedded in a matrix of biotite, recrystallized feldspar and recrystallized quartz. The porphyroclast is transected by some microfaults along which incipient recrystallization takes place. Subgrains are not well developed in this crystal.

Quartz texture

Two different areas of the sample were scanned by means of EBSD. The resulting texture (Fig 5.3.4.3-3) is unfortunately not well developed. The a -axes display no distinct pattern. The c -axes seem to concentrate around the centre of the plot with some tendency to rotate towards the orientation of the X -axis of the finite strain ellipsoid. It is not possible to consider this rotation as evidence, but just as a clue of a high-temperature deformation under amphibolite facies conditions.

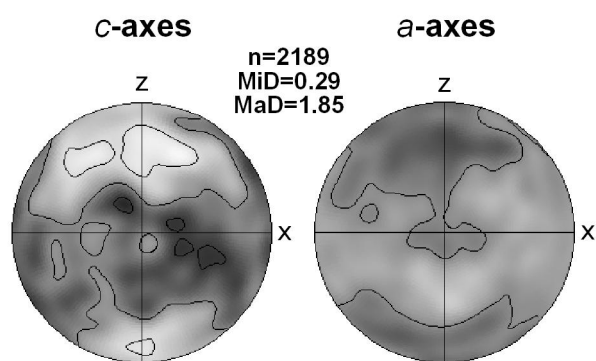


Figure 5.3.4.3-3. Quartz *a*- and *c*-axes patterns of sample Frg 91 obtained by means of EBSD. Equal area projection, lower hemispheres. n = number of data points, MiD = minimum density, MaD = maximum density. Density contours at 0.5; 1; 1.5. Black represents the maximum density. Data points were smoothed with a Gaussian of 10° full width half maximum.

5.4. Discussion: global consideration of sheared granitoids

The research carried out in the Bavarian Forest led to the achievement of a large amount of data, not only regarding the geology of the region, but also concerning some general issues on structural geology. The following discussion will focus first on the obtained results about fabrics, textures and strain in a general view, independently of regional considerations (chapter 5.4.1). Afterwards, we will concentrate on the geology of the region: Some considerations about the migration history of the intrusives of the southern Bavarian Forest will be outlined (chapter 5.4.2); then, the results obtained and their implications for the formation of different shear-zone systems in the course of several deformation phases will be analysed (chapter 5.4.3); this will be followed by the integration of new and pre-existing data at the scale of the Bavarian Forest and the Bohemian Massif (chapter 5.4.4); finally, an evaluation of different geodynamical models which may account for the development of the geological features found in the region will be presented (chapter 5.4.5).

5.4.1. Fabrics, textures and strain

5.4.1.1. Oblique foliations as shear-sense indicators

Compilations of the most commonly used shear-sense indicators have been published by many authors (e.g. Simpson and Schmid, 1983; Bjornerud, 1989; Hanmer and Passchier, 1991; Blenkinsop, 2000). Oblique foliations or shape fabrics defined by the SPO of quartz are amongst the most frequently used criteria. In spite of this, the example of the Saunstein dyke shows that the reliability of oblique foliations as a shear-sense indicator must be re-examined. The oblique foliation defined by quartz SPO (D_4) probably reflects a reactivation of the former sinistral shear zone during D_3 under dextral conditions (Fig. 5.3.3.2-6). In high-strain domains of the granite dyke, S and C planes became parallel to one another, sigmoidal structures are absent and porphyroclasts are scarce. The only available shear-sense indicators here are a few asymmetric folds and the asymmetric (dextral) SPO of quartz. By examining these high-strain domains, one could interpret the deformation in the shear zone as having been produced by a single, dextral episode, which would have important consequences on the regional interpretation of the shear zone in relation to other major shear zones. It is proposed, therefore, that quartz oblique foliations should only be used always in combination with other shear-sense criteria.

5.4.1.2. Development of lattice-preferred orientation in quartz

Lattice-preferred orientation patterns (or textures) of quartz are used to infer deformation mechanisms and temperatures. This information can also be obtained by means of fabrics analysis under the microscope, but in cases of weak deformations producing poorly developed fabric features the data delivered by microscopical observations might be insufficient. In such cases, EBSD studies provide valuable information: As shown in the Saunstein dyke and the Patersdorf granite, rocks that have suffered little deformation can develop a quartz texture. This is the case of samples Grf 615 (Fig. 5.3.3.2-8) and Pat 10 (Fig. 5.3.4.2-4). The Patersdorf locality provides an interesting example of weakly deformed rocks with better-developed textures than strongly deformed ones. This can be due to the fact that fine-grained rocks show a tendency to deform preferentially by grain boundary sliding instead of dislocation creep. This results in the development of no texture or in the destruction of pre-existing ones (Figs. 5.3.3.2-8, 5.3.3.3-6, 5.3.3.4-4, 5.3.4.1-4, 5.3.4.2-4).

5.4.1.3. Deformation mechanisms vs. temperature and grain-size

The temperature at which quartz and feldspar start to recrystallize under geological strain rates is about 300 and 450°C, respectively (e.g. Tullis, 1983; Passchier and Trouw, 1996). However, it has been demonstrated in many examples that sometimes the temperature is high enough for a given mineral to recrystallize but it does not recrystallize. This can be due to two factors: i) As proposed by Tullis and Yund (1977) for feldspars, crystals seem to need a certain amount of strain to recrystallize, apart from a sufficiently high temperature; ii) as long as some other soft elements exist in the rock, these will accommodate the deformation.

The first factor might be responsible for the fabrics observed in diatexites affected by D_2 , in which some feldspar grains did not recrystallize, although the temperature was well above 450°C.

The second factor is a plausible explanation for the fabrics of the Untermittlerdorf rhyolite, whose deformation was strongly controlled by its magmatic fabric: The bimodal grain-size distribution has important consequences on the activation of certain deformation mechanisms. The amount of strain accommodated by the quartz phenocrysts/porphyroclasts by intracrystalline deformation, recovery and dynamic recrystallization was evidently not high, since many crystals remained nearly unstrained, nor was it uniformly distributed in the whole rock, as each quartz grain reacted in a different way to the stresses. The strain of quartz porphyroclasts was promoted in areas of stress concentration, i.e. in the neighbourhood of other porphyroclasts. The recrystallization of quartz by subgrain rotation plus grain boundary migration requires relatively high temperatures of at least 480°C (Stipp et al., 2002). The quartz is ductile under these conditions, so why did some grains remain unstrained? On the other hand,

if the deformation temperature was $> 480^{\circ}\text{C}$, why did feldspar not start to recrystallize? The explanation to these apparently incongruent fabric features is that, even being the temperature high enough for quartz and feldspar to recrystallize, there are some other soft elements in the rock accommodating most of the strain. These are the mica aggregates and, most of all, the very fine-grained matrix, in which grain boundary sliding, perhaps accompanied by some diffusion, were most likely the dominant deformation mechanisms. Moreover, progressive deformation leads to the formation of white mica from feldspar in the matrix, enhancing reaction softening and further strain localisation in the matrix.

5.4.1.4. Strain localization

D_3 is preferentially localized in granites, rarely found in the country rock. The heat carried by the intrusions might have provoked a deformation at slightly higher temperature than the one of the host rock in some cases, especially in the case of the Untermittlerdorf rhyolite (the youngest one), but this seems to be more probably the exception than the rule: Indeed, the homogeneous textures and structures across the profile of the Saunstein dyke suggest that the dyke and the host were at the time of deformation thermally equilibrated at $500\text{-}550^{\circ}\text{C}$. Thus, the granites constituted soft corridors at which the deformation concentrated, allowing rigid translation of adjacent blocks. The granites are softer and deform more easily than the host rock, but not necessarily due to a thermal contrast, but rather to a mineralogical one: The granites are in general richer in quartz and therefore weaker.

The deformation of the Saunstein dyke is characterized by dramatic softening and strain localization at its margin due to several interacting processes: The initial strain localisation started a series of feedback processes leading to further strain localisation. The contact must have played an important role during D_3 . It probably represented a rheological boundary at which mechanically strong, feldspar-rich diatexite and soft, quartz-rich granite met. Stresses concentrate at the contact surface, affecting predominantly the softest rock type. In a first phase of D_3 , the concentration of stresses at the rheological boundary and their dissipation towards the centre of the dyke originated a stress distribution which might have been similar to that represented in Fig. 5.3.3.2-11. This stress distribution caused a strain and strain-rate gradient. As a consequence, the strain-rate gradient was probably responsible for a viscosity decay at the contact, promoting further strain localization and fluid access. The reduction in grain size promotes grain boundary sliding. The presence of a fluid gives way to reaction softening or hydrolytic weakening and formation of white mica in cleavage domains. Synkinematic white mica contributed to the softening of the rock by accommodating strain by frictional sliding along (001) planes. The stresses measurable from quartz grain size probably represent mainly the stress governing the first phase, since the deformation in the second phase was dominated not by dynamic recrystallization but

rather by frictional or grain boundary sliding in cleavage domains and fine-grained microlithons.

The existence of dioritic to granodioritic bodies with and without D_2 -overprint does not necessarily imply that these intrusions are different to each other in age. More probably, some of these bodies are more rigid than the diatexites, and consequently they can remain more or less undeformed inside a diatexite mass which flows around them. Further on, the deformation during D_2 was not homogeneous, but rather localized along discrete bands, occurring more or less randomly distributed over the study area, although more frequently next to the principal shears. The same holds for the small granitic bodies (mostly belonging to the group 2 of intrusives, as defined in chapter 5.2.3) scattered all over the Bavarian Forest, which are most probably older than the Untermittlerdorf rhyolite, and are in spite of this often undeformed (see chapter 5.3.1.4): Many of the granites did not suffer any deformation, although probably not due to a post-kinematic emplacement, but rather due to their having an unfavourable position or geometry to accommodate deformation.

5.4.2. Migration of intrusives in the southern Bavarian Forest

Although the hypersolidus evolution of intrusive bodies of the Bohemian Massif was not the main focus of this work, some conclusions about their ascent and emplacement can be outlined.

In the southern Bavarian Forest, the shape of the different magmatic bodies reflects the thermal evolution of the crust in which they ascended and froze. Elliptical, irregular or elongate intrusive bodies are usually older than ~ 310 Ma. They intruded into a relatively hot crust. Their shape and internal fabric is conditioned by the structure and rheology of the host in which they intruded and by the polyphase deformation history that they underwent. The way they ascended is not well known, but the exploitation of pre-existing anisotropies seems to be the most efficient mechanism in this context. Some contribution of diapirism is conceivable in some of the largest and more equidimensional bodies, such as the Hauzenberg granite II (Hauzenberg pluton) and the Saldenburg granite (Fürstenstein pluton).

Stoping is usually regarded as a process operating mostly in the upper crust, but the present work shows that it can play an important role also in deeper levels. Thus, the intrusion of several stocks, whose age might be similar to the one of the Saunstein dyke (~ 324 Ma), provoked pervasive stoping of the dioritic to granodioritic and migmatitic country rocks (see chapter 5.3.1.4). Also the emplacement of the Saldenburg granite was accompanied by stoping, i.e. by the incorporation of fragments of country rocks and older magmatic facies. In both cases, intrusion depths exceeded 15 km.

The intrusive bodies younger than ~ 310 are dykes of sharp and planar contacts, suggesting ascent by means of dyking in a relatively cold crust. A similar intrusion

sequence (stocks followed by planar dykes) is observed in the batholith of the Spanish Central System, also called Ávila batholith (Central Iberian Zone of the Iberian Massif; Bea et al., 1999; Bea et al., 2004).

5.4.3. Shear-zone systems and conditions governing their evolution

The deformations found in the rocks of the study area, D_1 to D_4 , reflect the thermal evolution of the region from granulite/amphibolite facies to greenschist facies conditions. The data achieved during this research, together with previous data of other authors, will be analysed in order to 1) propose a succession of deformation events, 2) estimate the temperature and pressure governing these events, 3) ascribe the activity of different shear-zone systems to their corresponding deformation phase, 4) infer the stress state that produced the deformations and 4) outline the temporal relationships between deformations and intrusions.

D_1 produced high-temperature fabrics under upper amphibolite to granulite facies conditions in the studied samples, probably coinciding with the thermal peak of the regional HT-LP metamorphism. Its kinematics is unknown. D_1 is usually obscured by later deformation phases, but still identifiable as a relict.

D_2 occurred under amphibolite to upper greenschist facies conditions in the studied samples, as evidenced by the microfabrics and textures presented here and by other authors (see below), and is responsible for a subvertical NW—SE striking foliation in migmatites and for the deformation at the Bayerischer Pfahl shear-zone system at its earlier stages. Most of the dioritic to granodioritic bodies and some of the granitic ones intruded prior to or during this deformation phase.

D_3 took place under upper greenschist to lower amphibolite facies conditions and is the deformation phase that caused the sinistral shear along planes trending ENE to ESE in granites. It is proposed that these sinistral shear zones in granites are not compatible with a N—S to NNW—SSE compression and do not belong to the Bayerischer Pfahl shear-zone system. They constitute themselves a separated shear-zone system, which was active during D_3 . Cross-cutting or abutting relationships between both shear-zone systems have not been found up to now. Our inferred deformation temperatures at the Bayerischer Pfahl and Buchberger Leite shear zones and in diatexites affected by D_2 are unfortunately not far away from the boundary between lower amphibolite and upper greenschist facies conditions, which is very close to the deformation temperature assumed during D_3 , so that the distinction between deformation phases remains somewhat diffuse in terms of temperature. Only a few of our examples of the Bayerischer Pfahl shear-zone system constitute a weak indication of higher or lower temperature than the one governing D_3 :

- rhomb $\langle a \rangle$ slip in Pat 11 (Fig. 5.3.4.2-4),
- a light tendency of a -axes to form one maximum instead of three at the Große Ohe profile (Fig. 5.3.4.1-4),
- a weak rotation of the c -axes towards the direction of the lineation at the Buchberger Leite location (Fig. 5.3.4.3-3),
- a larger variability of quartz and feldspar fabrics than in sinistrally sheared granites.

Nevertheless, all the spectrum of deformation temperatures recorded by other authors in the Bayerischer Pfahl shear-zone system (Beer, 1988; Brandmayr et al., 1990; Handler et al., 1991; Masch and Cetin, 1991; Brandmayr et al., 1995; Büttner, 1999) spans from upper amphibolite to lower greenschist facies conditions and even lower. That means that the principal direction of compression trending approximately N—S governed prior to and after D_3 .

Thus, after D_3 the existence of a following D_4 , with a similar arrangement of the principal stresses as D_2 , is postulated. D_4 caused the development of quartz oblique fabrics pointing to a different sense of shear as the D_3 fabrics. D_4 oblique foliations were found in the sinistrally sheared granites that are located closer to the Bayerischer Pfahl shear zone (outcrops south of Kleinarmschlag and Saunstein quarry), also suggesting that D_4 is linked to further dextral deformation at the Bayerischer Pfahl shear zone.

The microstructures and textures formed during D_3 are surprisingly similar to each other in the different studied specimens. The deformation temperature inferred is in most cases around 500-550°C, based on the recrystallization mechanisms (GBM and some contribution of SGR in quartz) and active glide systems observed (prism $\langle a \rangle$ slip in quartz leading to c -axes patterns with maxima around the Y -axis of the finite strain ellipsoid). The homogeneity in the results across a profile in the Saunstein dyke indicates that the dyke and the host were thermally equilibrated during the deformation. The homogeneity in the results from different examples points to D_3 being a deformation phase very localized in time, which interrupted for a geological moment the normal activity of the Bayerischer Pfahl shear-zone system. The Untermitteldorf rhyolite constitutes the only example which seems to break this homogeneity: Quartz seems to recrystallize by GBM and a more important component of SGR, some contribution of rhomb $\langle a \rangle$ slip is suggested by the LPO patterns, and feldspars show no signs of recrystallization. All of this points to a slightly lower temperature during deformation, probably around ~480-530°C. Both the barometric data and the aphanitic structure of the rock suggest a lower temperature also during its emplacement (see below). This constitutes a first indication for either 1) a recurring D_3 , i.e. D_3 probably occurred in two or more events, or 2) for a D_3 undergone at slightly different levels of the crust, today exposed at the same level due to later vertical movements. These possibilities will be discussed later again in the light of available data.

The geochemical and strain data of the Saunstein dyke point to a flattening geometry of the deformation with no volume change. This suggests transpression during the main phase of shearing (e.g. Sanderson and Marchini, 1984; Tikoff and Fossen, 1999) for this dyke, in which shear planes strike N070E to N090E. The principal compression direction could have been approximately NE—SW during D₃. Taking into account the variable strike of S₃ in the rest of the studied sinistrally sheared granites, between N056E and N122E (see Appendix 2), the trend of the principal compression must have been between N056 and N032E, in order to induce sinistral shear in all of them.

The available geochronological data provide the emplacement ages of two sinistrally sheared granitoids yielding:

- Saunstein dyke 324.4 ± 0.8 Ma, a U-Pb on monazite dating performed by Dr. W. Dörr (Galadí-Enríquez et al., 2005),
- Untermitteldorf rhyolite 315.0 ± 1.0 Ma, a U-Pb on zircon dating performed by Dr. W. Siebel and co-workers (Galadí-Enríquez et al., in prep.).

The geobarometric study of the sinistrally sheared granites provided maximum intrusion depths between 27 and 17 km for the sinistrally sheared granitoids. The deformation depth is around 19 and 14 km in two different samples. Two samples of the Bayerischer Pfahl shear zone provided maximum intrusion depths of 19 and 14 km, which could mean that they have intruded rather a bit later than the former ones and have been deformed under slightly lower temperature (beginning of D₄).

The scattering of the results about emplacement and deformation depth (Table 5.4.3-1) can be attributed to three factors: 1) to the uncertainties of the method, 2) to vertical movements, and 3) to an episodic occurrence of D₃. The first factor certainly plays an important role: As pointed out in chapters 5.3.3.2, 5.3.3.3, 5.3.3.4, and 5.3.4.1, the geobarometer used might provide imprecise results due to the fact that real geochemical systems are more complicated than the KMASH system, in which the geobarometer was calibrated. The second factor is possible, although the lack of evidence in the field, such as the existence of major faults or metamorphic gradients, makes it difficult to evaluate. Finally, supposing a simple scenario in which no significant differential vertical displacements took place between the studied granitoid bodies, an episodic occurrence of D₃ is regarded as plausible. Nevertheless, although the geobarometric results seem to reflect some trends correlatable with the age of the intrusions and their deformation, i.e. older intrusions tend to be deeper (Table 5.4.3-1), the uncertainties of the method seem to be large and the absolute numbers obtained cannot be considered to accurately constrain the real depths at which these processes took place.

	D ₃ overprint	age	maximum emplacement depth	deformation depth (D ₃)
Hochholz	yes	?	26.7 ± 2.0 km	?
Sand pit E Untermittlerdorf	yes	?	25.5 ± 1.5 km	?
Saunstein dyke	yes	324.4 ± 0.8 Ma ^c	21.7 ± 1.4 km	18.8 (+ 2.9/- 3.3) km
Steinberg	yes	?	18.2 ± 1.0 km	13.9 ± 0.7 km
Hauzenberg granite II	no	320 ± 3 Ma ^d	16-18 km ^d	-
Saldenburg granite	no	315 ± 3 Ma ^e	~20 km ^a ~17 km ^b 14-15 km ^g	-
Untermittlerdorf rhyolite	yes	315 ± 1 Ma ^f	16.6 ± 0.7 km	?

Table 5.4.3-1. Comparison between age and depth of intrusion and deformation in some granitoid bodies of the study area. In the case of the Saldenburg granite, a depth of 20 km (labelled with a) results from the application of the barometer of Massonne and Szpurka (1997), used in all samples of the present study, to the Si content of 3.11 atoms p.f.u. reported by Massonne (1984). Massonne (1984) calculated an emplacement depth of ~17 km (labelled with b) using the barometer of Massonne and Schreyer (1979), which provides lower pressures than the one of Massonne and Szpurka (1997). Therefore, the emplacement depth of 20 km must be considered for comparison in this study. Further labels: c) after Galadí-Enríquez et al. (2005), d) after Klein et al. (2007), e) after Chen et al. (2002) and Chen and Siebel (2004), f) after Galadí-Enríquez et al. (in prep.), g) after Dietl et al. (2005), the latter depth was calculated by means of hornblende thermobarometry on older granodioritic rocks which are supposed to have been reset by the emplacement of the Saldenburg granite.

5.4.4. Significance of D₃ in the Bavarian Forest and the Bohemian Massif

In the following lines, the available data will be discussed together with data of other authors. This will provide an overview about the present state of knowledge in the region and will serve as a previous step for the proposal of different geodynamic models which may account for the development of the geological features found in the region, especially those associated to D₃. A geodynamic model for the development of D₃ must take into account the P-T evolution of intrusives and country rocks and the structures present in the region.

The phengite barometry data roughly agree with other barometric data of the region. However, it is important to remark that the pressures obtained from the phengite geobarometer might be somewhat overestimated, as pointed out by some authors (e.g. Simpson et al., 2000). The obtained intrusion depths are regarded as maximum values, since the muscovite might have crystallised during the ascent prior to the emplacement (Zen, 1988). The obtained intrusion depths of the sheared granites indicate

intermediate to deep levels of the crust between 17 and 27 km. The available pressure and age data indicate that the Saldenburg granite intruded later and deeper than the Hauzenberg granite II. Nevertheless, it is unlikely that crustal thickening took place between both intrusions, and therefore the barometric results are considered to be only approximate and/or to reflect some post-emplacement crustal tilting. The latter possibility should be checked in the future by means of combined barometric and geochronological studies of intrusive bodies. It is well supported by the data that the Saunstein dyke is older and intruded at a deeper level than the Untermittlerdorf rhyolite. The Hauzenberg granite intruded after the Saunstein granite. Finally, the Saldenburg granite and the Untermittlerdorf rhyolite intruded coevally. All of this occurred in a general context of exhumation. D_3 occurred shortly after the intrusion of the Untermittlerdorf rhyolite, although an episodic occurrence of D_3 , both after and before this intrusion, is also possible, as suggested by the higher deformation pressure and slightly higher temperature inferred for the Saunstein dyke.

The temperature of the country rock during the emplacement of the Hauzenberg granite II (320 Ma) was ca. 550°C (Klein et al., 2007), which is the same temperature governing D_3 in the Saunstein and similar dykes. As already exposed, the temperature governing D_3 was, at least in the case of the Saunstein dyke, not influenced by any advective heat provided by the deformed granites themselves, although in the case of the youngest deformed granitic body, the Untermittlerdorf rhyolite, it is conceivable that it was slightly hotter than the country rock at the time of D_3 , as we will analyse in the course of this discussion.

After Kalt et al. (1999) the peak conditions during the HT-LP metamorphism reached 800-850°C and 0.5-0.7 GPa (18.4-25.8 km) at 323-326 Ma, whereas the last equilibration occurred at 770-846°C and 0.44-0.51 GPa (16.2-18.8 km) and a cooling rate of ca. 100°C/Ma during 2-3 Ma after peak conditions can be assumed (Kalt et al., 2000), which is compatible with a deformation temperature of about 550°C ca. 3 Ma after the metamorphic peak, i.e. some time after the intrusion of the Saunstein and similar dykes at 324 Ma. Nevertheless, Kalt et al. (1999) obtained these results from migmatitic gneisses located north of the Bayerischer Pfahl shear zone: It is possible that the diatexites of our study area, i.e. south of the Bayerischer Pfahl shear zone, would yield different values regarding age, pressure and temperature of the regional HT-LP metamorphism.

Cooling ages of biotite and muscovite typically range from 310 to 290 Ma in the study area (Harre et al, 1967; Christinas et al., 1991a; Brandmayr et al, 1995). The post-granitic dykes intruded after all ductile deformation phases at 302 ± 7 (Christinas et al., 1991b) and 299.0 ± 2.3 Ma (Propach et al., 2007) at a depth of 4-6 km and into a country rock with a temperature of $200 \pm 50^\circ\text{C}$ (Propach, 2002). These data provide information about the evolution of the crust after D_3 constraining its minimum age. Although the new maps of the Bavarian Environment Agency group all basaltic andesitic

to rhyolitic dykes under the rubric of the post-granitic dykes, attending primarily to their common aphanitic fabric, it has been already pointed out by Propach et al. (2007) that the rhyolitic end members might constitute a genetically distinct group, geochemically distinguishable from the more basic ones. This proposal is supported by recent results, pointing to the Untermitteldorf rhyolite as being 315.0 ± 1.0 Ma old and affected by D_3 , i.e. as being clearly older than the dated dacitic dykes.

Returning to the question of the thermal evolution of the study area, it has been mentioned that the crust cooled down from approximately 550 to 200°C between 320 and 300 Ma. Supposing that no further thermal perturbation occurred after 320 Ma, this cooling should have been achieved in an exponential way: This implies that the study area must have been at $T < 450^\circ\text{C}$ during the intrusion of the Untermitteldorf and Saldenburg granitoids (450°C would have been reached at a constant cooling rate, which was certainly not the case). These considerations, together with the deformation of the Untermitteldorf rhyolite at around 500°C at ≤ 315 Ma, imply that, in this particular case, the dyke still retained some of its thermal energy at the time of deformation. Since the dyke is very thin (no more than a few meters), its cooling probably occurred, in geological time scales, instantaneously. The conclusions of this reasoning are that 1) the intrusion of the Untermitteldorf dyke and its deformation occurred almost simultaneously, and 2) D_3 must have occurred in at least two events, the first one before and the second one immediately after the intrusion of the Untermitteldorf dyke. The possible role played by vertical movements will not be considered at the moment, due to the lack of robust geochronological, barometric and field evidence.

But the assumption that a simple cooling occurred after 320 Ma is not necessarily correct. In fact, some works (Finger et al., 2007 and references therein) sustain the existence of a HT-LP event as young as 330-315 Ma in the south-western Bohemian Massif. This period of time was in fact characterized by a strong input of advective heat (intrusion of plutons). Therefore, it would be conceivable that the temperature of the study area remained as high as 500-550°C until 315 Ma. As a consequence, the deformation D_3 of granitoids of different ages can be explained in a single event post-dating the youngest one of them, i.e. at ≤ 315 Ma. The differences in the deformation depth must be explained then as a consequence of the uncertainties of the method and/or later vertical movements, but this question must be solved in the future in the light of further evidence.

The measurement of magmatic foliations and lineations in the field and by means of AMS has revealed the internal structure of the plutons of the study area (Cloos et al, 1927; Troll, 1964; Dollinger, 1967; Dietl et al., 2005). The Hauzenberg pluton shows a magmatic foliation trending E—W, parallel to the foliation of the country rock, and a horizontal E—W lineation, which is compatible with a N—S compression and a E—W magma flow during the emplacement. The magmatic foliation of the Saldenburg granite strikes around N045E after Troll (1964) and around N060E after Dietl et al. (2005). It is

normally strongly dipping with a lineation plunging gently or moderately to the NE or SW.

Taking into account all the available data presented above, further discussions and investigations must evaluate two possibilities:

1. It seems probable that D_3 occurred in at least two events: D_{3A} and D_{3B} . D_{3A} must have occurred after the intrusion of the Saunstein granite, i.e. after 324 Ma, under a temperature of 500-550°C (host and dyke were thermally equilibrated) at a poorly constrained depth of about 14-19 km; D_{3B} occurred at about 315 Ma, i.e. at the time of intrusion of the Untermittlerdorf dyke, under a dyke temperature of ca. 500°C, being the host rock somewhat cooler. It remains unclear whether the Hauzenberg granite II intruded prior to, after or during D_{3A} , but the fact that it shows no sub-solidus deformation places no robust constraints in the tectonometamorphic evolution of the area, since D_3 was very localized in time and in space. During D_{3B} the Hauzenberg granite was already solid (freezing took around 3 Ma or more, Berger et al., 2002), whereas the intrusion of the Saldenburg granite, considering the datings available, occurred very close in time with the deformation.
2. It is also possible that the study area remained relatively hot, at a temperature of about 500°C, until the intrusion of the Saldenburg and Untermittlerdorf granitoids at 315 Ma. D_3 could have occurred then in a single event, probably during the intrusion. Placing D_3 much later than 315 Ma seems inappropriate, as suggested by the cooling ages available.

5.4.5. Geodynamic models

Looking for the causes for the change in the stress field that gave way to D_3 requires an evaluation of local and regional factors governing the stress state in the study area. Therefore, we will analyse first the regional processes that presumably took place at the time of D_3 . After that, the role played by local processes will be evaluated.

5.4.5.1. Models based on regional processes

As already mentioned, D_3 occurred as a response to a short period of NE—SW compression pre- and post-dated by a regional N—S to NNW—SSE compression. The significance of D_3 in the geological evolution of the Central European Variscides is still poorly understood. D_3 took place probably at the end of the Namurian or beginning of the Westphalian. In late-Variscan times, the Variscan internides had reached an important thickness (e.g. Ziegler, 1990), perhaps a critical thickness, and the convergence direction between Laurussia and Gondwana might have changed.

In order to propose a concrete tectonic model for a regional change of the principal compression direction from N—S/NNW—SSE to NE—SW, it is necessary to correlate diverse structures caused by this process in the whole Moldanubian Zone. This seems at present premature due to the following reasons:

- The structure of large areas of the Moldanubian Zone, especially concerning Late Variscan tectonics, is still poorly documented.
- The deformation history of the Moldanubian Zone seems to be quite complicated during the Carboniferous, especially in its northern sector, in which different authors (Stein, 1988; Tanner, 1995) reported several deformation phases which are hardly correlatable with each other.
- The age of the deformation phases is usually poorly constrained.
- The vertical movements along the main shear zones that occurred in Variscan and post-Variscan times have brought in contact different crustal levels: The present erosion level shows structures of diverse styles developed under different temperatures, which makes the recognition of structures of coeval development still more difficult. For the correlation of structures formed coevally it is necessary to bear in mind that the temperature and the orientation of the principal stresses might have been different depending on the block (=level) considered, which can be a possible explanation for the development of structures of different type under the same geotectonic framework. For example, given a horizontal σ_1 , folds and reverse ductile or brittle faults might form at upper levels (vertical σ_3), whereas ductile strike-slip shears (vertical σ_2) might develop at deeper levels. A huge amount of new geothermobarometric and geochronological studies is needed to overcome these limitations.

The aforementioned shortcomings become patent when comparing the results of different authors. For example, in the northern sector of the Moldanubian Zone, Stein (1988) reported the existence of open folds of sub-horizontal axes striking NNW—SSE to NW—SE (D_4) which probably developed in the Westphalian-Stephanian under a similar stress field as our D_3 (see chapter 5.2.1), whereas Tanner (1995; see also Tanner and Behrmann, 1995; Behrmann and Tanner, 1997) found folds with axis of similar strike (D_4), but steeply plunging to the NW, which were attributed to the Namurian. A late Carboniferous NE—SW compression has further been obtained for brittle-ductile reverse faults at the KTB superdeep well and surroundings in the Erbendorf-Vohenstrauß Zone (Zulauf, 1992), their age being between 310 and 296 Ma (Zulauf and Duyster, 1997), i.e. Westphalian-Stephanian. Concerning the relationships between the Moldanubian and Teplá-Barrandian units, from Late Devonian to Late Carboniferous times, mainly between 360 and 320 Ma, extensional collapse and sinking of the nearby Teplá-Barrandian unit is postulated by Zulauf (1994; see also Scheuven and Zulauf, 2000; Zulauf et al. 2002a, b; Zulauf and Vejnár, 2003). The development of ductile structures

in the Moldanubian rocks and at the West Bohemian and Central Bohemian shear zones was coeval with brittle tectonics in the Teplá-Barrandian (e.g. in the Mariánské Lázně fault, Zulauf et al., 2002a). The sense of tectonic transport was after these authors top-to-E or east-side-down, which is, at least apparently, in conflict with the proposal of Tanner (1995) suggesting that the main foliation (S_3) in the Moldanubian next to the West Bohemian Shear Zone was the result of an east-side up movement at some point in time during the Namurian.

In summary, the geotectonic framework was at this time very complex in Central Europe. A regional process responsible for the rotation of the main compression direction from N—S to NE—SW is impossible to elucidate at present. As for the meaning of the term “regional”, it might be used in a far-field, i.e. at the scale of the entire Variscan Orogen, or in an intermediate-field scope, i.e. at the scale of the Moldanubian Region (Moldanubian and Teplá-Barrandian units).

In a far-field scope, and following the proposal of Ziegler (1990), the rotation might have been caused by a change in the convergence direction between Laurussia and Gondwana at the end of the Carboniferous, whereas the detailed configuration and relative movements of the different crustal blocks remains somewhat obscure.

In an intermediate-field scope, the sinking of the cold Teplá-Barrandian block might have produced local perturbations of the regional stress field and lateral extrusion of the surrounding and underlying hot Moldanubian rocks. The sinking of the Teplá-Barrandian unit might have influenced and distorted the stress fields in the vicinity for a long time, either continuously or episodically, thus provoking anomalous stress fields in a far-field N—S to NW—SE convergent scenario. The effect of the sinking of the Teplá-Barrandian block on Moldanubian rocks is then envisaged as a combination of internal deformation and rigid translation of surrounding rocks which could have resulted in the development of (1) some of the contractive, ductile structures in the northern sector of the Moldanubian Zone, such as the NW—SE trending folds developed during the D_4 of Tanner (1995), or the D_4 open folds with horizontal axes trending NNW—SSE found by Stein (1988), (2) the sinistral overprint at the Bayerischer Pfahl shear zone observed by Mattern (1995), and (3) the sinistrally sheared granites described in the present work, which would represent shear zones along soft paths bounding blocks of relatively rigid behaviour (Fig. 5.4.5.1-1). This hypothesis is nevertheless only tentative and must be checked in the future by further investigations.

However, the sinking of the Teplá-Barrandian unit probably ended or was already very limited at and after 320 Ma. Thus, D_3 (supposed a single D_3 event) or at least D_{3B} occurred as the Teplá-Barrandian unit had already reached its final position relative to the Moldanubian. The operation of far-field mechanisms provoking a NE—SW compression must therefore be invoked to explain the whole D_3 or some part of it.

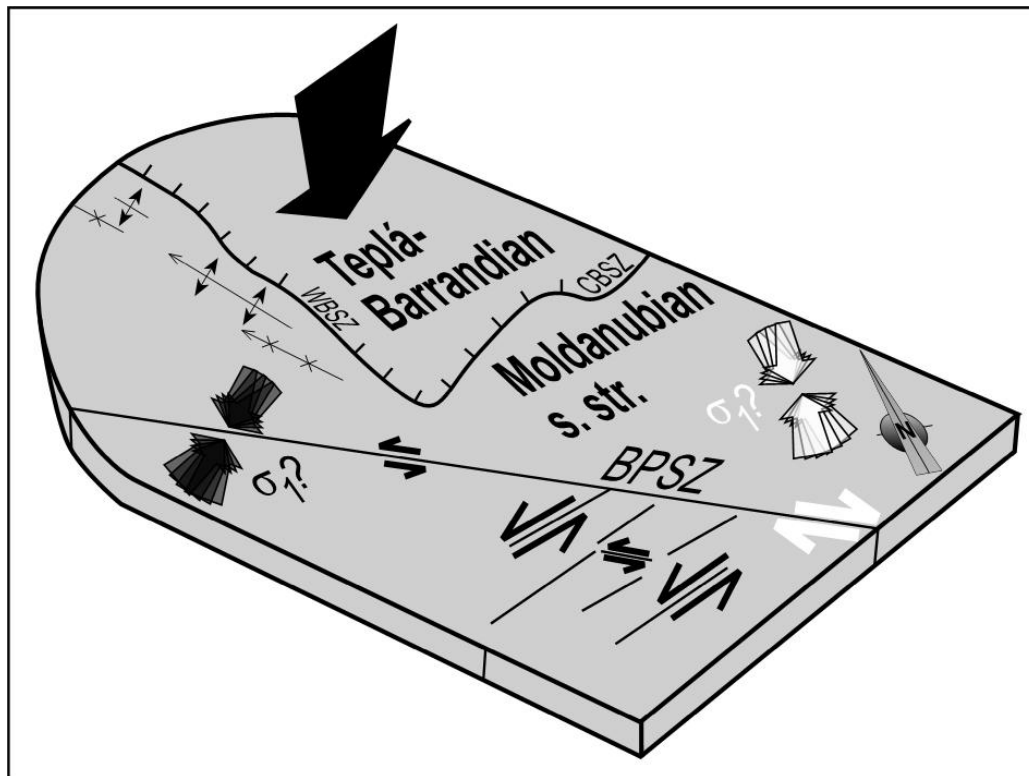


Figure 5.4.5.1-1. Sketch showing the sinking of the Teplá-Barrandian block as a potential regional, intermediate-field factor provoking a change in the stress field. White arrows represent the situation during D_2 and D_4 , black arrows are referring to D_3 . WBSZ: West Bohemian shear zone. CBSZ: Central Bohemian shear zone. BPSZ: Bayerischer Pfahl shear zone. The sketch exemplifies how the sinking of the Teplá-Barrandian unit could be responsible for the rotation of σ_1 to a NE—SW direction, causing the development of folds (antiform and synform symbols on picture representing D_4 of Stein (1988) and D_4 of Tanner (1995)), and sinistral shear in granites (strike-slip shears at the bottom of the picture, D_3 in this study). A sinistral re-activation of the Pfahl shear zone might also have occurred during D_3 , as proposed by Mattern (1995).

Whatever the geotectonic mechanism that caused the rotation of σ_1 to a NE—SW orientation, the new configuration of the principal stresses must explain not only the localized sinistral shear in granitic bodies, but also a possibly coeval ascent and emplacement of the Saldenburg granite. At the time of emplacement, at around 315 Ma, the country rocks were either (i) below 450°C or (ii) at around 500°C, depending on the model of thermal evolution considered, as discussed above.

In the first case, a temperature below 450°C is compatible with a level of the crust in or next to the brittle-ductile transition. In this context, the development of vertical weak planes, similar to joints parallel to σ_1 , is possible. Under NE—SW compression, we can imagine the ascent and emplacement of the Saldenburg magma exploiting those vertical anisotropy planes parallel to σ_1 and perpendicular to σ_3 (Fig. 5.4.5.1-2). This would explain the magmatic fabric oriented in NE—SW direction observed by Troll (1964) and

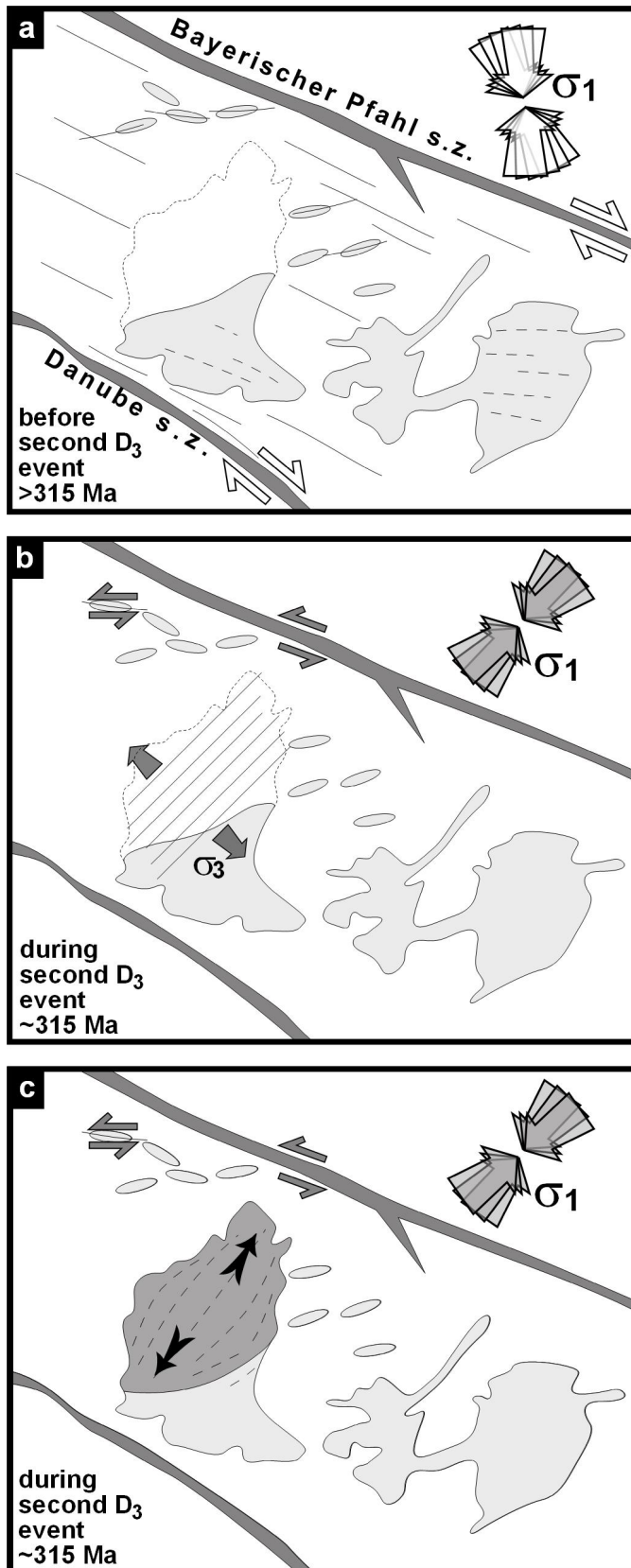


Figure 5.4.5.1-2. Sketch showing a possible explanation for the intrusion of the Saldenburg granite and the intrusion and deformation of the Untermitterdorf rhyolite. a) Situation before D_{3B} . Thin lines represent the foliation formed during D_2 and during D_{3A} : Continuous and dashed ones represent subsolidus and hypersolidus foliations, respectively. b) The rotation of the principal compression to a NE–SW direction leads to the formation of vertical weak planes parallel to σ_1 under brittle-ductile conditions. The deformation of the Untermitterdorf rhyolite takes place, and also a weak sinistral overprint at the Bayerischer Pfahl shear zone is possible at this stage. c) Intrusion of the Saldenburg granite, magmatic flow (black arrows) parallel to the weak planes and development of magmatic fabric (dashed lines).

Dietl et al. (2005) and the coeval occurrence of D_3 (D_{3B} in this framework). Similar cases of magmatic fabrics and feeding channels parallel to σ_1 in or above the brittle-ductile transition have been reported by Vigneresse (1995a, 1995c), Aranguren et al. (1996), and Vigneresse and Bouchez (1997).

In the second case (Fig. 5.4.5.1-3), we consider that the study area was at $T \sim 500^\circ\text{C}$ and, furthermore, that the location of the Saldenburg granite was probably pre-heated by the previous intrusion of the Tittling granite and the two-mica granite: As mentioned in chapter 5.3.1.5, the two-mica granite was still hot or even partially molten as the

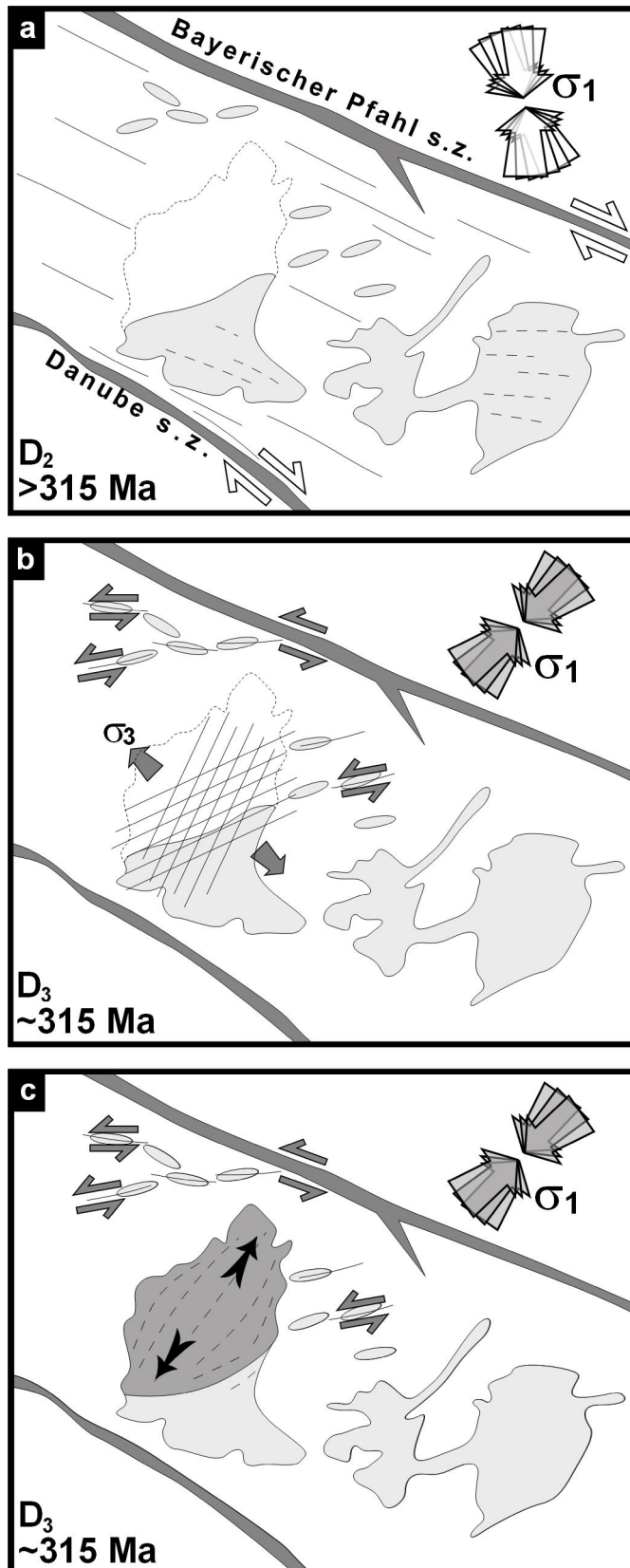


Figure 5.4.5.1-3. Sketch showing a possible explanation for the intrusion of the Saldenburg and Untermittlerdorf granitoids and the sinistral shearing of granitoid bodies. a) Situation during D_2 just before D_3 (single event). Pre-Saldenburg granite facies are represented. Thin lines represent the foliation formed at this stage: Continuous and dashed ones represent subsolidus and hypersolidus foliations, respectively. b) The rotation of the principal compression to a NE-SW direction leads to the formation of vertical, conjugate weak planes at some angle to σ_1 under ductile conditions. The deformation of sinistrally sheared granitoids takes place, and also a weak sinistral overprint at the Bayerischer Pfahl shear zone is possible. c) Intrusion of the Saldenburg granite, magmatic flow parallel to the average strike of weak planes and development of magmatic fabric (dashed lines).

Saldenburg granite intruded. The explanation for the emplacement of the Saldenburg granite, leading to NE—SW magmatic flow, the development of NE—SW trending magmatic fabrics, and the occurrence of D_3 (single event, in this framework), starts with the consideration that the NE—SW compression would have led to the shearing of some pre-existing granitoids and to the development of shear planes in the Fürstenstein area. There were possibly several of these planes forming a conjugate system at some angle to σ_1 . The Saldenburg magma intruded then along these planes, developing an average NE—SW fabric and destroying any evidence for the preceding deformation (Fig. 5.4.5.1-3).

5.4.5.2. Models based on local processes

The sinistrally sheared granites with ENE to ESE striking shear planes have been reported only in the area surrounding the Fürstenstein pluton so far. The intrusion of the Untermittlerdorf rhyolite and the Saldenburg granite and D_3 occurred coevally, supposed that D_3 occurred in one single event as the host rock was at about 500°C. Given this scenario, two models might be proposed:

Model 1. Since the intrusion of the Saldenburg granite is associated with D_3 in time, its internal structure must not necessarily be regarded as a consequence, but perhaps rather as the cause of the NE—SW compression. Further on, the structure of the Saldenburg granite can be explained in the context of the activity of the Bayerischer Pfahl shear-zone system, as the magmatic flow parallels the orientation of the NE—SW striking, conjugate Rodl shear zone and similar ones (Figs. 5.2.1-2, 5.2.2-1). Thus, it is conceivable that the migration of the Saldenburg magma started as a consequence of the N—S compression and exploited a NE—SW striking discontinuity. The latter controlled the site of magma ascent by focusing melt accumulation at depth, provided a favourable site for the initiation of dykes or diapirs and could have even functioned as feeding channel during the ascent. At the time of emplacement, the magma moved passively in NE—SW direction along the weak zone and pushed the country rocks aside to the NW and SE. This NW—SE expansion was accompanied by rigid translation with more or less contribution of shortening of the country rock. The interference between local NW—SE diverging forces (extension) and the regional N—S compression could have resulted in local NE—SW compression, which lasted only for a short time. This short-lived NE—SW compression led to D_3 . After the Saldenburg granite completed its emplacement and stopped pushing, the normal N—S compression was restored and D_3 ended, giving way to the next deformation phase D_4 (Fig. 5.4.5.2-1).

This process would explain the coeval intrusion of the Saldenburg granite and the Untermittlerdorf rhyolite, as well as the deformation of sinistrally sheared granitoids. In the case that D_3 was episodic, this process would explain the D_{3B} event.

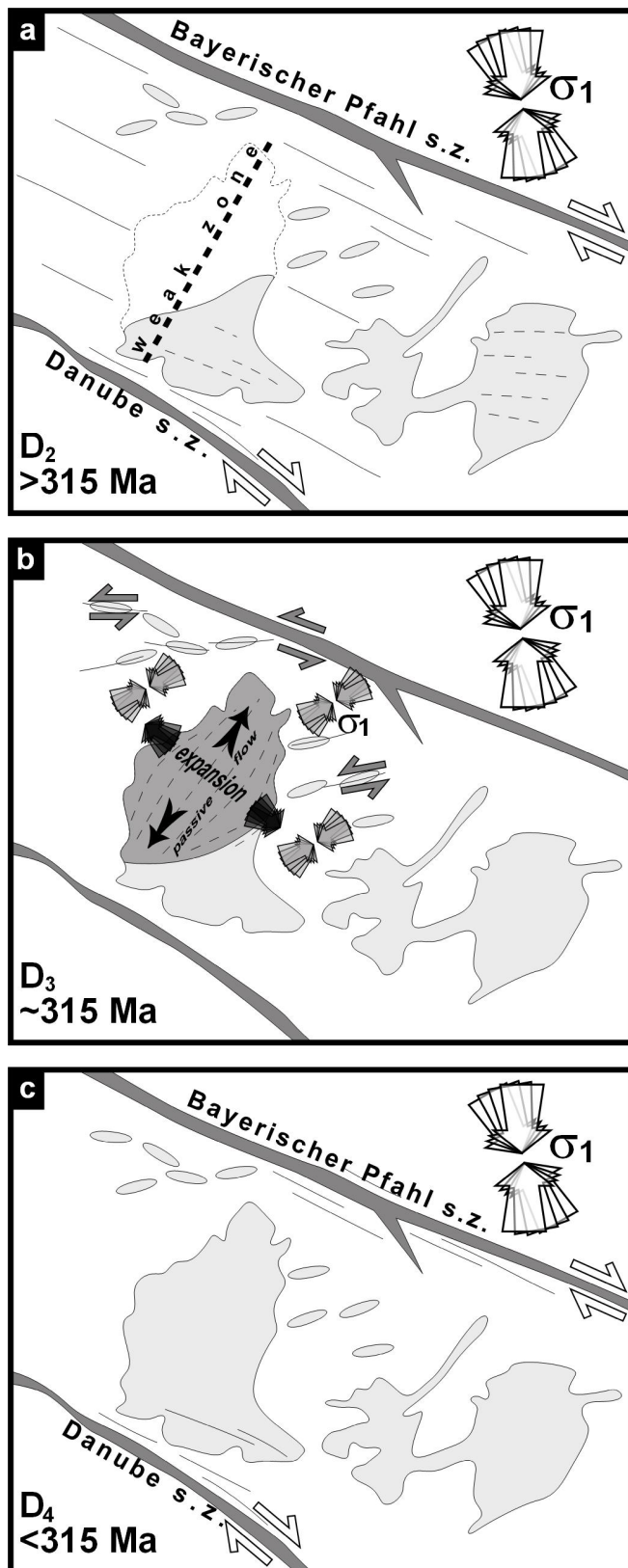


Figure 5.4.5.2-1. A possible scenario showing the change of orientation of σ_1 due to a local factor, which is the intrusion of the Saldenburg granite, supposing that the country rock was hot enough ($\sim 500^\circ\text{C}$) to allow D_3 to occur during one single event. a) Situation just before the intrusion of the Saldenburg granite (D_2). Pre-Saldenburg granite facies are represented. The white arrows show the position of σ_1 and the half-arrows the sense of shear during D_2 . Thin, continuous lines represent the subsolidus foliation, the dashed ones represent the hypersolidus foliation formed at this point in time. The generation of a weak zone that will act as a feeding channel activated the ascent of the Saldenburg granite magma. b) Situation during the emplacement of the Saldenburg granite (D_3). The magma flows passively in NE—SW direction (black thin arrows) and pushes the country rock to the NW and SE. The interference between local and regional stresses, represented in black and white thick arrows, respectively, results in a local NE—SW compression (grey arrows) in the neighbourhood of the Fürstenstein pluton. The grey half-arrows represent the sense of shear in sinistrally sheared granites. At this stage a steep mylonitic foliation striking ENE to ESE develops in granites (S_3). A shear sense reversal might have occurred at the

Bayerischer Pfahl shear zone at this time. c) Situation after the emplacement of the Saldenburg granite (D_4). The regional compression in N—S direction is restored, as well as the activity of the Bayerischer Pfahl shear-zone. The deformation is localized in the vicinity of the shear zones.

Model 2. Shear zones often show an irregular shape. In its present cartographic form, the Bayerischer Pfahl shear zone is straight, showing a more or less constant strike at about N120E, practically without irregularities. Nevertheless, the present shape of this shear zone is conditioned by a long deformation history spanning over several million years and governed by a wide variety of temperatures. Thus, it is conceivable that this shear zone might have had a more sinuous shape at earlier development stages. The next model proposed is based on this idea and considers the Bayerischer Pfahl as a sinuous shear zone, in which one or more releasing bends existed at the time of D₃ (Fig. 5.4.5.2-2). These releasing bends were areas in which NW—SE extension took place, provoking local perturbations of the stress fields in their neighbourhood. The local NW—SE extension would have led to local NE—SW compression in areas adjacent to releasing bends, with more or less interference between local and regional stresses, leading to the sinistral shear along planes trending ENE to ESE and to the development of weak planes parallel or at a low angle to the local σ_1 which were exploited by the Saldenburg granite for its ascent and emplacement (in a similar way as represented in Figs. 5.4.5.1-2b and 5.4.5.1-3b). The releasing bends were probably ephemeral and were later sealed and obscured by further deformation under dropping temperatures (Fig. 5.4.5.2-2). This model may account either for a single or for several D₃ events. However, no field evidence for such fossil releasing bends was found so far.

In summary, some near-, intermediate-, and far-field processes have been proposed to explain not only the characteristics of the studied sinistrally sheared granites, but also the data available about the geological framework in which they appear. The role played by each of the mentioned processes cannot be exactly postulated at present, but one or more of them could have operated during the Late Carboniferous, giving way to changes of the stress fields between D₂, D₃ and D₄.

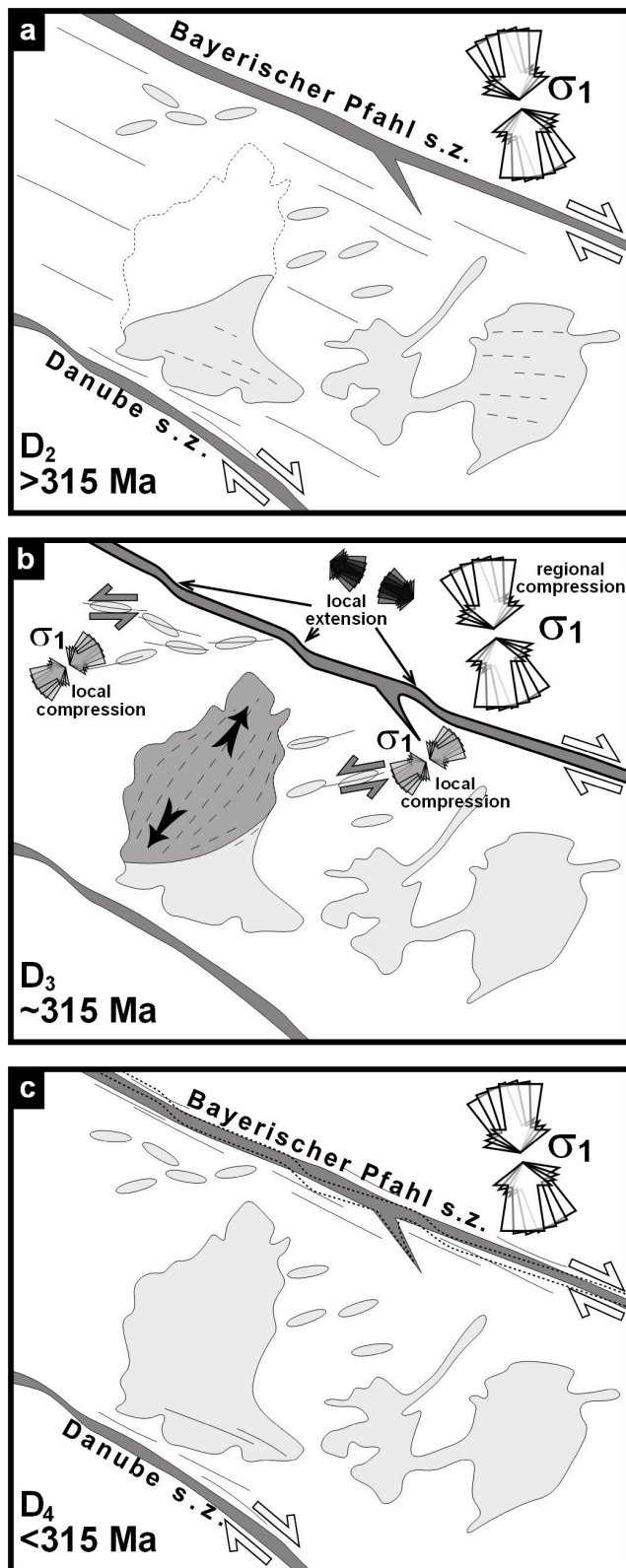


Figure 5.4.5.2-2. A possible scenario showing the change of orientation of σ_1 due to a local factor, which is the development of releasing bends at the Bayerischer Pfahl shear zone, supposing that the country rock was hot enough ($\sim 500^\circ\text{C}$) to allow D_3 to occur during one single event. a) Situation just before the intrusion of the Saldenburg granite (D_2). Pre-Saldenburg granite facies are represented. The white arrows show the position of σ_1 and the half-arrows the sense of shear during D_2 . Thin, continuous lines represent the subsolidus foliation, the dashed ones represent the hypersolidus foliation formed at this point in time. b) The development of one or more releasing bends at the Bayerischer Pfahl shear zone is schematically represented. A local NW—SE extension takes places at the releasing bends (black thick arrows). This originates, with more or less interference with the regional stresses, a local NE—SW compression in the neighbourhood of the Bayerischer Pfahl shear zone (grey arrows). This local compression is responsible for D_3 and for intrusion of the Saldenburg granite (the magma flows passively in NE—SW direction along weak planes parallel or at a low angle to σ_1). The grey half-arrows represent the sense of shear in sinistrally sheared granites. At this stage a steep mylonitic foliation striking ENE to ESE develops in granites (S_3 , thin lines). c) Situation

after the emplacement of the Saldenburg granite (D_4). The Bayerischer Pfahl shear zone becomes straighter. The deformation is localized in the vicinity of the shear zones. Any evidence for the formerly existing releasing bends (dashed line) is obscured by further deformation.

6. Conclusions

The present work has studied the role of different mechanisms in the ascent and emplacement of granitic bodies and the behaviour of these bodies on later deformation in different areas of the Variscan Orogen of western and central Europe. In the next lines, the conclusions of this research will be summarised. We will focus first on regional aspects of the studied rocks, concerning the ascent and emplacement of the granitoids studied in the Iberian Massif (chapter 6.1) and the tectonometamorphic evolution of the intrusives studied in the Bohemian Massif (chapter 6.2) in relation to their geological framework. Afterwards, some general conclusions about migration (chapter 6.3) and deformation of granitoids (chapter 6.4) will be recapitulated, regarding these processes independently from their regional geological context.

6.1. Migration of granitoids in the Iberian Massif

The ascent and emplacement mechanisms of granitic magmas were studied in depth on two intrusive bodies of the Iberian Massif: the La Bazana pluton and the Nisa-Albuquerque batholith. The reconstruction of the ascent and emplacement history of an intrusive body requires a detailed knowledge about its three-dimensional shape and structure. Thus, the gravimetric models presented, together with some new structural data, constitute the main contribution of this work to the hypersolidus history of Variscan granitoids.

The La Bazana pluton is a small, sub-circular body in map view that intruded into Cambrian slates, metagreywackes and volcanics of the Ossa-Morena Zone in the core of a late upright antiform. The intrusion took place at the end of or after the main Variscan ductile deformations. The granite shows a dome-shaped fabric pattern. Magmatic foliations usually dip shallowly towards the host rock. The NW–SE regional attitude of the main foliation in the country rock accommodates to the dome shape of the pluton, showing gentle deflections around it. Flattening of the host rock on top of the granite is indicated by boudinaged and folded veins. These structures are thought to be caused by the upward pushing of the magma during its ascent and arrival at the site of emplacement. The level of final emplacement was deduced from the mineral associations in the thermal aureole to be of 7–10 km in depth. The relatively deep level of emplacement is congruent with the lens shaped lateral expansion at the top of the granite body. Aeromagnetic data reveal no significant anomalies related to the granite, meaning that it is homogeneous in composition. Models of the residual gravity anomaly related to the granite body show that the granite has a teardrop–pipe shape widened at its top. The modelled granite thickness varies, depending on the assumed density contrasts, between 4 and 10 km, whereas its teardrop–pipe shape remains nearly unchanged. The results suggest that the magma ascended diapirically through the

middle crust until reaching a level of higher viscosity, where final emplacement accompanied by late-magmatic lateral expansion and vertical flattening took place.

The Nisa-Alburquerque batholith is a 1000 km² granitic body that intruded during the Late Carboniferous into rocks the Central Iberian Zone, the Central Unit, and the Ossa-Morena Zone after the Variscan ductile deformation phases. Its cartographic shape is elongate and parallel to the NW—SE to WNW—ESE Variscan structures. The new geophysical data, combined with previous petrologic, geochemical, isotopic and structural data, were used to infer the geometry and emplacement history of the dominant facies of the Nisa-Alburquerque batholith: the Coarse-Grained Granite. The latter is characterized by chaotic fabrics in the eastern part, NW—SE striking fabrics in the central sector and N—S striking fabrics in the western part. In general, the fabric parallels the longest dimension of the batholith, the external contacts and the regional foliation in the host rocks, except in the westernmost termination where it is strongly oblique to the regional foliation. Several datings on the Coarse-Grained Granite yielded ages between 285 and 310 Ma. Its intrusion depth was estimated to be 7-10 km. The batholith is modelled as an east-southeast inclined cylinder-shaped body that is rooted to the east and becomes rather flat-floored and superficial to the west. The eastern root, which coincides with more leucocratic and younger facies, is interpreted as the feeding channel. The internal fabric of the batholith can be explained as a result of the combination of nearly uniform to non-coaxial flow in the central part, producing NW—SE striking magmatic fabrics, and deceleration flow towards the western part. The N—S striking fabrics at the western end of the batholith are interpreted as an effect of the deceleration flow and the pushing of incoming magma batches. The intrusion is viewed as a continuous lateral magma flow from the eastern root guided towards the west through the southern limb of a kilometre-scale antiform. As mass-transfer mechanisms, a combination of rigid translation of the country rocks, stoping, and possibly ballooning is proposed.

6.2. Tectonometamorphic evolution of the Bavarian Forest

The research performed in the Bavarian Forest focused on the subsolidus evolution of some granitoids, especially those affected by the deformation phase referred to as D₃. The main contributions of the present work to the knowledge of the region are: 1) the geological mapping of the topographic sheet 1:25000 No. 7246 Tittling, which allowed a better understanding of some of the rock types present in the southern Bavarian Forest, as well as the discovery of several granitoid bodies affected by D₃; 2) the establishment of the main deformation phases occurred in the study area, D₁ to D₄, and their characterization in terms of kinematics, temperature and pressure by means of structural, EBSD, and barometric studies; 3) the proposal of some geodynamic models

integrating new and pre-existing data, which may account for the tectonometamorphic history of the area and, in particular, for the occurrence of D_3 .

Although the hypersolidus evolution of intrusive bodies of the Bohemian Massif was not the main focus of this work, some conclusions about their ascent and emplacement can be outlined. The shape of the different magmatic bodies reflects the thermal evolution of the crust in which they ascended and froze. Elliptical, irregular or elongate intrusive bodies, usually older than ~ 310 Ma, intruded into a relatively hot crust. The way they ascended is not well known, but the exploitation of pre-existing anisotropies seems to be the most efficient mechanism in this context. Some contribution of diapirism is conceivable in some of the largest and more equidimensional bodies, such as the Hauzenberg granite II (Hauzenberg pluton) and the Saldenburg granite (Fürstenstein pluton). Stoping was an important emplacement mechanism during the intrusion of several granitic stocks, which provoked the fragmentation of the dioritic to granodioritic and migmatitic country rocks. The intrusive bodies younger than ~ 310 are dykes of sharp and planar contacts, suggesting ascent through dykes in a relatively cold crust.

Four ductile deformation phases are proposed for the study area. D_1 produced high-temperature fabrics under upper amphibolite to granulite facies conditions, probably coinciding with the thermal peak of the regional HT-LP metamorphism. Its kinematics is unknown. D_1 is usually obscured by later deformation phases, but still identifiable as a relict. D_2 occurred under amphibolite to upper greenschist facies conditions in the studied samples, and is responsible for a subvertical NW—SE striking foliation in migmatites and for the deformation at the Bayerischer Pfahl shear-zone system at its earlier stages. Most of the dioritic to granodioritic bodies and some of the granitic ones intruded prior to or during this deformation phase, in which the main compression was probably oriented in N—S to NNW—SSE direction.

Many granitoid dykes and stocks were found to be affected by sinistral shear along planes trending ENE to ESE. Since this deformation, which is called D_3 in the present work, is not compatible with a N—S to NNW—SSE compression, it is proposed that these sinistral shear zones in granites do not belong to the Bayerischer Pfahl shear-zone system and constitute themselves a separated shear-zone system, which is called “ D_3 shear-zone system”. D_3 took place under upper greenschist to lower amphibolite facies conditions, as supported by the observed fabrics and by quartz LPO patterns. Both the intrusion and the deformation of the granites affected by D_3 occurred at deep to intermediate levels of the crust, whereas the deformation took place under NE—SW compression. Datings on two of the deformed granites yielded 324.4 ± 0.8 Ma (Saunstein granite) and 315.0 ± 1.0 Ma (Untermitteldorf rhyolite): Thus, the age D_3 is most probably ~ 315 Ma, although an episodic D_3 involving some additional, older pulses, is also conceivable. Nevertheless, quartz lattice preferred orientation patterns and microfabrics show similar characteristics in all the studied samples, suggesting that D_3 was localised in time and that the deformation temperature was in most cases not

influenced by any advective heat carried by the sheared intrusives themselves. In other words, the intrusion of most of the sheared granitoids was pre-kinematic with respect to D_3 .

After D_3 the existence of a following D_4 , with a similar arrangement of the principal stresses as D_2 , is postulated. D_4 produced further deformation at the Bayerischer Pfahl shear-zone system and neighbouring areas under greenschist facies conditions and below.

The geodynamic models proposed regard different regional and local processes, which might have been responsible for the change of the compression direction between D_2 , D_3 and D_4 . These models are summarized as follows:

1. As proposed by some authors (e.g. Ziegler, 1990), in late-Variscan times the convergence direction between Laurussia and Gondwana might have changed from NW—SE to E—W or NE—SW.
2. The sinking of the cold Teplá-Barrandian block at Late Devonian to Late Carboniferous times (Zulauf, 1994), might have produced local perturbations of the regional stress field and lateral extrusion of the surrounding and underlying hot Moldanubian rocks. The sinking of the Teplá-Barrandian unit might have influenced and distorted the stress fields in the vicinity for a long time, either continuously or episodically, thus provoking anomalous stress fields in a far-field N—S to NW—SE convergent scenario. The effect of the sinking of the Teplá-Barrandian block on Moldanubian rocks is then envisaged as a combination of internal deformation and rigid translation of surrounding rocks which could have resulted in the development of (1) some of the contractive, ductile structures in the northern sector of the Moldanubian Zone, such as the NW—SE trending folds developed during the D_4 of Tanner (1995), or the D_4 open folds with horizontal axes trending NNW—SSE found by Stein (1988), (2) the sinistral overprint at the Bayerischer Pfahl shear zone observed by Mattern (1995), and (3) the sinistrally sheared granites described in the present work, which would represent shear zones along soft paths bounding blocks of relatively rigid behaviour.
3. The intrusion of the Saldenburg granite is associated with D_3 in time. It is possible that the migration of the Saldenburg magma started as a consequence of the N—S compression and exploited a NE—SW striking discontinuity. At the time of emplacement, the magma moved passively in NE—SW direction and pushed the country rocks aside to the NW and SE. This NW—SE expansion was accompanied by rigid translation with more or less contribution of shortening of the country rock. The interference between local NW—SE diverging forces (extension) and the regional N—S compression could have resulted in local NE—SW compression, which lasted only for a short time and led to D_3 . After the Saldenburg granite completed its emplacement and stopped pushing, the normal

N—S compression was restored and D_3 ended, giving way to the next deformation phase D_4 .

4. The Bayerischer Pfahl shear zone is straight in its present cartographic form, but its shape is conditioned by a long deformation history spanning over several million years and governed by a wide variety of temperatures. It is conceivable that the Bayerischer Pfahl shear zone might have had a more sinuous shape at the time of D_3 , with one or more releasing bends. These releasing bends were areas in which NW—SE extension took place, provoking local perturbations of the stress fields in their neighbourhood. The interference between local NW—SE extension and regional N—S compression would have led to local NE—SW compression in areas adjacent to releasing bends, leading to the sinistral shear along planes trending ENE to ESE and to the development of weak planes parallel or at a low angle to the local σ_1 which were exploited by the Saldenburg granite for its ascent and emplacement. The releasing bends were probably ephemeral and were later sealed and obscured by further deformation under dropping temperatures.

6.3. Ascent and emplacement of granitoids

Beside implications for the regional geology of the study areas, the intrusive bodies shown in this work provided some contribution to the problem of magma migration, which is being discussed in recent papers.

The La Bazana granite constitutes a field example of how felsic magmas may reach the upper crust by diapirism. The observed lens shape at its upper part suggests that diapiric granites could evolve from teardrop shapes towards flat geometries during their final emplacement, by means of lateral expansion at the top.

The La Bazana and Nisa-Albuquerque intrusions illustrate that the migration direction, final location and shape of intrusive bodies is conditioned by the structure (anisotropy and heterogeneity) of the country rock. Thus, the aforementioned bodies intruded into antiformal structures at middle to upper levels of the crust. Reaching progressively more viscous levels, the magma stopped its upward movement and switched from vertical to horizontal migration. In the case of a small granitic body like the La Bazana pluton, this lateral movement may be limited and more or less radial. In the case of bigger intrusions, like the Nisa-Albuquerque batholith, this sideward migration may reach several tens of kilometres and polarize toward preferred orientations conditioned by regional structures.

Stoping is usually regarded as a process operating mostly in the upper crust, as observed for example in the Nisa-Albuquerque batholith, but the present work shows that it can play an important role also in deeper levels: As exemplified in the Bavarian

Forest, the intrusion of several stocks, whose age might be similar to the one of the Saunstein dyke (~324 Ma), provoked pervasive stoping of the dioritic to granodioritic and migmatic country rocks. Also the emplacement of the Saldenburg granite (~315 Ma) was accompanied by stoping, i.e. by the incorporation of fragments of country rocks and older magmatic facies. In both cases, intrusion depths exceeded 15 km.

Our results indicate that diapirism is a valid ascent mechanism even at intermediate to upper levels of the crust, as demonstrated by the La Bazana pluton. But evidence supporting indirectly the viability of diapirism can be found in other intrusives. In both the Iberian and the Bohemian Massif, it is common to find repeated intrusion of several magma batches at the same location. This holds for the Nisa-Alburquerque batholith and other composite intrusive bodies of the Iberian Massif; the Fürstenstein and the Hauzenberg plutons constitute also good examples of this, as well as several granodioritic to dioritic stocks all over the Bavarian Forest, which are systematically intruded by younger granites. This implies that younger magma batches use to benefit from older ones, which provide thermally and mechanically prepared pathways for their ascent. This constitutes a strong argument supporting the ideas of Marsh (1982) and Miller and Paterson (1999) suggesting that some thermal and mechanical models that reject diapirism as a valid ascent mechanism oversimplify the real conditions governing the rheological behaviour of the Earth's crust. These models usually regard magmas as isolated bubbles ascending through a homogeneous or nearly homogeneous crust. Further models of magma ascent should consider the crust as a thermally, compositionally and rheologically heterogeneous body, and the magmas not as isolated, but much more as nested batches following each other along one and the same pathway.

6.4. Deformation of granitoids

The research carried out on deformed granitoids of the Bavarian Forest led to the achievement of some results concerning general issues on structural geology, about fabrics, textures and strain in a general view, independently of regional considerations.

Oblique foliations defined by the SPO of quartz have been proven to fail when used as shear-sense indicators in some cases. In the case of the Saunstein dyke, most of the shear-sense criteria, such as σ -type mantled porphyroclasts, mica fishes and *S-C* structures, point to a sinistral shear sense, whereas quartz oblique foliations point to a later dextral reactivation. Thus, it must be concluded that quartz oblique foliations should be used with caution as shear-sense indicators, since they have a short-lived strain memory and are representative only for the very last strain increment.

EBSD studies are very useful in order to infer deformation mechanisms and temperatures. It has been shown that even rocks which underwent a weak deformation

might show relatively well-developed LPO patterns. Thus, the application of EBSD techniques might be useful for the study of deformations in rocks which appear nearly undeformed at first sight. On the other hand, for the interpretation of quartz LPO patterns it is necessary to bear in mind that their development is conditioned not only by the deformation temperature, but also by other factors amongst which the grain size of the rock seems to be a critical one: As we observed in many examples, fine-grained rocks tend to deform by means of grain-boundary sliding instead of dislocation creep, which results in the development of poorly-defined LPO patterns or in the destruction of pre-existing ones. This applies for primary, small grain sizes, but also for small grain sizes achieved during progressive deformation, i.e. LPO patterns might weaken or even disappear by increasing strain.

The influence of the grain size in the activation of certain deformation mechanisms leaves its imprint not only in the LPO patterns observed, but also in the microfabrics developed. As long as some fine-grained domains of the rock accommodate most of the strain by grain boundary sliding, some others like for example porphyroclasts or coarse-grained domains might remain nearly undeformed, even though the temperature would be high enough to allow their recrystallization. This effect becomes especially patent in rocks with bimodal grain-size distribution, as exemplified by the Untermittlerdorf rhyolite.

Strain localisation is a widespread phenomenon observed in many deformed rocks, also in the Bavarian Forest. The deformation referred to as D_3 is preferentially localised in granites. This is due to the fact that granites are usually richer in quartz than the surrounding country rocks, and therefore weaker. Thus, granites constituted soft corridors at which deformation concentrated. Strain localisation is a self-feeding process: As shown in the Saunstein dyke, once the deformation starts at a given location of the rock, the reduction in grain size promotes grain boundary sliding; in the same way, fluid access gives way to reaction softening or hydrolytic weakening, and formation of white mica in cleavage domains also promotes grain boundary sliding. The result is the permanent concentration of the deformation there where it initiates.

Finally, the phenomenon of strain localisation has important implications for the reliability of dated igneous rocks when used as time markers for deformations. Ductile deformations might occur not *en masse*, but rather in a spatially localized fashion. As we saw in the Bavarian Forest, the deformations D_2 to D_4 did not always affect all the rocks present in the region, and this is not necessarily due to a post-kinematic genesis with respect to the considered deformation phase. This is due to several factors, mainly: 1) As already mentioned, different rock types show different rheological behaviour, either due to thermal or mineralogical contrasts, i.e. hot rocks and rocks rich in quartz are softer and tend to accommodate more strain than surrounding rocks, and it obviously does not mean that the surrounding rocks are younger at all; 2) even though a given rock body might be softer than the surroundings, whether it accommodates some strain or not depends also on its position and geometry, i.e. only soft rock bodies

with favourable geometry, orientation and position will be able to accommodate strain and rigid translation of adjacent blocks. Thus, special care is needed when inferring the deformation history of a region based on the deformation of dated igneous rocks as time markers.

7. Perspectives

Exhaustive studies on intrusive bodies should integrate surface, geophysical, petrological, and structural data in order to propose models that explain their migration and deformation history. Most of the studies found in the literature use to offer only partial approaches to this issue, making use of a limited array of techniques.

One important deficiency of many studies about the ascent and emplacement history of plutons resides on the lack of constraints about their three-dimensional geometry. Several evolution models of plutons cropping out in or in the surroundings of the study areas are based only on surface data. This is, for example, the case for the Fürstenstein Pluton (Dietl et al., 2005), the Los Pedroches batholith (Aranguren et al., 1997), the plutons of the Burguillos anticline (Brun and Pons, 1981), and some plutons of Central Extremadura (Castro, 1986; Castro and Fernández, 1998; these plutons were later gravimetrically modelled by Campos et al., 1999). The systematic application of geophysical techniques in the future might considerably improve our understanding about the intrusion processes and their integration in the dynamics of the crust.

Whether the development of D_3 in the Bavarian Forest study area was caused by local or regional processes, or a combination of both, cannot be definitely stated at present. The body of evidence presented in this study, combined with the results published by other authors, is still insufficient to discriminate between the different evolution models proposed here. Nevertheless, the present work provides some hints for the investigation lines that might be followed and the hypotheses that might be explored in the future. Further works should try to check the possible existence of structures which can be correlated in time with the sinistral sheared granites in other parts of the Bavarian Forest and the Moldanubian Zone. This is key information in order to shed light on the causes for the development of D_3 .

A systematic sampling and analysis of the shear zones that constitute the Bayerischer Pfahl and the D_3 shear-zone systems would contribute to further constrain the temperature and time range at which the deformation took place and the possible existence of structures supporting components of vertical displacement. The existence of some vertical displacements at the Bayerischer Pfahl shear zone are assumed by some workers, but little evidence has been published so far.

The new maps at scale 1:25000 of the Bavarian Environment Agency, which are currently being published, will constitute an excellent foundation for searching appropriate sampling sites for both the Bayerischer Pfahl shear-zone system and the D_3 shear-zone system, as well as for the improvement of the inventory of Late Carboniferous structural elements.

One of the main uncertainties concerning the tectonothermal evolution of the Bavarian Forest is the P-T-t path followed by the migmatites during and after the Variscan

anatexis. New thermobarometric and geochronological studies, still lacking in some areas of the Bavarian Forest, would contribute to further constrain the conditions under which deformation and metamorphism took place. Systematic studies of deformed intrusives combining geochronological, thermobarometric, and structural data are essential in order to reconstruct the geological history of the Bavarian Forest and its integration in the context of the Bohemian Massif and the whole Variscan Orogen.

Finally, it would be interesting to study in depth how LPO patterns behave not only depending on the deformation temperature, but also depending on the grain-size of the rock, its mono- or polymineralic character and the strain intensity. This study could be undertaken by means of analogue modelling and would deliver key information in order to interpret LPO patterns in the future.

References

- Abalos, B., Azcarraga, J., Gil Ibarra, J.I., Mendia, M.S., Santos Zalduegui, J.F., 1996. Flow stress, strain rate and effective viscosity evaluation in a high-pressure metamorphic nappe (Cabo Ortegal, Spain). *Journal of Metamorphic Geology* 14, 227-248.
- Acocella, V., Mulugueta, G., 2001. Surface deformation induced by pluton emplacement: The case study of Amiata (Italy). *Physics and Chemistry of the Earth* 26, 355-362.
- Acocella, V., Mulugueta, G., 2002. Experiments simulating surface deformation induced by pluton emplacement. *Tectonophysics* 352, 275-293.
- Améglio, L., Vigneresse, J.L., Bouchez, J.L., 1997. Granite pluton geometry and emplacement mode inferred from combined fabric and gravity data. In: Bouchez, J.L., Hutton, D.H.W., Stephens, W.E. (eds.), *Granite: from Segregation of Melt to Emplacement Fabrics*, 199-214, Kluwer Academic Publishers.
- Aranguren, A., Larrea, F.J., Carracedo, M., Cuevas, J., Tubía, J.M., 1997. The Los Pedroches batholith (southern Spain): polyphase interplay between shear zones in transtension and setting of granites. In: Bouchez, J.L., Hutton, D.H.W., Stephens, W.E. (Eds.), *Granite: From Segregation of Melt to Emplacement Fabrics*, 215-229, Kluwer Academic Publishers.
- Aranguren, A., Tubia, J.M., Bouchez, J.L., Vigneresse, J.L., 1996. The Guitiriz granite, Variscan belt of northern Spain: extension-controlled emplacement of magma during tectonic escape. *Earth and Planetary Science Letters* 139, 165-176.
- Artmann, C., 2001. Erläuterungen zur geologischen Karte 7146 Grafenau (NW-Teil, nördlich Schönberg) und Untersuchungen zu den felsmechanischen Kennwerten der Mylonite der Pfahlzone. Unpublished Diploma Thesis, Technische Universität München.
- Azor, A., González Lodeiro, F., Simancas, J.F., 1994. Tectonic evolution of the Boundary between the Central Iberian and Ossa-Morena Zones (Variscan Belt, SW Spain). *Tectonics* 13, 45-61.
- Azor, A., Menéndez, L.G., Galindo-Zaldívar, J., Galadí-Enríquez, E., 2000. Structure of the Nisa-Alburquerque batholith (SW Iberian Massif). In: *Variscan-Appalachian Dynamics: The Building of the Upper Paleozoic Basement*, 15th International Conference on Basement Tectonics, abstracts, A Coruña (Spain).
- Bateman, R., 1984. On the role of diapirism in the segregation, ascent and final emplacement of granitoid magmas. *Tectonophysics* 110, 211-231.

Bayer, B., 1997. Geochemie und Petrographie von spätvariskischen Ganggesteinen des Vorderen Bayerischen Waldes. Unpublished Diploma Thesis, Ludwig Maximilians Univ. München.

Bea, F., Montero, P., Molina, J.F., 1999. Mafic precursors, peraluminous granitoids, and late lamprophyres in the Ávila batholith: A model for the generation of Variscan batholiths in Iberia. *Journal of Geology* 107, 399-419.

Bea, F., Villaseca, C., Bellido, F., 2004. El Batolito de Ávila (Sistema Central Español). In: Vera, J.A. (Ed.), *Geología de España*, SGE-IGME, Madrid, 101-110.

Beer, W.W., 1981. Die strukturelle Entwicklung der Metamorphite des Bayerischen Waldes. PhD Thesis, Univ. Göttingen.

Behrmann, J.H., 1985. Crystal plasticity and superplasticity in quartzite: a natural example. *Tectonophysics* 115, 101-129.

Behrmann, J.H., Mainprice, D., 1987. Deformation mechanisms in a high-temperature quartz-feldspar mylonite: evidence for superplastic flow in the lower continental crust. *Tectonophysics* 140, 297-305.

Behrmann, J.H., Tanner, D.C., 1997. Carboniferous tectonics of the Variscan basement collage in eastern Bavaria and western Bohemia. *Geologische Rundschau* 86 Suppl., 15-27.

Benn, K., Odonne, F., Lee, S.K.Y., Darcovich, K., 2000. Analogue scale models of pluton emplacement during transpression in brittle and ductile crust. *Transactions of the Royal Society of Edinburgh: Earth Sciences* 91, 111-121.

Benn, K., Odonne, F., Saint-Blanquat, M., 1998. Pluton emplacement during transpression in brittle crust: New views from analogue experiments. *Geology* 26, 1079-1082.

Berger, F., Kiehm, S., Klein, T., Dörr, W., Zulauf, G., 2002. Alter und Intrusionstiefe des Hauzenberger Granits. *Erlanger Geologische Abhandlungen, Sonderband* 3, 9-10.

Berner, H., Ramberg, H., Stephansson, O., 1972. Diapirism in theory and experiment. *Tectonophysics* 15, 197-218.

Berthé, D., Choukroune, P., Jegouzo, P., 1979. Orthogneiss, mylonite and non coaxial deformation of granites: the example of the South Armorican Shear Zone. *Journal of Structural Geology* 1, 31-42.

Bjornerud, M., 1989. Toward a unified conceptual framework for shear-sense indicators. *Journal of Structural Geology* 11, 1045-1049.

- Blaha, U., in press. Geologische Karte von Bayern 1:25 000, Erläuterungen zum Blatt Nr. 7145 Schöfweg. Bayerisches Landesamt fuer Umwelt, München.
- Blaha, U., Siebel, W., 2006. Geologische Karte von Bayern 1:25000, Blatt Nr. 7145 Schöfweg. Bayerisches Landesamt fuer Umwelt, München.
- Blenkinsop, T., 2000. Deformation microstructures and mechanisms in minerals and rocks. Kluwer Academic Publishers.
- Blümel, P., 1995. The Moldanubian Zone in Bavaria. In: Dallmeyer, R.D., Franke, W., Weber, K. (Eds.), Pre-Permian geology of Central and Eastern Europe, 462-464, Springer.
- Bohlen, S.R., Montana, A., Kerrick, D.M., 1991. Precise determinations of the equilibria kyanite-sillimanite and kyanite-andalusite and a revised triple point for Al_2SiO_5 polymorphs. *American Mineralogist* 76, 677-680.
- Borradaile, G.J., 1988. Magnetic susceptibility, petrographics and strain. *Tectonophysics* 156, 1-20.
- Bouchez, J.L., 1997. Granite is never isotropic: an introduction to AMS studies of granitic rocks. In: Bouchez, J.L., Hutton, D.H.W., Stephens, W.E. (Eds.), *Granite: From Segregation of Melt to Emplacement Fabrics*, 95-112, Kluwer Academic Publishers.
- Bouchez, J.L., Pêcher, A., 1981. The Himalayan Main Central Thrust pile and its quartz-rich tectonites in central Nepal. *Tectonophysics* 78, 23-50.
- Boullier, A.M., Gueguen, Y., 1975. SP-Mylonites: origin of some mylonites by superplastic flow. *Contributions to Mineralogy and Petrology* 50, 93-104.
- Brandmayr, M., Dallmeyer, R.D., Handler, R., Wallbrecher, E., 1990. Age and kinematics of shear zones in the southern Bohemian Massif: evidence from the Rodl shear zone. Terranes in the circum-atlantic Paleozoic orogens, International Conference on Paleozoic orogens in Central Europe, conference abstracts, Göttingen-Giessen Aug.-Sept. 1990.
- Brandmayr, M., Dallmeyer, R.D., Handler, R., Wallbrecher, E., 1995. Conjugate shear zones in the Southern Bohemian Massif (Austria): implications for Variscan and Alpine tectonothermal activity. *Tectonophysics* 248, 97-116.
- Brandmayr, M., Loizenbauer, J., Wallbrecher, E., 1999. Contrasting P-T conditions during conjugate shear zone development in the Southern Bohemian Massif, Austria. *Mitteilungen der Österreichischen Geologischen Gesellschaft* 90, 11-29.
- Brown, D., Tryggvason, A., 2001. Ascent mechanism of the Dzhabyk batholith, southern Urals: constraints from URSEIS reflection seismic profiling. *Journal of the Geological Society, London* 158, 881-884.

- Brun, J.P., Pons, J., 1981. Strain patterns of pluton emplacement in a crust undergoing non-coaxial deformation, Sierra Morena, Southern Spain. *Journal of Structural Geology* 3, 219-229.
- Bundesanstalt fuer Geowissenschaften und Rohstoffe, 1993. Geologische Karte der Bundesrepublik Deutschland 1:1 000 000, Hannover.
- Burg, J.P., Iglesias, M., Laurent, Ph., Matte, Ph., Ribeiro, A., 1981. Variscan intracontinental deformation: The Coimbra-Córdoba Shear Zone (SW Iberian Peninsula). *Tectonophysics* 78, 161-177.
- Büttner, S.H., 1999. The geometric evolution of structures in granite during continuous deformation from magmatic to solid-state conditions: an example from the central European Variscan Belt. *American Mineralogist* 84, 1781-1792.
- Büttner, S., Kruhl, J.H., 1997. The evolution of a late-Variscan high-T/low-P region: the southeastern margin of the Bohemian massif. *Geologische Rundschau* 86, 21-38.
- Campos, R., Gumiel, P., Tejero, R., Plata, J.L., 1999. Modelización gravimétrica de los granitoides del sector central de Extremadura. *Revista Sociedad Geológica España* 12, 461-476.
- Campos, R., Plata, J.L., 1991. Gravity Survey. In: Gumiel, P., Antón-Pacheco, C., Campos R. (Eds.), *Development of new multidisciplinary techniques for mineral exploration in several areas of the western Iberian Peninsula*, ITGE Special Publication, 55-66.
- Castro, A., 1986. Structural pattern and ascent model in the Central Extremadura batholith, Hercynian Belt, Spain. *Journal of Structural Geology* 8, 633-645.
- Castro, A., Fernández, C., 1998. Granite intrusion by externally induced growth and deformation of the magma reservoir, the example of the Plasenzuela pluton, Spain. *Journal of Structural Geology* 20, 1219-1228.
- Chatterjee, N.D., Flux, S., 1986. Thermodynamic mixing properties of muscovite-paragonite crystalline solutions at high temperatures and pressures, and their geological applications. *Journal of Petrology* 27, 677-693.
- Chatterjee, N.D., Johannes, W., 1974. Thermal stability and standard thermodynamic properties of synthetic 2M1 muscovite, $KAl_2[AlSi_3O_{10}(OH)_2]$. *Contributions to Mineralogy and Petrology* 48, 89-114.
- Chen, F., Siebel, W., 2004. Zircon and titanite geochronology of the Fürstenstein granite massif, Bavarian Forest, SW Bohemian Massif: pulses of the late Variscan magmatic activity. *European Journal of Mineralogy* 16, 777-788.

- Chen, F., Siebel, W., Satir, M., 2002. Zircon geochronology and geochemistry of the Fürstensteiner pluton, Bavaria Forest. *Berichte der Deutschen Mineralogischen Gesellschaft* 14, 33.
- Christie, J.M., Ord, A., Koch, P.S., 1980. Relationship between recrystallized grain size and flow stress in experimentally deformed quartzite. *EOS Transactions American Geophysical Union* 61, 377.
- Christinas, P., Köhler, H., Müller-Sohnius, D., 1991a. Alterstellung und Genese der Palite des Vorderen Bayerischen Waldes (Nordostbayern). *Geologica Bavarica* 96, 87-107.
- Christinas, P., Köhler, H., Müller-Sohnius, D., 1991b. Rb-Sr-Alterbestimmungen an Intrusiva des Hauzenberges Massivs, Nordostbayern. *Geologica Bavarica* 96, 109-118.
- Clemens, D., 1998. Observations on the origins and ascent mechanisms of granitic magmas. *Journal of the Geological Society, London* 155, 843-851.
- Clemens, D., Mawer, C.K., 1992. Granitic magma transport by fracture propagation. *Tectonophysics* 204, 339-360.
- Cloos, H., Balk, E., Cloos, E., Scholtz, H., 1927. Die Plutone des Passauer Waldes. Ihr Bau und Werdegang und ihre innere Tektonik. *Monogr. zur Geol. und Paleont., Ser. II, H. 3*. Berlin.
- Corti, G., Morati, G., Sani, F., 2005. Relations between surface faulting and granite intrusions in analogue models of strike-slip deformation. *Journal of Structural Geology* 27, 1547-1562.
- Coutinho, J., Desmons, J., Kräutner, H., Peinado, M., Sassi, F., Schmid, R., Sen, S., 2002. Towards a unified nomenclature in metamorphic petrology: Amphibolite and Granulite. A proposal on behalf of the IUGS Subcommittee on the Systematics of Metamorphic Rocks. Web version of 31.10.2002, http://www.bgs.ac.uk/SCMR/scmr_products.html.
- Cruden, A., 1998. On the emplacement of tabular granites. *Journal of the Geological Society, London* 155, 853-862.
- Dallmeyer, R.D., Franke, W., Weber, K. (Eds.), 1995. *Pre-Permian geology of Central and Eastern Europe*, Springer.
- Dehls, J.F., Cruden, A.R., Vigneresse, J.L., 1998. Fracture control of late Archean pluton emplacement in the northern Slave Province, Canada. *Journal of Structural Geology* 20, 1145-1154.
- Dietl, C., Gößmann, M., de Wall, H., 2005. Kombinierte aktive und passive Plutonplatznahme in einer verdickten Kruste – Erste Ergebnisse von

gesteinsmagnetischen und petrologischen Untersuchungen a, Fürstensteiner Intrusivkomplex (Bayerischer Wald). *Zeitschrift der Deutschen Geologischen Gesellschaft* 155/2-4, 311-328.

Dixon, J.M., 1975. Finite strain and progressive deformation in models of diapiric structures. *Tectonophysics* 28, 89-124.

Dollinger, U., 1967. Das Hauzenberger Granitmassiv und seine Umrahmung. In: Troll, G. (Ed.), *Führer zu geologisch-petrographischen Exkursionen im Bayerischen Wald. Teil I: Aufschlüsse im Mittel- und Ostteil*. *Geologica Bavarica* 58, 145-168.

Drescher, F. K., 1930. Zur Genese der Diorite von Fürstenstein (Bayrischer Wald). *Neues Jahrbuch für Mineralogie, Geologie und Paläontologie, Beil.-Bd.* 60, 445-530.

England, R.W., 1990. The identification of granitic diapirs. *Journal of the Geological Society, London* 147, 931-933.

England, R.W., 1992. The genesis, ascent, and emplacement of the Northern Arran Granite, Scotland: Implications for granitic diapirism. *Geological Society of America Bulletin* 104, 606-614.

Etheridge, M.A., Wilkie, J.C., 1981. An assessment of dynamically recrystallized grain size as a palaeopiezometer in quartz-bearing mylonite zones. *Tectonophysics* 78, 475-508.

Expósito, I., 2000. *Evolución estructural de la mitad septentrional de la Zona de Ossa – Morena, y su relación con el límite Zona de Ossa – Morena / Zona Centroibérica*. PhD Thesis, Univ. Granada.

Fernández Carrasco, J., Coullaut, J.L., Aguilar, J.M., 1981. Mapa de la hoja nº 875 (Jerez de los Caballeros) del Mapa Geológico de España a escala 1: 50.000. IGME.

Finger, F., Gerdes, A., Janoušek, V., René, M., Riegler, G., 2007. Resolving the Variscan evolution of the Moldanubian sector of the Bohemian Massif: the significance of the Bavarian and the Moravo-Moldanubian tectonometamorphic phases. *Journal of Geosciences* 52, 9-28.

Finger, F., Roberts, M.P., Haunschmid, B., Schermaier, A., Steyrer, H.P., 1997. Variscan granitoids of central Europe: their typology, potential sources and tectonothermal relations. *Mineralogy and Petrology* 61, 67-96.

Fischer, G., 1926. Über Verbreitung und Entstehung der Titanitfleckengesteine im Bayrischen Wald. *Cbl. Min. Geol. und Paläont., A*, 155-168.

Franke, W., 1989. Tectonostratigraphic units in the Variscan belt of central Europe. In: Dallmeyer, R.D. (Ed.), *Terranes in the Circum-Atlantic Palaeozoic Ocean*. *Geological Society of America Special Paper* 230, 67-90.

- Franke, W., 1992. Phanerozoic structures and events in central Europe. In: Blundell, D., Freeman, R., Mueller, S. (Eds), *A Continent Revealed — The European Geotraverse*, 164-179, Cambridge University Press.
- Franke, W., 2000. The mid-European segment of the Variscides: tectonostratigraphic units, terrane boundaries and plate tectonic evolution. In: Franke, W., Haak, V., Oncken, O., Tanner, D. (Eds.), *Orogenic Processes: Quantification and Modelling in the Variscan Belt*, Geological Society of London Special Publications 179, 35-61.
- Frentzel, A., 1911. Das Passauer Granitmassiv. *Geognostische Jahrbücher* 24, 105-192.
- Freudenberger, W., 1996. Deckgebirge nördlich der Donau. In: Bayerisches Geologisches Landesamt (Ed.), *Erläuterungen zur Geologischen Karte von Bayern 1:500 000*, 4th ed., 259-265, München.
- Galadí-Enríquez, E., in press. Geologische Karte von Bayern 1:25 000, Erläuterungen zum Blatt Nr. 7246 Tittling. Bayerisches Landesamt für Umwelt, München.
- Galadí-Enríquez, E., Blaha, U., Siebel, W., Rohrmüller, J., in prep.. Polyphase intrusion and deformation of igneous bodies and their significance in the tectonometamorphic history of the Bavarian Forest, Central European Variscides.
- Galadí-Enríquez, E., Galindo-Zaldívar, J., Simancas, F., Expósito, I., 2003. Diapiric emplacement in the upper crust of a granitic body: the La Bazana Granite (SW Spain). *Tectonophysics* 361, 83-96.
- Galadí-Enríquez, E., Zulauf, G., 2006. Geologische Karte von Bayern 1:25000, Blatt Nr. 7246 Tittling. Bayerisches Landesamt fuer Umwelt, München.
- Galadí-Enríquez, E., Zulauf, G., Heidelberg, F., Dörr, W., Rohrmüller, J., 2005. Variscan dyke emplacement and sinistral strike slip in the Bavarian Forest (SE Germany): constraints on the evolution of the Bavarian Pfahl shear zone. *Schriftenreihe der Deutschen Gesellschaft für Geowissenschaften* 39, 111-112.
- Gapais, D., Barbarin, B., 1986. Quartz fabric transition in a cooling syntectonic granite (Hermitage Massif, France). *Tectonophysics* 125, 357-370.
- Gébelin, A., Martelet, G., Chen, Y., Brunel, M., Faure, M., 2006. Structure of late Variscan Millevaches leucogranite massif in the French Massif Central: AMS and gravity modelling results. *Journal of Structural Geology* 28, 148-169.
- González Menéndez, L.G., 1998. Petrología y geoquímica del batolito granítico de Nisa-Alburquerque. PhD Thesis, Universidad de Granada.
- González Menéndez, L.G., 2002. Petrología del batolito granítico de Nisa-Alburquerque. *Revista de la Sociedad Geológica de España* 15, 233-246.

González Menéndez, L., Azor, A., 2006. Estructura interna del batolito granítico de Nisa-Alburquerque. *Geogaceta* 40, 131-134.

González Menéndez, L., Bea, F., 2004. El Batolito de Nisa-Alburquerque. In: Vera, J.A. (Ed.), *Geología de España*, SGE-IGME, Madrid, 120-122.

Goult, N.R., Dobson, A.J., Jones, G.D., Al-Kindi, S.A., Holland, J.G., 2001. Gravity evidence for diapiric ascent of the Northern Arran Granite. *Journal of the Geological Society*, London 158, 869-876.

Gower, R.J.W., Simpson, C., 1992. Phase boundary mobility in naturally deformed, high-grade quartzofeldspathic rocks: evidence for diffusional creep. *Journal of Structural Geology* 14, 301-314.

Grant, J.A., 1986. The isocon diagram — A simple solution to Gresens' equation for metasomatic alteration. *Economic Geology* 81, 1976-1982.

Haederle, M., Atherton, M.P., 2002. Shape and intrusion style of the Coastal Batholith, Peru. *Tectonophysics* 345, 17-28.

Handler, R., Brandmayr, M., Wallbrecher, E., 1991. The Rodl shear zone in the southern Bohemian Massif. *Zentralblatt für Geologie und Paläontologie. Teil I H.1*, 69-86.

Hanmer, S., Passchier, C., 1991. Shear-sense indicators: a review. *Geological Survey of Canada Paper* 90-17.

Harre, W., Kreuzer, H., Lenz, H., Müller, P., 1967. Zwischenbericht über K/Ar und Rb/Sr-Datierungen von Gesteinen aus dem osbayerisch-österreichischen Kristallin. Bundesanstalt für Bodenforschung, Datierungsbericht 5/67, Archiv-Nr. 25/338.

Hemingway, B.S., Robie, R.A., Evans, H.T., Kerrick, D.M., 1991. Heat capacities and entropies of sillimanite, fibrolite, andalusite, kyanite, and quartz and the Al_2SiO_5 phase diagram. *American Mineralogist* 76, 1597-1613.

Hoffmann, R., 1962. Die Tektonik des Bayerischen Pfahls. *Geologische Rundschau* 52, 332-346.

Holdaway, M.J., 1971. Stability of andalusite and the aluminium silicate phase diagram. *American Journal of Science* 271, 97-131.

Horn, P., Köhler, H., Müller-Sohnius, D., 1986. Rb/Sr-Isotopengeochemie hydrothermaler Quarze des bayerischen Pfahles und eines Flusspat-Schwerspat-Ganges von Nabburg-Wölsendorf/Bundesrepublik Deutschland. *Chemical Geology (Isotope Geoscience Section)* 58, 259-272.

I. G. N., 1976. Mapa de España de Anomalía de Bouguer, e: 1:1000.000.

- Instituto Tecnológico Geominero de España, 1994. Mapa geológico de la Península Ibérica, Baleares y Canarias 1:1000000.
- Jackson, M.P.A., Talbot, C.J., 1994. Advances in Salt Tectonics. In : Hancock, P.L. (Ed.), Continental Deformation, 159-179, Pergamon Press.
- Jessell, M.W., Lister, G.S., 1990. A simulation of the temperature dependence of quartz fabrics. In: Knipe, R.J., Rutter, E.H. (Eds.), Deformation Mechanisms, Rheology and Tectonics, Geological Society Special Publication 54, 353-362.
- Johannes, W., Holtz, F., 1996. Petrogenesis and experimental petrology of granitic rocks. Minerals and rocks 22. Springer.
- Julivert, M., Fontboté, J.M., Ribeiro, A., Conde, L., 1972. Mapa tectónico de la Península Ibérica y Baleares, escala 1:1.000.000 y memoria explicativa. Instituto Geológico y Minero de España, Madrid.
- Julivert, M., Fontboté, J.M., Ribeiro, A., Nabais-Conde, L.E., 1974. Mapa tectónico de la Península Ibérica y Baleares, escala 1:1.000.000. Instituto Geológico y Minero de España, Madrid.
- Julivert, M., Martínez, F.J., 1983. Estructura de conjunto y visión global de la Cordillera Herciniana. In: Comba, J.A. (Ed.), Geología de España, Libro Jubilar J.M. Ríos. Instituto Geológico y Minero de España, Madrid.
- Kalt, A., Berger, A., Blümel, P., 1999. Metamorphic evolution of cordierite-bearing migmatites from the Bayerische Wald (Variscan Belt, Germany). *Journal of Petrology* 40, 601-627.
- Kalt, A., Corfu, F., Wijbrans, J.R., 2000. Time calibration of a P-T path from a Variscan high-temperature low-pressure metamorphic complex (Bayerische Wald, Germany), and the detection of inherited monazite. *Contributions to Mineralogy and Petrology* 138, 143-163.
- Kerr, A.D., Pollard, D.D., 1998. Toward more realistic formulations for the analysis of laccoliths. *Journal of Structural Geology* 20, 1783-1793.
- Klein, T., Kiehm, S., Siebel, W., Shang, C.K., Rohrmüller, J., Dörr, W., Zulauf, G., 2007. Age and emplacement of late-Variscan granites of the western Bohemian Massif with main focus on the Hauzenberg granitoids (European Variscides, Germany). *Lithos* (in press).
- Koch, A., 1998. Geologie und Goldvorkommen im Moldanubikum zwischen Tittling und Perlesreut, Bayerischer Wald. Unpublished Diploma Thesis, Technische Universität München.

- Koch, P.S., 1983. Rheology and microstructures of experimentally deformed quartz aggregates. PhD Thesis, University of California.
- Kossmat, F., 1927. Gliederung des varistischen Gebirgsbaus. *Abhandlungen des sächsischen geologischen Landesamtes* 1, 1-84.
- Kretz, R., 1983. Symbols for rock-forming minerals. *American Mineralogist* 68, 277-279.
- Kruhl, J.H., 1996. Prism- and basal-plane parallel subgrain boundaries in quartz: a microstructural geothermobarometer. *Journal of Metamorphic Geology* 14, 581-589.
- Kurian, P.J., Krishna, M.R., Nambiar, C.G., Murthy, B.V.S., 2001. Gravity field and subsurface geometry of the Kalpatta granite, South India and the tectonic significance. *Gondwana Research* 4, 105-111.
- Law, R.D., 1990. Crystallographic fabrics: a selective review of their applications to research in structural geology. In: Knipe, R.J., Rutter, E.H. (Eds.), *Deformation Mechanisms, Rheology and Tectonics*, Geological Society Special Publication 54, 335-352.
- Leake, B. E., Woolley, A. R., Arps, C. E. S., Birch, W. D., Gilbert, M. C., Grice, J. D., Hawthorne, F. C., Kato, A., Kisch, H. J., Krivovichev, V. C., Linthout, K., Laird, J., Mandarino, J., Maresch, W. V., Nickel, E. H., Rock, N. M. S., Schumacher, J. C., Smith, D. C., Stephenson, N. C. N., Ungaretti, L., Whittaker, E. J. W., Youzhi, G., 1997. Nomenclature of amphiboles. Report of the Subcommittee on Amphiboles of the International Mineralogical Association. Commission on New Minerals and Mineral Names. *European Journal of Mineralogy* 9, 623-651.
- Le Maitre, R.W., Bateman, P., Dudek, A., Keller, J., Lameyre, J., Le Bas, M.J., Sabine, P.A., Schmid, R., Sorensen, H., Streckeisen, A., Woolley, A.R., Zanettin, B., 1989. A classification of igneous rocks and glossary of terms. Blackwell Scientific Publications.
- Le Maitre, R.W., Streckeisen, A., Zanettin, B., Le Bas, M.J., Bonin, B., Bateman, P., Bellieni, G., Dudek, A., Efremova, S., Keller, J., Lameyre, J., Sabine, P.A., Schmid, R., Sørensen, H., Woolley, A.R., 2002. *Igneous Rocks. A classification and glossary of terms*. Cambridge University Press.
- Lister, J.R., Kerr, R.C., 1991. Fluid-Mechanical models of crack propagation and their application to magma transport in dykes. *Journal of Geophysical Research* 96, 10049-10077.
- Lister, G.S., Snoke, A.W., 1984. S—C Mylonites. *Journal of Structural Geology* 6, 617-638.
- Lotze, F., 1945. Zur Gliederung der Varisziden der Iberischen Meseta. *Geotekt. Forsch.* 6, 78-92.

- Mahon, K.I., Harrison, T.M., Drew, D.A., 1988. Ascent of a granitoid diapir in a temperature varying medium. *Journal of Geophysical Research* B93, 1174-1188.
- Mainprice, D., Bouchez, J.L., Blumenfeld, P., Tubia, J.M., 1986. Dominant *c* slip in naturally deformed quartz: Implications for dramatic plastic softening at high temperature. *Geology* 14, 819-822.
- Marsh, B.D., 1982. On the mechanics of igneous diapirism, stoping and zone melting. *American Journal of Science* 282, 808-855.
- Martínez Poyatos, D.J., Simancas, J.F., Azor, A., González Lodeiro, F., 1998. Evolution of a Carboniferous piggyback basin in the southern Central Iberian Zone (Variscan Belt, SW Spain). *Bulletin Société géologique France* 169, 573-578.
- Masberg, H.P., Hoffer, E., Hoernes, S., 1992. Microfabrics indicating granulite-facies metamorphism in the low-pressure central Damara Orogen, Namibia. *Precambrian Research* 55, 243-257.
- Masch, L., Cetin, B., 1991. Gefüge, Deformationsmechanismen und Kinematik in ausgewählten Hochtemperatur-Mylonitzonen im Moldanubikum des Bayerischen Waldes. *Geologica Bavarica* 96, 7-27.
- Massonne, H.J., 1984. Bestimmung von Intrusionstiefen variszischer granite Mitteleuropas und Neuschottlands anhand der Chemie ihrer Hellglimmer. *Fortschritte der Mineralogie, Beihefte*, 62/1, 147-149.
- Massonne, H.J., Schreyer, W., 1979. Synthese von Phengiten im System K_2O - MgO - Al_2O_3 - SiO_2 - H_2O bei Wasserdrucken bis 35 kbar. *Fortschritte der Mineralogie* 57, Beiheft 1, 98-99.
- Massonne, H.J., Schreyer, W., 1987. Phengite geobarometry based on the limiting assemblage with K-feldspar, phlogopite and quartz. *Contributions to Mineralogy and Petrology* 96, 212-224.
- Massonne, H.J., Szpurka, Z., 1997. Thermodynamic properties of white micas on the basis of high-pressure experiments in the systems K_2O - MgO - Al_2O_3 - SiO_2 - H_2O and K_2O - FeO - Al_2O_3 - SiO_2 - H_2O . *Lithos* 41, 229-250.
- Matte, P., 1986. Tectonics and plate tectonics model for the Variscan belt of Europe. *Tectonophysics* 126, 329-374.
- Matte, P., 1991. Accretionary history and crustal evolution of the Variscan belt in Western Europe. *Tectonophysics* 196, 309-337.
- Matte, P., 2001. The Variscan collage and orogeny (480-290 Ma) and the tectonic definition of the Armorica microplate: a review. *Terra Nova* 13, 122-128.

- Matte, P., Maluski, H., Rajlich, P., Franke, W., 1990. Terrane boundaries in the Bohemian Massif: Result of large-scale Variscan shearing. *Tectonophysics* 177, 151-170.
- Mattern, F., 1995. Late Carboniferous to early Triassic shear sense reversals at strike-slip faults in eastern Bavaria. *Zentralblatt für Geologie und Paläontologie Teil I* 1993, 1471-1490.
- McCaffrey, K.J.W., 1992. Igneous emplacement in a transpressive shear zone: Ox Mountains igneous complex. *Journal of the Geological Society, London* 149, 221-235.
- Mendes, F., 1967-68. Contribution a l'étude géochronologique, par la méthode au strontium, des formations cristallines du Portugal. *Geocronología, Facultad de Ciencias de Lisboa*.
- Mercier, J.C.C., Anderson, D.A., Carter, N.L., 1977. Stress in the lithosphere: Inferences from steady state flow of rocks. *Pure and Applied Geophysics* 115, 199-226.
- Miller, R.B., Paterson, S.R., 1999. In defense of magmatic diapirs. *Journal of Structural Geology* 21, 1161-1173.
- Morgan, S.S., Law, R.D., Nyman, M.W., 1998. Laccolith-like emplacement model for the Papoose Flat pluton based on porphyroblast-matrix analysis. *Geological Society of America Bulletin* 110, 96-110.
- Ohst, E., Troll, G., 1981. Porphyrite in der Umgebung von Waldkirchen. *Der Aufschluss, Sonderband* 31, 125-151.
- Ord, A., Christie, J.M., 1984. Flow stresses from microstructures in mylonitic quartzites of the Moine Thrust zone, Assynt area, Scotland. *Journal of Structural Geology* 6, 639-654.
- Ossan, A., 1923. Über Titanitfleckengranite. *Neues Jahrbuch für Mineralogie, Bil.-Bd.* 48, 223-239.
- Ott, W.D., 1983. Geologische Karte von Bayern 1:25 000, Erläuterungen zum Blatt Nr. 6943 Viechtach. Bayerisches Geologisches Landesamt, München.
- Ott, W.D., 1988. Geologische Karte von Bayern 1:25 000, Erläuterungen zum Blatt Nr. 7147/48 Freyung/Bischofsreut. Bayerisches Geologisches Landesamt, München.
- Passchier, C.W., Trouw, R.A.J., 1996. *Microtectonics*. Springer.
- Paterson, S.R., Fowler, T.K., 1993. Re-examining pluton emplacement processes. *Journal of Structural Geology* 15, 191-206.
- Paterson, S.R., Fowler, T.K., Schmidt, K.L., Yoshinobu, A.S., Yuan, E.S., Miller, R.B., 1998. Interpreting magmatic fabric patterns in plutons. *Lithos* 44, 53-82.

- Paterson, S.R., Miller, R.B., 1998. Mid-crustal magmatic sheets in the Cascades Mountains, Washington: implications for magma ascent. *Journal of Structural Geology* 20, 1345-1363.
- Paterson, S.R., Vernon, R.H., 1995. Bursting the bubble of ballooning plutons: A return to nested diapirs emplaced by multiple processes. *Geological Society of America Bulletin* 107, 1356-1380.
- Paterson, S.R., Vernon, R.H., Fowler, T.K., 1991. Aureole tectonics. *Reviews in Mineralogy* 26, 673-722.
- Paterson, S.R., Vernon, R.H., Tobisch, O.T., 1989. A review of criteria for identification of magmatic and tectonic foliation in granitoids. *Journal of Structural Geology* 11, 349-364.
- Peach, C.J., Lisle, R.J., 1979. A FORTRAN IV program for the analysis of tectonic strain using deformed elliptical markers. *Computers and Geosciences* 5, 325-334.
- Pérez-Estaún, A., Bea, F., (Eds.) 2004. Macizo Ibérico. In: Vera, J.A. (Ed.), *Geología de España*, 19-230, SGE-IGME, Madrid.
- Petford, N., 1996. Dykes or diapirs?. *Transactions of the Royal Society of Edinburgh: Earth Sciences* 87, 105-114.
- Petford, N., Kerr, R.C., Lister, J.R., 1993. Dike transport of granitoid magmas. *Geology* 21, 845-848.
- Petford, N., Lister, J.R., Kerr, R.C., 1994. The ascent of felsic magmas in dykes. *Lithos* 32, 161-168.
- Petford, N., Cruden, A.R., McCaffrey, K.J.W., Vigneresse, J.L., 2000. Granite magma formation, transport and emplacement in the Earth's crust. *Nature* 408, 669-673.
- Platt, J.P., 1984. Secondary cleavages in ductile shear zones. *Journal of Structural Geology* 6, 439-442.
- Plaumann, S., 1995. Die Schwerekarte 1:500 000 der Bundesrepublik Deutschland (Bouguer-Anomalien). Blatt Süd. *Geologisches Jahrbuch* E 53, 3-13.
- Pons, J., Debat, P., Oudin, C., Valero, J., 1991. Emplacement kinematics of the syntectonic Saraya granite (Senegal, West Africa). *Bulletin de la Société Géologique de France* 162, 1075-1082.
- Prior, D.J., Boyle, A.P., Brenker, F., Cheadle, M.C., Day, A., López, G., Peruzzo, L., Potts, G.J., Reddy, S., Spiess, R., Timms, N.E., Trimby, P., Wheeler, J., Zetterström, L., 1999. The application of electron backscatter diffraction and orientation contrast imaging in the SEM to textural problems in rocks. *American Mineralogist* 84, 1741-1759.

- Propach, G., 2002. Postmagmatic mineral parageneses of dykes may be used to estimate the PT data of their country rocks – An example from the Bayerischer Wald, Germany. *Neues Jahrbuch für Mineralogie, Abhandlungen* 9, 424-432.
- Propach, G., Baumann, A., Schulz-Schmalschläger, M., Grauert, B., 2000. Zircon and monazite U-Pb ages of Variscan granitoid rocks and gneisses in the Moldanubian zone of eastern Bavaria, Germany. *Neues Jahrbuch für Geologie und Paläontologie Monatshefte* 6, 345-377.
- Propach, G., Bayer, B., Chen, F., Frank, C., Hölzl, S., Hofmann, B., Köhler, H., Siebel, W., Troll, G., 2007. Geochemistry and petrology of late Variscan magmatic dykes of the Bavarian Forest, Germany. *Neues Jahrbuch für Mineralogie, Abhandlungen* (in press).
- Ramsay, J.G., Graham, R.H., 1970. Strain variations in shear belts. *Canadian Journal of Earth Sciences* 7, 786-813.
- Ramsay, J.G., Huber, M.I., 1983. *The Techniques of Modern Structural Geology. Volume 1: Strain Analysis.* Academic Press.
- Roberts, S., Sanderson, D.J., Gumiel, P., Dee, S., 1991. Tectonic and fluid evolution of auriferous quartz veins from La Codosera area, SW Spain. *Economic Geology* 86, 1012-1022.
- Rodríguez Suárez, J.I., 1985. *Petrografía, blastesis y deformación en la aureola de contacto del plutón de Nisa-Alburquerque.* Diploma Thesis, Univ. Oviedo.
- Rohrmüller, J., Mielke, H., Gebauer, D., 1996. Gesteinsfolge des Grundgebirges nördlich der Donau und im Molassenuntergrund. In: Bayerisches Geologisches Landesamt (Ed.), *Erläuterungen zur Geologischen Karte von Bayern 1:500 000, 4th Ed.*, 16–54, München.
- Roig, J.Y., Faure, M., Truffert, C., 1998. Folding and granite emplacement inferred from structural, strain, TEM and gravimetric analyses: the case study of the Tulle antiform, SW French Massif Central. *Journal of Structural Geology* 20, 1169-1189.
- Román-Berdiel, T., Gapais, D., Brun, J.P., 1995. Analogue models of laccolith formation. *Journal of Structural Geology* 17, 1337-1346.
- Román-Berdiel, T., Gapais, D., Brun, J.P., 1997. Granite intrusion along strike-slip zones in experiment and nature. *American Journal of Science* 297, 651-678.
- Rubin, A.M., 1995. Getting granite dikes out of the source region. *Journal of Geophysical Research* 100, 5911-5929.
- Salman, K., 2002. *Estudio petrológico, geoquímico y geocronológico de los granitoides del área Monesterio-Cala, Zona de Ossa-Morena (Macizo Ibérico).* PhD Thesis, Univ. Granada.

- Sánchez Carretero, R., Eguíluz, L., Pascual, E., Carracedo, M., 1990. Part V, Igneous Rocks. In: Dallmeyer, R.D., Martínez García, E., (Eds.), *Pre-Mesozoic Geology of Iberia*, 292-312, Springer Verlag.
- Sanderson, D.J., Marchini, W.R.D., 1984. Transpression. *Journal of Structural Geology* 6, 449-458.
- Sanderson, D.J., Roberts, S., McGowan, J.A., Gumiel, P., 1991. Hercynian transpressional tectonics at the southern margin of the Central Iberian Zone, west Spain. *Journal Geological Society London* 148, 893-898.
- Sant'Ovaia, Bouchez, J.L., Noronha, F., Leblanc, D., Vigneresse, J.L., 2000. Composite-laccolith emplacement of the post-tectonic Vila Pouca de Aguiar granite pluton (northern Portugal): a combined AMS and gravity study. *Transactions of the Royal Society of Edinburgh: Earth Sciences* 91, 123-137.
- Scheuvens, D., Zulauf, G., 2000. Exhumation, strain localization, and emplacement of granitoids along the western part of the Central Bohemian shear zone (Bohemian Massif). *International Journal of Earth Sciences* 89, 617-630.
- Schmid, S.W., Casey, M., 1986. Complete fabric analysis of some commonly observed quartz *c*-axis patterns. *Geophysical Monograph* 36, 263-286.
- Schmidl, H.W., 2000. Geologische Kartierung im Passauer Wald, eines Teilgebietes auf dem Gradabteilungsblatt Nr. 7246 Tittling (SE-Ecke) zwischen Tittling, Röhrnbach and Hutthurm. Unpublished Diploma Thesis, Ludwig Maximilians Universität München.
- Scholtz, H., 1927. Das Saldenburger Granitmassiv und seine Umgebung. In: Cloos, H., Balk, E., Cloos, E., Scholtz, H., *Die Plutone des Passauer Waldes. Ihr Bau und Werdegang und ihre innere Tektonik. Monogr. zur Geol. und Paleont., Ser. II, H. 3*, 137-180.
- Schwerdtner, W.M., 1995. Local displacement of diapir contacts and its importance to pluton emplacement study. *Journal of Structural Geology* 17, 907-910.
- Siebel, W., 1998. Variszischer spät- bis postkollisionaler Plutonismus in Deutschland: Regionale Verbreitung, Stoffbestand und Altersstellung. *Zeitschrift für geologische Wissenschaften* 26, 329-358.
- Siebel, W., Blaha, U., Chen, F., Rohrmüller, J., 2005. Geochronology and geochemistry of a dyke-host rock association and implications for the formation of the Bavarian Pfahl shear zone, Bohemian Massif. *International Journal of Earth Sciences* 94, 8-23.
- Simancas, J.F., Galindo-Zaldívar, J., Azor, A., 2000. Three-dimensional shape and emplacement of the Cardenchoxa deformed pluton (Variscan Orogen, southwestern Iberian Massif). *Journal of Structural Geology* 22, 489-503.

- Simancas, J.F., Carbonell, R., González Lodeiro, F., Pérez Estaún, A., Juhlin, C., Ayarza, P., Kashubin, A., Azor, A., Martínez Poyatos, D., Almodóvar, G.R., Pascual, E., Sáez, R., Expósito, I., 2003. Crustal Structure of the transpressional Variscan Orogen of SW Iberia: SW Iberia deep seismic reflection profile (IBERSEIS). *Tectonics* 22. doi: 10.1029/2002TC001479
- Simancas, J.F., Martínez Poyatos D.J., Expósito, I., Azor, A., González Lodeiro, F., 2001. Structure of the SW Iberian Massif on Both Sides of a Variscan Suture: the Ossa-Morena / Central Iberian Contact. *Tectonophysics* 332, 295-308.
- Simpson, C., Schmid, S.M., 1983. An evaluation of criteria to deduce the sense of movement in sheared rocks. *Geological Society of America Bulletin* 94, 1288-1288.
- Simpson, G.D.H., Thompson, A.B., Connolly, J.A.D., 2000. Phase relations, singularities and thermobarometry of metamorphic assemblages containing phengite, chlorite, biotite, K-feldspar, quartz and H₂O. *Contributions to Mineralogy and Petrology* 139, 555-569.
- Stein, E., 1988. Die strukturgeologische Entwicklung im Übergangsbereich Saxothuringikum/Moldanubikum in NE-Bayern. *Geologica Bavarica* 92, 5-131.
- Steiner, L., 1968. Alkalisierung im Pfahlgebiet am Beispiel der Palitgesteine des Bayrischen Waldes. Unpublished PhD Thesis, Univ. München.
- Steiner, L., 1969. Kalifeldspatisierung in den Palitgesteinen des Pfahlgebietes. *Geologica Bavarica* 60, 163-170.
- Steiner, L., 1972. Alkalisierung im Grundgebirge des Bayrischen Waldes. *Neues Jahrbuch für Mineralogie Abhandlungen* 116, 132-166.
- Stipp, M., Stünitz, H., Heilbronner, R., Schmid, S.M., 2002. The eastern Tonale fault zone: a "natural laboratory" for crystal plastic deformation of quartz over a temperature range from 250 to 700°C. *Journal of Structural Geology* 24, 1861-1884.
- Stipp, M., Tullis, J., 2003. The recrystallized grain size piezometer for quartz. *Geophysical Research Letters* 30(21), 2088, doi: 10.1029/2003GL018444.
- Suess, F. E., 1903. Bau und Bild der Böhmischen Masse. In: Diener, C., Hoernes, R., Suess F. E., Uhlig, V. (Eds.), *Bau und Bild Österreichs*. Temsky-Freytag, Wien.
- Talbot, J.Y., Faure, M., Chen, Y., Martelet, G., 2005. Pull-apart emplacement of the Margeride granitic complex (French Massif Central). Implications for the late evolution of the Variscan orogen. *Journal of Structural Geology* 27, 1610-1629.
- Tanner, D. C., 1995. Strukturen und Gefüge in hochgradig metamorphen Gneisen der mittleren Oberpfalz und Westböhmens. *Giessener Geologische Schriften* 57. PhD Thesis, Univ. Giessen.

- Tanner, D. C., Behrmann, J. H., 1995. The Variscan tectonics of the Moldanubian gneisses, Obepfälzer Wald: A compressional story. *Neues Jahrbuch für Geologie und Paläontologie Abhandlungen* 197, 331-355.
- Teipel, U., 2003. Obervendischer und unterordovizischer Magmatismus im Bayerischen Wald. *Münchener Geologische Hefte*, A 33.
- Teipel, U., Galadí-Enríquez, E., Kroemer, E., in press. Geologische Karte von Bayern 1:25000, Blatt Nr. 7146 Grafenau. Bayerisches Landesamt fuer Umwelt, München.
- Telford, W. M., Geldart, L. P., Sheriff, R. E., 1995. *Applied Geophysics*, 2nd Ed., Cambridge University Press.
- Tennyson, C., 1960. Berylliumminerale und ihre pegmatitische Paragenese in den Graniten von Tittling: Bayerischer Wald. *Neues Jahrbuch für Mineralogie Abhandlungen* 94, 1253-1265.
- Tennyson, C., 1981. Zur Mineralogie der Pegmatite des Bayerischen Waldes. *Der Aufschluss*, Sonderband 31, 49-73.
- Tikoff, B., Fossen, H., 1999. Three-dimensional reference deformations and strain facies. *Journal of Structural Geology* 21, 1497-1512.
- Troll, G., 1964. Das Intrusivgebiet von Fürstenstein (Bayerischer Wald). *Geologica Bavarica* 52.
- Troll, G., 1966. Über Metabasite des Bayerischen Waldes. 1. Zur Petrographie und Petrochemie apatit- und biotitreicher Metabasite im nördlichen Passauer Wald. *Neues Jahrbuch für Mineralogie Abhandlungen* 106, 72-105.
- Troll, G., 1967. Steinbrüche im Intrusivgebiet von Fürstenstein. In: Troll, G., *Führer zu geologisch-petrographischen Exkursionen im Bayerischen Wald. Teil I: Aufschlüsse im Mittel- und Ostteil*. *Geologica Bavarica* 58, 133-144
- Troll, G., Ohst, E., 1984. Porphyrite des Bayerischen Waldes zwischen Granitintrusionen und Pfahlquarzbildung. *Fortschritte der Mineralogie* 62, 244-246.
- Troll, G., Winter, H., 1969. Zur Petrographie und Geochemie von Anatexiten und ihren basischen Einschlüssen im Passauer Wald, Niederbayern. *Geologica Bavarica* 60, 52-94.
- Tullis, J., 1983. Deformation of feldspars. In: Ribbe, P.H. (Ed.), *Feldspar Mineralogy*. Mineralogical Society of America, *Reviews in Mineralogy* 2, 297-323.
- Tullis, J., Yund, R.A., 1977. Experimental deformation of dry Westerly granite. *Journal of Geophysical Research* 82, 5705-5718.
- Tuttle, O.F., Bowen, N.L., 1958. Origin of granite in the light of experimental studies in the system NaAlSi₃O₈ - KAlSi₃O₈ - H₂O. *Geol. Soc. Am. Mem.* 74, 153 pp.

- Twiss, R.J., 1977. Theory and applicability of a recrystallized grain size piezometer. *Pure and Applied Geophysics* 115, 227-244.
- Twiss, R.J., 1980. Static theory of size variation with stress for subgrains and dynamically recrystallized grains. U.S. Geological Survey, Open File Report 80-625, 665-683.
- Unzog, W., 1990. Beispiele von Strainanalysen in Kristallingebieten. TSK III, 3. Symposium für Tektonik, Strukturgeologie, Kristallingeologie. Graz, 19. - 21.4.1990, 265-266.
- Urban, M., Synek, J., 1995. Moldanubian Region. Structure. In: Dallmeyer, R.D., Franke, W., Weber, K. (Eds.), *Pre-Permian geology of Central and Eastern Europe*, 429-443, Springer.
- Vegas, N., Aranguren, A., Tubía, J.M., 2001. Granites built by sheeting in a fault stepover (the Sanabria Massifs, Variscan Orogen, NW Spain). *Terra Nova* 13, 180-187.
- Vigneresse, J.L., 1990. Use and misuse of geophysical data to determine the shape at depth of granitic intrusions. *Geological Journal* 25, 248-260.
- Vigneresse, J.L., 1995a. Control of granite emplacement by regional deformation. *Tectonophysics* 249, 173-186.
- Vigneresse, J.L., 1995b. Crustal regime of deformation and ascent of granitic magma. *Tectonophysics* 249, 187-202.
- Vigneresse, J.L., 1995c. Far- and near-field deformation and granite emplacement. *Geodinamica Acta* 8, 211-227.
- Vigneresse, J.L., Bouchez, J.L., 1997. Successive granitic magma batches during pluton emplacement: the Case of Cabeza de Araya (Spain). *Journal of Petrology* 38, 1767-1776.
- Villaseca, C., Barbero, L., Herreros, V., 1998b. A re-examination of the typology of peraluminous granite types in intracontinental orogenic belts. *Transactions of the Royal Society of Edinburgh: Earth Sciences* 89, 113-119.
- Villaseca, C., Barbero, L., Rogers, G., 1998a. Crustal origin of Hercynian peraluminous granitic batholiths of Central Spain: petrological, geochemical and isotopic (Sr, Nd) constraints. *Lithos* 43, 55-79.
- Voll, G., 1960. Stoff, Bau und Alter in der Grenzzone Moldanubikum/Saxothuringikum in Bayern unter besonderer Berücksichtigung gabbroider, amphibolitischer und kalksilikatführender Gesteine. *Beihefte zum Geologischen Jahrbuch* 42.

- von Gümbel, C.W., 1868. Geognostische Beschreibung des Königreiches Bayern. II Abt. Ostbayerisches Grenzgebirge. Gotha.
- Wallbrecher, E., Brandmayr, M., Handler, R., 1990. Kinematische Untersuchungen an Blattverschiebungszonen in der südlichen Böhmisches Masse. Österreichische Beiträge zu Meteorologie und Geophysik 3, 97-120.
- Wang, T., Wang, X., Li, W., 2000. Evaluation of multiple emplacement mechanisms: the Huichizi granite pluton, Qinling orogenic belt, central China. *Journal of Structural Geology* 22, 505-518.
- Watson, E.B., Harrison, T.M., 1983. Zircon saturation revisited: temperature and composition effects in a variety of crustal magma types. *Earth and Planetary Science Letters* 64, 295-304.
- Weinberg, R.F., 1996. Ascent mechanism of felsic magmas: news and views. *Transactions of the Royal Society of Edinburgh: Earth Sciences* 87, 95-103.
- Weinberg, R.F., 1999. Mesoscale pervasive felsic magma migration: alternatives to dyking. *Lithos* 46, 393-410.
- Weinberg, R.F., Podladchikov, Y.Y., 1995. The rise of solid-state diapirs. *Journal of Structural Geology* 17, 1183-1195.
- Weiss, S., 1981. Geologisch-petrographische Untersuchungen im NE-Teil des Saldenburger Granitmassivs und im Gneisrahmen des Ilzgebietes, Vorderer Bayerischer Wald. Unpublished Diploma Thesis, Ludwig Maximilians Univ. München.
- White, S.H., 1979. Paleostress estimates in the Moine Thrust zone. *Nature* 280, 222-223.
- Wimmenauer, W., Bryhni, I., 2002. Towards a unified nomenclature in metamorphic petrology: Migmatites and related rocks. A proposal on behalf of the IUGS Subcommission on the Systematics of Metamorphic Rocks. Web version of 31.07.2002, http://www.bgs.ac.uk/scmr/docs/paper_6/scmr_mig.pdf.
- Wyllie, P.J., 1977. Crustal anatexis: an experimental review. *Tectonophysics* 43, 41-71.
- Yardley, B.W.D., 1989. *An Introduction to metamorphic petrology*. Longman.
- Yenes, M., Álvarez, F., Gutiérrez-Alonso, G., 1999. Granite emplacement in orogenic compressional conditions: the La Alberca--Béjar granitic area (Spanish Central System, Variscan Iberian Belt). *Journal of Structural Geology* 21, 1419-1440.
- Zen, E., 1988. Phase relations of peraluminous granitic rocks and their petrogenetic implications. *Ann. Rev. Earth Planet. Sci.* 16, 21-51.
- Ziegler, P.A., 1990. *Geological Atlas of Western and Central Europe*, 2nd ed. Elsevier.

- Zulauf, G., 1992. Late to post-Variscan deformation phases and palaeostresses in the KTB pilot research well (Bohemian Massif, Germany). *Tectonophysics* 202, 1-21.
- Zulauf, G., 1994. Ductile normal faulting along the West Bohemian shear zone (Moldanubian/Teplá-Barrandian boundary): evidence for late Variscan extensional collapse in the Variscan Internides. *Geologische Rundschau*, 83, 276-292.
- Zulauf, G., Bues, C., Dörr, W., Vejnar, Z., 2002a. 10 km minimum throw along the West Bohemian shear-zone: Evidence for dramatic crustal thickening and high topography in the Bohemian Massif (European Variscides). *International Journal of Earth Sciences* 91, 850-864.
- Zulauf, G., Dörr, W., Fiala, J., Kotková, J., Maluski, H., Valverde-Vaquero, P., 2002b. Evidence for high-temperature diffusional creep preserved by rapid cooling of lower crust (North Bohemian shear zone, Czech Republic). *Terra Nova* 14, 343-354.
- Zulauf, G., Duyster, J., 1997. Supracrustal intraplate thickening of Variscan basement due to Alpine foreland compression: Results from the superdeep well KTB (Bohemian Massif, Germany). *Tectonics* 16, 730-743.
- Zulauf, G., Schitter, F., Riegler, G., Finger, F., Fiala, J., Vejnar, Z., 1999. Age constraints on the Cadomian evolution of the Teplá-Barrandian unit (Bohemian Massif) through electron microprobe dating of metamorphic monazite. *Zeitschrift der deutschen geologischen Gesellschaft* 150, 627-639.
- Zulauf, G., Vejnar, Z., 2003. Variszische Fahrstuhltektonik und cadomisches Basement im Westteil der Böhmisches Masse (Exkursion I am 25. April 2003). *Jber. Mitt. oberrhein. geol. Ver., N. F.* 85, 295-315, Stuttgart

Appendix 1:
geological map of sheet No. 7246
Tittling, Bavaria (Germany)
(simplified after Galadí-Enríquez and
Zulauf, 2006)

Geological map of sheet No. 7246 Tittling, Bavaria (Germany)

Carboniferous to Triassic

Carboniferous to Permian

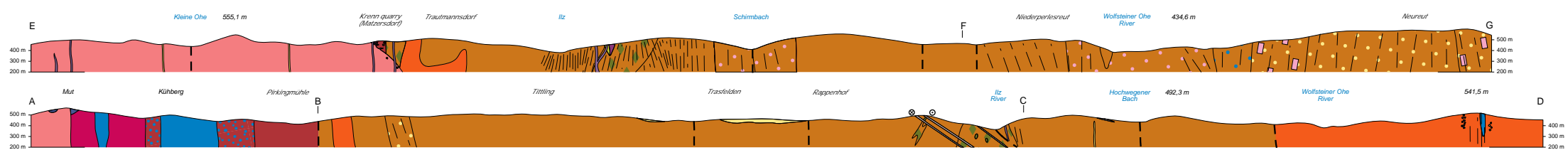
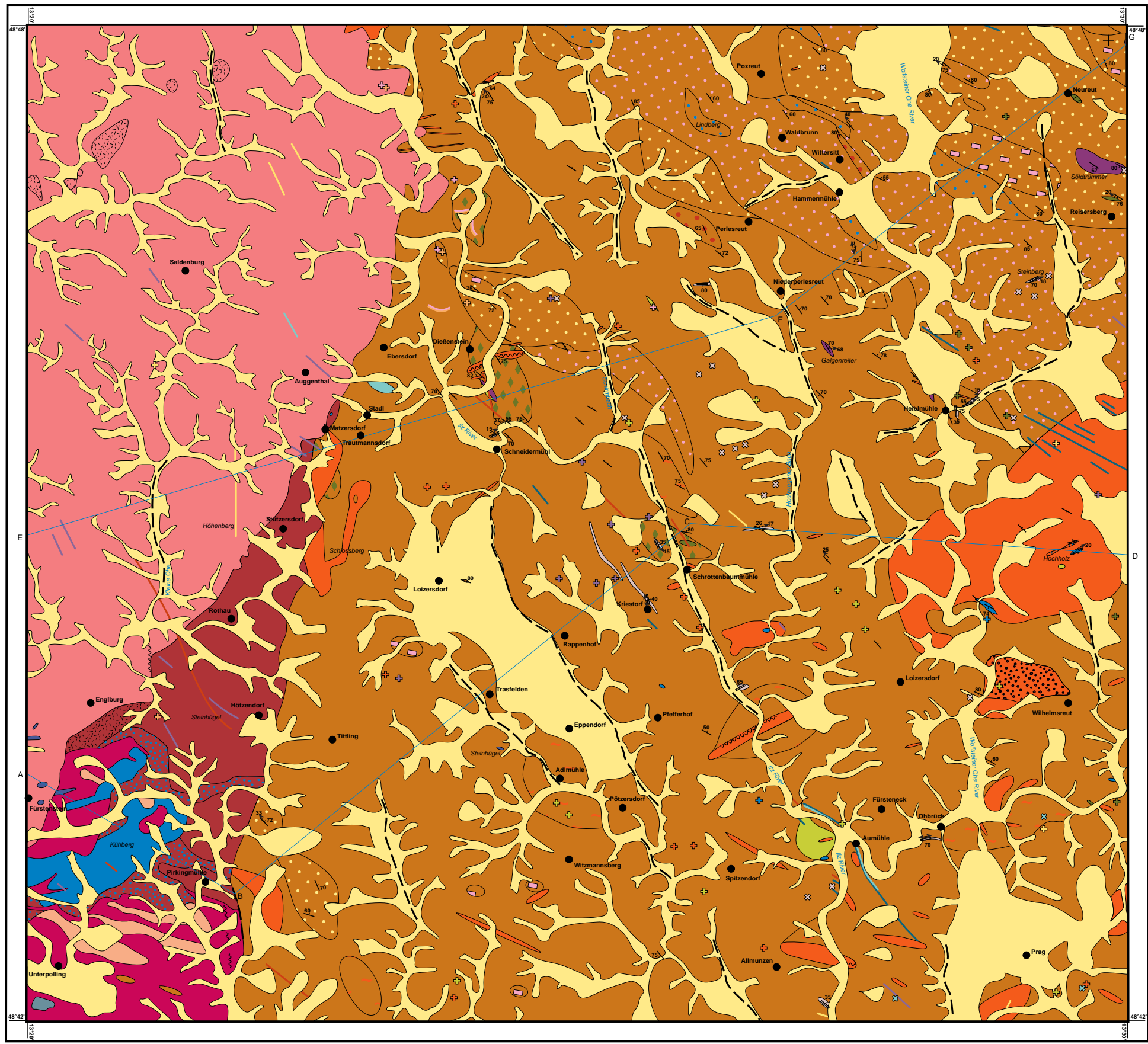
Carboniferous

Early Paleozoic to Neoproterozoic

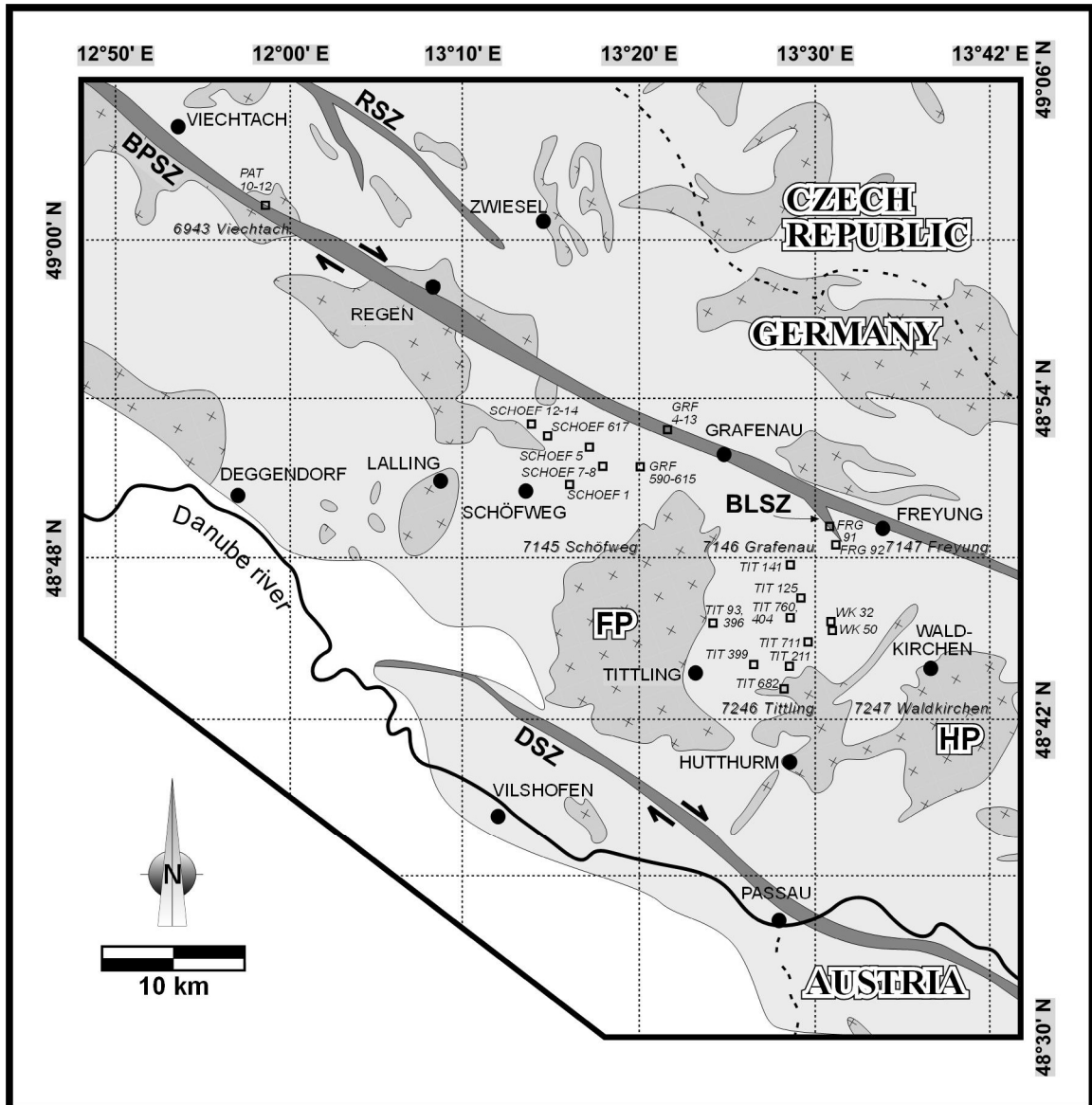
- post-Variscan cover
- Variscan basement mineralisations**
 - quartz, cross: intercalation
- Variscan igneous rocks***
 - dykes**
 - post-granitic dyke, intermediary to acid ("Porphyrite"); cross: intercalation
 - andesitic
 - dacitic
 - rhyolitic
 - pegmatite, cross: intercalation
 - aplite, cross: intercalation
- plutonic rocks**
 - granite, fine to medium grained; cross: intercalation
 - with diatexite fragments
 - with quartz-biotite diorite fragments
 - quartz-biotite diorite, cross: intercalation
 - diorite
 - Fürstenstein Pluton:*
 - granite, porphyritic, medium to coarse grained ("Saldenburg granite")
 - with xenoliths of fine- to coarse-grained two-mica granite
 - two-mica granite, fine to medium grained
 - granite to granodiorite, medium grained ("Tittling granite")
 - with gneiss fragments
 - granodiorite, medium grained
 - granodiorite with titanite spots, fine grained, contained in younger facies in form of xenoliths ("Engburgit")
 - biotite tonalite, fine grained ("Fürstenstein quartz-mica diorite")
 - biotite tonalite, medium grained ("Unterpolling granodiorite")
 - granite to granodiorite, fine grained

*old names found in the literature are written between quotation marks

- Moldanubicum**
 - migmatic rocks**
 - light-coloured diatexite
 - crosscut by granite veins
 - porphyritic
 - garnet bearing
 - hornblende-diatexite
 - dark-coloured diatexite
 - porphyritic
 - hypersthene-bearing diatexite
 - light-coloured
 - garnet bearing
- metamorphosed magmatic rocks**
 - metabasite (undifferentiated); cross: intercalation
 - amphibolite, cross: intercalation
 - amphibole-pyroxene-plagioclase-biotite gneiss
 - metultramafic rock, serpentinite
- metamorphosed sedimentary rocks**
 - quartz-biotite-cordierite-feldspar granulite
 - calc-silicate granulites (intercalation)
- fault rocks**
 - mylonite, cross: intercalation
 - foliated area in granitoids
- symbols**
 - fault (assumed)
 - strike and dip of the principal foliation; vertical, horizontal
 - strike and dip of the mylonitic foliation; vertical
 - trend and plunge of the mineral or stretching lineation; horizontal
 - trend and plunge of fold axes
 - profile line



Appendix 2: sampling sites



Geological map of the south-eastern part of the Bohemian Massif simplified after Bundesanstalt fuer Geowissenschaften und Rohstoffe (1993), showing location of sampling sites. White: post-Variscan cover. Light grey: metamorphic rocks. Medium grey with crosses: intrusive rocks, mainly granites and granodiorites. Dark grey: major faults and fault rocks. RSZ Runding shear zone, BPSZ Bayerischer Pfahl shear zone, BLSZ Buchberger Leite shear zone, DSZ Danube shear zone, FP Fürstenstein pluton, HP Hauzenberg pluton. Dashed lines represent the limits of topographic sheets at scale 1:25000: Number and name of the relevant ones are indicated.

sinistrally sheared dykes and stocks (D ₃ shear-zone system)								
locality	sample	topographic sheet 1:25000	geogr. coord	GK coord.	foliation S ₃ (shear bands)	lineation L ₃ (R=rake, P=plunge)	kinemat.	comm.*
south of Innernzell	Schoef 1	No. 7145 Schoefweg	48° 50' 41.8" N 13° 16' 15.5" E	R 4593275 H 5412610	N077E/80S	R: 5°→N257E P: 5°→N256E	sinistral, reverse	
south of Kleinarm- schlag	Schoef 5	No. 7145 Schoefweg	48° 52' 04.1" N 13° 17' 26.5" E	R 4594680 H 5415175	N122E/50N	P: 10°→N310E	sinistral, normal	
Abersber- ger Holz	Schoef 7, 8	No. 7145 Schoefweg	48° 51' 27.1" N 13° 18' 10.7" E	R 4595600 H 5414050	N103E/45N	P: 31°→N067E	sinistral, reverse	
Unter- mitterdorf dyke	Schoef 12, 13, 14	No. 7145 Schoefweg	48° 52' 59.9" N 13° 14' 02.8" E	R 4590500 H 5416830	N079E/78N to N103E/78N	R: 15° →W to subhoriz. P: 15°→N262E to subhoriz.	sinistral, normal	B,T
sand pit east of Unter- mitterdorf	Schoef 617	No. 7145 Schoefweg	48° 52' 30.4" N 13° 14' 58.5" E	R 4591650 H 5415940	N076E/77S	R: 25°→N076E P: 24°→N078E	sinistral, normal	B
Saunstein quarry	Grf 590- 615	No. 7146 Grafenau	48° 51' 24.2" N 13° 20' 03.5" E	R 4597900 H 5414000	N070E/90 to N090E/90	subhoriz.	sinistral	B,T
Schneider- mühl	Tit 93, 396	No. 7246 Tittling	48° 45' 39.1" N 13° 24' 17.5" E	R 4603274 H 5403434	N065E/90	P: 15°→N065E	sinistral	T
Steinberg	Tit 125	No. 7246 Tittling	48° 46' 27.8" N 13° 29' 09.2" E	R 4609200 H 5405050	N070E/60S	P: 17°→N080E	sinistral, normal	B
Loizersdorf	Tit 211	No. 7246 Tittling	48° 43' 56.9" N 13° 28' 32.9" E	R 4608550 H 5400375	N105E/60S	P: 13°→N277E	sinistral, reverse	
Schrotten- baumühle	Tit 399	No. 7246 Tittling	48° 44' 00.5" N 13° 26' 29.7" E	R 4606030 H 5400440	N060E/65N	subhoriz.? (brittle overprint)	sinistral?	
Ohbruck	Tit 682	No. 7246 Tittling	48° 43' 05.5" N 13° 28' 09.6" E	R 4608105 H 5398780	N080E/70S	subhoriz.	sinistral	
Heiblmühle	Tit 760, 404	No. 7246 Tittling	48° 45' 43.2" N 13° 28' 34.1" E	R 4608510 H 5403660	N070E/55N	P: 5° →N067E	sinistral	T
Hochholz	Tit 711	No. 7246 Tittling	48° 44' 49.3" N 13° 29' 34.2" E	R 4609770 H 5402020	N060E/85N	subhoriz.	sinistral	B
Goggers- reut 1	Wk 32	No. 7247 Waldkirchen	48° 45' 48.8" N 13° 30' 40.2" E	R 5390560 H 5403850	N060E/82S	subhoriz.	sinistral	
Goggers- reut 2	Wk 50	No. 7247 Waldkirchen	48° 45' 40.7" N 13° 30' 43.9" E	R 5390630 H 5430600	N056E/72N	subhoriz.	sinistral	

*comments: B = barometry data available; T = quartz-texture data available

Bayerischer Pfahl shear-zone system								
locality	sample	lithology	geogr. coord	GK coord.	foliation S ₂ (shear bands)	lineation L ₂ (R=rake, P=plunge)	kinemat.	comm.*
Große Ohe top. sheet No. 7146 Grafenau	Grf 6	gneiss	48° 52' 38.6" N 13° 21' 27.1" E	R 4599562 H 5416326	N121E/80N	subhoriz.	dextral	T
	Grf 8	mylonite	48° 52' 23.8" N 13° 21' 25.6" E	R 4599540 H 5415870	N114E/70N	R: 5°→N294E	dextral	
	Grf 9	mylonite	48° 52' 22.5" N 13° 21' 27.1" E	R 4599572 H 5415831	N111E/64N	subhoriz.	dextral	B,T
	Grf 13	mylonite	48° 52' 18.4" N 13° 21' 30.0" E	R 4599633 H 5415704	N105E/75S	R: 5°→N295E	dextral	T
	Grf 5	mylonite	48° 52' 12.9" N 13° 21' 29.3" E	R 4599621 H 5415536	N100E/88S	R: 10°→N280E	dextral	T
	Grf 4	diatexite	48° 52' 09.7" N 13° 21' 37.6" E	R 4599793 H 5415439	N090E/78S	R: 5°→N090E	dextral	T
Patersdorf top. sheet No. 6943 Viechtach	Pat 10	granite mylonite	49° 01' 08.0" N 12° 59' 43.5" E	R 4572800 H 5431650	N131E/76N	subhoriz.	dextral	B,T
	Pat 11	granite mylonite	49° 01' 07.2" N 12° 59' 40.1" E	R 4572730 H 5431625	N125E/90	subhoriz.	dextral	B,T
	Pat 12	mylonite (phylonite)	49° 01' 01.6" N 12° 59' 38.0" E	R 4572690 H 5431450	N081E/76S	R: 27°→N081E	dextral, reverse	B,T
Buchberger Leite top. sheet No. 7147 Freyung	Frg 91	mylonite	48° 48' 44.8" N 13° 30' 10.0" E	R 5390050 H 5409300	N170E/90	P: 20°→N170E	dextral	T

*comments: B = barometry data available; T = quartz-texture data available

other samples								
topographic sheet 1:25000	sample	lithology	geogr. coord	GK coord.	foliation S ₂ (shear bands)	lineation L ₂ (R=rake, P=plunge)	kinemat.	comm.*
No. 7246 Tittling	Tit 141	hypersthene- bearing diatexite	48° 47' 39.2" N 13° 28' 34.9" E	R 4608457 H 5407242	N120E/80NE	R: 8°→ N120E	dextral, normal	
No. 7147 Freyung	Frg 92	dark- coloured diatexite	48° 48' 25.1" N 13° 30' 22.5" E	R 5390292 H 5408685	N135E/60SW	subhoriz.	dextral	T

*comments: T = quartz-texture data available

Appendix 3: microprobe analyses of phengites

Electron microprobe analyses of different populations of white micas. Cations calculated by charge balance assuming 22 negative charges and total Fe as Fe²⁺. mv: mean value. sd: standard deviation. The mean number of Si atoms p.f.u., written in bold type, and the standard deviation were used for the construction of P-T-graphics included in the text.

Sample Grf 9

No.	K ₂ O	Na ₂ O	CaO	BaO	FeO _t	MgO	MnO	Cr ₂ O ₃	Al ₂ O ₃	TiO ₂	SiO ₂	F	Cl	Total	K	Na	Ca	Ba	Fe ²⁺	Mg	Mn	Cr	Al	Ti	Si	Total	
igneous white mica:																											
80	10.42	0.63	0.02	0.00	1.24	0.74	0.03	0.00	34.84	1.00	45.72	0.49	0.00	95.12	0.910	0.082	0.001	0.000	0.069	0.074	0.001	0.000	2.752	0.050	3.064	7.005	
81	10.47	0.50	0.04	0.00	1.29	0.71	0.04	0.01	34.44	1.04	45.67	0.38	0.00	94.59	0.919	0.065	0.003	0.000	0.073	0.071	0.002	0.001	2.734	0.053	3.076	6.996	
82	10.40	0.75	0.01	0.00	1.29	0.69	0.02	0.03	35.24	1.05	45.68	0.40	0.00	95.56	0.904	0.097	0.001	0.000	0.072	0.069	0.001	0.001	2.770	0.053	3.047	7.015	
83	10.54	0.70	0.01	0.00	1.26	0.77	0.03	0.01	35.36	1.04	45.96	0.49	0.00	96.17	0.912	0.090	0.001	0.000	0.070	0.076	0.002	0.001	2.765	0.052	3.049	7.017	
84	10.51	0.69	0.00	0.00	1.34	0.75	0.01	0.02	35.08	0.84	45.43	0.41	0.01	95.09	0.919	0.090	0.000	0.000	0.075	0.075	0.001	0.001	2.775	0.042	3.048	7.026	
85	10.40	0.77	0.01	0.00	1.24	0.82	0.00	0.01	34.77	1.05	45.45	0.49	0.00	95.00	0.911	0.100	0.001	0.000	0.070	0.082	0.000	0.001	2.753	0.053	3.053	7.023	
86	10.77	0.51	0.02	0.00	1.07	0.64	0.00	0.01	35.51	0.84	45.52	0.34	0.00	95.23	0.939	0.066	0.002	0.000	0.060	0.064	0.000	0.001	2.799	0.042	3.044	7.016	
87	10.71	0.55	0.00	0.00	1.29	0.69	0.00	0.00	35.56	0.47	45.39	0.45	0.01	95.12	0.936	0.071	0.000	0.000	0.072	0.069	0.000	0.000	2.812	0.024	3.045	7.030	
88	10.84	0.42	0.01	0.00	1.12	0.75	0.02	0.07	34.40	2.56	45.64	0.40	0.00	96.23	0.939	0.055	0.001	0.000	0.062	0.074	0.001	0.003	2.694	0.128	3.032	6.988	
89	10.85	0.43	0.02	0.00	1.39	0.69	0.02	0.00	35.80	0.53	45.39	0.40	0.00	95.53	0.945	0.056	0.001	0.000	0.078	0.069	0.001	0.000	2.820	0.027	3.033	7.031	
90	10.19	0.70	0.03	0.00	1.36	0.80	0.03	0.00	34.91	1.00	45.59	0.38	0.01	95.01	0.890	0.091	0.002	0.000	0.076	0.080	0.002	0.000	2.758	0.050	3.056	7.005	
91	10.52	0.69	0.03	0.00	1.21	0.70	0.01	0.01	35.21	0.82	45.29	0.47	0.00	94.97	0.921	0.090	0.002	0.000	0.068	0.070	0.001	0.000	2.789	0.042	3.043	7.026	
92	11.04	0.34	0.01	0.00	1.03	0.55	0.03	0.00	35.96	0.57	45.04	0.37	0.00	94.94	0.967	0.044	0.001	0.000	0.058	0.055	0.002	0.000	2.847	0.029	3.026	7.027	
96	10.69	0.52	0.07	0.00	1.01	0.64	0.02	0.01	35.30	0.95	45.21	0.47	0.00	94.87	0.937	0.067	0.005	0.000	0.057	0.064	0.001	0.001	2.797	0.048	3.039	7.016	
97	10.41	0.75	0.03	0.00	1.20	0.71	0.02	0.00	35.03	0.75	45.53	0.46	0.01	94.90	0.912	0.097	0.002	0.000	0.068	0.071	0.001	0.000	2.774	0.038	3.059	7.021	
98	10.09	0.65	0.01	0.00	2.27	0.95	0.04	0.00	34.92	0.67	45.27	0.40	0.00	95.27	0.883	0.084	0.001	0.000	0.127	0.095	0.002	0.000	2.763	0.034	3.039	7.029	
99	10.56	0.60	0.02	0.00	1.19	0.76	0.04	0.00	35.35	0.51	45.90	0.42	0.00	95.33	0.919	0.077	0.001	0.000	0.066	0.076	0.002	0.000	2.783	0.025	3.066	7.016	
100	10.81	0.42	0.03	0.00	1.37	0.74	0.01	0.00	35.46	0.84	45.97	0.34	0.01	96.01	0.936	0.055	0.002	0.000	0.076	0.073	0.001	0.000	2.776	0.042	3.053	7.013	
101	10.62	0.65	0.04	0.00	1.25	0.71	0.02	0.03	35.05	0.92	45.52	0.50	0.01	95.33	0.928	0.085	0.003	0.000	0.070	0.071	0.001	0.002	2.769	0.046	3.050	7.025	
102	10.51	0.68	0.01	0.00	1.21	0.78	0.03	0.00	35.11	0.85	46.01	0.48	0.01	95.68	0.913	0.087	0.001	0.000	0.068	0.077	0.002	0.000	2.757	0.043	3.066	7.013	
103	10.99	0.19	0.00	0.00	1.92	1.36	0.00	0.01	32.23	1.58	47.14	0.53	0.00	95.95	0.957	0.025	0.000	0.000	0.107	0.135	0.000	0.001	2.538	0.080	3.150	6.993	
104	10.91	0.32	0.02	0.00	1.51	0.67	0.07	0.01	35.26	1.11	46.10	0.34	0.01	96.33	0.942	0.041	0.002	0.000	0.084	0.066	0.004	0.001	2.754	0.055	3.055	7.004	
105	10.76	0.41	0.02	0.00	1.42	0.68	0.03	0.00	34.83	0.73	45.31	0.42	0.00	94.60	0.947	0.054	0.002	0.000	0.080	0.068	0.002	0.000	2.771	0.037	3.059	7.019	
106	10.65	0.53	0.02	0.00	1.22	0.77	0.03	0.00	35.40	0.94	45.66	0.40	0.01	95.62	0.926	0.068	0.001	0.000	0.068	0.076	0.002	0.000	2.782	0.047	3.044	7.014	
107	10.56	0.64	0.03	0.00	1.29	0.71	0.01	0.02	35.73	0.77	45.70	0.36	0.01	95.82	0.915	0.082	0.002	0.000	0.072	0.070	0.001	0.001	2.800	0.038	3.039	7.021	
108	10.47	0.64	0.03	0.00	1.18	0.76	0.00	0.00	35.43	1.08	45.92	0.56	0.01	96.08	0.906	0.083	0.002	0.000	0.066	0.075	0.000	0.000	2.772	0.054	3.048	7.006	
109	10.38	0.82	0.05	0.00	1.23	0.76	0.02	0.02	35.56	0.98	45.85	0.44	0.00	96.09	0.897	0.105	0.003	0.000	0.068	0.075	0.001	0.001	2.780	0.049	3.041	7.021	
110	10.97	0.39	0.00	0.00	1.12	0.63	0.00	0.00	35.37	0.89	46.05	0.35	0.00	95.76	0.951	0.050	0.000	0.000	0.062	0.062	0.000	0.000	2.773	0.044	3.063	7.006	
111	10.37	0.71	0.00	0.00	1.28	0.73	0.01	0.00	34.85	1.01	45.23	0.41	0.00	94.59	0.911	0.092	0.000	0.000	0.072	0.074	0.001	0.000	2.769	0.051	3.049	7.018	
112	10.26	0.60	0.00	0.00	1.33	0.75	0.03	0.00	34.86	0.98	45.08	0.40	0.01	94.29	0.904	0.078	0.000	0.000	0.075	0.076	0.001	0.000	2.777	0.050	3.046	7.007	
mv	10.58	0.59	0.02	0.00	1.28	0.73	0.02	0.01	35.19	0.92	45.59	0.42	0.00	95.35	0.922	0.076	0.001	0.000	0.072	0.072	0.001	0.000	2.775	0.046	3.049	7.016	
sd	0.23	0.14	0.02	0.00	0.22	0.07	0.02	0.01	0.38	0.36	0.30	0.06	0.00	0.55	0.019	0.018	0.001	0.000	0.012	0.007	0.001	0.001	0.028	0.018	0.011	0.010	

Sample Grf 9 (continued)

No.	K ₂ O	Na ₂ O	CaO	BaO	FeO _t	MgO	MnO	Cr ₂ O ₃	Al ₂ O ₃	TiO ₂	SiO ₂	F	Cl	Total	K	Na	Ca	Ba	Fe ²⁺	Mg	Mn	Cr	Al	Ti	Si	Total	
	very fine-grained white mica (synkinematic):																										
72	11.08	0.21	0.05	0.00	2.17	0.91	0.05	0.02	34.78	0.05	45.78	0.40	0.00	95.51	0.970	0.028	0.003	0.000	0.122	0.091	0.003	0.001	2.752	0.003	3.074	7.046	
73	10.70	0.26	0.03	0.00	2.55	0.90	0.00	0.00	35.27	0.04	44.62	0.38	0.01	94.77	0.945	0.033	0.002	0.000	0.144	0.091	0.000	0.000	2.816	0.002	3.022	7.057	
74	11.13	0.25	0.03	0.03	1.36	0.53	0.04	0.00	35.49	0.06	44.88	0.37	0.01	94.18	0.985	0.033	0.002	0.001	0.077	0.054	0.003	0.000	2.839	0.003	3.046	7.041	
75	10.13	0.22	0.05	0.01	3.34	1.57	0.04	0.04	33.02	0.05	45.99	0.44	0.01	94.90	0.894	0.028	0.003	0.000	0.189	0.158	0.002	0.002	2.635	0.002	3.113	7.027	
78	10.81	0.14	0.03	0.00	3.29	1.50	0.05	0.00	32.26	0.20	45.73	0.48	0.01	94.50	0.962	0.018	0.002	0.000	0.188	0.153	0.003	0.000	2.597	0.010	3.124	7.058	
93	10.83	0.22	0.01	0.00	2.12	1.11	0.00	0.01	33.40	0.44	45.78	0.49	0.00	94.40	0.959	0.028	0.001	0.000	0.120	0.112	0.000	0.001	2.673	0.022	3.109	7.025	
95	11.22	0.23	0.02	0.08	2.02	1.15	0.00	0.00	33.77	0.04	46.09	0.59	0.01	95.22	0.987	0.030	0.002	0.002	0.114	0.116	0.000	0.000	2.687	0.002	3.112	7.051	
mv	10.84	0.22	0.03	0.02	2.41	1.09	0.03	0.01	34.00	0.13	45.55	0.45	0.01	94.78	0.957	0.028	0.002	0.000	0.136	0.111	0.002	0.001	2.714	0.006	3.086	7.044	
sd	0.37	0.04	0.01	0.03	0.71	0.36	0.02	0.01	1.21	0.15	0.57	0.08	0.01	0.47	0.032	0.005	0.001	0.001	0.041	0.037	0.001	0.001	0.091	0.008	0.039	0.013	

Sample Grf 605

No.	K ₂ O	Na ₂ O	CaO	BaO	FeO ₁	MgO	MnO	Cr ₂ O ₃	Al ₂ O ₃	TiO ₂	SiO ₂	F	Total	K	Na	Ca	Ba	Fe ²⁺	Mg	Mn	Cr	Al	Ti	Si	Total	
porphyroclasts, core:																										
10	10.70	0.39	0.00	0.00	4.01	0.54	0.11	0.00	32.80	0.44	45.74	0.10	94.83	0.949	0.051	0.000	0.000	0.228	0.055	0.006	0.000	2.630	0.022	3.111	7.051	
11	9.64	0.35	0.04	0.00	5.86	0.65	0.20	0.02	31.29	0.39	46.10	0.02	94.55	0.859	0.047	0.003	0.000	0.335	0.066	0.011	0.001	2.522	0.020	3.153	7.018	
12	10.75	0.37	0.00	0.00	4.43	0.54	0.12	0.00	32.25	0.45	45.76	0.00	94.66	0.956	0.049	0.000	0.000	0.253	0.055	0.007	0.000	2.594	0.023	3.123	7.059	
15	10.82	0.33	0.00	0.00	4.66	0.65	0.13	0.02	32.00	0.33	45.97	0.00	94.91	0.961	0.043	0.000	0.000	0.266	0.066	0.008	0.001	2.571	0.017	3.133	7.066	
16	10.92	0.42	0.00	0.00	4.07	0.63	0.11	0.00	32.45	0.41	46.21	0.25	95.46	0.964	0.055	0.000	0.000	0.231	0.063	0.006	0.000	2.591	0.021	3.131	7.063	
17	10.74	0.42	0.00	0.00	4.17	0.62	0.09	0.02	32.55	0.31	46.08	0.15	95.14	0.950	0.055	0.000	0.000	0.236	0.063	0.005	0.001	2.604	0.016	3.127	7.057	
18	11.05	0.43	0.00	0.03	4.09	0.56	0.09	0.02	32.79	0.47	45.92	0.00	95.44	0.975	0.057	0.000	0.001	0.231	0.056	0.005	0.001	2.617	0.024	3.108	7.075	
31	10.68	0.33	0.00	0.02	4.68	0.64	0.14	0.00	32.05	0.43	45.92	0.00	94.88	0.948	0.044	0.000	0.001	0.267	0.065	0.008	0.000	2.574	0.022	3.129	7.058	
32	10.87	0.33	0.00	0.00	4.63	0.63	0.19	0.00	31.72	0.44	46.17	0.15	95.13	0.966	0.044	0.000	0.000	0.264	0.064	0.011	0.000	2.547	0.023	3.146	7.063	
33	10.68	0.30	0.00	0.02	4.17	0.64	0.08	0.00	32.11	0.44	45.82	0.00	94.25	0.952	0.040	0.000	0.000	0.239	0.065	0.004	0.000	2.589	0.023	3.134	7.045	
34	10.61	0.37	0.00	0.00	4.03	0.66	0.11	0.00	32.53	0.42	46.17	0.00	94.91	0.938	0.049	0.000	0.000	0.229	0.067	0.006	0.000	2.600	0.022	3.131	7.041	
35	10.89	0.31	0.00	0.00	4.52	0.64	0.15	0.00	32.13	0.44	46.32	0.29	95.70	0.962	0.041	0.000	0.000	0.256	0.065	0.008	0.000	2.566	0.023	3.138	7.058	
56	10.88	0.24	0.00	0.00	5.21	0.66	0.16	0.00	31.09	0.38	45.63	0.00	94.25	0.977	0.032	0.000	0.000	0.301	0.068	0.009	0.000	2.526	0.020	3.145	7.077	
57	10.59	0.35	0.00	0.00	4.49	0.63	0.15	0.00	31.70	0.36	45.89	0.33	94.49	0.946	0.046	0.000	0.000	0.258	0.065	0.009	0.000	2.562	0.019	3.146	7.050	
66	11.06	0.27	0.00	0.02	4.66	0.72	0.25	0.01	31.40	0.01	46.19	0.23	94.81	0.987	0.036	0.000	0.000	0.267	0.074	0.015	0.000	2.535	0.000	3.164	7.079	
mv	10.72	0.35	0.00	0.01	4.51	0.63	0.14	0.01	32.06	0.38	45.99	0.10	94.89	0.953	0.046	0.000	0.000	0.257	0.064	0.008	0.000	2.575	0.020	3.135	7.057	
sd	0.33	0.05	0.01	0.01	0.50	0.05	0.05	0.01	0.53	0.11	0.20	0.12	0.43	0.029	0.007	0.001	0.000	0.029	0.005	0.003	0.000	0.033	0.006	0.015	0.016	
porphyroclasts, rim:																										
9	10.81	0.28	0.00	0.00	4.37	0.54	0.14	0.00	32.42	0.41	45.67	0.08	94.72	0.961	0.038	0.000	0.000	0.250	0.054	0.008	0.000	2.608	0.021	3.117	7.057	
13	10.82	0.33	0.00	0.03	3.97	0.55	0.09	0.05	32.24	0.45	45.80	0.00	94.33	0.964	0.043	0.000	0.001	0.227	0.056	0.005	0.003	2.598	0.023	3.130	7.050	
14	10.94	0.32	0.00	0.03	4.75	0.71	0.19	0.01	31.70	0.44	46.33	0.25	95.66	0.968	0.042	0.000	0.001	0.270	0.072	0.011	0.000	2.537	0.023	3.146	7.068	
19	10.79	0.23	0.01	0.02	5.15	0.65	0.09	0.00	31.62	0.37	45.99	0.46	95.37	0.960	0.031	0.000	0.000	0.294	0.066	0.005	0.000	2.545	0.019	3.141	7.063	
30	10.80	0.23	0.00	0.06	5.02	0.72	0.17	0.00	30.98	0.32	46.87	0.10	95.29	0.957	0.031	0.000	0.001	0.286	0.073	0.010	0.000	2.484	0.016	3.188	7.047	
36	11.03	0.28	0.01	0.00	4.98	0.69	0.15	0.00	31.76	0.43	46.36	0.21	95.89	0.975	0.037	0.000	0.000	0.282	0.069	0.009	0.000	2.537	0.022	3.142	7.073	
55	10.75	0.22	0.01	0.02	4.67	0.64	0.17	0.01	31.90	0.35	46.01	0.17	94.91	0.956	0.029	0.001	0.000	0.267	0.065	0.010	0.000	2.566	0.018	3.139	7.052	
58	10.95	0.25	0.00	0.00	4.71	0.65	0.14	0.00	31.74	0.31	46.01	0.25	95.01	0.975	0.033	0.000	0.000	0.269	0.066	0.008	0.000	2.556	0.016	3.144	7.067	
65	10.86	0.18	0.01	0.00	4.93	0.69	0.15	0.01	30.83	0.03	45.77	0.21	93.66	0.982	0.024	0.001	0.000	0.286	0.071	0.009	0.001	2.520	0.001	3.174	7.067	
mv	10.86	0.26	0.00	0.02	4.73	0.65	0.14	0.01	31.69	0.34	46.09	0.19	94.98	0.967	0.034	0.000	0.000	0.270	0.066	0.008	0.000	2.550	0.018	3.147	7.061	
sd	0.09	0.05	0.00	0.02	0.37	0.07	0.03	0.02	0.52	0.13	0.38	0.13	0.69	0.009	0.006	0.000	0.000	0.021	0.007	0.002	0.001	0.038	0.007	0.022	0.009	
cleavage domains:																										
1	10.80	0.16	0.00	0.05	5.28	0.73	0.19	0.01	30.35	0.32	46.01	0.00	93.88	0.973	0.021	0.000	0.001	0.305	0.075	0.011	0.000	2.475	0.017	3.182	7.061	
2	10.70	0.21	0.00	0.01	4.93	0.76	0.15	0.00	30.82	0.33	46.39	0.46	94.74	0.957	0.028	0.000	0.000	0.283	0.077	0.009	0.000	2.492	0.017	3.183	7.046	
3	9.71	0.20	0.03	0.00	5.71	0.71	0.14	0.00	30.86	0.28	46.21	0.00	93.84	0.870	0.027	0.002	0.000	0.328	0.072	0.008	0.000	2.503	0.014	3.179	7.004	
4	10.76	0.19	0.00	0.00	5.20	0.75	0.23	0.02	29.35	0.39	44.72	0.25	91.87	0.997	0.026	0.000	0.000	0.309	0.080	0.014	0.001	2.458	0.021	3.178	7.084	
6	10.31	0.12	0.00	0.00	6.58	0.80	0.21	0.01	27.98	0.40	48.80	0.25	95.45	0.916	0.016	0.000	0.000	0.375	0.081	0.012	0.001	2.248	0.020	3.326	6.995	

Sample Grf 605 (continued)

No.	K ₂ O	Na ₂ O	CaO	BaO	FeO _t	MgO	MnO	Cr ₂ O ₃	Al ₂ O ₃	TiO ₂	SiO ₂	F	Total	K	Na	Ca	Ba	Fe ²⁺	Mg	Mn	Cr	Al	Ti	Si	Total	
cleavage domains:																										
21	10.82	0.22	0.01	0.01	5.12	0.75	0.22	0.00	30.41	0.32	45.93	0.25	94.06	0.976	0.029	0.001	0.000	0.296	0.077	0.013	0.000	2.480	0.017	3.178	7.068	
22	10.77	0.24	0.01	0.00	4.95	0.78	0.14	0.00	30.79	0.30	46.80	0.25	95.03	0.958	0.032	0.001	0.000	0.283	0.079	0.008	0.000	2.477	0.016	3.194	7.047	
23	10.95	0.25	0.00	0.00	5.03	0.77	0.18	0.00	30.94	0.27	46.86	0.00	95.24	0.971	0.033	0.000	0.000	0.286	0.078	0.010	0.000	2.481	0.014	3.188	7.060	
24	10.57	0.23	0.01	0.06	4.95	0.75	0.17	0.01	29.71	0.32	44.66	0.19	91.63	0.979	0.032	0.001	0.002	0.294	0.079	0.010	0.000	2.487	0.017	3.172	7.073	
25	10.33	0.21	0.00	0.00	4.90	0.72	0.27	0.00	29.91	0.32	47.18	0.00	93.84	0.925	0.028	0.000	0.000	0.282	0.074	0.016	0.000	2.423	0.016	3.242	7.006	
26	10.41	0.18	0.03	0.06	5.22	0.76	0.19	0.01	30.45	0.30	46.52	0.19	94.31	0.933	0.024	0.002	0.002	0.300	0.078	0.011	0.000	2.468	0.016	3.198	7.031	
27	10.76	0.29	0.00	0.00	5.17	0.65	0.19	0.00	30.77	0.70	45.50	0.31	94.34	0.969	0.038	0.000	0.000	0.299	0.067	0.011	0.000	2.506	0.037	3.144	7.070	
28	10.30	0.21	0.01	0.05	4.85	0.76	0.16	0.00	30.89	0.14	47.43	0.00	94.81	0.912	0.027	0.001	0.001	0.276	0.077	0.009	0.000	2.473	0.007	3.221	7.004	
29	10.94	0.23	0.01	0.02	4.59	0.75	0.15	0.01	31.26	0.28	46.76	0.15	95.13	0.970	0.031	0.000	0.000	0.261	0.076	0.009	0.000	2.507	0.014	3.182	7.051	
37	11.00	0.15	0.00	0.00	5.41	0.75	0.18	0.03	30.73	0.33	47.24	0.00	95.81	0.970	0.019	0.000	0.000	0.306	0.076	0.010	0.001	2.453	0.017	3.199	7.052	
42	9.18	0.19	0.01	0.00	4.99	0.74	0.19	0.01	28.82	0.33	45.07	0.02	89.56	0.859	0.026	0.001	0.000	0.300	0.079	0.012	0.001	2.439	0.018	3.236	6.970	
43	10.47	0.22	0.01	0.00	5.39	0.80	0.12	0.00	29.74	0.37	45.94	0.19	93.24	0.951	0.029	0.001	0.000	0.314	0.083	0.007	0.000	2.443	0.019	3.201	7.048	
44	11.04	0.23	0.02	0.00	5.04	0.78	0.16	0.01	30.81	0.38	46.39	0.13	94.97	0.985	0.030	0.002	0.000	0.288	0.079	0.009	0.000	2.485	0.020	3.174	7.071	
45	10.83	0.23	0.00	0.02	4.93	0.81	0.17	0.01	30.67	0.33	46.92	0.21	95.15	0.963	0.030	0.000	0.001	0.281	0.082	0.010	0.001	2.465	0.017	3.199	7.048	
46	10.93	0.17	0.00	0.00	5.37	0.78	0.13	0.02	30.66	0.34	46.33	0.23	94.96	0.976	0.023	0.000	0.000	0.308	0.080	0.008	0.001	2.477	0.018	3.176	7.067	
47	10.53	0.20	0.00	0.00	5.15	0.79	0.20	0.01	30.63	0.40	46.34	0.00	94.25	0.943	0.027	0.000	0.000	0.296	0.080	0.012	0.000	2.480	0.021	3.183	7.041	
48	10.97	0.15	0.00	0.00	5.28	0.79	0.16	0.00	30.28	0.42	47.10	0.15	95.29	0.975	0.019	0.000	0.000	0.301	0.081	0.009	0.000	2.433	0.022	3.210	7.049	
51	10.76	0.29	0.00	0.00	4.93	0.75	0.09	0.00	31.74	0.41	46.62	0.00	95.59	0.949	0.037	0.000	0.000	0.279	0.075	0.005	0.000	2.532	0.021	3.154	7.052	
52	10.90	0.28	0.00	0.00	5.11	0.74	0.17	0.00	31.26	0.36	46.07	0.15	95.03	0.972	0.037	0.000	0.000	0.292	0.076	0.010	0.000	2.520	0.018	3.151	7.075	
53	9.70	0.18	0.02	0.07	5.10	0.70	0.16	0.04	29.88	0.23	45.56	0.00	91.64	0.889	0.024	0.001	0.002	0.300	0.074	0.010	0.002	2.478	0.012	3.206	6.998	
59	10.51	0.27	0.02	0.02	4.91	0.77	0.20	0.00	30.81	0.35	46.32	0.17	94.35	0.940	0.036	0.002	0.000	0.282	0.079	0.012	0.000	2.493	0.018	3.180	7.043	
60	10.01	0.16	0.00	0.00	4.72	0.73	0.19	0.01	29.37	0.26	48.84	0.21	94.49	0.886	0.021	0.000	0.000	0.268	0.074	0.011	0.000	2.353	0.013	3.319	6.945	
61	10.86	0.19	0.00	0.00	5.23	0.76	0.15	0.00	31.02	0.27	46.83	0.12	95.45	0.962	0.025	0.000	0.000	0.297	0.077	0.009	0.000	2.486	0.014	3.183	7.054	
62	10.94	0.30	0.00	0.01	5.08	0.81	0.23	0.06	30.70	0.23	46.66	0.19	95.20	0.974	0.039	0.000	0.000	0.290	0.083	0.013	0.003	2.471	0.012	3.186	7.072	
63	10.49	0.21	0.02	0.00	4.82	0.80	0.17	0.00	30.00	0.46	45.41	0.00	92.37	0.958	0.029	0.001	0.000	0.282	0.084	0.010	0.000	2.478	0.024	3.182	7.048	
64	10.65	0.32	0.00	0.03	4.70	0.67	0.16	0.04	31.99	0.05	46.33	0.17	95.09	0.945	0.042	0.000	0.001	0.267	0.068	0.009	0.002	2.565	0.002	3.153	7.054	
68	10.49	0.25	0.01	0.00	4.67	0.85	0.16	0.00	32.12	0.24	48.78	0.00	97.57	0.900	0.032	0.001	0.000	0.257	0.084	0.009	0.000	2.492	0.012	3.211	6.997	
69	10.83	0.19	0.01	0.00	4.97	0.76	0.22	0.03	30.44	0.27	46.10	0.41	94.22	0.975	0.025	0.001	0.000	0.287	0.078	0.013	0.002	2.479	0.014	3.185	7.060	
70	10.44	0.32	0.01	0.05	4.92	0.81	0.16	0.00	32.45	0.21	49.77	0.39	99.52	0.881	0.040	0.001	0.001	0.266	0.078	0.009	0.000	2.477	0.010	3.224	6.988	
mv	10.58	0.22	0.01	0.01	5.09	0.76	0.18	0.01	30.55	0.32	46.60	0.15	94.47	0.946	0.029	0.001	0.000	0.292	0.078	0.010	0.001	2.470	0.017	3.196	7.039	
sd	0.42	0.05	0.01	0.02	0.35	0.04	0.03	0.01	0.90	0.11	1.13	0.13	1.73	0.036	0.006	0.001	0.001	0.021	0.004	0.002	0.001	0.053	0.006	0.039	0.033	

Sample Pat 10

No.	K ₂ O	Na ₂ O	CaO	BaO	FeO _t	MgO	MnO	Cr ₂ O ₃	Al ₂ O ₃	TiO ₂	SiO ₂	F	Cl	Total	K	Na	Ca	Ba	Fe ²⁺	Mg	Mn	Cr	Al	Ti	Si	Total	
medium-sized crystals:																											
3	10.82	0.23	0.34	0.01	2.68	1.00	0.01	0.01	33.02	0.52	45.54	0.36	0.00	94.54	0.960	0.030	0.025	0.000	0.153	0.101	0.001	0.001	2.649	0.026	3.099	7.044	
4	10.89	0.39	0.01	0.07	2.44	0.93	0.02	0.00	33.94	0.17	45.79	0.42	0.01	95.08	0.959	0.050	0.001	0.002	0.138	0.094	0.001	0.000	2.703	0.009	3.094	7.051	
5	11.00	0.32	0.00	0.00	2.75	1.10	0.04	0.00	32.81	0.70	45.74	0.39	0.01	94.85	0.974	0.042	0.000	0.000	0.156	0.111	0.002	0.000	2.626	0.036	3.106	7.053	
9	10.86	0.31	0.01	0.07	2.93	1.20	0.02	0.02	32.51	0.43	45.86	0.43	0.00	94.64	0.964	0.041	0.001	0.002	0.167	0.121	0.001	0.001	2.609	0.022	3.123	7.052	
10	10.80	0.29	0.01	0.02	2.59	0.95	0.00	0.00	33.33	0.53	45.52	0.40	0.01	94.46	0.958	0.039	0.001	0.001	0.147	0.097	0.000	0.000	2.673	0.027	3.097	7.038	
11	11.04	0.21	0.01	0.08	2.59	0.94	0.03	0.00	33.36	0.50	45.66	0.30	0.00	94.72	0.977	0.028	0.001	0.002	0.147	0.095	0.002	0.000	2.668	0.025	3.099	7.044	
12	10.82	0.31	0.03	0.00	2.40	1.10	0.07	0.02	32.48	1.37	45.97	0.36	0.00	94.91	0.955	0.041	0.002	0.000	0.136	0.111	0.004	0.001	2.591	0.070	3.111	7.021	
13	11.00	0.31	0.00	0.06	2.89	1.21	0.03	0.00	32.18	0.57	45.53	0.44	0.01	94.24	0.982	0.041	0.000	0.002	0.166	0.124	0.002	0.000	2.599	0.030	3.119	7.064	
14	10.97	0.34	0.02	0.04	3.13	1.20	0.02	0.02	32.63	0.62	45.86	0.44	0.01	95.30	0.969	0.044	0.002	0.001	0.177	0.121	0.001	0.001	2.607	0.031	3.108	7.063	
16	10.73	0.36	0.03	0.00	2.88	1.05	0.05	0.03	33.06	0.52	46.24	0.45	0.01	95.42	0.943	0.047	0.002	0.000	0.162	0.106	0.003	0.002	2.627	0.026	3.118	7.036	
17	10.93	0.39	0.02	0.01	2.59	0.94	0.06	0.00	33.71	0.79	45.92	0.36	0.00	95.72	0.957	0.051	0.002	0.000	0.145	0.095	0.003	0.000	2.669	0.040	3.084	7.046	
18	10.94	0.36	0.00	0.06	2.84	1.06	0.04	0.01	33.40	0.50	45.68	0.51	0.01	95.40	0.964	0.047	0.000	0.002	0.161	0.107	0.002	0.000	2.662	0.026	3.089	7.059	
19	10.98	0.26	0.00	0.04	2.79	1.34	0.02	0.00	31.77	0.67	46.17	0.44	0.00	94.47	0.976	0.034	0.000	0.001	0.159	0.136	0.001	0.000	2.554	0.034	3.149	7.044	
20	10.89	0.40	0.00	0.00	2.44	0.83	0.04	0.00	33.97	0.89	45.75	0.29	0.00	95.50	0.954	0.053	0.000	0.000	0.137	0.083	0.002	0.000	2.690	0.045	3.074	7.039	
21	11.09	0.28	0.00	0.06	3.06	1.10	0.00	0.02	32.94	0.60	45.24	0.45	0.00	94.83	0.985	0.037	0.000	0.002	0.174	0.112	0.000	0.001	2.647	0.031	3.084	7.072	
22	10.77	0.33	0.00	0.03	2.55	1.03	0.02	0.01	33.39	0.50	45.87	0.45	0.00	94.95	0.950	0.043	0.000	0.001	0.144	0.104	0.001	0.001	2.663	0.025	3.104	7.036	
25	10.98	0.30	0.01	0.01	2.68	1.12	0.00	0.00	32.18	1.02	45.89	0.40	0.00	94.59	0.974	0.039	0.001	0.000	0.153	0.114	0.000	0.000	2.582	0.052	3.124	7.039	
117	10.58	0.27	0.01	0.04	2.77	1.12	0.01	0.00	32.46	0.57	45.44	0.38	0.01	93.66	0.946	0.036	0.001	0.001	0.159	0.114	0.001	0.000	2.625	0.030	3.118	7.031	
118	9.79	0.17	0.01	0.00	2.78	1.08	0.04	0.01	33.00	0.57	45.76	0.47	0.01	93.69	0.870	0.023	0.001	0.000	0.159	0.110	0.002	0.000	2.653	0.029	3.121	6.969	
mv	10.84	0.31	0.03	0.03	2.73	1.07	0.03	0.01	32.95	0.63	45.76	0.41	0.00	94.79	0.959	0.040	0.002	0.001	0.155	0.108	0.002	0.000	2.637	0.032	3.106	7.042	
sd	0.28	0.06	0.08	0.03	0.20	0.12	0.02	0.01	0.61	0.25	0.24	0.06	0.01	0.56	0.025	0.008	0.006	0.001	0.012	0.013	0.001	0.001	0.039	0.013	0.018	0.022	
small-sized crystals:																											
6	10.92	0.32	0.03	0.00	2.72	0.89	0.00	0.00	32.77	1.28	45.46	0.44	0.00	94.83	0.967	0.042	0.002	0.000	0.155	0.090	0.000	0.000	2.625	0.065	3.090	7.037	
7	9.97	0.26	0.05	0.00	2.14	0.74	0.02	0.00	33.99	0.80	45.72	0.44	0.01	94.15	0.880	0.035	0.004	0.000	0.121	0.075	0.001	0.000	2.713	0.041	3.096	6.965	
8	10.78	0.43	0.04	0.00	3.21	1.12	0.03	0.03	33.04	0.96	45.23	0.45	0.02	95.32	0.953	0.057	0.003	0.000	0.182	0.113	0.001	0.001	2.641	0.049	3.067	7.068	
29	11.03	0.35	0.00	0.00	2.50	1.06	0.04	0.02	33.22	0.52	45.90	0.40	0.01	95.05	0.973	0.046	0.000	0.000	0.141	0.107	0.002	0.001	2.649	0.027	3.106	7.052	
31	11.12	0.30	0.00	0.04	2.79	1.09	0.03	0.02	32.89	0.97	45.88	0.49	0.00	95.62	0.979	0.039	0.000	0.001	0.158	0.109	0.002	0.001	2.617	0.049	3.098	7.053	
32	10.87	0.45	0.02	0.00	2.41	0.76	0.00	0.01	34.45	0.78	45.73	0.35	0.01	95.84	0.949	0.059	0.002	0.000	0.135	0.076	0.000	0.001	2.719	0.039	3.063	7.042	
33	10.89	0.33	0.03	0.03	3.05	1.20	0.02	0.02	32.45	0.45	45.36	0.44	0.01	94.28	0.972	0.044	0.002	0.001	0.175	0.123	0.001	0.001	2.620	0.023	3.107	7.068	
34	11.02	0.23	0.00	0.06	2.45	0.91	0.04	0.00	33.67	0.52	45.60	0.32	0.00	94.81	0.973	0.030	0.000	0.002	0.139	0.092	0.002	0.000	2.689	0.026	3.089	7.042	
35	11.02	0.23	0.02	0.03	2.93	1.41	0.02	0.00	31.36	0.97	46.49	0.40	0.00	94.87	0.976	0.030	0.001	0.001	0.167	0.143	0.001	0.000	2.512	0.050	3.159	7.038	
36	10.89	0.33	0.01	0.00	2.69	1.02	0.02	0.05	32.69	1.21	45.70	0.38	0.01	95.01	0.962	0.043	0.001	0.000	0.152	0.103	0.001	0.003	2.611	0.062	3.097	7.037	
37	10.86	0.34	0.02	0.06	2.70	1.06	0.01	0.00	33.20	0.53	45.37	0.38	0.01	94.54	0.964	0.045	0.002	0.002	0.154	0.108	0.001	0.000	2.665	0.027	3.089	7.056	
38	10.74	0.25	0.03	0.04	3.40	1.41	0.06	0.02	31.93	0.45	45.99	0.42	0.02	94.74	0.954	0.033	0.002	0.001	0.194	0.143	0.004	0.001	2.565	0.023	3.134	7.053	
39	11.16	0.23	0.03	0.00	2.51	1.04	0.00	0.00	32.70	1.45	45.33	0.26	0.01	94.71	0.989	0.031	0.002	0.000	0.143	0.105	0.000	0.000	2.620	0.074	3.081	7.044	

Sample Pat 10 (continued)

No.	K ₂ O	Na ₂ O	CaO	BaO	FeO _t	MgO	MnO	Cr ₂ O ₃	Al ₂ O ₃	TiO ₂	SiO ₂	F	Cl	Total	K	Na	Ca	Ba	Fe ²⁺	Mg	Mn	Cr	Al	Ti	Si	Total	
small-sized crystals:																											
40	11.05	0.24	0.04	0.07	3.62	1.45	0.04	0.03	31.46	0.50	45.59	0.53	0.00	94.61	0.988	0.032	0.003	0.002	0.208	0.148	0.002	0.002	2.545	0.026	3.128	7.083	
mv	10.88	0.31	0.02	0.02	2.79	1.08	0.02	0.01	32.84	0.81	45.67	0.41	0.01	94.88	0.963	0.040	0.002	0.001	0.159	0.110	0.001	0.001	2.628	0.041	3.100	7.046	
sd	0.29	0.07	0.02	0.03	0.41	0.22	0.02	0.02	0.88	0.34	0.33	0.07	0.01	0.47	0.027	0.009	0.001	0.001	0.024	0.023	0.001	0.001	0.060	0.017	0.026	0.027	
crystals included in feldspar:																											
1	10.92	0.37	0.01	0.03	2.33	0.84	0.01	0.06	33.87	0.32	45.52	0.36	0.00	94.65	0.965	0.049	0.001	0.001	0.132	0.085	0.001	0.003	2.708	0.016	3.087	7.048	
2	10.63	0.49	0.00	0.03	2.12	0.64	0.03	0.01	34.60	0.46	45.45	0.41	0.01	94.88	0.935	0.064	0.000	0.001	0.120	0.065	0.002	0.000	2.753	0.023	3.068	7.031	
15	10.97	0.26	0.01	0.06	2.88	1.29	0.03	0.02	31.51	0.53	46.23	0.56	0.00	94.35	0.978	0.035	0.001	0.002	0.165	0.131	0.002	0.001	2.541	0.027	3.163	7.045	
23	10.50	0.33	0.02	0.00	2.36	0.98	0.01	0.02	33.05	0.66	45.77	0.36	0.01	94.06	0.932	0.043	0.002	0.000	0.134	0.099	0.000	0.001	2.652	0.034	3.115	7.012	
24	10.92	0.29	0.00	0.00	2.63	1.14	0.05	0.00	32.70	0.74	45.67	0.42	0.01	94.55	0.969	0.038	0.000	0.000	0.150	0.115	0.003	0.000	2.624	0.038	3.109	7.045	
26	11.10	0.25	0.02	0.04	2.72	1.15	0.05	0.00	32.39	0.56	45.70	0.46	0.00	94.43	0.988	0.033	0.001	0.001	0.155	0.117	0.003	0.000	2.608	0.029	3.121	7.057	
27	10.65	0.21	0.03	0.00	2.88	1.50	0.03	0.00	31.39	0.43	46.88	0.48	0.00	94.47	0.944	0.028	0.002	0.000	0.164	0.152	0.002	0.000	2.516	0.022	3.188	7.018	
28	11.08	0.19	0.00	0.02	3.21	1.54	0.04	0.00	31.01	0.64	45.82	0.47	0.01	94.02	0.994	0.025	0.000	0.000	0.185	0.157	0.003	0.000	2.515	0.033	3.153	7.066	
30	10.76	0.37	0.01	0.24	2.25	0.77	0.02	0.00	34.72	0.34	45.40	0.33	0.01	95.22	0.945	0.048	0.001	0.006	0.127	0.078	0.001	0.000	2.758	0.017	3.060	7.041	
41	11.10	0.20	0.02	0.01	3.65	1.57	0.05	0.03	31.32	0.46	45.72	0.43	0.00	94.55	0.992	0.027	0.001	0.000	0.209	0.160	0.003	0.002	2.531	0.024	3.135	7.084	
42	11.15	0.24	0.01	0.15	3.43	1.48	0.03	0.00	31.69	0.44	46.19	0.46	0.00	95.27	0.988	0.032	0.001	0.004	0.195	0.150	0.002	0.000	2.540	0.022	3.141	7.076	
43	10.98	0.23	0.05	0.05	3.27	1.57	0.04	0.03	30.94	0.54	45.61	0.42	0.01	93.74	0.988	0.031	0.004	0.001	0.189	0.161	0.002	0.002	2.518	0.028	3.149	7.073	
mv	10.90	0.29	0.02	0.05	2.81	1.20	0.03	0.01	32.43	0.51	45.83	0.43	0.00	94.52	0.968	0.038	0.001	0.001	0.160	0.123	0.002	0.001	2.605	0.026	3.124	7.050	
sd	0.21	0.09	0.02	0.07	0.50	0.33	0.01	0.02	1.36	0.13	0.42	0.06	0.00	0.46	0.023	0.011	0.001	0.002	0.029	0.035	0.001	0.001	0.093	0.007	0.039	0.023	

Sample Pat 11

No.	K ₂ O	Na ₂ O	CaO	BaO	FeO _t	MgO	MnO	Cr ₂ O ₃	Al ₂ O ₃	TiO ₂	SiO ₂	F	Cl	Total	K	Na	Ca	Ba	Fe ²⁺	Mg	Mn	Cr	Al	Ti	Si	Total	
small magmatic crystals:																											
44	10.42	0.30	0.02	0.08	2.13	0.83	0.02	0.00	34.46	0.16	45.18	0.28	0.01	93.88	0.924	0.039	0.001	0.002	0.121	0.085	0.001	0.000	2.763	0.008	3.074	7.019	
45	10.51	0.20	0.04	0.15	2.98	1.56	0.03	0.00	31.82	0.75	46.13	0.31	0.01	94.48	0.932	0.027	0.003	0.004	0.170	0.159	0.002	0.000	2.552	0.038	3.139	7.026	
46	10.52	0.30	0.02	0.05	2.47	1.07	0.02	0.00	33.33	0.75	45.82	0.36	0.01	94.72	0.928	0.039	0.002	0.001	0.140	0.108	0.001	0.000	2.658	0.038	3.100	7.016	
47	10.52	0.25	0.05	0.10	2.43	1.17	0.03	0.00	33.00	0.60	46.11	0.32	0.01	94.59	0.928	0.033	0.004	0.003	0.138	0.118	0.002	0.000	2.634	0.030	3.122	7.011	
48	10.46	0.30	0.05	0.15	2.10	0.80	0.00	0.01	34.01	0.57	44.99	0.28	0.02	93.74	0.931	0.040	0.003	0.004	0.120	0.082	0.000	0.001	2.736	0.029	3.071	7.017	
49	11.16	0.31	0.04	0.04	2.09	0.96	0.05	0.02	33.10	1.48	45.39	0.30	0.02	94.94	0.985	0.041	0.003	0.001	0.118	0.097	0.003	0.001	2.643	0.075	3.075	7.042	
50	10.85	0.30	0.05	0.08	2.07	1.09	0.01	0.01	33.69	0.49	46.19	0.28	0.00	95.11	0.952	0.038	0.004	0.002	0.116	0.109	0.000	0.001	2.672	0.025	3.108	7.026	
51	10.89	0.23	0.01	0.15	2.57	1.51	0.04	0.00	32.37	0.55	46.42	0.24	0.01	94.99	0.960	0.030	0.001	0.004	0.145	0.152	0.003	0.000	2.579	0.028	3.138	7.039	
52	10.14	0.29	0.05	0.00	2.16	0.76	0.00	0.00	33.78	0.76	45.49	0.24	0.02	93.69	0.899	0.038	0.004	0.000	0.123	0.077	0.000	0.000	2.708	0.039	3.094	6.981	
53	11.16	0.30	0.02	0.09	2.06	0.87	0.00	0.00	34.42	0.54	45.41	0.25	0.00	95.12	0.981	0.039	0.001	0.002	0.116	0.087	0.000	0.000	2.736	0.027	3.062	7.053	
54	9.62	0.26	0.04	0.11	2.79	1.00	0.05	0.02	33.79	0.51	46.25	0.29	0.01	94.74	0.844	0.033	0.003	0.003	0.157	0.100	0.003	0.001	2.679	0.026	3.111	6.961	
55	9.91	0.31	0.06	0.13	2.55	1.08	0.04	0.00	33.54	0.57	45.93	0.31	0.01	94.42	0.874	0.040	0.004	0.003	0.144	0.108	0.002	0.000	2.674	0.029	3.106	6.985	
56	10.99	0.26	0.00	0.14	2.32	1.19	0.05	0.00	33.27	0.67	46.24	0.27	0.00	95.41	0.964	0.034	0.000	0.004	0.131	0.120	0.003	0.000	2.638	0.034	3.110	7.036	
57	9.82	0.22	0.04	0.14	2.81	1.45	0.05	0.03	31.95	0.75	46.40	0.26	0.02	93.94	0.871	0.029	0.003	0.004	0.160	0.147	0.003	0.002	2.561	0.039	3.156	6.974	
58	10.66	0.33	0.04	0.14	2.66	1.01	0.06	0.02	33.26	0.71	45.46	0.29	0.01	94.63	0.944	0.043	0.003	0.004	0.151	0.102	0.003	0.001	2.663	0.036	3.088	7.038	
59	10.31	0.29	0.03	0.14	2.51	1.14	0.00	0.00	32.96	0.60	46.24	0.35	0.00	94.57	0.909	0.038	0.002	0.004	0.142	0.115	0.000	0.000	2.629	0.031	3.129	6.999	
60	11.15	0.23	0.02	0.17	2.78	1.50	0.03	0.00	32.62	0.49	46.07	0.32	0.00	95.37	0.983	0.031	0.001	0.005	0.157	0.151	0.002	0.000	2.599	0.025	3.115	7.068	
61	10.75	0.31	0.03	0.14	2.30	1.00	0.05	0.00	33.35	0.48	44.57	0.18	0.01	93.18	0.965	0.041	0.002	0.004	0.133	0.103	0.003	0.000	2.708	0.025	3.070	7.054	
62	10.93	0.30	0.01	0.02	2.15	1.15	0.03	0.01	33.53	0.69	45.79	0.35	0.00	94.96	0.962	0.039	0.001	0.001	0.121	0.115	0.002	0.001	2.669	0.035	3.092	7.038	
63	10.66	0.29	0.03	0.08	2.46	1.12	0.00	0.00	32.79	0.83	46.07	0.31	0.03	94.67	0.941	0.037	0.002	0.002	0.139	0.113	0.000	0.000	2.618	0.042	3.121	7.017	
64	10.23	0.29	0.02	0.01	2.59	1.08	0.00	0.00	33.16	0.92	46.27	0.40	0.01	94.97	0.898	0.037	0.001	0.000	0.146	0.108	0.000	0.000	2.633	0.047	3.117	6.988	
65	10.27	0.27	0.25	0.09	2.63	1.11	0.04	0.00	32.75	1.03	46.09	0.37	0.02	94.93	0.905	0.036	0.018	0.002	0.149	0.112	0.002	0.000	2.609	0.052	3.115	6.999	
66	11.07	0.30	0.04	0.13	2.22	0.98	0.04	0.05	33.94	0.50	45.53	0.21	0.00	95.00	0.975	0.039	0.003	0.003	0.125	0.099	0.002	0.003	2.703	0.026	3.076	7.053	
67	10.51	0.31	0.04	0.15	2.58	0.96	0.02	0.01	33.47	0.55	45.96	0.25	0.01	94.81	0.926	0.040	0.003	0.004	0.146	0.097	0.001	0.001	2.666	0.028	3.106	7.016	
68	10.94	0.30	0.00	0.12	2.72	1.27	0.03	0.00	33.00	0.75	45.83	0.28	0.00	95.23	0.964	0.039	0.000	0.003	0.154	0.127	0.002	0.000	2.628	0.038	3.097	7.052	
69	11.05	0.40	0.03	0.12	1.77	0.66	0.01	0.00	35.46	0.58	45.53	0.23	0.00	95.85	0.962	0.052	0.002	0.003	0.099	0.066	0.001	0.000	2.790	0.029	3.039	7.043	
70	10.91	0.23	0.02	0.05	2.42	1.12	0.03	0.00	32.97	0.71	46.04	0.41	0.01	94.91	0.962	0.030	0.001	0.001	0.137	0.113	0.002	0.000	2.630	0.036	3.116	7.029	
mv	10.61	0.28	0.04	0.10	2.42	1.09	0.03	0.01	33.33	0.67	45.83	0.29	0.01	94.70	0.936	0.037	0.003	0.003	0.137	0.110	0.002	0.000	2.659	0.034	3.102	7.021	
sd	0.42	0.04	0.05	0.05	0.29	0.22	0.02	0.01	0.77	0.23	0.46	0.06	0.01	0.59	0.037	0.005	0.003	0.001	0.017	0.023	0.001	0.001	0.058	0.012	0.026	0.027	
crystals included in feldspar:																											
71	10.42	0.11	0.05	0.15	2.72	1.67	0.03	0.00	30.39	0.01	49.00	0.54	0.02	95.11	0.914	0.014	0.004	0.004	0.153	0.167	0.002	0.000	2.409	0.001	3.296	6.963	

Sample Pat 12

No.	K ₂ O	Na ₂ O	CaO	BaO	FeO _t	MgO	MnO	Cr ₂ O ₃	Al ₂ O ₃	TiO ₂	SiO ₂	F	Cl	Total	K	Na	Ca	Ba	Fe ²⁺	Mg	Mn	Cr	Al	Ti	Si	Total	
large crystals, core:																											
2	9.39	0.24	0.03	0.21	1.05	0.66	0.01	0.03	35.19	0.85	45.56	0.31	0.01	93.54	0.826	0.032	0.002	0.005	0.059	0.067	0.001	0.000	2.800	0.043	3.075	6.911	
3	10.33	0.26	0.04	0.17	2.56	1.27	0.06	0.02	33.01	0.74	44.42	0.36	0.00	93.25	0.929	0.035	0.003	0.004	0.148	0.131	0.004	0.000	2.683	0.039	3.063	7.038	
6	10.64	0.31	0.02	0.23	1.21	0.68	0.01	0.03	34.65	0.55	45.10	0.19	0.00	93.62	0.944	0.041	0.001	0.006	0.069	0.069	0.001	0.000	2.779	0.028	3.069	7.006	
9	10.83	0.38	0.04	0.27	0.97	0.56	0.02	0.00	35.87	0.70	45.04	0.27	0.02	94.97	0.948	0.050	0.003	0.007	0.054	0.056	0.001	0.000	2.839	0.035	3.025	7.019	
10	10.74	0.27	0.04	0.21	1.49	0.92	0.02	0.03	33.89	0.74	45.46	0.24	0.00	94.04	0.951	0.035	0.003	0.006	0.085	0.093	0.001	0.000	2.713	0.038	3.087	7.011	
11	10.77	0.45	0.02	0.30	0.83	0.46	0.00	0.04	36.09	0.43	45.00	0.30	0.00	94.67	0.945	0.058	0.001	0.008	0.047	0.046	0.000	0.000	2.864	0.022	3.029	7.019	
14	10.38	0.30	0.03	0.22	2.30	0.84	0.01	0.00	33.99	0.57	45.02	0.31	0.01	93.98	0.922	0.039	0.002	0.006	0.131	0.085	0.001	0.000	2.731	0.029	3.069	7.017	
17	10.35	0.21	0.02	0.21	1.51	1.15	0.01	0.02	32.81	0.53	46.76	0.23	0.01	93.82	0.914	0.027	0.001	0.006	0.086	0.116	0.001	0.000	2.620	0.027	3.168	6.966	
18	10.53	0.26	0.04	0.20	1.49	1.08	0.00	0.02	32.89	0.58	44.77	0.36	0.00	92.21	0.952	0.034	0.003	0.005	0.086	0.111	0.000	0.000	2.688	0.030	3.104	7.014	
21	10.73	0.23	0.03	0.16	1.60	1.14	0.02	0.00	32.11	0.66	46.57	0.25	0.01	93.50	0.954	0.030	0.002	0.004	0.091	0.116	0.001	0.000	2.582	0.034	3.177	6.990	
mv	10.47	0.29	0.03	0.22	1.50	0.88	0.02	0.02	34.05	0.63	45.37	0.28	0.01	93.76	0.928	0.038	0.002	0.006	0.086	0.089	0.001	0.000	2.730	0.032	3.087	6.999	
sd	0.42	0.07	0.01	0.04	0.56	0.28	0.02	0.01	1.37	0.13	0.75	0.06	0.01	0.76	0.038	0.009	0.001	0.001	0.032	0.029	0.001	0.000	0.092	0.006	0.051	0.037	
large crystals, rim:																											
1	10.69	0.37	0.03	0.24	1.03	0.60	0.03	0.05	34.74	0.72	44.72	0.27	0.00	93.49	0.951	0.049	0.002	0.006	0.059	0.061	0.001	0.000	2.795	0.037	3.052	7.014	
4	10.71	0.38	0.01	0.19	0.99	0.67	0.00	0.00	35.22	0.69	45.25	0.31	0.01	94.44	0.942	0.050	0.001	0.005	0.056	0.067	0.000	0.000	2.800	0.035	3.052	7.008	
5	10.42	0.30	0.02	0.15	1.46	0.87	0.03	0.03	34.03	0.62	45.31	0.29	0.00	93.51	0.926	0.039	0.001	0.004	0.083	0.088	0.001	0.000	2.733	0.032	3.088	6.996	
7	10.77	0.31	0.03	0.21	1.15	0.55	0.01	0.04	34.86	0.65	44.92	0.25	0.00	93.76	0.955	0.041	0.002	0.006	0.066	0.056	0.001	0.000	2.796	0.033	3.056	7.011	
8	10.14	0.17	0.08	0.10	1.74	1.33	0.00	0.03	32.52	0.56	47.37	0.32	0.02	94.37	0.890	0.022	0.005	0.003	0.098	0.133	0.000	0.000	2.580	0.028	3.189	6.949	
12	10.65	0.36	0.05	0.27	1.05	0.62	0.03	0.06	35.45	0.54	44.88	0.21	0.01	94.18	0.940	0.047	0.003	0.007	0.059	0.063	0.002	0.000	2.828	0.027	3.038	7.014	
13	10.71	0.33	0.02	0.25	1.09	0.70	0.02	0.02	34.77	0.82	45.48	0.26	0.00	94.47	0.942	0.043	0.001	0.007	0.061	0.070	0.001	0.000	2.765	0.042	3.068	7.000	
15	10.58	0.30	0.01	0.17	1.60	0.90	0.04	0.00	34.15	0.78	45.40	0.28	0.02	94.22	0.935	0.040	0.001	0.004	0.091	0.091	0.002	0.000	2.728	0.040	3.076	7.007	
16	10.88	0.31	0.01	0.23	1.21	0.98	0.00	0.00	33.67	0.45	45.48	0.27	0.00	93.50	0.968	0.041	0.001	0.006	0.069	0.100	0.000	0.000	2.709	0.023	3.105	7.022	
19	10.17	0.34	0.03	0.21	1.70	0.72	0.00	0.02	34.04	0.77	44.37	0.30	0.01	92.68	0.913	0.045	0.002	0.006	0.098	0.074	0.000	0.000	2.764	0.040	3.057	7.000	
20	10.69	0.21	0.03	0.14	1.70	1.48	0.04	0.03	31.23	0.45	46.96	0.39	0.01	93.37	0.954	0.028	0.002	0.004	0.097	0.151	0.002	0.000	2.519	0.023	3.214	6.994	
22	10.03	0.25	0.04	0.24	1.56	1.06	0.01	0.00	33.28	0.70	45.70	0.25	0.01	93.13	0.893	0.033	0.003	0.006	0.089	0.108	0.000	0.000	2.678	0.036	3.120	6.967	
mv	10.54	0.30	0.03	0.20	1.36	0.87	0.02	0.02	34.00	0.65	45.49	0.28	0.01	93.76	0.934	0.040	0.002	0.005	0.077	0.088	0.001	0.000	2.725	0.033	3.093	6.999	
sd	0.28	0.06	0.02	0.05	0.30	0.30	0.01	0.02	1.21	0.12	0.87	0.05	0.01	0.58	0.024	0.008	0.001	0.001	0.017	0.030	0.001	0.000	0.093	0.006	0.056	0.021	
small crystals:																											
23	10.56	0.39	0.03	0.34	1.05	0.72	0.00	0.03	34.58	0.86	45.13	0.27	0.02	93.98	0.934	0.052	0.002	0.009	0.060	0.073	0.000	0.000	2.766	0.044	3.063	7.003	
24	10.55	0.30	0.02	0.19	1.29	0.91	0.00	0.01	33.90	0.80	45.17	0.34	0.00	93.48	0.939	0.040	0.001	0.005	0.074	0.092	0.000	0.000	2.727	0.041	3.083	7.002	
25	10.28	0.29	0.03	0.21	1.36	0.83	0.04	0.02	34.02	0.87	45.34	0.26	0.02	93.56	0.912	0.038	0.002	0.006	0.077	0.084	0.002	0.000	2.729	0.044	3.086	6.980	
26	10.72	0.35	0.00	0.27	1.06	0.63	0.06	0.05	35.08	0.72	45.12	0.28	0.01	94.34	0.945	0.046	0.000	0.007	0.060	0.063	0.003	0.000	2.796	0.037	3.051	7.009	
27	10.53	0.39	0.01	0.29	0.98	0.64	0.02	0.09	35.28	0.75	45.30	0.28	0.00	94.56	0.925	0.051	0.001	0.008	0.055	0.065	0.001	0.000	2.802	0.038	3.052	6.997	
28	10.69	0.45	0.01	0.30	1.00	0.55	0.04	0.00	35.50	0.78	44.65	0.20	0.01	94.17	0.943	0.059	0.001	0.008	0.057	0.055	0.002	0.000	2.833	0.040	3.023	7.021	
29	10.60	0.27	0.03	0.16	1.39	0.94	0.02	0.03	33.35	0.92	45.53	0.18	0.01	93.44	0.943	0.036	0.002	0.004	0.079	0.096	0.001	0.000	2.682	0.047	3.106	6.996	

Sample Pat 12 (continued)

No.	K ₂ O	Na ₂ O	CaO	BaO	FeO _t	MgO	MnO	Cr ₂ O ₃	Al ₂ O ₃	TiO ₂	SiO ₂	F	Cl	Total	K	Na	Ca	Ba	Fe ²⁺	Mg	Mn	Cr	Al	Ti	Si	Total	
small crystals:																											
31	10.23	0.36	0.02	0.13	1.42	0.67	0.01	0.03	34.62	0.72	45.07	0.23	0.01	93.52	0.907	0.047	0.001	0.004	0.081	0.068	0.001	0.000	2.776	0.037	3.066	6.987	
32	10.45	0.32	0.03	0.31	1.98	0.71	0.00	0.03	34.14	0.52	44.82	0.22	0.00	93.53	0.932	0.043	0.002	0.008	0.113	0.073	0.000	0.000	2.753	0.027	3.067	7.018	
33	9.09	0.29	0.09	0.19	4.06	2.16	0.07	0.04	31.41	0.69	44.65	0.24	0.01	93.00	0.820	0.038	0.007	0.005	0.235	0.223	0.004	0.000	2.562	0.036	3.090	7.022	
34	9.40	0.30	0.08	0.19	4.33	2.14	0.05	0.03	31.53	0.57	44.27	0.23	0.01	93.11	0.850	0.040	0.006	0.005	0.251	0.221	0.003	0.000	2.578	0.029	3.071	7.055	
35	10.42	0.34	0.02	0.33	1.60	0.86	0.00	0.02	34.48	0.53	44.63	0.24	0.01	93.47	0.929	0.045	0.001	0.009	0.091	0.088	0.000	0.000	2.778	0.027	3.051	7.019	
36	10.49	0.46	0.04	0.24	1.14	0.66	0.00	0.04	35.14	0.70	44.77	0.24	0.01	93.93	0.928	0.060	0.003	0.006	0.065	0.066	0.000	0.000	2.811	0.036	3.039	7.014	
37	10.09	0.22	0.03	0.15	1.92	1.27	0.02	0.05	32.41	0.50	46.13	0.27	0.01	93.07	0.900	0.029	0.002	0.004	0.110	0.129	0.001	0.000	2.615	0.026	3.158	6.974	
38	10.66	0.32	0.05	0.20	1.39	0.98	0.01	0.06	33.81	1.06	45.91	0.32	0.01	94.78	0.936	0.041	0.004	0.005	0.078	0.099	0.001	0.000	2.686	0.054	3.094	6.998	
39	10.09	0.17	0.03	0.11	2.33	1.55	0.03	0.04	30.89	0.47	47.62	0.21	0.00	93.54	0.895	0.023	0.002	0.003	0.133	0.157	0.002	0.000	2.477	0.024	3.240	6.956	
40	10.01	0.19	0.06	0.13	2.05	1.21	0.03	0.04	32.49	0.39	47.18	0.25	0.02	94.06	0.882	0.025	0.004	0.003	0.116	0.122	0.002	0.000	2.588	0.020	3.189	6.951	
42	9.13	0.24	0.07	0.11	4.30	1.94	0.08	0.01	31.68	0.55	44.58	0.19	0.02	92.89	0.824	0.032	0.005	0.003	0.249	0.200	0.005	0.000	2.586	0.028	3.087	7.020	
43	10.39	0.23	0.03	0.18	1.67	1.08	0.01	0.00	32.67	0.52	45.76	0.27	0.00	92.81	0.930	0.030	0.002	0.005	0.096	0.111	0.001	0.000	2.645	0.027	3.143	6.989	
44	10.83	0.33	0.02	0.25	1.07	0.67	0.03	0.00	34.78	0.75	45.10	0.29	0.01	94.14	0.957	0.044	0.001	0.007	0.061	0.068	0.002	0.000	2.779	0.038	3.058	7.015	
mv	10.26	0.31	0.03	0.21	1.87	1.06	0.03	0.03	33.59	0.68	45.34	0.25	0.01	93.67	0.912	0.041	0.003	0.006	0.107	0.108	0.002	0.000	2.699	0.035	3.091	7.001	
sd	0.51	0.08	0.02	0.07	1.09	0.51	0.02	0.02	1.44	0.17	0.85	0.04	0.01	0.56	0.039	0.010	0.002	0.002	0.063	0.053	0.001	0.000	0.102	0.009	0.054	0.024	

Sample Schoef 12

No.	K ₂ O	Na ₂ O	CaO	BaO	FeO _t	MgO	MnO	Cr ₂ O ₃	Al ₂ O ₃	TiO ₂	SiO ₂	F	Cl	Total	K	Na	Ca	Ba	Fe ²⁺	Mg	Mn	Cr	Al	Ti	Si	Total	
white mica aggregates (magmatic):																											
81	10.67	0.42	0.03	0.00	1.33	0.63	0.00	0.01	34.82	0.01	45.09	0.61	0.00	93.63	0.949	0.055	0.002	0.000	0.076	0.064	0.000	0.001	2.800	0.001	3.077	7.025	
82	10.85	0.32	0.02	0.01	1.35	0.72	0.04	0.00	34.37	0.01	45.22	0.65	0.00	93.55	0.967	0.042	0.002	0.000	0.077	0.073	0.002	0.000	2.770	0.001	3.092	7.027	
83	11.00	0.27	0.01	0.00	1.50	0.74	0.02	0.00	34.56	0.05	45.28	0.67	0.00	94.10	0.976	0.036	0.001	0.000	0.085	0.075	0.001	0.000	2.774	0.003	3.083	7.034	
84	10.98	0.25	0.01	0.00	1.61	0.71	0.02	0.00	34.57	0.05	44.91	0.65	0.00	93.75	0.979	0.033	0.001	0.000	0.092	0.072	0.001	0.000	2.787	0.002	3.071	7.039	
85	10.58	0.40	0.02	0.03	1.42	0.67	0.01	0.01	34.62	0.14	45.21	0.61	0.01	93.73	0.940	0.053	0.001	0.001	0.081	0.068	0.001	0.001	2.782	0.007	3.082	7.016	
86	10.84	0.37	0.01	0.00	1.43	0.75	0.00	0.02	34.58	0.02	45.37	0.63	0.01	94.02	0.961	0.049	0.001	0.000	0.081	0.076	0.000	0.001	2.773	0.001	3.087	7.030	
87	10.74	0.32	0.04	0.00	2.02	0.79	0.00	0.00	34.26	0.13	45.08	0.63	0.01	94.02	0.956	0.043	0.003	0.000	0.115	0.081	0.000	0.000	2.757	0.006	3.077	7.037	
88	10.70	0.44	0.04	0.00	1.31	0.69	0.02	0.00	35.23	0.04	45.50	0.65	0.00	94.61	0.942	0.057	0.003	0.000	0.074	0.069	0.001	0.000	2.804	0.002	3.072	7.024	
89	10.85	0.31	0.02	0.00	1.76	0.60	0.03	0.00	34.59	0.18	44.71	0.50	0.02	93.57	0.968	0.041	0.002	0.000	0.101	0.062	0.002	0.000	2.792	0.009	3.062	7.038	
90	10.70	0.36	0.01	0.00	1.54	0.76	0.02	0.01	34.46	0.03	45.40	0.66	0.01	93.96	0.950	0.048	0.001	0.000	0.088	0.078	0.001	0.001	2.766	0.001	3.091	7.023	
91	10.73	0.40	0.02	0.02	1.51	0.80	0.01	0.02	34.62	0.05	45.32	0.68	0.00	94.17	0.951	0.052	0.001	0.000	0.086	0.081	0.001	0.001	2.774	0.003	3.081	7.030	
92	10.60	0.44	0.00	0.00	1.37	0.85	0.02	0.00	35.04	0.00	45.76	0.74	0.01	94.83	0.931	0.057	0.000	0.000	0.077	0.086	0.001	0.000	2.783	0.000	3.084	7.019	
93	10.72	0.34	0.02	0.00	1.41	0.69	0.00	0.02	35.08	0.00	45.42	0.58	0.01	94.29	0.946	0.044	0.001	0.000	0.080	0.070	0.000	0.001	2.800	0.000	3.076	7.019	
94	10.62	0.27	0.04	0.00	1.79	1.02	0.01	0.00	34.30	0.00	45.14	0.60	0.01	93.80	0.945	0.036	0.003	0.000	0.102	0.104	0.001	0.000	2.759	0.000	3.081	7.030	
95	10.90	0.22	0.02	0.00	1.73	0.78	0.04	0.01	34.40	0.04	45.22	0.63	0.00	93.99	0.969	0.029	0.002	0.000	0.099	0.079	0.002	0.001	2.765	0.002	3.083	7.031	
96	10.83	0.39	0.04	0.00	1.47	0.81	0.05	0.00	34.63	0.02	45.32	0.75	0.01	94.32	0.959	0.052	0.003	0.000	0.084	0.082	0.003	0.000	2.774	0.001	3.080	7.037	
97	10.57	0.29	0.02	0.00	1.51	0.63	0.03	0.02	34.27	0.00	44.60	0.50	0.01	92.45	0.952	0.039	0.001	0.000	0.087	0.065	0.002	0.001	2.791	0.000	3.081	7.018	
98	10.70	0.44	0.03	0.00	2.01	0.94	0.06	0.00	34.13	0.11	45.08	0.62	0.01	94.12	0.952	0.059	0.002	0.000	0.115	0.095	0.003	0.000	2.745	0.006	3.076	7.051	
99	10.66	0.46	0.02	0.00	1.42	0.76	0.00	0.00	34.80	0.12	45.70	0.64	0.00	94.59	0.939	0.061	0.002	0.000	0.080	0.077	0.000	0.000	2.771	0.006	3.087	7.021	
100	11.10	0.31	0.00	0.00	1.36	0.65	0.00	0.02	34.85	0.04	45.32	0.56	0.01	94.23	0.983	0.041	0.000	0.000	0.077	0.065	0.000	0.001	2.789	0.002	3.078	7.037	
mv	10.77	0.35	0.02	0.00	1.54	0.75	0.02	0.01	34.61	0.05	45.23	0.63	0.01	93.98	0.956	0.046	0.002	0.000	0.088	0.076	0.001	0.000	2.778	0.003	3.080	7.029	
sd	0.15	0.07	0.01	0.01	0.21	0.10	0.02	0.01	0.29	0.05	0.28	0.06	0.01	0.50	0.014	0.009	0.001	0.000	0.012	0.010	0.001	0.000	0.016	0.003	0.007	0.009	
white mica included in feldspar:																											
101	10.56	0.29	0.10	0.00	1.99	0.61	0.03	0.05	34.13	0.80	45.19	0.47	0.02	94.24	0.935	0.038	0.007	0.000	0.113	0.062	0.002	0.003	2.734	0.041	3.071	7.007	
102	10.87	0.30	0.01	0.00	1.64	0.69	0.01	0.00	34.17	0.83	45.17	0.52	0.00	94.20	0.963	0.039	0.001	0.000	0.093	0.069	0.001	0.000	2.739	0.042	3.071	7.019	
103	10.79	0.39	0.07	0.00	1.35	0.57	0.00	0.00	35.05	0.15	45.30	0.51	0.01	94.19	0.953	0.051	0.005	0.000	0.077	0.058	0.000	0.000	2.801	0.007	3.071	7.024	
very fine-grained white mica (synkinematic):																											
69	10.58	0.30	0.05	0.01	1.52	0.51	0.01	0.00	35.07	0.30	44.63	0.64	0.00	93.61	0.942	0.039	0.003	0.000	0.087	0.052	0.001	0.000	2.825	0.015	3.050	7.014	
79	10.91	0.27	0.02	0.00	1.57	0.59	0.00	0.00	34.92	0.44	45.32	0.56	0.00	94.59	0.962	0.036	0.001	0.000	0.089	0.059	0.000	0.000	2.784	0.022	3.066	7.019	

Sample Schoef 617

No.	K ₂ O	Na ₂ O	CaO	FeO _t	MgO	Al ₂ O ₃	SiO ₂	F	Total	K	Na	Ca	Fe ₂₊	Mg	Al	Si	Total
porphyroclasts, core:																	
1	9.36	0.40	0.14	3.08	0.94	30.91	44.89	0.27	89.72	0.866	0.054	0.010	0.183	0.100	2.585	3.185	6.983
2	9.70	0.40	0.11	2.21	1.00	32.37	46.77	0.35	92.56	0.864	0.053	0.008	0.127	0.101	2.608	3.197	6.958
3	9.41	0.49	0.16	2.18	0.92	31.83	45.46	0.40	90.46	0.858	0.067	0.012	0.128	0.096	2.626	3.181	6.968
5	9.37	0.42	0.09	2.43	1.12	31.27	44.96	0.56	89.65	0.864	0.057	0.007	0.144	0.118	2.607	3.180	6.977
6	9.54	0.51	0.07	2.28	1.13	31.98	44.39	0.76	89.88	0.878	0.070	0.005	0.135	0.119	2.663	3.136	7.006
7	9.85	0.59	0.07	2.13	1.09	32.08	44.40	0.60	90.20	0.905	0.081	0.005	0.126	0.115	2.667	3.131	7.029
9	9.74	0.38	0.11	2.21	0.99	32.65	46.10	0.26	92.16	0.872	0.050	0.008	0.127	0.102	2.645	3.168	6.971
10	9.89	0.40	0.07	2.23	0.99	32.76	46.83	0.48	93.16	0.876	0.052	0.005	0.126	0.100	2.625	3.183	6.969
11	9.61	0.42	0.07	2.25	0.98	33.14	47.23	0.32	93.70	0.844	0.055	0.005	0.127	0.099	2.633	3.185	6.948
12	9.83	0.39	0.08	1.97	0.98	32.84	46.98	0.60	93.07	0.870	0.051	0.006	0.112	0.099	2.629	3.190	6.957
13	10.00	0.41	0.06	2.39	1.07	32.26	46.36	0.68	92.55	0.894	0.054	0.005	0.137	0.110	2.608	3.181	6.989
14	9.64	0.40	0.09	2.42	1.09	32.21	46.42	0.33	92.28	0.862	0.054	0.007	0.139	0.112	2.607	3.187	6.968
15	9.72	0.49	0.06	2.15	1.00	32.51	46.52	0.54	92.45	0.867	0.065	0.004	0.123	0.102	2.623	3.185	6.970
16	9.86	0.42	0.08	2.20	1.04	31.94	45.93	0.42	91.47	0.891	0.056	0.006	0.128	0.107	2.611	3.185	6.984
18	9.77	0.38	0.07	2.21	0.96	32.92	46.62	0.34	92.92	0.867	0.050	0.005	0.126	0.098	2.642	3.175	6.963
19	9.90	0.47	0.06	2.30	1.11	32.52	47.14	0.53	93.50	0.874	0.061	0.004	0.131	0.112	2.597	3.195	6.975
21	9.76	0.42	0.04	2.18	0.93	32.48	45.70	0.64	91.51	0.881	0.057	0.003	0.126	0.096	2.651	3.164	6.979
23	9.63	0.41	0.07	2.35	0.96	32.62	46.08	0.64	92.12	0.863	0.055	0.005	0.135	0.098	2.644	3.169	6.968
25	10.25	0.46	0.00	2.42	1.09	32.49	46.96	0.72	93.66	0.906	0.060	0.000	0.137	0.110	2.598	3.186	6.998
26	10.12	0.38	0.02	2.46	1.04	32.60	46.49	0.50	93.11	0.900	0.051	0.002	0.140	0.106	2.622	3.172	6.992
28	10.08	0.36	0.03	2.20	0.92	33.46	47.20	0.52	94.26	0.883	0.046	0.002	0.124	0.092	2.649	3.171	6.969
29	10.07	0.47	0.04	2.39	1.09	33.02	46.73	0.29	93.80	0.889	0.062	0.003	0.135	0.110	2.634	3.163	6.995
30	10.07	0.36	0.04	2.21	0.92	32.88	46.57	0.56	93.04	0.894	0.047	0.003	0.126	0.093	2.640	3.173	6.977
mv	9.79	0.43	0.07	2.30	1.01	32.42	46.21	0.49	92.23	0.877	0.057	0.005	0.132	0.104	2.627	3.176	6.978
sd	0.24	0.06	0.04	0.21	0.07	0.58	0.86	0.15	1.40	0.016	0.008	0.003	0.013	0.008	0.022	0.016	0.018
porphyroclasts, rim:																	
4	9.61	0.43	0.06	2.41	1.09	32.37	46.04	0.47	92.01	0.863	0.058	0.005	0.139	0.112	2.628	3.171	6.975
8	9.91	0.45	0.09	2.20	1.00	32.23	45.13	0.21	91.01	0.901	0.061	0.007	0.128	0.104	2.652	3.151	7.005
17	9.75	0.35	0.10	2.10	1.02	32.37	47.30	0.63	93.00	0.863	0.047	0.007	0.120	0.103	2.592	3.213	6.945
20	9.66	0.38	0.08	2.39	1.15	32.22	46.66	0.68	92.53	0.862	0.051	0.006	0.137	0.117	2.599	3.193	6.964
24	10.46	0.22	0.01	2.50	1.12	31.76	46.27	0.76	92.33	0.940	0.030	0.001	0.144	0.115	2.582	3.191	7.003
27	9.78	0.36	0.09	2.35	1.07	32.77	47.59	0.64	94.00	0.858	0.047	0.006	0.132	0.108	2.599	3.202	6.951
mv	9.86	0.37	0.07	2.32	1.07	32.29	46.50	0.56	92.48	0.881	0.049	0.005	0.133	0.110	2.609	3.187	6.974
sd	0.31	0.08	0.03	0.14	0.06	0.33	0.89	0.20	1.00	0.033	0.011	0.002	0.009	0.006	0.026	0.023	0.025

Sample Tit 125

No.	K ₂ O	Na ₂ O	CaO	BaO	FeO _i	MgO	MnO	Cr ₂ O ₃	Al ₂ O ₃	TiO ₂	SiO ₂	F	Total	K	Na	Ca	Ba	Fe ²⁺	Mg	Mn	Cr	Al	Ti	Si	Total	
porphyroclasts, core:																										
2	10.74	0.37	0.02	0.01	2.94	0.63	0.07	0.04	34.02	0.48	46.45	1.01	96.76	0.935	0.048	0.001	0.000	0.164	0.062	0.004	0.002	2.679	0.024	3.103	7.024	
3	10.90	0.42	0.01	0.00	2.92	0.55	0.06	0.00	34.37	0.36	46.59	0.70	96.86	0.946	0.054	0.001	0.000	0.162	0.054	0.003	0.000	2.696	0.018	3.100	7.034	
4	10.84	0.57	0.00	0.03	2.74	0.60	0.09	0.00	34.49	0.40	46.17	0.90	96.83	0.943	0.073	0.000	0.001	0.153	0.060	0.005	0.000	2.713	0.020	3.081	7.050	
5	10.90	0.43	0.00	0.00	2.61	0.54	0.08	0.07	34.04	0.53	45.84	0.92	95.96	0.957	0.056	0.000	0.000	0.147	0.054	0.005	0.003	2.703	0.027	3.087	7.039	
6	11.11	0.38	0.00	0.01	2.75	0.50	0.06	0.02	33.86	0.44	45.40	1.01	95.54	0.983	0.049	0.000	0.000	0.156	0.050	0.004	0.001	2.709	0.022	3.082	7.057	
16	10.91	0.46	0.02	0.00	2.92	0.60	0.11	0.01	34.03	0.46	46.41	1.01	96.92	0.950	0.059	0.001	0.000	0.163	0.059	0.006	0.000	2.679	0.023	3.100	7.042	
17	10.75	0.49	0.03	0.07	2.83	0.62	0.10	0.00	34.37	0.40	47.01	0.85	97.53	0.926	0.062	0.002	0.002	0.156	0.061	0.006	0.000	2.680	0.020	3.109	7.025	
18	10.83	0.46	0.01	0.00	2.87	0.58	0.07	0.00	34.36	0.49	46.35	0.59	96.63	0.941	0.060	0.001	0.000	0.160	0.058	0.004	0.000	2.699	0.025	3.089	7.037	
36	10.51	0.49	0.00	0.01	2.68	0.63	0.06	0.00	34.38	0.42	46.55	0.86	96.59	0.913	0.064	0.000	0.000	0.149	0.062	0.003	0.000	2.701	0.021	3.102	7.015	
37	10.65	0.52	0.00	0.00	2.50	0.61	0.06	0.00	34.34	0.41	46.80	1.10	96.99	0.923	0.067	0.000	0.000	0.139	0.061	0.003	0.000	2.691	0.020	3.112	7.017	
mv	10.81	0.46	0.01	0.01	2.78	0.58	0.08	0.01	34.23	0.44	46.36	0.89	96.66	0.942	0.059	0.001	0.000	0.155	0.058	0.004	0.001	2.695	0.022	3.097	7.034	
sd	0.16	0.06	0.01	0.02	0.15	0.04	0.02	0.02	0.22	0.05	0.46	0.15	0.56	0.020	0.008	0.001	0.001	0.008	0.004	0.001	0.001	0.012	0.003	0.011	0.014	
porphyroclasts, rim:																										
1	10.74	0.32	0.01	0.01	3.19	0.62	0.08	0.00	33.52	0.40	46.52	0.88	96.29	0.939	0.041	0.001	0.000	0.179	0.062	0.004	0.000	2.652	0.020	3.122	7.022	
7	10.58	0.31	0.00	0.02	3.08	0.55	0.03	0.00	33.29	0.44	46.41	0.83	95.55	0.930	0.041	0.000	0.001	0.174	0.056	0.002	0.000	2.649	0.022	3.133	7.006	
15	10.73	0.38	0.01	0.00	2.80	0.65	0.08	0.03	33.41	0.73	47.05	1.16	97.02	0.932	0.049	0.001	0.000	0.156	0.065	0.004	0.002	2.624	0.036	3.136	7.006	
19	10.76	0.39	0.00	0.00	3.02	0.54	0.09	0.00	34.25	0.41	46.68	1.54	97.67	0.933	0.050	0.000	0.000	0.168	0.053	0.005	0.000	2.686	0.021	3.106	7.022	
35	11.09	0.35	0.00	0.03	2.80	0.57	0.10	0.00	34.10	0.43	46.51	1.05	97.02	0.965	0.045	0.000	0.001	0.156	0.057	0.006	0.000	2.683	0.021	3.104	7.038	
38	10.98	0.43	0.01	0.00	2.56	0.58	0.07	0.00	34.13	0.53	46.38	0.99	96.67	0.957	0.056	0.001	0.000	0.143	0.057	0.004	0.000	2.689	0.027	3.101	7.034	
mv	10.81	0.36	0.01	0.01	2.91	0.59	0.07	0.01	33.78	0.49	46.59	1.08	96.70	0.943	0.047	0.000	0.000	0.163	0.058	0.004	0.000	2.664	0.025	3.117	7.021	
sd	0.19	0.05	0.01	0.01	0.23	0.04	0.02	0.01	0.42	0.12	0.25	0.26	0.73	0.014	0.006	0.000	0.000	0.013	0.004	0.001	0.001	0.026	0.006	0.015	0.013	
cleavage domains:																										
8	11.06	0.30	0.01	0.00	3.09	0.54	0.03	0.03	33.94	0.21	47.05	0.96	97.23	0.959	0.038	0.001	0.000	0.172	0.054	0.002	0.002	2.661	0.011	3.129	7.027	
9	10.85	0.27	0.00	0.00	3.20	0.64	0.08	0.01	33.23	0.32	45.96	1.07	95.62	0.959	0.036	0.000	0.000	0.182	0.065	0.005	0.000	2.657	0.016	3.117	7.036	
10	10.79	0.39	0.10	0.00	3.33	0.66	0.09	0.01	32.97	0.36	46.58	1.11	96.39	0.947	0.050	0.007	0.000	0.187	0.066	0.005	0.001	2.617	0.018	3.136	7.035	
11	10.67	0.36	0.07	0.00	3.76	0.67	0.08	0.00	32.00	0.36	46.85	1.32	96.13	0.942	0.047	0.005	0.000	0.213	0.067	0.005	0.000	2.555	0.018	3.173	7.025	
12	11.01	0.22	0.04	0.00	3.63	0.64	0.10	0.08	32.76	0.54	46.64	1.16	96.81	0.965	0.028	0.003	0.000	0.204	0.064	0.006	0.004	2.596	0.027	3.136	7.033	
13	10.84	0.29	0.01	0.00	3.45	0.69	0.14	0.00	32.99	0.47	48.13	0.94	97.94	0.932	0.037	0.001	0.000	0.191	0.068	0.008	0.000	2.566	0.023	3.176	7.002	
14	10.25	0.18	0.04	0.02	3.27	0.63	0.08	0.04	32.96	0.07	46.35	0.94	94.84	0.909	0.024	0.003	0.001	0.186	0.064	0.005	0.002	2.641	0.004	3.151	6.990	
20	11.01	0.21	0.06	0.00	3.76	0.73	0.10	0.02	31.53	0.23	47.21	1.09	95.94	0.973	0.027	0.004	0.000	0.213	0.073	0.006	0.001	2.519	0.012	3.200	7.028	
22	10.63	0.34	0.01	0.00	3.06	0.54	0.07	0.04	33.50	0.45	45.93	1.03	95.57	0.938	0.044	0.001	0.000	0.173	0.054	0.004	0.002	2.673	0.023	3.109	7.021	
26	10.92	0.32	0.00	0.02	2.68	0.44	0.10	0.00	34.42	0.04	46.95	0.92	96.80	0.948	0.042	0.000	0.001	0.149	0.043	0.005	0.000	2.701	0.002	3.126	7.017	
27	10.78	0.41	0.05	0.01	3.02	0.48	0.08	0.00	34.13	0.03	47.30	0.92	97.20	0.932	0.053	0.003	0.000	0.168	0.047	0.005	0.000	2.669	0.002	3.139	7.018	
28	11.10	0.29	0.01	0.00	2.79	0.55	0.04	0.00	33.85	0.48	46.91	1.10	97.10	0.964	0.037	0.000	0.000	0.155	0.055	0.002	0.000	2.659	0.024	3.126	7.022	
29	11.11	0.27	0.01	0.00	3.65	0.71	0.08	0.00	32.17	0.44	46.51	1.24	96.20	0.982	0.035	0.001	0.000	0.207	0.072	0.005	0.000	2.571	0.023	3.153	7.047	

Sample Tit 125 (continued)

No.	K ₂ O	Na ₂ O	CaO	BaO	FeO _t	MgO	MnO	Cr ₂ O ₃	Al ₂ O ₃	TiO ₂	SiO ₂	F	Total	K	Na	Ca	Ba	Fe ²⁺	Mg	Mn	Cr	Al	Ti	Si	Total	
cleavage domains:																										
30	10.92	0.38	0.02	0.00	2.68	0.57	0.09	0.02	33.66	0.43	46.94	1.01	96.71	0.950	0.049	0.001	0.000	0.149	0.057	0.005	0.001	2.649	0.022	3.134	7.019	
31	10.85	0.34	0.00	0.00	2.86	0.59	0.06	0.00	33.67	0.45	46.68	0.79	96.29	0.947	0.045	0.000	0.000	0.160	0.059	0.003	0.000	2.657	0.023	3.125	7.019	
32	10.69	0.42	0.01	0.05	2.68	0.55	0.09	0.02	33.82	0.51	45.90	0.90	95.65	0.940	0.055	0.001	0.001	0.151	0.055	0.005	0.001	2.691	0.026	3.099	7.027	
33	11.14	0.23	0.01	0.00	3.52	0.66	0.10	0.00	33.07	0.48	46.79	1.37	97.38	0.972	0.029	0.001	0.000	0.197	0.066	0.006	0.000	2.610	0.024	3.133	7.039	
34	10.87	0.27	0.00	0.00	3.38	0.74	0.12	0.03	32.97	0.29	46.84	0.88	96.38	0.952	0.035	0.000	0.000	0.190	0.074	0.007	0.001	2.609	0.015	3.145	7.028	
39	11.06	0.24	0.01	0.00	3.03	0.58	0.11	0.02	33.12	0.49	46.79	0.99	96.44	0.968	0.031	0.001	0.000	0.170	0.058	0.006	0.001	2.621	0.025	3.141	7.022	
40	10.43	0.32	0.01	0.00	2.84	0.61	0.08	0.00	33.66	0.48	46.97	1.12	96.51	0.908	0.041	0.000	0.000	0.159	0.060	0.005	0.000	2.651	0.024	3.138	6.987	
41	10.61	0.29	0.01	0.01	2.73	0.59	0.07	0.03	33.96	0.48	46.74	1.40	96.92	0.923	0.038	0.001	0.000	0.152	0.058	0.004	0.001	2.673	0.024	3.122	6.997	
42	10.99	0.23	0.00	0.01	3.55	0.62	0.10	0.04	32.56	0.38	46.28	0.88	95.63	0.972	0.030	0.000	0.000	0.201	0.063	0.006	0.002	2.604	0.020	3.140	7.038	
43	10.56	0.23	0.01	0.00	3.06	0.51	0.09	0.00	34.33	0.33	47.91	1.12	98.15	0.904	0.029	0.001	0.000	0.168	0.050	0.005	0.000	2.657	0.016	3.146	6.975	
44	10.90	0.30	0.02	0.02	3.31	0.59	0.08	0.01	33.23	0.25	46.73	0.59	96.03	0.954	0.039	0.001	0.001	0.186	0.059	0.004	0.001	2.631	0.012	3.140	7.029	
45	10.40	0.40	0.02	0.02	2.91	0.50	0.07	0.00	34.40	0.33	46.66	1.12	96.83	0.903	0.052	0.002	0.001	0.162	0.049	0.004	0.000	2.702	0.016	3.109	7.001	
46	9.67	0.30	0.05	0.00	3.03	0.49	0.08	0.00	34.71	0.28	47.35	1.01	96.96	0.833	0.039	0.004	0.000	0.168	0.048	0.004	0.000	2.704	0.014	3.129	6.941	
47	8.94	0.24	0.03	0.00	2.90	0.51	0.07	0.00	35.29	0.37	48.03	1.46	97.82	0.761	0.030	0.002	0.000	0.158	0.050	0.004	0.000	2.718	0.018	3.139	6.880	
mv	10.70	0.30	0.02	0.01	3.15	0.59	0.08	0.01	33.44	0.35	46.85	1.05	96.57	0.935	0.039	0.002	0.000	0.177	0.059	0.005	0.001	2.639	0.018	3.137	7.011	
sd	0.48	0.07	0.02	0.01	0.34	0.08	0.02	0.02	0.85	0.14	0.56	0.19	0.78	0.046	0.009	0.002	0.000	0.020	0.008	0.001	0.001	0.049	0.007	0.021	0.035	

Sample Tit 711

No.	K ₂ O	Na ₂ O	CaO	BaO	FeO _i	MgO	MnO	Cr ₂ O ₃	Al ₂ O ₃	TiO ₂	SiO ₂	F	Total	K	Na	Ca	Ba	Fe ²⁺	Mg	Mn	Cr	Al	Ti	Si	Total	
large porphyroclasts, core:																										
2	10.63	0.27	0.05	0.08	4.25	1.06	0.05	0.01	30.04	0.67	45.85	0.00	92.95	0.963	0.037	0.003	0.002	0.247	0.110	0.003	0.000	2.461	0.035	3.187	7.047	
3	11.00	0.30	0.01	0.03	4.42	1.12	0.08	0.00	30.43	0.83	47.02	0.13	95.37	0.974	0.039	0.001	0.001	0.251	0.113	0.005	0.000	2.436	0.042	3.193	7.054	
4	10.84	0.24	0.05	0.01	4.19	1.13	0.05	0.03	30.23	1.02	47.29	0.40	95.48	0.959	0.032	0.003	0.000	0.237	0.114	0.003	0.000	2.417	0.052	3.208	7.026	
5	10.89	0.28	0.03	0.00	4.31	1.09	0.07	0.00	30.24	1.01	46.70	0.00	94.61	0.970	0.036	0.002	0.000	0.246	0.111	0.004	0.000	2.434	0.052	3.189	7.045	
6	10.96	0.28	0.05	0.03	4.44	1.17	0.04	0.01	30.72	0.46	46.95	0.06	95.18	0.971	0.037	0.004	0.001	0.252	0.119	0.002	0.000	2.460	0.024	3.190	7.060	
7	10.99	0.27	0.05	0.00	4.72	1.15	0.03	0.01	31.23	0.58	47.32	0.19	96.54	0.961	0.036	0.003	0.000	0.265	0.115	0.002	0.000	2.470	0.029	3.176	7.058	
8	10.82	0.25	0.04	0.06	4.84	1.13	0.08	0.01	30.87	0.57	47.76	0.17	96.58	0.945	0.033	0.003	0.001	0.271	0.113	0.004	0.000	2.439	0.029	3.201	7.039	
9	10.74	0.31	0.07	0.01	4.47	1.24	0.00	0.00	30.60	0.46	46.73	0.37	95.00	0.955	0.041	0.005	0.000	0.255	0.126	0.000	0.000	2.461	0.024	3.188	7.056	
10	10.85	0.27	0.08	0.01	4.76	1.22	0.01	0.00	30.81	0.52	47.70	0.00	96.22	0.949	0.036	0.005	0.000	0.267	0.122	0.000	0.000	2.437	0.026	3.202	7.046	
12	10.94	0.22	0.04	0.05	4.72	1.10	0.10	0.00	29.76	0.42	45.69	0.06	93.09	0.995	0.029	0.003	0.001	0.275	0.114	0.006	0.000	2.447	0.022	3.187	7.080	
19	10.82	0.23	0.01	0.03	4.65	1.15	0.01	0.01	29.65	0.44	45.92	0.50	93.40	0.983	0.031	0.001	0.001	0.271	0.119	0.001	0.000	2.436	0.023	3.201	7.065	
20	10.74	0.21	0.00	0.02	4.32	1.12	0.05	0.00	30.02	0.46	46.53	0.33	93.79	0.967	0.028	0.000	0.000	0.249	0.115	0.003	0.000	2.443	0.024	3.212	7.040	
21	10.87	0.25	0.00	0.00	4.59	1.08	0.05	0.03	30.17	0.53	47.09	0.27	94.93	0.967	0.034	0.000	0.000	0.262	0.110	0.003	0.000	2.428	0.027	3.215	7.045	
22	10.88	0.26	0.01	0.00	4.80	1.16	0.04	0.00	30.33	0.55	47.02	0.35	95.40	0.966	0.034	0.001	0.000	0.273	0.117	0.003	0.000	2.433	0.028	3.200	7.055	
23	10.69	0.29	0.01	0.01	4.45	1.17	0.07	0.01	29.78	0.53	46.76	0.19	93.97	0.959	0.039	0.001	0.000	0.256	0.120	0.004	0.000	2.417	0.027	3.219	7.044	
24	10.68	0.31	0.01	0.02	4.66	1.13	0.08	0.02	30.62	0.47	46.93	0.44	95.35	0.947	0.040	0.001	0.000	0.265	0.115	0.004	0.000	2.456	0.024	3.194	7.048	
27	10.82	0.27	0.01	0.00	4.44	1.14	0.01	0.03	30.39	0.67	46.81	0.31	94.90	0.963	0.035	0.001	0.000	0.254	0.116	0.000	0.000	2.446	0.034	3.196	7.046	
29	10.99	0.26	0.00	0.06	4.35	1.07	0.03	0.10	30.84	0.64	46.85	0.10	95.31	0.973	0.034	0.000	0.002	0.247	0.108	0.002	0.000	2.470	0.033	3.183	7.052	
36	10.73	0.23	0.01	0.00	4.59	1.19	0.08	0.00	29.95	0.48	44.43	0.15	91.82	0.990	0.031	0.000	0.000	0.271	0.125	0.005	0.000	2.499	0.026	3.144	7.091	
37	10.56	0.26	0.00	0.00	4.66	1.19	0.07	0.00	29.46	0.78	43.98	0.21	91.16	0.982	0.036	0.000	0.000	0.278	0.126	0.004	0.000	2.479	0.042	3.140	7.088	
38	10.60	0.29	0.01	0.00	4.62	1.22	0.03	0.05	29.19	0.75	44.81	0.23	91.78	0.979	0.039	0.000	0.000	0.273	0.128	0.002	0.000	2.438	0.040	3.175	7.075	
39	10.54	0.26	0.02	0.03	4.75	1.23	0.08	0.00	29.38	0.60	44.80	0.33	92.03	0.972	0.036	0.001	0.001	0.281	0.130	0.005	0.000	2.450	0.032	3.170	7.077	
62	11.01	0.31	0.00	0.03	4.55	1.15	0.04	0.01	30.49	0.61	46.98	0.21	95.40	0.975	0.041	0.000	0.001	0.259	0.117	0.003	0.000	2.443	0.031	3.193	7.063	
63	10.60	0.42	0.03	0.00	4.63	1.27	0.08	0.00	30.58	1.03	47.45	0.23	96.32	0.929	0.055	0.002	0.000	0.260	0.127	0.004	0.000	2.422	0.052	3.188	7.040	
68	10.81	0.21	0.00	0.00	4.71	1.15	0.02	0.00	30.74	0.57	47.42	0.19	95.81	0.951	0.028	0.000	0.000	0.266	0.115	0.001	0.000	2.446	0.029	3.201	7.037	
69	10.30	0.17	0.01	0.01	4.61	1.15	0.03	0.01	31.11	0.65	47.86	0.42	96.33	0.899	0.022	0.001	0.000	0.258	0.115	0.002	0.000	2.457	0.033	3.206	6.993	
70	9.11	0.13	0.01	0.03	4.83	1.18	0.08	0.02	31.75	0.62	48.75	0.31	96.83	0.785	0.017	0.001	0.001	0.267	0.116	0.005	0.000	2.472	0.031	3.220	6.914	
82	11.03	0.33	0.01	0.05	4.45	1.20	0.04	0.04	30.46	0.57	47.49	0.63	96.29	0.972	0.043	0.001	0.001	0.252	0.121	0.002	0.000	2.427	0.029	3.209	7.056	
83	11.08	0.36	0.00	0.05	4.76	1.08	0.07	0.04	30.74	0.97	46.78	0.13	96.05	0.977	0.047	0.000	0.001	0.269	0.109	0.004	0.000	2.451	0.049	3.165	7.073	
86	10.98	0.32	0.00	0.00	4.65	1.07	0.09	0.02	31.06	0.71	46.37	0.31	95.59	0.973	0.043	0.000	0.000	0.265	0.109	0.005	0.000	2.489	0.036	3.154	7.073	
87	11.02	0.35	0.00	0.05	4.68	1.15	0.01	0.04	30.74	0.79	46.56	0.34	95.72	0.977	0.046	0.000	0.001	0.266	0.116	0.001	0.000	2.463	0.041	3.165	7.075	
88	10.87	0.31	0.00	0.01	4.75	1.14	0.06	0.00	30.84	0.64	46.64	0.42	95.66	0.963	0.040	0.000	0.000	0.270	0.115	0.003	0.000	2.471	0.032	3.170	7.064	
90	10.85	0.39	0.00	0.00	4.54	1.24	0.06	0.00	30.78	0.86	47.60	0.50	96.82	0.948	0.051	0.000	0.000	0.255	0.124	0.003	0.000	2.432	0.043	3.192	7.048	
91	10.94	0.28	0.00	0.00	4.74	1.19	0.02	0.00	30.86	1.00	47.47	0.21	96.72	0.956	0.037	0.000	0.000	0.265	0.119	0.001	0.000	2.437	0.050	3.181	7.047	
92	11.01	0.32	0.00	0.04	4.86	1.23	0.05	0.00	30.72	0.39	47.18	0.33	96.14	0.970	0.042	0.000	0.001	0.275	0.124	0.003	0.000	2.448	0.020	3.190	7.073	

Sample Tit 711 (continued)

No.	K ₂ O	Na ₂ O	CaO	BaO	FeO _t	MgO	MnO	Cr ₂ O ₃	Al ₂ O ₃	TiO ₂	SiO ₂	F	Total	K	Na	Ca	Ba	Fe ²⁺	Mg	Mn	Cr	Al	Ti	Si	Total	
large porphyroclasts, core:																										
98	10.85	0.32	0.03	0.00	4.97	1.16	0.05	0.01	30.53	0.92	46.85	0.31	96.00	0.958	0.042	0.002	0.000	0.282	0.117	0.003	0.000	2.437	0.047	3.173	7.062	
mv	10.78	0.28	0.02	0.02	4.60	1.16	0.05	0.01	30.45	0.66	46.73	0.26	95.01	0.959	0.037	0.001	0.001	0.263	0.118	0.003	0.000	2.449	0.034	3.188	7.051	
sd	0.33	0.06	0.02	0.02	0.18	0.05	0.03	0.02	0.55	0.19	0.99	0.15	1.55	0.035	0.007	0.002	0.001	0.011	0.006	0.002	0.000	0.019	0.010	0.019	0.030	
large porphyroclasts, rim:																										
1	9.92	0.28	0.04	0.00	4.35	1.05	0.07	0.02	30.66	0.64	46.61	0.17	93.80	0.887	0.037	0.003	0.000	0.250	0.107	0.004	0.000	2.478	0.033	3.196	6.994	
11	10.75	0.24	0.05	0.00	4.46	1.20	0.05	0.02	30.06	0.38	46.85	0.31	94.37	0.962	0.032	0.004	0.000	0.256	0.122	0.003	0.000	2.432	0.019	3.216	7.046	
13	10.86	0.20	0.03	0.05	5.20	1.14	0.10	0.00	29.65	0.14	46.35	0.39	94.11	0.981	0.027	0.002	0.001	0.301	0.118	0.006	0.000	2.421	0.008	3.211	7.075	
18	10.57	0.12	0.02	0.00	4.38	1.16	0.11	0.04	26.52	0.99	43.05	0.38	87.33	1.031	0.017	0.001	0.000	0.274	0.130	0.007	0.000	2.339	0.056	3.222	7.077	
25	11.10	0.17	0.01	0.01	3.97	1.07	0.04	0.00	30.56	0.44	46.66	0.23	94.26	0.993	0.023	0.001	0.000	0.228	0.110	0.002	0.000	2.470	0.022	3.200	7.049	
26	10.63	0.21	0.04	0.04	4.96	1.20	0.07	0.01	30.63	0.54	47.25	0.27	95.84	0.937	0.028	0.003	0.001	0.281	0.121	0.004	0.000	2.441	0.028	3.196	7.038	
28	10.64	0.27	0.02	0.00	4.26	1.24	0.02	0.00	30.47	0.61	46.97	0.23	94.72	0.945	0.035	0.002	0.000	0.243	0.126	0.001	0.000	2.448	0.031	3.202	7.033	
35	10.79	0.17	0.03	0.10	4.68	1.14	0.02	0.00	30.40	0.53	44.37	0.23	92.45	0.991	0.023	0.002	0.003	0.276	0.119	0.001	0.000	2.524	0.028	3.125	7.092	
61	10.93	0.28	0.00	0.00	4.80	1.10	0.08	0.00	30.43	0.72	46.56	0.15	95.05	0.973	0.037	0.000	0.000	0.274	0.112	0.004	0.000	2.449	0.037	3.179	7.065	
64	10.57	0.34	0.07	0.03	4.39	1.18	0.04	0.03	30.33	0.85	46.81	0.02	94.64	0.939	0.044	0.005	0.001	0.250	0.119	0.002	0.000	2.438	0.044	3.193	7.036	
67	10.98	0.26	0.00	0.00	4.36	1.09	0.08	0.00	31.38	0.68	47.04	0.23	96.10	0.963	0.033	0.000	0.000	0.245	0.109	0.005	0.000	2.491	0.035	3.168	7.050	
81	11.10	0.18	0.00	0.03	4.47	1.07	0.02	0.03	31.00	0.61	47.40	0.17	96.07	0.974	0.023	0.000	0.001	0.252	0.108	0.001	0.000	2.461	0.031	3.193	7.044	
84	11.08	0.31	0.02	0.00	4.44	1.24	0.05	0.00	30.84	0.43	47.41	0.40	96.22	0.974	0.040	0.002	0.000	0.250	0.124	0.003	0.000	2.451	0.022	3.197	7.063	
85	10.97	0.26	0.01	0.00	4.62	0.95	0.09	0.00	31.26	0.83	46.70	0.52	96.22	0.967	0.034	0.001	0.000	0.261	0.096	0.005	0.000	2.492	0.042	3.157	7.055	
89	11.15	0.26	0.01	0.00	4.56	1.09	0.06	0.06	30.83	0.67	46.99	0.19	95.88	0.984	0.034	0.000	0.000	0.258	0.110	0.003	0.000	2.460	0.034	3.181	7.065	
mv	10.80	0.23	0.02	0.02	4.53	1.13	0.06	0.01	30.33	0.60	46.47	0.26	94.47	0.967	0.031	0.002	0.000	0.260	0.115	0.004	0.000	2.453	0.031	3.189	7.052	
sd	0.32	0.06	0.02	0.03	0.30	0.08	0.03	0.02	1.14	0.21	1.19	0.12	2.26	0.032	0.008	0.001	0.001	0.018	0.009	0.002	0.000	0.041	0.011	0.025	0.023	
small porphyroclasts:																										
14	9.85	0.24	0.04	0.00	4.47	1.08	0.04	0.00	30.77	0.45	46.83	0.25	94.01	0.878	0.032	0.003	0.000	0.255	0.110	0.002	0.000	2.481	0.023	3.203	6.988	
15	10.71	0.25	0.05	0.02	4.54	1.14	0.04	0.00	30.01	0.65	46.52	0.15	94.10	0.960	0.033	0.004	0.001	0.261	0.117	0.002	0.000	2.433	0.034	3.200	7.046	
16	10.95	0.22	0.03	0.00	4.56	1.13	0.07	0.02	30.13	0.60	46.26	0.35	94.32	0.983	0.029	0.002	0.000	0.263	0.116	0.004	0.000	2.447	0.031	3.188	7.064	
17	11.01	0.26	0.07	0.06	4.94	1.16	0.00	0.00	30.05	0.38	45.88	0.21	94.00	0.994	0.035	0.005	0.002	0.286	0.119	0.000	0.000	2.453	0.020	3.177	7.091	
30	10.40	0.28	0.04	0.08	4.23	1.13	0.06	0.00	30.92	0.40	47.29	0.33	95.16	0.919	0.037	0.003	0.002	0.240	0.115	0.003	0.000	2.471	0.020	3.206	7.016	
31	10.62	0.20	0.04	0.00	4.83	1.14	0.04	0.00	30.27	0.31	46.89	0.10	94.44	0.948	0.027	0.003	0.000	0.277	0.117	0.002	0.000	2.442	0.016	3.210	7.041	
32	10.90	0.24	0.01	0.04	6.24	1.22	0.04	0.00	29.29	0.35	45.52	0.21	94.05	0.991	0.032	0.001	0.001	0.364	0.127	0.002	0.000	2.407	0.018	3.174	7.116	
33	10.86	0.25	0.03	0.03	4.28	1.12	0.03	0.00	30.77	0.30	46.07	0.25	93.98	0.975	0.033	0.002	0.001	0.247	0.115	0.002	0.000	2.499	0.015	3.175	7.064	
34	10.76	0.32	0.03	0.02	4.57	1.09	0.00	0.04	30.36	0.58	46.40	0.13	94.27	0.963	0.042	0.002	0.000	0.262	0.111	0.000	0.000	2.458	0.030	3.187	7.057	
47	11.15	0.21	0.00	0.00	4.44	0.98	0.04	0.00	30.53	0.98	46.74	0.25	95.33	0.989	0.028	0.000	0.000	0.253	0.099	0.002	0.000	2.449	0.050	3.181	7.053	
48	10.69	0.22	0.00	0.00	5.04	1.38	0.07	0.03	28.72	0.38	48.84	0.38	95.73	0.943	0.029	0.000	0.000	0.285	0.139	0.004	0.000	2.291	0.020	3.305	7.015	
49	10.77	0.27	0.01	0.00	4.39	1.07	0.06	0.02	31.55	0.39	47.15	0.25	95.94	0.946	0.036	0.000	0.000	0.247	0.108	0.004	0.000	2.505	0.020	3.176	7.042	
50	9.87	0.22	0.04	0.03	4.60	1.07	0.02	0.00	30.34	0.41	46.72	0.17	93.49	0.886	0.029	0.003	0.001	0.264	0.110	0.001	0.000	2.461	0.021	3.215	6.991	
51	11.25	0.22	0.00	0.02	4.81	1.14	0.07	0.00	30.74	0.28	47.14	0.46	96.12	0.993	0.029	0.000	0.001	0.272	0.115	0.004	0.000	2.455	0.014	3.193	7.076	

Sample Tit 711 (continued)

No.	K ₂ O	Na ₂ O	CaO	BaO	FeO _t	MgO	MnO	Cr ₂ O ₃	Al ₂ O ₃	TiO ₂	SiO ₂	F	Total	K	Na	Ca	Ba	Fe ²⁺	Mg	Mn	Cr	Al	Ti	Si	Total	
small porphyroclasts:																										
52	10.93	0.37	0.01	0.00	4.55	1.13	0.07	0.04	30.43	0.65	47.35	0.08	95.60	0.964	0.048	0.001	0.000	0.258	0.114	0.004	0.000	2.428	0.033	3.205	7.054	
53	10.76	0.29	0.00	0.02	4.71	1.17	0.04	0.00	30.40	0.53	46.73	0.44	95.08	0.958	0.038	0.000	0.000	0.269	0.119	0.002	0.000	2.448	0.027	3.192	7.054	
54	11.31	0.24	0.00	0.01	4.45	1.13	0.04	0.00	31.57	0.36	47.63	0.29	97.02	0.985	0.031	0.000	0.000	0.249	0.112	0.002	0.000	2.486	0.018	3.182	7.065	
55	11.02	0.30	0.00	0.00	4.54	1.09	0.03	0.01	30.48	0.85	46.60	0.27	95.19	0.980	0.039	0.000	0.000	0.259	0.111	0.002	0.000	2.451	0.044	3.178	7.063	
56	10.81	0.29	0.01	0.00	4.55	1.15	0.03	0.00	30.52	0.70	46.47	0.46	94.98	0.964	0.038	0.000	0.000	0.260	0.117	0.002	0.000	2.460	0.036	3.179	7.056	
57	10.85	0.25	0.00	0.00	4.33	1.07	0.04	0.03	30.45	0.84	46.39	0.29	94.54	0.970	0.033	0.000	0.000	0.248	0.109	0.002	0.000	2.461	0.043	3.181	7.047	
58	10.91	0.21	0.00	0.00	4.55	1.08	0.07	0.00	31.02	0.61	47.48	0.44	96.35	0.956	0.027	0.000	0.000	0.256	0.108	0.004	0.000	2.460	0.031	3.194	7.037	
59	11.05	0.26	0.00	0.00	4.50	1.15	0.05	0.00	30.71	0.65	46.87	0.17	95.40	0.978	0.034	0.000	0.000	0.255	0.117	0.003	0.000	2.458	0.033	3.183	7.061	
65	11.06	0.28	0.00	0.05	4.62	1.14	0.09	0.00	30.57	0.57	46.72	0.00	95.10	0.982	0.037	0.000	0.001	0.263	0.116	0.005	0.000	2.455	0.029	3.182	7.070	
66	10.77	0.24	0.00	0.03	5.03	1.23	0.03	0.01	30.61	0.43	47.34	0.37	96.09	0.949	0.032	0.000	0.001	0.284	0.124	0.001	0.000	2.438	0.022	3.199	7.050	
73	10.75	0.22	0.01	0.00	4.77	1.08	0.06	0.00	31.23	0.74	47.60	0.36	96.81	0.938	0.029	0.001	0.000	0.267	0.107	0.003	0.000	2.463	0.037	3.185	7.030	
74	11.10	0.24	0.01	0.00	4.53	1.06	0.05	0.00	30.97	0.67	47.04	0.17	95.84	0.978	0.031	0.001	0.000	0.256	0.106	0.003	0.000	2.468	0.034	3.180	7.057	
75	10.97	0.19	0.02	0.00	4.65	1.01	0.06	0.00	30.80	0.41	46.33	0.33	94.78	0.980	0.025	0.001	0.000	0.267	0.103	0.003	0.000	2.488	0.021	3.174	7.063	
76	10.95	0.32	0.08	0.05	4.70	1.20	0.05	0.00	31.25	0.42	47.74	0.04	96.78	0.953	0.041	0.006	0.001	0.262	0.119	0.003	0.000	2.461	0.021	3.189	7.056	
77	11.36	0.23	0.00	0.03	4.64	1.10	0.04	0.00	31.32	0.53	47.03	0.42	96.70	0.997	0.030	0.000	0.001	0.261	0.111	0.002	0.000	2.485	0.027	3.166	7.078	
78	11.22	0.31	0.00	0.02	4.51	1.11	0.00	0.02	30.43	1.29	46.85	0.06	95.82	0.990	0.040	0.000	0.000	0.256	0.112	0.000	0.000	2.428	0.066	3.172	7.064	
79	11.25	0.24	0.00	0.00	4.58	1.10	0.04	0.02	31.10	0.58	47.29	0.19	96.39	0.986	0.032	0.000	0.000	0.258	0.110	0.002	0.000	2.466	0.029	3.181	7.065	
80	11.28	0.26	0.00	0.03	4.72	1.14	0.05	0.00	30.94	0.48	47.28	0.23	96.41	0.991	0.034	0.000	0.001	0.266	0.114	0.003	0.000	2.457	0.024	3.185	7.074	
93	11.05	0.26	0.00	0.00	4.79	1.23	0.04	0.04	30.57	0.60	47.12	0.02	95.72	0.975	0.035	0.000	0.000	0.271	0.124	0.002	0.000	2.439	0.031	3.189	7.065	
94	11.05	0.28	0.00	0.00	4.57	1.19	0.02	0.05	30.61	0.58	46.91	0.06	95.33	0.979	0.037	0.000	0.000	0.260	0.121	0.001	0.000	2.451	0.030	3.187	7.066	
95	10.54	0.37	0.04	0.03	4.63	1.21	0.10	0.01	31.13	0.68	47.00	0.23	95.97	0.926	0.049	0.003	0.001	0.261	0.121	0.005	0.000	2.475	0.035	3.170	7.046	
96	10.88	0.19	0.00	0.00	4.20	1.08	0.05	0.00	30.69	0.59	46.61	0.32	94.60	0.970	0.025	0.000	0.000	0.240	0.110	0.003	0.000	2.474	0.030	3.188	7.042	
97	11.16	0.27	0.03	0.00	4.29	1.01	0.03	0.00	31.48	0.57	47.21	0.34	96.38	0.978	0.035	0.002	0.000	0.241	0.101	0.002	0.000	2.495	0.029	3.174	7.056	
99	11.04	0.26	0.02	0.04	4.42	1.28	0.02	0.04	31.25	0.04	47.85	0.19	96.43	0.964	0.034	0.002	0.001	0.248	0.128	0.001	0.000	2.469	0.002	3.207	7.055	
mv	10.89	0.26	0.02	0.02	4.62	1.13	0.04	0.01	30.66	0.55	46.94	0.24	95.37	0.965	0.034	0.001	0.000	0.263	0.115	0.002	0.000	2.456	0.028	3.190	7.054	
sd	0.33	0.04	0.02	0.02	0.33	0.08	0.02	0.01	0.57	0.22	0.60	0.13	0.96	0.027	0.006	0.002	0.001	0.020	0.008	0.001	0.000	0.034	0.011	0.023	0.024	
all data:																										
mv	10.83	0.26	0.02	0.02	4.60	1.14	0.05	0.01	30.52	0.60	46.78	0.25	95.08	0.963	0.035	0.001	0.000	0.262	0.116	0.003	0.000	2.452	0.031	3.189	7.052	
sd	0.33	0.05	0.02	0.02	0.27	0.07	0.03	0.02	0.69	0.21	0.89	0.14	1.50	0.031	0.007	0.001	0.001	0.017	0.007	0.001	0.000	0.030	0.011	0.022	0.026	

Appendix 4: microprobe analyses of feldspars

Electron microprobe analyses of feldspars. Cations calculated by charge balance assuming 8 oxygen atoms per formula unit. Ba and Fe were also analysed: their concentration as oxides is always below 0.1 wt% and was not listed.

Sample Grf 605								
Ca ²⁺	Na ⁺	K ⁺	Si ⁴⁺	Al ³⁺	Total			
0.11	0.84	0.01	2.93	1.07	4.96	porphyroclast 1	mantle	
0.11	0.84	0.01	2.90	1.10	4.97			
0.12	0.84	0.01	2.90	1.10	4.97			
0.06	0.88	0.01	2.97	1.04	4.95		porphyroclast 1	core
0.00	0.04	1.01	3.01	0.97	5.03			
0.00	0.04	0.97	3.01	0.98	5.01			
0.00	0.05	0.96	3.00	0.99	5.01			
0.00	0.10	0.92	3.00	0.99	5.02			
0.00	0.09	0.93	3.00	0.99	5.01			
0.08	0.88	0.01	2.95	1.05	4.97	porphyroclast 2	mantle	
0.12	0.84	0.01	2.92	1.08	4.97			
0.09	0.90	0.01	2.94	1.06	4.99			
0.00	0.03	1.00	3.01	0.98	5.02		porphyroclast 2	core
0.00	0.05	0.97	3.01	0.98	5.01			
0.00	0.03	1.00	3.01	0.98	5.02			
0.00	0.03	0.99	3.01	0.98	5.01			
0.00	0.03	0.99	3.01	0.98	5.02			
0.00	0.03	0.98	3.01	0.98	5.01			
0.00	0.06	0.97	3.01	0.98	5.02	porphyroclast 3	core	
0.00	0.06	0.97	3.01	0.98	5.02			
0.00	0.04	0.99	3.00	0.99	5.03			
0.00	0.04	0.99	3.00	0.99	5.02		porphyroclast 3	mantle
0.00	0.04	1.00	2.99	0.99	5.03			
0.08	0.87	0.01	2.95	1.06	4.96			
0.10	0.86	0.01	2.91	1.09	4.98			
0.07	0.89	0.01	2.94	1.07	4.98	porphyroclast 4	mantle	
0.07	0.80	0.00	3.06	0.93	4.88			
0.10	0.86	0.01	2.92	1.09	4.98			
0.07	0.89	0.01	2.94	1.06	4.98		porphyroclast 4	core
0.00	0.04	0.99	3.00	0.99	5.02			
0.00	0.04	0.97	3.00	0.99	5.01			
0.00	0.03	1.00	3.00	0.99	5.02			
0.00	0.04	0.98	3.00	0.99	5.02			
0.00	0.04	0.99	3.00	0.99	5.02			
0.00	0.04	0.99	3.00	0.99	5.02	porph. 5	core	
0.00	0.07	0.96	3.00	1.00	5.02			
0.00	0.05	0.98	3.00	0.99	5.02			
0.00	0.07	0.95	3.00	0.99	5.01		porph. 5	mantle
0.00	0.04	0.98	3.00	0.99	5.01			
0.03	0.92	0.01	2.98	1.03	4.97			

The average composition of feldspars is An₀ Ab₅ Or₉₅ in cores and An₉ Ab₉₀ Or₁ in mantles.

Sample Tit 125								
Ca ²⁺	Na ⁺	K ⁺	Si ⁴⁺	Al ³⁺	Total			
0.00	0.04	0.98	2.98	1.02	5.03	porphyroclast 1	core	
0.00	0.06	0.96	2.97	1.03	5.02			
0.00	0.03	0.98	2.98	1.02	5.02			
0.00	0.04	0.98	2.98	1.02	5.02		porphyroclast 1	mantle
0.00	0.04	0.99	2.97	1.04	5.03			
0.04	0.93	0.01	2.97	1.04	4.99			
0.07	0.95	0.01	2.94	1.04	5.01			
0.04	0.95	0.01	2.97	1.03	4.99			
0.04	0.95	0.01	2.98	1.02	4.99			
0.03	0.97	0.01	2.99	1.00	5.00	porphyroclast 2	mantle	
0.06	0.93	0.01	2.95	1.04	5.00			
0.04	0.94	0.01	2.97	1.03	4.99			
0.03	0.93	0.01	2.97	1.04	4.98			
0.00	0.04	0.98	2.99	1.01	5.01		porphyroclast 2	core
0.00	0.03	0.99	2.99	1.01	5.02			
0.00	0.04	0.96	2.98	1.02	5.01			
0.00	0.03	0.98	2.99	1.00	5.01			
0.00	0.03	0.99	2.99	1.00	5.02	porphyroclast 3	core	
0.00	0.03	0.97	2.98	1.02	5.01			
0.00	0.05	0.97	2.98	1.02	5.02			
0.00	0.04	0.97	2.99	1.02	5.01			
0.00	0.07	0.93	2.99	1.01	5.01		porphyroclast 3	mantle
0.00	0.09	0.92	2.99	1.01	5.02			
0.03	0.95	0.01	2.97	1.03	4.99			
0.06	0.96	0.01	2.97	1.01	5.01			
0.03	0.94	0.01	2.98	1.02	4.99	porphyroclast 4	mantle	
0.03	0.95	0.01	2.98	1.02	4.99			
0.03	0.95	0.01	2.98	1.02	4.99			
0.05	0.93	0.00	2.96	1.04	4.98			
0.06	0.91	0.01	2.95	1.05	4.98		porphyroclast 4	core
0.06	0.93	0.01	2.95	1.05	5.00			
0.00	0.09	0.93	2.98	1.01	5.02			
0.00	0.10	0.91	2.98	1.02	5.02			
0.00	0.03	0.96	2.99	1.01	5.00			
0.00	0.07	0.94	2.98	1.02	5.01			
0.00	0.04	0.97	2.99	1.01	5.01			
0.00	0.04	0.96	2.99	1.01	5.01			
0.00	0.03	0.98	2.99	1.01	5.01	porphyroclast 4	core	
0.00	0.03	0.98	2.99	1.01	5.01			

The average composition of feldspars is An₀ Ab₅ Or₉₆ in cores and An₄ Ab₉₅ Or₁ in mantles.

Sample Tit 711							
Ca ²⁺	Na ⁺	K ⁺	Si ⁴⁺	Al ³⁺	Total		
0.13	0.85	0.01	2.89	1.11	4.98	porphyroclast 1	mantle
0.07	0.92	0.01	2.94	1.06	5.00		
0.04	0.93	0.01	3.00	0.99	4.97		
0.00	0.04	0.98	3.00	0.99	5.01		core
0.00	0.03	0.99	3.00	1.00	5.01		
0.00	0.03	0.98	3.00	1.00	5.01		
0.00	0.04	0.99	2.99	1.00	5.02		
0.00	0.07	0.93	3.00	1.00	5.01		
0.12	0.86	0.01	2.88	1.12	4.99	porphyroclast 2	mantle
0.10	0.85	0.01	2.92	1.09	4.96		
0.07	0.89	0.00	2.94	1.07	4.97		
0.11	0.76	0.01	2.99	1.01	4.89		
0.13	0.82	0.00	2.88	1.13	4.97		core
0.00	0.07	0.95	3.00	1.00	5.01		
0.00	0.03	0.98	3.00	1.00	5.01		
0.00	0.07	0.96	3.00	1.00	5.02		
0.00	0.08	0.94	2.99	1.00	5.01		
0.00	0.06	0.96	3.00	1.00	5.01		
0.00	0.06	0.96	2.99	1.01	5.01	porphyroclast 3	core
0.00	0.08	0.94	2.99	1.00	5.01		
0.00	0.04	0.97	2.99	1.00	5.01		
0.00	0.05	0.97	3.00	0.99	5.01		
0.00	0.03	0.98	3.00	1.00	5.01		mantle
0.11	0.84	0.01	2.89	1.12	4.98		
0.06	0.91	0.00	2.95	1.06	4.98		
0.11	0.84	0.01	2.90	1.11	4.97		
0.11	0.87	0.01	2.90	1.10	4.98	porphyroclast 4	mantle
0.11	0.85	0.01	2.89	1.11	4.98		
0.10	0.87	0.01	2.90	1.10	4.99		
0.04	0.92	0.01	2.97	1.04	4.98		
0.00	0.04	0.97	3.00	0.99	5.01		
0.00	0.06	0.95	3.00	0.99	5.01		core
0.00	0.06	0.96	3.00	0.99	5.01		
0.00	0.07	0.95	2.99	1.00	5.01		
0.00	0.07	0.94	3.00	0.99	5.01		
0.00	0.07	0.95	3.00	1.00	5.02		

The average composition of feldspars is An₀ Ab₅ Or₉₅ in cores and An₉ Ab₉₀ Or₁ in mantles.

Appendix 5: abbreviations

General abbreviations

AMS – anisotropy of the magnetic susceptibility
BLG – bulging
BPSZ – Bayerischer Pfahl shear zone
CIZ – Central Iberian Zone
EBSD – electron backscatter diffraction
EDS – energy dispersive spectroscopy
emu – electromagnetic unit
GBM – grain boundary migration
GBMR – grain boundary migration recrystallization
HT – high temperature
IGRF – International Geomagnetic Reference Field
IUGS – International Union of Geological Sciences
LOI – loss on ignition
LP – low pressure
LPO – lattice preferred orientation
LREE – light rare earth elements
MZ – Moldanubian Zone
OMZ – Ossa-Morena Zone
p.f.u. – per formula unit
RRE – rare earth elements
SGR – subgrain rotation
SGRR – subgrain rotation recrystallization
SI – international system
SPO – shape preferred orientation
s.z. – shear zone
W – Water

Mineral abbreviations

* after Kretz (1983)

Ab* - Albite	Hy - Hypersthene
Amp - Amphibole	Ms* - Muscovite
An - Anorthite	Opx* - Orthopyroxene
And* - Andalusite	Or - Orthoclase
As - Aluminium silicate	Ph - Phengite
Bt* - Biotite	Pl* - Plagioclase
Cpx - Clinopyroxene	Px - Pyroxene
Crd* - Cordierite	Qtz* - Quartz
Fs - Feldspar	Sil* - Sillimanite
Grt* - Garnet	Ttn* - Titanite
Hbl* - Hornblende	WM - White mica
Kfs* - K-feldspar	

Physical magnitudes and units

ρ – density
g – gravity acceleration
k – magnetic susceptibility
 μ – magnetic permeability
A – ampere
m – meter
N – newton (SI unit for force equivalent to 10^5 dyne in the cgs system)
Wb – weber (SI unit for magnetic flux)
mGal – miligal (unit for gravity acceleration equivalent to 10^{-5} m/s²)
T – tesla (SI unit for magnetic induction equivalent to N/A·m)
nT – nanotesla (= 10^{-9} T)
GPa – gigapascal (unit for pressure equivalent to 10^9 pascal)
kbar – kilobar (unit for pressure equivalent to 10^8 pascal)

Elena Galadí-Enríquez

Diplom-Geologin

Akademische Geoinformatikerin

Geboren am 28. Juli 1977 in Córdoba, Spanien

Hochschulausbildung

- | | |
|-----------------|---|
| 10/1995-06/2000 | Studium der Geologie an der Universität Granada, Spanien. Abschluss mit dem Grad „Licenciada en Geología“ (entspr. „Diplom-Geologin“) |
| 10/2005-10/2006 | Fernstudium „Geographische Informationssysteme UNIGIS professional“ an der Universität Salzburg. Abschluss mit dem Grad „Akademische Geoinformatikerin“ |

Beruflicher und wissenschaftlicher Werdegang

- | | |
|-----------------|--|
| 04/1999-07/2000 | Stipendiatin am Institut für Geodynamik der Universität Granada, Spanien, unter der Leitung von Prof. Dr. Jesús Galindo-Zaldívar

Aufgaben: gravimetrische, magnetische und strukturgeologische Untersuchungen zur Erkundung der Form und Struktur geologischer Körper |
| 12/2000-01/2001 | DAAD-Stipendiatin am geologischen Institut der Universität Erlangen-Nürnberg unter der Leitung von Prof. Dr. Gernold Zulauf

Aufgaben: strukturgeologische Analyse an Gesteinen der Böhmisches Masse |
| 04/2001-01/2002 | Stipendiatin am Institut für Geodynamik der Universität Granada, Spanien, unter der Leitung von Prof. Dr. Jesús Galindo-Zaldívar

Aufgaben: gravimetrische, magnetische und strukturgeologische Untersuchungen zur Erkundung der Form und Struktur plutonischer Körper der Iberischen Masse; Teilnahme an der Durchführung des seismischen Reflexionsprofils <i>IBERSEIS</i> |
| 05/2002-01/2004 | Angestellte der Universität Erlangen-Nürnberg unter der Leitung von Prof. Dr. Gernold Zulauf; externe Mitarbeiterin des Bayerischen Geologischen Landesamtes

Aufgaben: geologische Kartierung des Blattes TK 25 Nr. 7246 Tittling (Bayerischer Wald) und damit verbundene Büro- und Labortätigkeiten |
| 06/2004-09/2004 | Angestellte der Universität Erlangen-Nürnberg unter der Leitung von Prof. Dr. Gernold Zulauf; externe Mitarbeiterin des Bayerischen Geologischen Landesamtes

Aufgaben: strukturgeologische Analyse hydrogeologisch relevanter, spröder Deformationen im Fürstensteiner und Hauzenberger Pluton (Bayerischer Wald) |
| 10/2004-12/2005 | Angestellte der Universität Frankfurt a. M. unter der Leitung von Prof. Dr. Gernold Zulauf; externe Mitarbeiterin des Bayerischen Geologischen Landesamtes bzw. des Landesamtes für Umwelt

Aufgaben: strukturgeologische Analyse hydrogeologisch relevanter, spröder Deformationen im Fürstensteiner und Hauzenberger Pluton (Bayerischer Wald) |
| seit 04/2006 | Angestellte des Bayerischen Landesamtes für Umwelt zur Mitarbeit am Referat 102 „Landesaufnahme Geologie und Boden Ost“

Aufgaben: geologische Kartierung und damit verbundene Büro- und Labortätigkeiten, digitale Erstellung und Kompilation geologischer Karten, Dokumentierung geologisch relevanter Aufschlüsse |

Elena Galadí-Enríquez

Master degree in Geology

Postgraduate in Geoinformatics

Born on July 28, 1977 in Córdoba, Spain

Education

10/1995-06/2000 Geology study at the University of Granada, Spain. Completion with degree „Licenciada en Geología“ (Master degree in Geology)

10/2005-10/2006 „Geographic Information Systems UNIGIS professional“ distance learning at the University of Salzburg. Completion with degree „Akademische Geoinformatikerin“ (Postgraduate in Geoinformatics)

Professional and scientific career

04/1999-07/2000 Scholarship at the Department of Geodynamics, University of Granada, Spain, under direction of Prof. Dr. Jesús Galindo-Zaldívar

Functions: gravimetric, magnetic and structural-geological research of the shape and structure of geological bodies

12/2000-01/2001 DAAD- Scholarship at the Institute of Geology, University of Erlangen-Nürnberg, Germany, under direction of Prof. Dr. Gernold Zulauf

Functions: structural-geological analysis on rocks of the Bohemian Massif

04/2001-01/2002 Scholarship at the Department of Geodynamics, University of Granada, Spain, under direction of Prof. Dr. Jesús Galindo-Zaldívar

Functions: gravimetric, magnetic and structural-geological research of the shape and structure of plutonic bodies of the Iberian Massif; participation on the performance of the seismic profile *IBERSEIS*

05/2002-02/2004 Employee at the University of Erlangen-Nürnberg, Germany, under direction of Prof. Dr. Gernold Zulauf; external collaborator of the Bavarian Geology Agency

Functions: geological mapping of topographic sheet 1:25000 No. 7246 Tittling (Bavarian Forest) and related laboratory and bureau tasks

06/2004-09/2004 Employee at the University of Erlangen-Nürnberg, Germany, under direction of Prof. Dr. Gernold Zulauf; external collaborator of the Bavarian Geology Agency

Functions: structural-geological analysis of hydrogeologically relevant, brittle deformations in the Fürstenstein and Hauzenberg Plutons (Bavarian Forest)

10/2004-12/2005 Employee at the University of Frankfurt a. M., Germany, under direction of Prof. Dr. Gernold Zulauf; external collaborator of the Bavarian Geology Agency (later Bavarian Environment Agency)

Functions: structural-geological analysis of hydrogeologically relevant, brittle deformations in the Fürstenstein and Hauzenberg Plutons (Bavarian Forest)

since 04/2006 Employee at the Bavarian Environment Agency, Unit 102 „Geological and Pedological Survey East“

Functions: geological mapping and related laboratory and bureau tasks, digital production and compilation of geological maps, documentation of sites of geological interest